Magnetically Enhanced Quadrupole Mass Spectrometer

Thesis submitted in accordance with the requirements of the University of Liverpool

for the degree of

Doctor in Philosophy

by

Simon Maher

Department of Electrical Engineering and Electronics

University of Liverpool

September 2013

Synopsis

The Quadrupole Mass Filter (QMF) is the key component of a Quadrupole Mass Spectrometer (QMS) first described by Nobel laureate Wolfgang Paul and co-worker Helmut Steinwedel in 1953. The QMS remains a widely used analytical tool for separating charged species in space according to their mass-to-charge ratio, with an extensive range of applications in both industry and research.

In the original work of Paul and Steinwedel much emphasis was placed on the fact that the QMF separates ions due to the quadrupolar electric field (comprising dc and ac components) and without the use of magnetic fields. In the present thesis both experimental and theoretical work is presented, to demonstrate that the application of a magnetic field to a QMS enhances device performance. Theoretical work has focussed on the analytical investigation of the Mathieu equation for this particular case. This has led to an extensive simulation study of a QMS under the application of static and dynamic magnetic fields.

A method is described that enables the three-dimensional (3D) fields of a simple QMF to be determined to a high accuracy. The technique produces accurate field values and was used to investigate fringe field effects particularly at the entrance to the QMF where they can often be detrimental to performance. Moreover, a two-dimensional (2D) software model was used to study the behaviour of the QMF and modified to incorporate the effect of applying a magnetic field. The software model is capable of accurate simulation of spectra allowing the user to specify QMF dimensions and various applied input signals including, electrode geometries, dimensions and operating parameters.

A new performance method has been developed that allows the effective stability diagram of the QMS to be mapped numerically for given operational

conditions. This method generates an effective stability diagram which enables instrument behaviour to be predicted and provides a means for optimising performance. Using this method the stability diagram has been effectively mapped for a QMS with a static transverse magnetic field applied in zone 1. This provides an insight into the fundamental workings of this device therefore allowing operating parameters to be optimised accordingly.

The ability to scan a range of ion masses and provide uniformity of the effect of the magnetic field is a necessary requirement for a viable mass spectrometer instrument. The proof-of-concept for this novel instrument is demonstrated using a dynamic magnetic field. In order to implement the magnetic field with the conventional scanning method a Helmholtz coil electromagnet was used; this allowed the magnetic field intensity to be altered by varying the current. A custom current ramp was designed and built to operate the Helmholtz coil. This was manually synchronised with a commercial quadrupole mass spectrometer to provide a constant peak width mass scan demonstrating the proof-of-concept for a magnetically enhanced QMS.

A magnetically enhanced QMS is a novel instrument that has improved performance with more powerful monitoring and sensing capabilities than conventional QMS instruments available hitherto. One of the challenges of developing and deploying portable MS is that of reducing the size (to render the MS system portable), whilst at the same time maintaining instrument performance in terms of resolution, sensitivity and mass range. Such an instrument in deployment should find a range of applications.

Acknowledgements

The University of Liverpool coat of arms depicts an open book inscribed with the Latin phrase “*fiat lux*” (which is translated “*let there be light*”) the first words spoken by God at the beginning of time in the book of Genesis. This is an expression that incorporates so many facets relevant to science: knowledge, truth, wisdom, design, creativity, energy and so much more. It is in this light that my PhD training has been undertaken. This process has not been without its struggles and I have received significant help and guidance from so many to whom I am indebted and sincerely grateful for their kindness.

First and foremost my thanks is aimed heavenwards to the Lord God Almighty for all that He has given me.

I owe a huge debt of gratitude to my supervisor, Prof. Stephen Taylor, who gave me the opportunity to undertake research in his group and continues to provide a constant flow of support and encouragement. It has been a great privilege to work under his guidance.

I am very thankful to Dr. J. R. Gibson, acting as my secondary supervisor, who has provided a wealth of advice and assistance throughout this work.

I am also extremely grateful to the Department of Electrical Engineering & Electronics at the University of Liverpool and the Engineering and Physical Sciences Research Council (EPSRC) for awarding me a Doctoral Training Grant without which I would not have been able to undertake this research.

I offer my sincerest thanks to the many past and present members of the Mass Spectrometry group for their help and whole-hearted support: Dr. S. U. Syed, Mr. F. P. Jjunju, Dr. B. Brkic, Dr. T. J. Hogan, Dr. F. Salarzaei, Dr. J. Sreekumar, Dr. K. Evans, Dr. V. Leus, Mr. S. Giannoukos and Mrs. M. Juno.

I would like to express my thanks for the help and technical assistance received from the staff at Q-Technologies (Liverpool, UK): Dr. N. France, Mr. D. Taylor, Mrs. A. Standish and Mr. A. Taylor.

Many thanks to Dr. R. T. Smith who has been a great source of advice and encouragement and to Mr. D. M. Hughes from the Department of Mathematical Sciences (University of Liverpool) for his advice, suggestions and assistance.

Special thanks to Mr Jonathan Maher, Mr Graham Swift and Dr. R. T. Smith for proof reading this thesis. This version of the thesis is that corrected in response to the comments of the examiners following the viva. The contribution of the examiners, Prof. John F. J. Todd and Prof. Simon Maskell, in this respect is acknowledged.

I would like to acknowledge the help and assistance provided by technical staff at the University of Liverpool. From the Department of Electrical Engineering: Mr. A. Roby, Mr. R. Wratten, Mr G. Cook, Mr. J. Carrick, Ms. J. Anson, Mr. J. Lynch and Mr. A. Edwards; from the School of Engineering: Mr. D. Atkinson and Mr. M. Jahme; from the e-Science team thanks are due to Dr. Ian Smith for his assistance in utilising the Condor High Throughput Computing Service. I would like to thank Dr. M. Egan of the Ultra Mixing and Processing Facility (Department of Chemistry) for his kindness in lending specialist equipment and Ms. Zelda Chatten at the Harold Cohen Library for her assistance in locating several obscure research articles.

I am very grateful for the abundance of love and wholehearted support received from my family and friends. For my wife, Amy, who has always been a great encouragement and has been so supportive and patient with me. For my beloved son Timothy who brings such joy to my heart. For my parents, the late & great David and Susan, who have been an inspiration and have always, supported, taught, encouraged

and prayed for me – whose example and guidance has influenced all my endeavours. As well to David, Jonathan, Hannah, Rebecca, and David, Jenny, Billy, Sue; Maria and Billy; John and the late Anne; the late John (Spud) and Gertie (3G) – thank you all for your warmth, encouragement, generosity and banter. To all the saints at Larkhill for their encouragement, prayers and support – thank you.

Thank you all so very much!

> "Blessed be the Lord, who daily loadeth us with benefits, even the God of our salvation. Selah." (Psalm 68:19)

Contents

Figures

Tables

Abbreviations

2D	Two dimensional
3D	Three dimensional
BEM	Boundary Element Method
CI	Chemical Ionisation
CID	Collision Induced Dissociation
DESI	Desorption Electrospray Ionisation
DF	Double Focusing
DOF	Distance of Flight
EI	Electron Ionisation
ESI	Electrospray Ionisation
FAB	Fast-Atom Bombardment
FD	Field Desorption
FTICR	Fourier Transform Ion Cyclotron Resonance
GC	Gas Chromatography
GUI	Graphical User Interface
ICR	Ion Cyclotron Resonance
IMS	Imaging Mass Spectrometry
LC	Liquid Chromatography
MALDI	Matrix Assisted Laser Desorption/Ionisation
MIMS	Membrane Inlet Mass Spectrometry
MS	Mass Spectrometry
MS/MS	Tandem Mass Spectrometry
QIT	Quadrupole Ion Trap
QMA	Quadrupole Mass Analyser
QMF	Quadrupole Mass Filter
QMS	Quadrupole Mass Spectrometer
QQQ	Triple Quadrupole Mass Spectrometer
Q-TOF	Quadrupole Time of Flight
RGA	Residual Gas Analyser
SF	Single Focusing
SIMS	Secondary Ion Mass Spectrometry
TOF	Time of Flight

Symbols

a	Mathieu stability parameter
B	Magnetic field intensity
e	Charge on electron
E	Electric field intensity
f	Frequency of rf supply
L	Length of analyser electrodes
m	Mass
m/z	Mass-to-charge ratio
N	Number of rf cycles
q	Mathieu stability parameter
r	Radius of the analyser electrodes
r_0	Inscribed electrode radius
rf	Radio Frequency
r_{ie}	Ion source exit radius
t	Time
U	Direct potential
V	Alternating potential
v	Ion velocity
V_{ion}	Nominal ion source accelerating voltage
x_0	Initial displacement of ion from *x*-axis
x_{max}	Maximum displacement of ion from *x*-axis
y_0	Initial displacement of ion from *y*-axis
y_{maz}	Maximum displacement of ion from *y*-axis
z	Charge number
Δm	Mass spectral peak width measured at a given percentage of peak height
ξ	Modified time parameter
ϕ	Electric potential
ω	Angular frequency of rf supply

Chapter 1 : Introduction

BACKGROUND

1.1 Mass Spectrometry

Mass Spectrometry (MS) is a powerful technique for identifying unknown compounds, quantifying known compounds, and exploring molecular structures. This year (2013) marks a century of MS, which was first pioneered by Nobel laureate Sir J. J. Thomson in 1913 [1]. Since that time MS has become a subject area of enormous scope and the mass spectrometer has become an invaluable analytical tool for a wide range of professionals including, physicists, chemists, biologists, physicians, astronomers, geologists, physiologists and materials scientists. Mass spectrometers are used in a wide range of applications in the chemical, electronics, food processing, petroleum, and pharmaceutical industries. They are routinely used to monitor nuclear facilities, detect environmental pollution, diagnose drug abuse and monitor the residual gases in vacuum systems. Mass spectrometers are used for underwater monitoring in the ocean depths and for extra-terrestrial investigations during space missions.

According to a recent study, the world market for MS reached US $2.9 billion in 2011 and is forecast to grow to US $3.92 billion in 2015 [2]. The growth in sales is sustained by persistent advances in technology that have positioned MS as a primary detection method in drug discovery and development, in pharmaceutical quality assurance/quality control, for radiometric dating, helium-based leak detection and several other applications [3]. Notably, the advancing capability of measuring relative abundance has led to the rapid expansion in the field of quantitative proteomic mass spectrometry.

All mass spectrometers operate by performing three main functions:

(i) Generation of gas-phase ions

(ii) Separation of ions based on their mass-to-charge ratio, and,

(iii) Detection of the number of ions for each mass-to-charge ratio (*m/z*).

The main steps involved are shown, in figure 1.1, below:

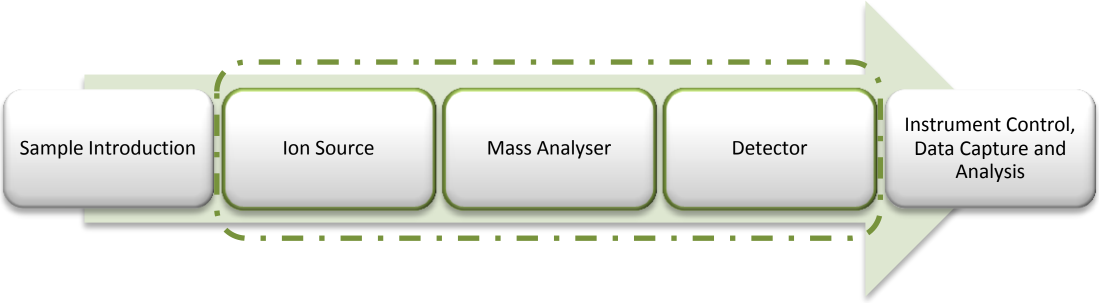

Figure 1.1: MS stages

Samples are introduced into the MS instrument using a variety of methods. In the ion source region, neutral samples are ionised and then transported into the mass analyser. The heart of any mass spectrometer is the mass analyser. This is usually a region of low pressure (high vacuum) in which the ions are separated according to their mass-to-charge ratio electrically, magnetically or a combination of both. After separation of the ions, they are detected and the generated signal is processed for display to the user as a mass spectrum.

There are various types of mass spectrometer available and they are usually differentiated based on the method of mass analysis (and hence the physical principle of operation) that the instrument incorporates (see table 1.1). The quadrupole mass spectrometer (QMS) is one of the most common mass analysers and it is examined extensively in this work.

Mass Analyser	Separation Principle
Magnetic Sector	Momentum
Electrostatic Sector	Kinetic Energy
Quadrupole, Quadrupole Ion Trap	Path Stability
Ion Cyclotron Resonance, Orbitrap	Orbital Frequency
Time-of-Flight	Velocity

Table 1.1: Physical principles governing mainstream mass analysers

Figure 1.2 provides a generic overview of MS technology considered in the larger scheme of analytical chemistry. This figure is non-exhaustive and also highlights some of the other competing techniques for mass analysis:

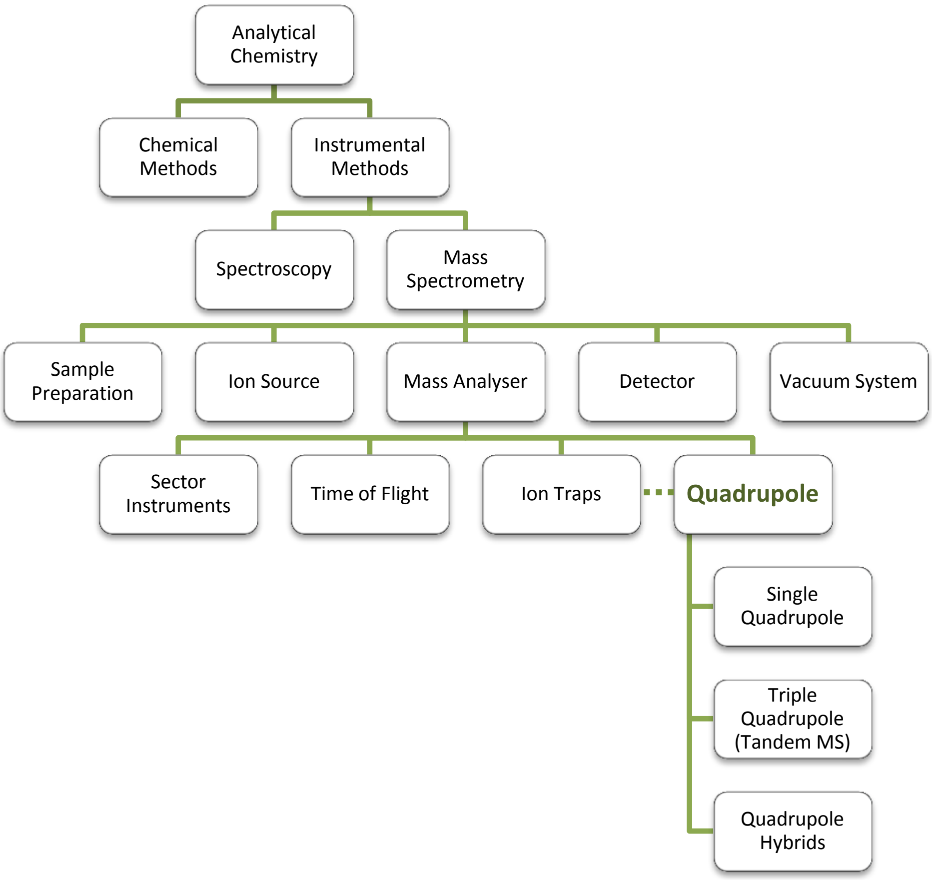

Figure 1.2: MS Hierarchy

1.1.1 Performance Criteria

The performance of a mass analyser is typically defined by the following criteria: mass accuracy, resolution, mass range, scan speed, sensitivity, dynamic range and tandem analysis capabilities.

Mass Accuracy

The mass accuracy is the ability to measure or calibrate the instrument response against a known entity. This is usually measured in parts per million (ppm) or milli mass units (mmu). This is the ability with which the analyser can *accurately* provide *m/z* information and is related to instrument stability and resolution.

Mass accuracy is typically defined as:

$$Mass\ Accuracy = \frac{\frac{m}{z}\,measured\ error}{actual\,\frac{m}{z}} \qquad (1.1)$$

The measured error is the difference between the exact mass (found by summing the masses of each atom in a molecule) and the mass determined experimentally. For example, let the exact mass of a molecule (calculated by adding up the masses of each atom in the molecule) equal 200.00Da. The measured mass (experimentally measured value) is 200.02Da. Then the difference is 0.02Da or 20mmu. The mass accuracy is then calculated as $\frac{0.02}{200} = 0.0001$ and typically given in terms of ppm (i.e., 100ppm).

Resolution

Resolution is the ability of a mass spectrometer to distinguish between ions of different *m/z*. Greater resolution corresponds to the improved ability to separate different ions (peaks of the mass spectrum).

Resolution is defined as:

$$Resolution = \frac{m}{\Delta m} \tag{1.2}$$

where, *m* is the *m/z* of a specified peak and *Δm* is the width of the peak at a height that is a given fraction of the maximum peak height. In this work the 10% peak height definition is used unless otherwise stated. It is also common to see 50% peak height definition used in the literature (also known as full width at half maximum, FWHM). The parameters used for defining resolution are illustrated in figure 1.3:

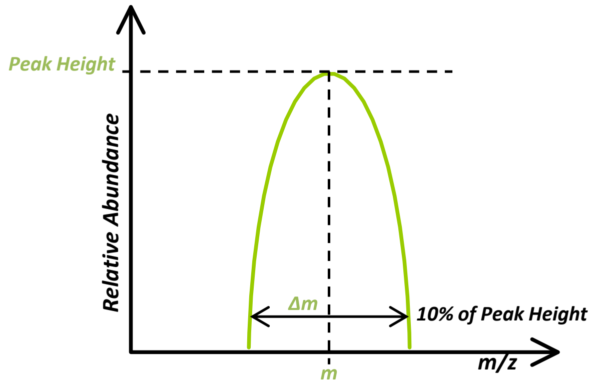

Figure 1.3: Relationship between *m* and *Δm* for a single mass peak

Mass Range

The mass range is the range of *m/z* amenable to analysis by a given mass analyser.

Scan Speed

Scan speed is a measure of the rate at which the mass analyser can scan over a particular mass range. It is the number of spectra per unit time that can be generated.

Sensitivity

Two different measures of sensitivity are recommended according to the International Union of Pure and Applied Chemistry (IUPAC) [4]. The first, which is suitable for relatively non-volatile materials as well as gases, depends upon the observed change in ion current for a particular amount or change of flow rate of sample though the ion source. The second method of stating sensitivity, which is most suitable for gases, depends upon the change of ion current related to the change of partial pressure of the sample in the ion source. The second method is more common for QMS where the sensitivity, S, is typically measured in Amps per torr,

$$S = \frac{I^{+}}{P} \tag{1.3}$$

where I^{+} is the ion current measured at the detector and P is the partial pressure of the gas.

Dynamic Range

There is an upper limit to the magnitude of signal a mass spectrometer can measure without saturating the detector. If this is exceeded then part of the signal is lost. Similarly there is a lower limit to the magnitude of a signal that can be measured and distinguished from electronic and chemical background noise. The ratio of the maximum and minimum signals that can be detected gives a measure of the dynamic range of a mass spectrometer.

Tandem Analysis Capability

The term “tandem” mass analysis refers to events being either tandem in space or tandem in time. Tandem mass analysis in space is performed by multiple consecutive mass analysers attached together whereas tandem mass analysis in time is performed with the same analyser, which isolates the ion of interest, fragments it, and analyses the fragment ions. The purpose is to provide structural information about a molecule from the fragmentation of the parent ion.

Tandem mass analysis can be performed *n* times, where *n* relates to the number of analyses performed. This is often given as MS^n. For example, tandem analysis can be performed using 3 quadrupole instruments arranged consecutively in space with the central quadrupole acting as a collisional cell/ion guide to fragment the parent ion of interest. This is termed a ‘triple quadrupole’ and has two analysis stages, hence $n = 2$.

1.1.2 Mass Analyser Comparison

In any comparison of different mass analyser technologies, the intended application becomes an important consideration. The choice of mass analyser, in any particular application, is governed by both performance characteristics (table 1.2) as well as cost and instrument size (table 1.3). For example, consider a quantitative application which involves measuring only known compounds; a complete mass spectrum is unnecessary for this type of analysis. The acquisition of a complete mass spectrum is essential however for qualitative/quantitative applications, in which the sample composition may not be entirely known. The quadrupole mass analyser can also be operated in selected-ion monitoring mode which is well suited for quantitative applications.

Furthermore, certain mass analysers are more amenable to being combined with other (separation) techniques. Gas Chromatography-Mass Spectrometry (GC-MS) and Liquid Chromatography-Mass Spectrometry (LC-MS) combine the features of gas/liquid chromatography and mass spectrometry to identify different substances within a test sample. In principle GC-MS experiments may be carried out using any method of mass analysis; however, the vast majority of commercial GC-MS units utilise a quadrupole MS [5]. The quadrupole mass analyser is well suited for chromatography as it allows rapid scanning and uses low voltages, which make it tolerant of relatively high operating pressures, such as those encountered in LC-MS [6].

Performance Measure	**Quadrupole**	**Ion Trap**	**Time of Flight**	**Magnetic Sector**	**Fourier Transform ICR**	**Orbitrap**
Accuracy	100ppm	100ppm	200-2000ppm	<5ppm	<5ppm	<5ppm
Resolution	4,000	4,000	8,000	30,000	100,000	>100,000
Mass Range	<4,000	4,000-10,000	>300,000	10,000	10,000	<4,000
Scan Speed	~1 sec	~1 sec	milliseconds	<5 sec	~1 sec	<5 sec
Tandem MS	MS^2 (triple quad)	MS^n	MS^2	MS^2	MS^n	MS^n

Table 1.2: Comparison of typical performance characteristics (adapted from [2])

Mass Analyser	**Advantages**	**Disadvantages**
Quadrupole	✓ Tolerant of high pressures ✓ Well suited for electro-spray ✓ Small size and light weight ✓ Inexpensive ✓ Simple to operate	✗ Mass range limited to ~<4,000 *m/z* ✗ Low resolution ✗ Electrode contamination can compromise resolution and sensitivity ✗ Poor adaptability to certain ionisation technologies in particular Matrix Assisted Laser Desorption Ionisation (MALDI)
Ion Trap	✓ Well suited for coupling with ambient ionisation sources ✓ Small size ✓ Medium resolution ✓ Well suited for tandem MS (MS^n, $n \leq 4$)	✗ Mass range limited to ~<10,000 *m/z* ✗ High machining tolerances for 2D linear ion trap (LIT) electrodes
Magnetic Sector	✓ Capable of high resolution ✓ Capable of exact mass measurements ✓ Medium mass range ✓ Multi-collector analysis	✗ Not tolerant of high pressure ✗ Expensive ✗ Instrumentation is very bulky ✗ Relatively slow scanning
Time of Flight	✓ Highest mass range ✓ Very fast scan speed ✓ Ease of adoption to MALDI (due to pulsing nature of technique)	✗ Low resolution ✗ Difficulty of adaptation to certain ionisation technologies in particular electro-spray
Fourier Transform ICR	✓ High resolution ✓ Well suited for tandem MS (MS^n, $n \leq 4$)	✗ High vacuum ($<10^{-7}$ Torr) required ✗ Superconducting magnet required ✗ Expensive ✗ Instrumentation is very bulky
Orbitrap	✓ High resolution ✓ High sensitivity ✓ High dynamic range ✓ No magnetic fields required	✗ Expensive ✗ Mass resolution and accuracy are linearly proportional to signal acquisition time

Table 1.3: Mass Analyser Advantages and Disadvantages

References

[1] J. J. Thomson, *Rays of Positive Electricity and Their Application to Chemical Analyses*: Longmans, Green, 1913.

[2] TechNavio, "Global Mass Spectrometry Market 2011-2015," 2012.

[3] M. T. Ceramics. (2008). *Advanced Materials in Mass Spectrometry Instruments*. Available: http://www.pharmaceuticalonline.com/Doc/Advanced-Materials-In-Mass-Spectrometry-0001

[4] A. D. McNaught and A. Wilkinson, *Compendium of chemical terminology* vol. 1669: Blackwell Science Oxford, 1997.

[5] Agilent-Technologies. (2007). *Considerations for Selecting GC/MS or LC/MS for Metabolomics*. Available: http://www.chem.agilent.com/Library/selectionguide/Public/5989-6328EN.pdf

[6] R. E. Ardrey, "Liquid Chromatography," in *Liquid Chromatography – Mass Spectrometry: An Introduction*, ed: John Wiley & Sons, Ltd, 2003, pp. 7-31.

Chapter 2 : Literature Review

HISTORICAL OVERVIEW

2.1: A Century of Mass Spectrometry

One hundred years has passed since the ground-breaking work of Sir. J. J. Thomson who developed the mass spectrometer in 1913 [1]. In this review the major achievements in mass spectrometry (MS) of the past century are noted including those leading up to the initial work of Thomson. Particular emphasis is given to the developments relating to Quadrupole Mass Spectrometry (QMS) first described by Wolfgang Paul and his co-worker Helmut Steinwedel at the University of Bonn in 1953 [2] (some 40 years after the pioneering work of Thomson).

Due to the vastness of the subject area and the quality of the manifold research efforts that have been undertaken over the last 100 years (and more) contributing to the foundations and furtherance of MS, it is to be understood that not all of the key contributions may have been included in this historical review. The progress of science is often achieved by the small incremental steps of a large number of researchers and the achievements reported herein are only a representation of the work.

2.1.1 Laying the Foundations

Mass spectrometers are instruments which analyse substances according to the mass-to-charge ratio (*m/z*) of constituent molecules allowing both qualitative and quantitative analyses. In order to achieve this, chemical compounds must first be **ionised**, then **separated** (based on *m/z*) and finally **detected** to produce a meaningful output for the user. Furthermore the separation and (typically) the ionisation processes are carried out ***in vacuo***.

Mass spectrometry, in its modern form, has been the consequence of important scientific and technological advances in the past. In particular developments in the 19th century which elucidated the electrical nature of matter and later the application of Newtonian mechanics to the motion of electrical charges (electrodynamics) were to prove significant in the foundations of MS. Historically ideas on the atomic nature of matter can be traced back to the ancient Greeks (Democritus). However such ideas were to lay dormant for nearly 2000 years until undergoing a revival in the 19th century through scientists like Dalton (laws of chemical combination), Maxwell (kinetic theory of gases) and Faraday (ions in electrolysis) to name but a few [3].

The first stage of MS is to generate ions. The term “ion” (along with the terms “anion” and “cation”) was first introduced by Faraday in 1834 [4]. He used it to describe the charge carriers which passed between electrodes immersed in an aqueous medium. In 1870 the English physicist Crookes invented the ‘Crookes tube’, an electrical discharge tube developed from the earlier ‘Geissler tube’. The key advancement made by Crookes was to use an improved Sprengel vacuum pump [5]. The reduced tube pressure meant an increased mean free path for the negatively charged particles making up the cathode ray beams. The term ‘cathode ray’ (beam of electrons) itself was first introduced by German scientist Eugen Goldstein, an early investigator of charged particles and discharge tubes, to describe the light emissions from the Crookes tube [6]. In 1886 he discovered what he termed ‘canal rays’ (positively charged species) while studying the electrical discharges observed when the cathode of a cathode-ray tube was perforated [7]. He observed that these canal rays travelled in the opposite direction to the (then unidentified) negatively charged particles of cathode rays and therefore must be positively charged.

In 1895 French physicist Jean Perrin confirmed that canal rays were positively charged and that the charge magnitude was approximately equal to that of the cathode rays [8]. This paved the way for the historic experiments of Thomson in 1897, in which he discovered the electron (which he named a ‘corpuscle’) [9]. He confirmed that cathode rays consist of negatively charged particles and was able to measure the ratio of the electric charge of a particle to its mass (e/m). Using a similar experimental approach to Perrin, Thomson deflected the cathode rays with a magnet to see if the charge could be separated from the rays. He found that it could not. When the cathode rays were deflected with a magnet away from the detector no appreciable signal was observed. Whereas when the cathode rays were deflected towards the detector the signal increased. In his second experiment, Thomson attempted to deflect the cathode rays by applying an electric field produced from a pair of metal plates, previously carried out by Hertz in 1892 [10]. Thomson was able to observe the beam deflection produced by the electrically charged metal plates. Hertz had previously observed no effect on the rays. This was possibly due to poor vacuum conditions and/or space charge effects on or near the sides of the tube shielding the externally applied field. In the third of Thomson’s historic experiments he used a combination of electric and magnetic fields and was able to infer the *e/m* ratio of the corpuscles.

By adjusting the magnetic field strength in the region between the metal plates Thomson was able to cancel the deflection essentially balancing the forces due to the electric and magnetic fields. Using the force law recently developed by Lorentz in 1892 which combines the force contributions from the electric and magnetic fields [11], Thomson was able to deduce the mean velocity of the particles. Thomson then proceeded to measure the deflection of the cathode rays due to the electric field alone; knowing the length, separation and applied voltage across the metal plates as well as the horizontal speed of the rays, the charge to mass ratio (*e/m*) was calculated using the relation[1]:

$$\tan\theta = \left(\frac{e}{m}\right)\frac{Vl}{dv_x^2} \tag{2.1}$$

Here, V is the voltage applied to the plates, l is the length of the plates, d is the plate separation, v_x is horizontal velocity of the cathode rays, *e/m* is the charge to mass ratio of the cathode rays and θ is the angle of the beam deflection.

Thomson had discovered the essential nature of the cathode rays; however, the nature of canal rays remained to be identified. The magnetic and electric deflection of canal rays was first measured by Wilhelm Wien in 1898 who found that the velocity of canal rays was much smaller than that of the cathode rays. The ratio *e/m* was also smaller. Notably in his experiments, Wien identified an unknown positive particle (which we know as a proton) to be equal in mass to the hydrogen atom [12]. Thomson, in considering the work of Wien with canal rays (positive rays), commented:

---

[1] Note: the original notation of Thomson is not used here

"The composition of these positive rays [investigated by W. Wien] is much more complex than that of the cathode rays, for whereas the particles in the cathode rays are all of the same kind, there are in the positive rays many different kinds of particles. We can, however, by the following method sort these particles out…" [13]

Thomson began working with positive rays in 1899 following his interest in the experiments of Wien [14]. By 1911, using a refined version of Wien's experimental setup, but notably using a highly exhausted chamber (improved vacuum) and a photographic plate (improved detector), Thomson was able to distinguish different "electric atomic weights" (the ratio of m/e for a compound compared to hydrogen m/e) [15, 16]. The magnetic and electric fields were oriented so as to produce orthogonal deflections such that a parabolic curve was recorded on the photographic plate for identical species of varying speed. The lines recorded represented the different electric atomic weights of the residual gases in the chamber which had been ionised and deflected accordingly on the photographic plate.

2.1.2 The Birth of Mass Spectrometry

Parabola Spectrograph

In 1912, Thomson invented the world's first scanning mass spectrometer [17] (then called a 'parabola spectrograph'). In doing so, he first had to refine his detection method to be able to measure relative abundance. He removed the photographic plate and instead made a parabolic slit in a metal plate and placed a Faraday cup behind it connected to an electroscope. By adjusting the magnetic field each positive ion beam could be deflected through the slit and the intensity measured. Thomson could then plot a mass spectrum of ion abundance against relative mass. Mass spectrometry was born.

Ion detection methods had shifted from fluorescent tubes [18] to photographic plates [16] and now ion collectors (Faraday cup). The difference is subtle yet significant. Photographic plates (and fluorescent tubes) provided a visible trace of all the various ions i.e., simultaneous detection of all present *e/m* species at any given time. However, these detection methods were only capable of providing a qualitative and at best semi-quantitative measurement. The net result was an image spectrum (figure 2.2). Whereas incorporating ion counting detection methods and causing only a single *e/m* to be recorded for a given setup, Thomson was able to produce a mass spectrum providing both qualitative and quantitative measures (figure 2.1).

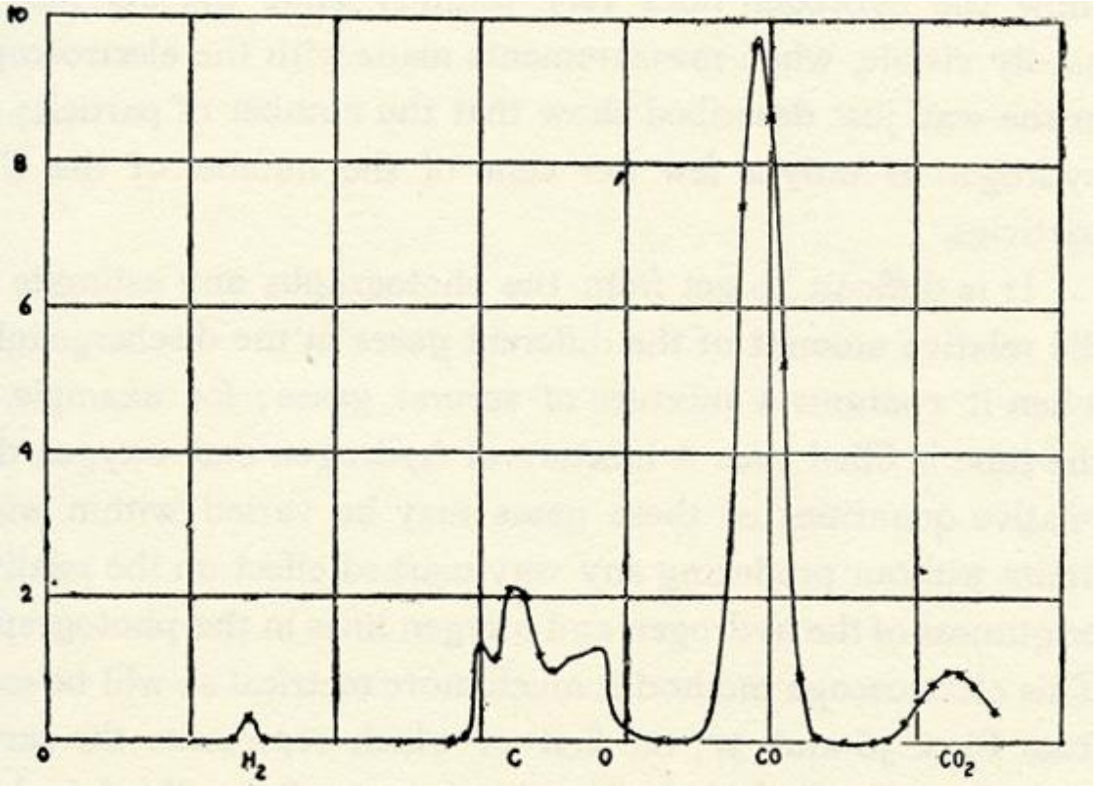

Figure 2.1: Thomson's Mass Spectrum: Carbon Monoxide (CO) [1]

In 1913, Thomson published a monograph entitled “Rays of Positive Electricity and Their Application to Chemical Analysis” [1]. The foresight of

Thomson regarding the power of this analytical technique was evident, as in the foreword he wrote:

"... one of the main reasons for writing this book was the hope that it might induce others, and especially chemists, to try this method of analysis. I feel sure that there are many problems in Chemistry which could be solved with far greater ease by this than by any other method."

The first major result of MS came about in the same year. While investigating positive rays, Thomson using neon in his discharge tube channelled a beam of neon ions through his apparatus and observed two different parabolic light patches on the photographic plate, one corresponding to atomic weight 20 and the other 22 (figure 2.2). At this point stable elements where thought to be mono-isotopic by the scientific community. At first Thomson was cautious in his interpretation and instead left the topic open ruling out several of his own suggestions (such as doubly charged carbon dioxide, neon hydride and a new element). He concluded,

"... neon is not a simple gas but a mixture of two gases, one of which has an atomic weight about 20 and the other about 22." [13]

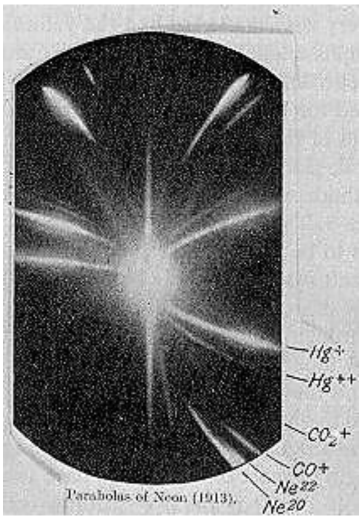

Figure 2.2: Parabola Spectrograph result showing isotopes of ^{20}Ne and ^{22}Ne

Mass Spectrograph

Following the end of the First World War Aston, previously a research assistant to Thomson but now under the direction of Rutherford, re-defined the concept of isotopes to include stable and not just radioactive elements [19-23]. In doing so he developed the mass spectrograph, an instrument superior to the parabola spectrograph with a resolving power 10x greater which he used to discover 212 naturally occurring isotopes.

Single Focusing Magnetic Sector

Around the same time in 1918, Dempster at the University of Chicago constructed a magnetic sector analyser and laid the ground work for electron impact ionisation [24]. Using his magnetic sector analyser, Dempster discovered several isotopes including three isotopes of magnesium [25], four isotopes of zinc [26] and is credited with the discovery of uranium 235.

Dempster's magnetic sector analyser established the basic design theory that is still used for sector instruments today (figure 2.3). In Dempster's instrument ions are accelerated from the ion source (G) through a narrow slit (S_1). They are then deflected through 180° by a homogenous magnetic field in the analyser region (A) and ions of a particular *e/m* are allowed to pass through a second slit (S_2) and register a charge on the electrometer (E).

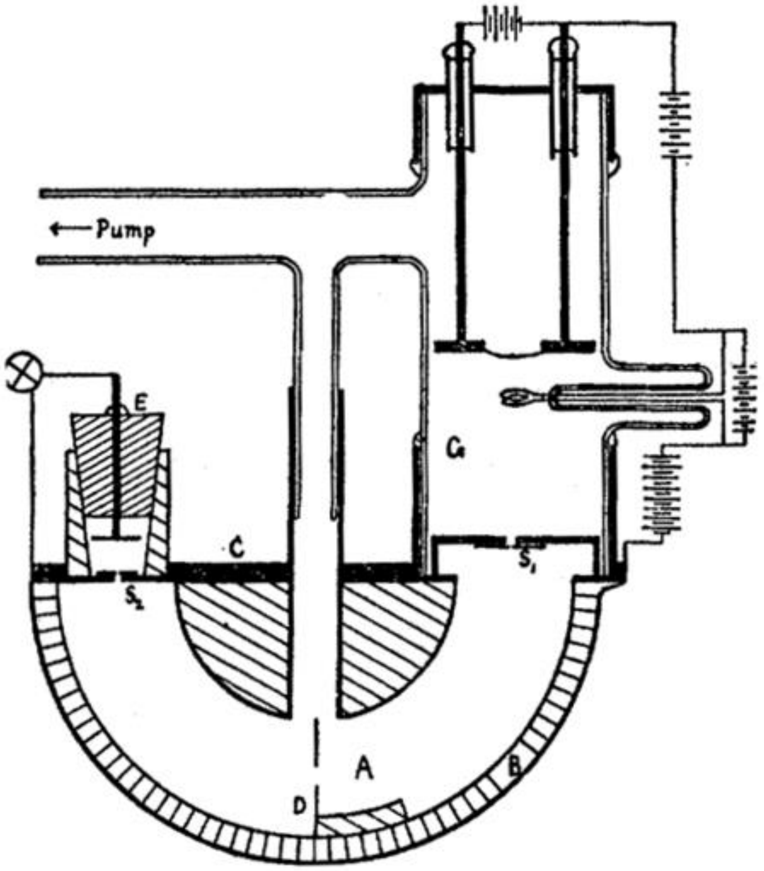

Figure 2.3: Dempster's 180° magnetic sector instrument [24]

2.1.3 The Growth of Mass Spectrometry

In 1929, Bleakney improved on the work of Dempster to develop the electron impact ion source [27]; which today is a standard ionisation source in MS. In electron impact ionisation (also known as electron ionisation (EI)), energetic electrons produced by thermionic emission interact with gas phase neutrals to produce ions. The improvement of Bleakney was to separate the fields controlling the electron and ion beams giving improved measurements of molecular ionisation and dissociation. Furthermore, the resulting mass spectrum would include a fragmentation pattern which could be considered as a “finger print” for characterising a given sample. Further progress with EI sources was made by several researchers in the 1930s including Mattauch [28], Herzog [29], Bainbridge [30], and

Nier [31]. Such advances led to the use of MS in the study of complex molecular structures, such as hydrocarbons [32].

The resolution of the 180° magnetic sector instrument, as developed by Dempster, was hampered by the initial entry conditions of the ions into the analyser which was sensitive to the ion velocity (large ion energy spread). The creation of a mono-energetic ion beam was achieved by Bleakney [27, 33] and Bainbridge [30] who incorporated velocity filters into the magnetic sector instrument. The basis of the velocity filter (also known as Wien filter) was previously developed by Wien in his investigations of canal rays [12]. This had been employed in Aston’s Mass Spectrograph which consisted of electric and magnetic fields perpendicular to each other creating a velocity spectrum and allowing a narrow band of ion velocities to be transmitted [19].

Further improvements in technology and understanding of the sector instrument led to the development of the double focusing sector instrument. This instrument incorporates both direction and velocity focusing to refocus ions using a magnetic sector and an electric sector. The instrument is able to obtain higher resolution and sensitivity than a single focusing instrument with a velocity filter because it refocuses ion beams that are inhomogeneous in both velocity and direction without loss of signal. The first double focusing instrument was described by Mattauch and Herzog in 1934 [28]. Similar instruments were developed in the 1930s by Dempster [34] and Bainbridge & Jordan [35]. Nier [36, 37] and Johnson & Nier [38] developed an arrangement that was particularly successful in reducing second order angular aberrations (i.e., improving second-order direction focusing). The design used a 90° electrostatic analyser, followed by a 60° magnetic sector field, eradicating the interference of the electromagnet with the ion source and detector.

Up until the early 1950s the majority of mass spectrometers (or spectrographs) which had been developed relied on magnetic fields for mass analysis. These instruments are commonly referred to as ‘static’. Static instruments have (electric and/or magnetic) fields that remain largely constant during the passage of an ion, exemplified by the mass spectrograph which records various *e/m* ion beams at different locations on a photographic plate. A dynamic instrument uses time varying (dynamic) fields to focus ions of a given *e/m* on to a suitable detector allowing rapid identification of a wide range of constituent components from a sample.

In 1946, Stephens described a new concept for dynamic MS using time dispersion [39], which became known as Time-of-Flight (TOF) MS. A TOF MS uses differences in ion transit time through a drift (electric field) region to separate ions of different masses. It operates on the principle that ions of the same kinetic energy but different masses take distinct time intervals to traverse a fixed distance.

The end of the 1940s saw the development of a new technique used for surface science analysis: Secondary Ion Mass Spectrometry (SIMS). It had long been known that the bombardment of a solid sample surface with a focused primary ion beam caused the emission of secondary ions characteristic of the sample. SIMS is a technique which collects and analyses the desorbed (secondary) ions. The process was first noted by Thomson in 1910 [15]. With the aid of improved vacuum technology, Herzog and Viehbock performed the first SIMS experiments in 1949 [40]. The benefits of this technique for surface analysis opened up a number of application areas such as a NASA project for moon rock analysis [41].

Furthermore, in 1949, a crucial step towards high resolution and high accuracy MS was made by Hipple and co-workers who described Ion Cyclotron

Resonance (ICR) MS [42, 43]. Their initial aim was to determine the Faraday constant by measuring the cyclotron resonance frequency of protons. The basis of their development was the pioneering work of Lawrence and Livingston who developed the cyclotron in the early 1930s accelerating protons at high speed for nuclear physics experiments [44].

In 1953, a new concept in mass analysis, the Quadrupole Mass Spectrometer (QMS), was first described by Paul and Steinwedel [2]. They described a new type of dynamic mass analyser which separates ions based on their stability within a quadrupolar field (without the need of magnetic fields), using a combination of oscillating and static electric fields. In this way the quadrupole mass analyser is often referred to as a quadrupole mass filter (QMF) since its operation is based on scanning (typically) a range of voltages (corresponding to a range of masses) in such a manner that only a narrow band of ions will have stable trajectories (and hence be transmitted) corresponding to a given mass present. At that time they filed patents in several countries for the QMF [45] and the quadrupole ion trap (QIT) which utilises a three dimensional field to trap ions.

An adaptation of the QMF was proposed by one of Paul's co-workers (von Zahn) in 1963 who invented the monopole [46]. The monopole geometry consists of one circular electrode and an angled v-shaped electrode producing one quarter of the QMF field. Initially this instrument was met with much interest until it was realised that this device was inferior to the QMF due to the poor peak shape and low sensitivity. Interestingly a relatively recent report by Sheretov et al. showed that using hyperbolic geometry for both electrodes improves resolution by 4x and sensitivity one hundred fold over the conventional monopole design [47].

The QMS became a very popular instrument among analysts due to its suitability for coupling with gas chromatography (GC). The combination of these two methods GC and MS provides a powerful means for identification of substances within a test sample and is often described as the “gold standard” for forensic substance analysis. The role of GC is to separate mixtures into their components with the MS identifying and quantifying each component. The original investigator of this combination of techniques was Beynon in 1956 [48]. The QMS is the prime MS for coupling with GC due to its fast scanning speeds. Relatively low mass compounds are typically investigated (< ~500Da), where the need for high resolution spectra is not normally required.

The years 1960-69 saw a host of new developments in MS. Perhaps the most significant was the inception of tandem mass spectrometry (MS/MS) underpinned by collision induced dissociation (CID) (also known as collisionally activated dissociation). In MS/MS, a pre-cursor ion is first selected by a mass analyser, then it is fragmented by CID, followed by mass analysis of the product ions. The result is a fragmented spectrum of the specified pre-cursor ion providing valuable information regarding the identity and structure of the primary ion. The technique was initially applied extensively to the study of natural products. Since that time MS/MS has become a benchmark procedure for structural elucidation of compounds such as protein sequencing in peptide identification [49].

Other notable developments during this era included a variety of ion sources extending the range of samples that could be examined and hence the applicability of MS to new fields. Chemical Ionisation (CI) has a similar ionisation process to EI but is a ‘softer[2]’ ionisation method; enhancing the abundance of the molecular ion. The main difference with CI is that the gas pressure in the ionisation source is raised by injecting a reagent gas which increases the probability of forming protonated or deprotonated molecular ions (depending on the reagent gas used) [50].

Another ‘soft’ ionisation technique, electrospray ionisation (ESI) was invented in 1968 by Dole [51]. The original work of Dole was extended by Fenn et al. resulting in an ionisation source suitable for the ionisation and subsequent analysis of biological macromolecules [52]. This later resulted in Fenn receiving a share of the 2002 Nobel prize for chemistry. The study of the electrification of liquid droplets itself has a long history preceding MS. The ionisation mechanism is complex but essentially the technique involves an analyte solution being sprayed from a small diameter electrode tip due to an applied high voltage.

The ionisation of samples in solution for MS was also extended by the use of a membrane interface (known as membrane inlet or membrane introduction - mass spectrometry (MIMS)). MIMS is a technique that allows the direct introduction of specific components of a liquid, solid or gas into the MS vacuum chamber via a semipermeable membrane. It was used in 1963 by Hoch and Kok [53] who originally presented it as a technique for monitoring respiratory gases *in situ* during photosynthesis. Since then it has been applied to a range of applications such as: blood gas analysis [54] and fermentation monitoring [55].

A notable milestone in the quest for high performance MS was met in the early 1970s through the development of the Fourier transform ion cyclotron resonance (FTICR) MS by Marshall and Comisarow [56]. The foundational principles of this technique are derived from conventional ICR MS [42] and the use

---

[2] ‘Soft’ ionisation refers to the formation of a large proportion of ions without breaking chemical bonds. Whereas, ‘hard’ ionisation would result in chemical bonds being broken and formation of a large proportion of fragment ions.

of FT in nuclear magnetic resonance (NMR) [57]. In FTICR MS ions introduced are trapped in a Penning trap [58] where they are excited by an oscillating electric field until they are separated out according to their *e/m*, rotating in phase at their cyclotron frequencies. The ion signal is detected as an image current and the resulting signal is converted from the frequency domain by applying FT to give a mass spectrum.

Other key developments in the 1970s included the coupling of liquid chromatography to MS (LC-MS) providing very high sensitivity and selectivity for complex mixtures [59, 60]. The first triple quadrupole (QQQ) was invented by Morrison and McGilvery in 1974 and further developed by Enke and Yost for tandem mass spectrometry [61]. A new ionisation technique was developed similar to SIMS, plasma desorption (PD) ionisation (also known as fission fragment ionisation), where solid samples are bombarded with ions and neutrals formed as a result of nuclear fission of a suitable nuclide (such as Californium-252) [62].

The 1980s saw several key developments in ionisation technologies expanding the horizon of MS even further. In 1981, the SIMS technique for examining desorbed secondary ions from a solid surface took a big step forward in being applicable to liquid target surfaces through the development of a technique known as fast atom bombardment (FAB) [63]. The technique involves dissolving the analyte in a non-volatile solvent (matrix) and the liquid surface is bombarded by a beam of fast atoms (typically from an inert gas) under vacuum. The result is continuous desorption of ions allowing analysis of substances which previously had proved difficult.

In 1984, the ESI technique originally invented by Dole received considerable development by Fenn who was able to successfully ionise large and fragile polar biomolecules for MS analysis [52, 64]. Due to the multiple charged ions created by

ESI, the extensive mass range required for MS is reduced, allowing spectra to be obtained for biomolecules with weights exceeding 100,000Da[3].

A rival “soft” ionisation technique for ionising biomolecules and large organic molecules was originally invented by Tanaka (who shared the Nobel prize for chemistry in 2002 with Fenn) [67]. The method was further developed extensively by Hillenkamp, Karas and co-workers in 1985 [65]. Matrix-assisted laser desorption/ionisation (MALDI) relies on a matrix material having an absorption band that closely matches the energy (frequency) of the laser beam. The matrix and the analyte are mixed and the energy absorbed by the matrix is inferred to the sample substance causing it to desorb and ionise. High yields of protonated molecular ions are produced with few fragment ions. A major difference between MALDI and ESI is that MALDI produces far fewer multiple charged ions meaning a larger mass range MS instrument is required. Since MALDI is a pulsed technique it couples well to TOF MS which generally has a very large mass range (theoretically unlimited). The fundamental principles of MALDI can be traced back to the earlier developments in laser desorption (LD) ionisation in the early 1960s [66].

From the 1980s until the present day the application of MS to biological research has continued to grow. Improvements in technology and methodologies have made MS an essential tool in structural biology. In the 1990s two significant analyser developments were made. The first of these was a new hybrid instrument developed by combining quadrupole and time-of-flight technologies (Q-TOF) providing ultra-high sensitivity MS/MS for low-femtomole/attomole-range biopolymer sequencing [68]. The Q-TOF is similar to QQQ except the last quadrupole section is replaced by a reflecting TOF analyser orthogonal to the ion

---

[3] The dalton (Da) or the unified atomic mass unit (u) is the standard unit used for indicating mass on an atomic or molecular scale.

beam. Since the TOF is used in the final stage the ion signals are recorded in parallel and with improved resolution and mass accuracy.

The second major instrument development in the 1990s was the invention of the orbitrap by Makarov [69, 70] a new, ultra high performance mass analyser similar in essence to the Kingdon trap [71] and quadrupole ion trap. The orbitrap has axially symmetric electrodes and uses electrostatic fields to create a quadro-logarithmic potential. Mass spectra are generated in a similar manner to FTICR MS whereby the image current from the dynamically trapped ions is converted from the time domain by Fourier transform. The performance benefits, in terms of high mass accuracy and high resolution, are due to the energy independence of injected ions and the high accuracy with which the field can be defined.

In 1997, MALDI TOF MS was first used for visualising the spatial distribution of molecules [72], as opposed to SIMS, giving way to further developments in MS imaging (MSI) [73]. MSI provides further possibilities for MS investigation by combining molecular mass and spatial information for visualising molecules on complex surfaces. A challenge for MSI is increasing the image resolution in a timely manner whilst maintaining sufficient sample throughput.

A major thrust towards ambient ionisation/sampling for MS was proliferated in 2004 leading to several developments in atmospheric pressure ionisation techniques [74, 75]. This requires the ionisation stage to be completed outside of the vacuum (at atmospheric pressure) and uses direct sampling for MS analysis with no/minimal sample preparation. The ions generated at ambient conditions are introduced into the mass analyser via an atmospheric pressure interface. The benefits of ambient ionisation are particularly well-suited for portable and miniature systems which can provide *in situ* analysis for point-of-care biomedical applications [76].

Furthermore, certain ambient ionisation technologies such as desorption electrospray ionisation (DESI) are well suited for MSI allowing *in vivo* analysis [77].

A new instrumental concept was recently demonstrated in 2011 [78], Distance-of-Flight (DOF) MS which is similar in essence to TOF yet quite distinct. Whereas TOF separates ions in time, DOF separates ions in space. This is achieved by measuring the spatial location of an ion at a specified time after the initial ion acceleration via a position sensitive detector. DOF MS is still in its infancy as an MS technique but would appear to offer the same benefits as TOF MS but with more possibilities due to the spatial distribution of ions and without the limitations related to temporal ion detection.

2.1.4 The Future for Mass Spectrometry

A century has passed since the foundational work of Thomson who is widely regarded as the pioneer of Mass Spectrometry. Thomson realised the enormous potential of the technique exemplified by his writing in 1913 [1], *"there are many problems in Chemistry which could be solved with far greater ease by this [method]."* Judging by the scope and wide use of MS in the present day, Thomson's foresight may have been understated. MS is today an established *bona fide* clinical tool, a ubiquitous and indispensable research instrument with an enormous application range. Arguably, no other device has contributed to so many fields over the past 50 years (fig. 2.4).

A century from now it is impossible to tell what advances will be made in the field and how far reaching MS applications will be. Advances in MS miniaturisation, portability, versatility and ruggedness have led to mass spectrometers being deployed in a variety of harsh environments [79] not limited to our own planet [80, 81]. A pertinent question for the future is whether MS will find a place in our homes and/or workplaces as a measurement device for personalised biomedicine. Perhaps the question should be prefaced ‘when’?

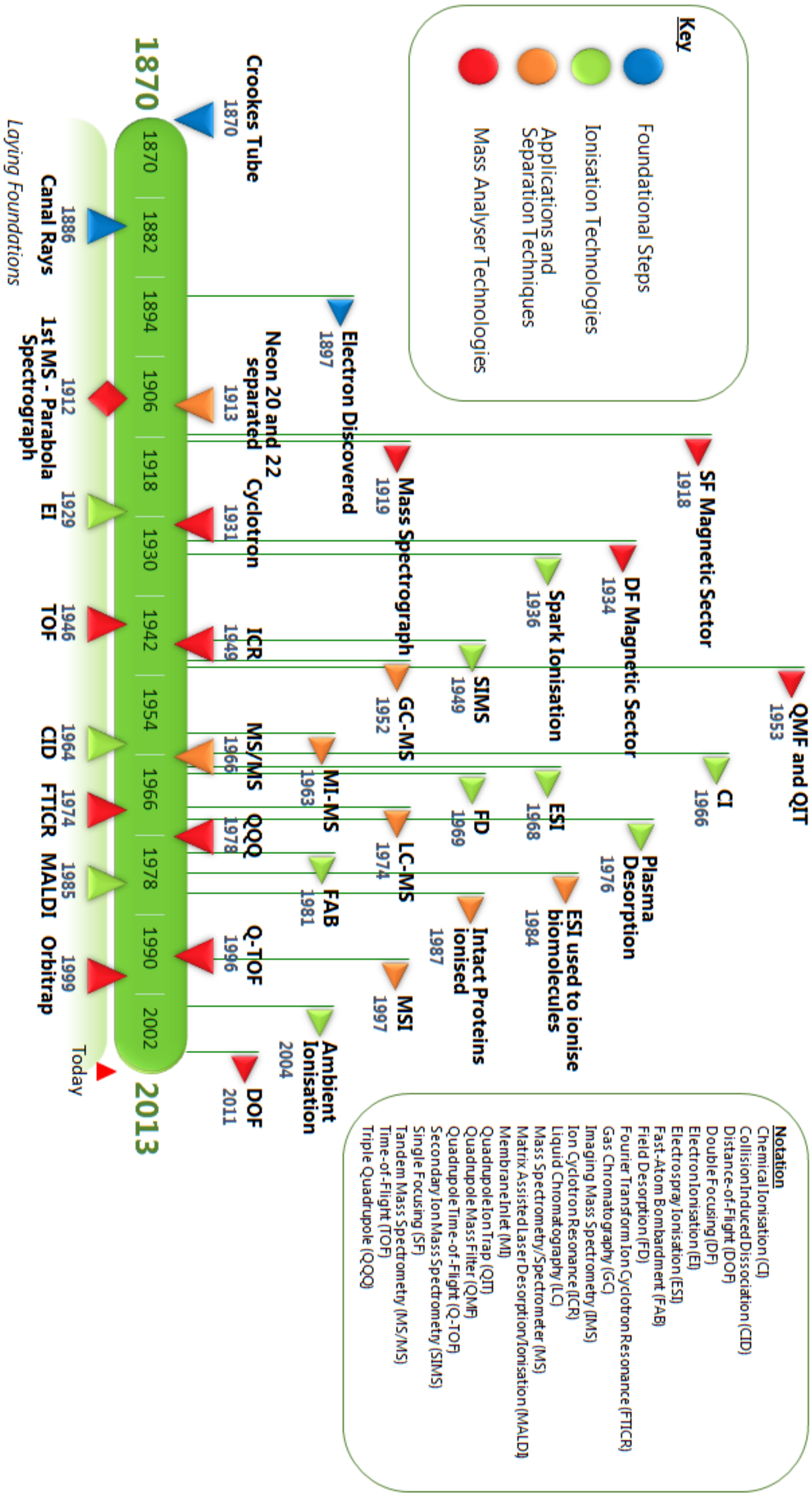

Figure 2.4: Timeline summarising the major advancements in MS

2.2 Focusing on Quadrupole Mass Spectrometry and Allied Topics

The focus for the remainder of this chapter is directed towards Quadrupole Mass Spectrometry. This year (2013) also marks the 60th anniversary since the invention of the quadrupole mass spectrometer (QMS) by Paul and Steinwedel [2]. The QMS as a system (figure 2.5) consists of an ion source, quadrupole mass filter (QMF) and an ion detector (as well as electronic controls and vacuum system). A simple QMF consists of four parallel electrodes, ideally of hyperbolic cross section, accurately positioned in a radial arrangement such that they are equally spaced about a central axis. The mass resolving properties of a QMF[4] relate to the intrinsic stability (or instability) of ion trajectories within the field region defined by the electrodes (see Chapter 3 for a detailed description of how the QMS works).

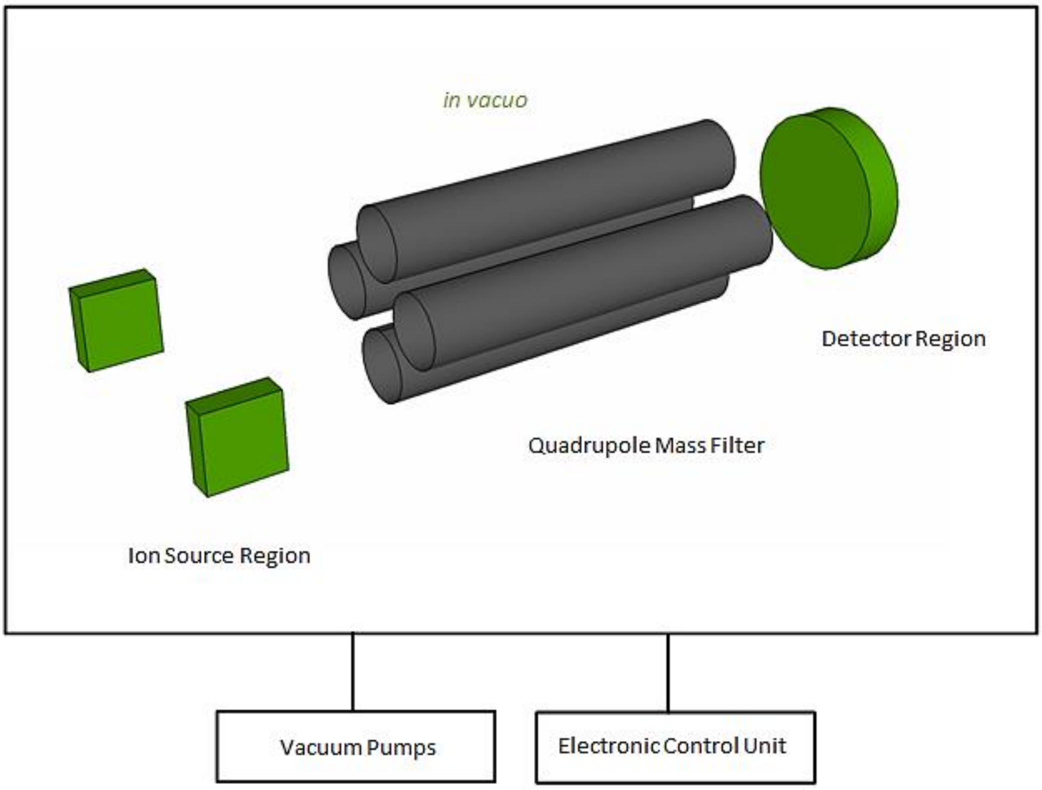

Figure 2.5: Simplified basic outline of a basic QMS system (not showing electrical connections)

---

[4] In the literature QMF, quadrupole mass analyser (QMA) and QMS are often used interchangeably as descriptions for the same device. A distinction can be made for the term QMS which is often used to describe the system (ion source, mass analyser and detector) as opposed to the analyser in isolation.

Since the pioneering work of Paul and co-workers much research has been undertaken studying the performance and behaviour of the QMS, reviewed by Dawson [82] and more recently Douglas [83].

2.2.1 Laying the Foundations

The foundational steps for the QMS can be traced back to the French mathematician Émile Mathieu (1835-1890). The equation named after him [84] is a special case of the Hill equation [85] having only one harmonic mode. The equations of motion for an ion in an ideal QMF can be described mathematically by solutions to the Mathieu equation. These solutions describing the ion motion can be classified as stable or unstable depending on their boundedness (see Chapter 3.1.4).

Besides the general development in Mass Spectrometry (MS), the development of the QMS is closely related to the developments of high energy particle accelerators. The use of time varying (dynamic) focusing used in linear accelerators laid much of the ground work for ion focusing and electro-dynamic mass spectrometers. The strong focusing properties of quadrupolar fields was first recognised by physicist Christofilos. In 1950 he filed for a patent [86] entitled *"Focusing System for Ions and Electrons"* in which he describes a particle accelerator design similar in geometry to a QMF but with electrodes helically arranged, uniformly twisted about the central/axial axis. In 1952, the strong-focusing alternating-gradient principle was demonstrated by Courant et al. who confined a fast beam of protons with a series of magnetic quadrupole fields alternating in space [87].

2.2.2 Initial Development of the Quadrupole Mass Filter

These developments prefaced the invention of the quadrupole mass filter (QMF) first described by Paul and Steinwedel in 1953 [2]. It should be noted however, that around the same time (and independently), Post developed a similar device [88]. For the QMF, the spatial periodicity is replaced with time varying quasi-stationary fields which, for specified conditions, allow certain *m/z* ions to be focused (stabilised). The first mass spectrum was obtained in 1954, where complete separation of ^{85}Rb and ^{87}Rb was achieved with a frequency scanned QMF (figure 2.6) [89, 90].

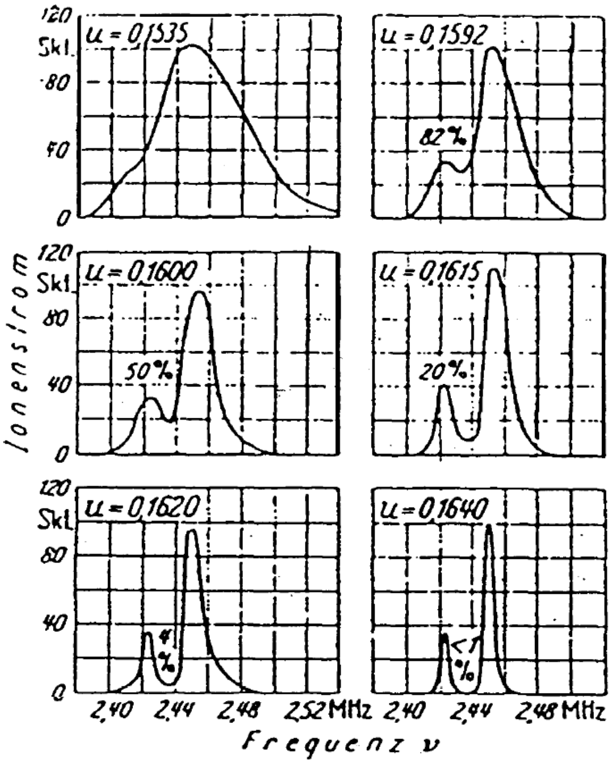

Figure 2.6: First QMF spectra of Rubidium isotopes (^{85}Rb and ^{87}Rb) [90]

The thrust of the initial development of the QMF during the 1950s was undertaken by Paul et al. who filed several patents regarding the device [2, 90, 91]. In 1962, von Zahn (a colleague of Paul) constructed a QMF with a field radius of 3.5cm and length of 5.82m. The instrument was so long that it had to be hung vertically down a stair case [92] but was capable of achieving a high resolution of ~16,000 [89, 93].

The ability to control resolution and transmission electronically as well as the general simplicity of construction, robustness, and relatively low cost meant that the QMF was an ideal analytical instrument for space exploration and upper atmosphere research. This led to a surge in QMF instrumentation research and development during the early 1960s and consequently led to commercial development of the instrument.

2.2.2.1 Circular Cross-Section Electrode Geometry

The ideal electrode geometry for generation of a quadrupole electric field utilises a hyperbolic cross-section[5] such that the potential at any point within the field region is proportional to the square of the distance from the origin of reference. The subsequent equations of motion are independent (i.e., they can be reduced to a set of decoupled equations). The quadrupolar field can be approximated by the use of round/circular cross-section electrodes, although field imperfections exist and perturbations become more apparent further away from the central field region. This is exemplified analytically by coupling between the equations of motion describing the ion trajectories in the field region. The electric field can be represented as a sum of multipole terms of the potential $\emptyset(x,y)$ (assuming a two-dimensional field structure) [94]:

$$\emptyset(x,y) = \sum_{N=0}^{\infty} A_N \emptyset_N(x,y) \qquad (2.2)$$

where A_N is the amplitude of a multipole $\emptyset_N$ with 2N poles. For an ideal quadrupolar field all terms are zero except for N=2 $\left(\frac{A_2\emptyset_2}{r_0^2}\right)$. The N=0 term represents the quadrupole offset potential, N=1 is a dipole potential, etc.

---

[5] Note that often in the literature and in this thesis the notation ‘hyperbolic electrodes’ is used interchangeably with and for the proper term ‘hyperbolic cross-section electrodes’. The same notation is also used for other 2 dimensional geometric shapes such as circular.

In order to reduce the field perturbations and to better approximate the hyperbolic field, several investigations have been undertaken to determine the ideal ratio ${r}/{r_0}$ of the radius of the electrode (r) to the inscribed radius (r_0) (the distance from the centre of the quadrupole field to an electrode) which determines the relative magnitudes of the individual terms of the multipole field. When cylindrical electrodes are used, instead of hyperbolic, the multipole terms $N = 6, 10, 14, \ldots$ are present (see equation 2.2). In order to eliminate the dodecapole term ($N = 6$) Denison used a numerical approach [95] and calculated ${r}/{r_0} \cong 1.1468$, which assumed a grounded cylindrical housing enclosure around the electrodes of radius $3.54 \times r_0$. Reuben [96], using a semi-analytical method, found a more precise value of ${r}/{r_0} \cong 1.14511$ was required to eliminate the dodecapole term for the same configuration. Gibson and Taylor [97, 98] investigated this problem numerically but using a 'top-down' approach by simulating the QMF as a complete two-dimensional system to determine the ${r}/{r_0}$ ratio which gives optimal performance. They concluded that $1.12 < {r}/{r_0} < 1.13$. They also noted that the electrode housing has a very small effect on the QMS behaviour. Douglas and Konenkov [94] came to a similar conclusion explaining the behaviour in terms of the relationship between the $N = 6$ and $N = 10$ multipole terms. By using ${r}/{r_0} \cong 1.13$, the sixth and tenth terms tend to compensate for each other minimising their overall influence.

The main advantages of circular electrodes (as opposed to the ideal hyperbolic form) are due to the ease of manufacture and mounting. However, the drawbacks include reduced ion transmission, poorer resolution and distorted peak shapes. Brubaker and Chamberlin performed a detailed series of experiments comparing performance between hyperbolic and round rods (albeit ${r}/{r_0}$ was not optimal) and found using hyperbolic electrodes provides a two-fold improvement in resolution (measured at the same sensitivity) [99]. Simulation studies by Gibson and Taylor [100], using an optimal value for ${}^{r}/_{r_0}$, also found hyperbolic electrodes outperformed circular. They showed that circular electrode QMFs exhibit a 'tail' structure (and in some cases a distinct precursor peak) on the low mass side of a mass spectral peak which is also dependent upon the initial ion conditions and the number of field cycles an ion experiences.

2.2.2.2 Fringing Fields

Fringe fields are present at the entrance and exit of any practical system due to end effects; this means that the field of the QMF does not retain its uniform value at the end of the electrodes. Even when hyperbolic electrodes are used and an ideal quadrupolar field is generated to a high degree of accuracy, a decline in performance can occur as ions traverse the fringing fields at the entrance and exit of the QMF. These fields are complex and do not match the ideal fields required. The first investigation of fringe field effects was by Brubaker [101-103], who used the results to develop an *rf* only pre-filter (delayed DC ramp) and demonstrated a one hundred fold increase in sensitivity at the same resolving power. Fite achieved a delayed DC ramp effect by using a leaky dielectric material which appears to RF fields as a dielectric but to DC fields as a conductor and was able to observe experimentally an increase in resolution by a factor of 5 [104]. Pre-filters improve performance and are generally incorporated in modern, high specification instruments. Alternative methods for eliminating fringing field effects have been proposed such as a lens design which allows ions to be injected at a point within the analyser where fringing field effects are negligible [105].

The fringing fields at the entrance to the QMF have a more profound influence than those at the exit since they are often defocussing and can cause premature rejection. Exiting fringing fields can also be defocusing but can be overcome by a strong attractive force brought about by floating the detector at a high potential. Fringe fields encountered by an ion entering the QMF are not always defocussing and transmission depends on the number of field cycles an ion spends in the fringing field. Dawson [106] proposed a linear model of the potential in the fringing field and found the optimum number of cycles spent in the fringing fields for maximum transmission to be ~2 (for operation in stability zone 1). Hunter and McIntosh [107, 108] determined the fringe fields using a relaxation technique and fitted a more realistic exponential expression to these fields.

2.2.2.3 Stability Zone 3

The stability zone is a theoretical concept derived from the Mathieu equation depicting regions of ion stability and instability which can be related to instrument operation settings (see Chapter 3.1.5 for more details). Most commercial QMS instruments operate in stability zone 1. However, there are certain advantages, such as mass spectral peak shape, reduction of low mass tailing, and increased resolution, to be obtained if the QMS is operated in the third stability zone. It has previously been demonstrated that QMS operation in stability zone 3 can provide the required resolution to separate low mass isotopes [109-111], and carbon monoxide (nominal mass 28Da; calculated ionic mass 27.99437Da) from nitrogen (nominal mass 28Da; calculated ionic mass 28.00559Da) [112]. Operation in stability zone 3 requires higher operating voltages, which is considered to be a disadvantage. Nevertheless, with the development of miniature QMFs (see 2.2.2.4), the increased voltage requirement may not be considered a major drawback [113]. Stability zone 1 has a tip at (a = 0.23699, q = 0.706) in aq space and is approximately triangular in shape. Stability zone 3 is approximately a rhomboid in terms of its shape. It has two tips accessible by scanning positively in q. An upper left tip (a = 3.16, q = 3.23), and a lower right tip (a = 2.52, q = 2.82). Operation in these regions can allow high resolution mass scanning to be achieved [83]; furthermore, zone 1 does not cause any interference when operating in either tip region of zone 3 as the scan line gradient required does not pass through it. For operation in stability zone 3 the ions require a lower exposure to number of alternating potential field cycles to achieve the same resolution compared with zone 1, albeit at the expense of reduced transmission [114].

2.2.2.4 Portability and Miniaturisation

A key aim for portable and miniature MS systems is to be able to perform measurements *in situ* at the point of interest. This means that the sample is no longer required to be taken to the laboratory but effectively the laboratory can be taken to the sample allowing real-time data to be collected from the sample in its native environment.

The difference between ‘portable’ and ‘miniature’ depends upon how one defines such terms. Various analyser criteria can be used such as volume, weight, power consumption, and whether the system can run on battery power alone etc. Other criteria must also be considered, for example device ruggedness and whether operation can be achieved in harsh environments. In practice, the MS system and device performance are paramount: the sensitivity, response time, resolution and mass range of the system must be fit for the application purpose. Underpinning all such criteria is the cost of the system itself.

In many cases, it is not the mass analyser itself, but the associated vacuum and electronic components that limit the development of an entirely miniaturised system. Vacuum technology continues to advance with smaller turbomolecular pumps commercially available. Other options include ion-getter pumps which can be operated without a forestage pump and have no moving parts [115]. Smaller mass analysers have reduced vacuum requirements. Wang et al. demonstrated a novel means of reducing vacuum requirement (and improving sensitivity) by only exposing the region within the electrodes to the vacuum (as opposed to the entire QMF), hence reducing the effective vacuum chamber size [116].

A miniaturised QMF will have a significantly reduced vacuum requirement because of the reduced path length allowing more ion-neutral collisions per unit length. Reasonable performance has been reported at pressure in the region of $\sim 1\times 10^{-4}$ torr demonstrating peak widths of ~0.9 Da (at 10% peak height) for N_2^+ [117]. Furthermore, the QMF operating voltages are also reduced due to the inverse square relationship between inscribed electrode radius and voltage [118].

When scaling down the dimensions (by a factor n) of a QMS it leads to a smaller overall volume and surface area (reduced by a factor of n^3 and n^2, respectively). While the reduced volume adds to the overall robustness of the device, the reduced surface area of the instrument leads to a signal loss by a factor of n^2 [119]. The reduced sensitivity can be reclaimed by using an array of miniature quadrupoles in parallel [120, 121]. Arrays allow individual electrodes to be used as components for multiple QMFs decreasing relative size and power requirements whilst increasing relative sensitivity. If a QMF is reduced by a factor k, an array of $k \times k$ filters will regain the drop off in sensitivity and yet will have a smaller physical footprint (size and weight) than the original quadrupole by a factor of ~ *k* [120].

2.2.2.5 QMF with Magnetic Field Applied

In the original work of Paul et al. [2, 45, 90] much emphasis was placed on the fact that the QMS separates ions due to the electrodynamic quadrupolar field and without the use of magnetic fields. Magnetic fields have long been used in ion sources [37], magnetic deflection instruments [24] and in ion traps [122]. However, surprisingly little work has been done in relation to the application of a magnetic field (***B***) to the quadrupole mass filter (QMF). Interference from strong stray magnetic fields of FT-ICR MS with *rf*-only quadrupole (and multipole) ion guides is well-known [123-125]. Likewise interference of stray magnetic fields from plasma based experiments with QMS performance has been noted [126].

In the early 1950s Portisky and Gerrard [127] studied theoretically the motion of an electron in a two-dimensional electrostatic quadrupolar field combined with a uniform magnetic field (0, 0, B_z) normal to the electric field. However, in this case the electric field used was static and not time varying as is the case for the QMS. Nevertheless, they found that the electron trajectory to consist of a simple harmonic motion along an ellipse whose centre moves along a hyperbola allowing the electrons to drift into regions of higher or lower potential.

In the late 1950s, the first investigation of the application of a magnetic field to a three dimensional quadrupole ion trap was performed by Fischer [128]. His work was more concerned with the effect of the magnetic field upon the motion of the electrons in the trap rather than the ions.

A similar theoretical investigation was undertaken by Kubicek [129] who studied the possibility of a mass spectrometer with just a time varying magnetic field

(0, 0, $B_z(t)$) applied (and no electric potential applied) – a solenoid with sinusoidal variation in time. The analysis showed it was possible to separate ions of different mass by adjusting the parameters of the magnetic field and that the geometrical configuration is much simpler than a conventional QMF, requiring only a conducting tube to be placed inside the solenoid. However, ions with low initial axial energy are required and there are practical difficulties associated with achieving large magnitude and high frequency magnetic fields with a yokeless solenoid.

Carrico [130] conducted a brief theoretical investigation for another similar case with a uniform magnetic field (0, 0, B_z) but crucially with an electrodynamic quadrupolar field as used for a QMS. He was able to remove x-y coupling by making a coordinate system transformation. He concluded that the solutions for the magnetic field case have the same stability properties as a conventional QMF. He noted that the effect of the magnetic field is equivalent to a change $er_0^2B_z/4m$ in the direct component of the applied voltage.

An analytical study by Pavlenko and Toporoba [131] considered ion motion in a QMS with a uniform transverse magnetic field applied (0, B_y, 0). They concluded from the study that the presence of the magnetic field increases the resolution of the instrument and that it is possible to operate the QMS in any stability region. Independently of this study, investigations at the University of Liverpool have demonstrated experimentally an improved resolution by application of an axial (0, 0, B_z) or transverse (B_x, 0, 0) static magnetic field [132-136]. The orientation of the $\boldsymbol{B}$ field vector is described in terms of a Cartesian coordinate system whereby the $\boldsymbol{B}$ field is projected axially (along the z-axis), or transversely (along either the x- or y-axes). With respect to the QMF, the x-axis refers to the plane consisting of the positive potential electrodes and the *y*-axis refers to the plane of the negative potential electrode pair.

2.3 Concluding Remarks

Mass Spectrometry is a field of enormous scope and is an established analytical method of choice for a wide range of applications. Since its inception, advances in MS have largely been a consequence of improvements in instrumentation. In his Nobel lecture, Wolfgang Paul commented [89]:

“There are many examples in physics showing that higher precision revealed new phenomena, inspired new ideas or confirmed or dethroned well established theories. On the other hand new experimental techniques conceived to answer special questions in one field of physics became very fruitful in other fields too, be it in chemistry, biology or engineering.”

Since their invention in the 1953 and subsequent rapid development in the 1960s - 1970s, quadrupole mass spectrometers have impacted a wide range of scientific fields. Geometrically simple, yet complex in operation, the QMS remains a widely used analytical tool, for separating charged species in space according to their mass-to-charge ratio, with an extensive range of applications in both industry and research.

Fringing fields are important in the functioning of the QMF and can be detrimental to performance. Several previous investigations to calculate fringe fields have used significant approximations. Understanding the effect of fringing fields on QMF performance is considered to be an area requiring further investigation. This is particularly important for low-specification QMS instruments, which do not have pre-filters. Accurate models predicting their behaviour for a wide range of conditions are not reported.

It is commonplace for QMSs to be operated in stability zone 1. Conventional QMS performance and behaviour in stability zone 1 is well documented. Certain applications require higher resolution not readily attainable when operating in zone 1. Improved resolution has been demonstrated when operating in stability zone 3. QMS performance when operating in stability zone 3 has not received extensive investigation and it is considered that further research is required.

Recent investigations have been concerned with the case of a *static* magnetic field (***B***) applied to the body of a QMF and have demonstrated relative resolution enhancement for a single mass peak for a given set of conditions. This feature has potential to offer a simple and low cost resolution enhancement. However, for a viable magnetically enhanced QMS to be realised it is necessary to generate consistent mass spectra for a range of *m/z* and not only for isolated peaks. Moreover, a detailed analysis is required to understand the underpinning features of the magnetically enhanced instrument. Understanding the effect of the magnetic field on the stability diagram is important for optimal operation. It is also necessary to determine whether the technique provides an ultimate performance enhancement (as opposed to relative performance enhancements that have been published in the literature). Such questions have been investigated in this thesis in subsequent chapters.

References

[1] J. J. Thomson, *Rays of Positive Electricity and Their Application to Chemical Analyses*: Longmans, Green, 1913.

[2] W. Paul, and H. Steinwedel. "Ein neues massenspektrometer ohne magnetfeld," *Zeitschrift Naturforschung Teil A* 8: 448, 1953.

[3] D. M. Considine and G. D. Considine, *Van Nostrand's scientific encyclopedia*: Wiley, 2002.

[4] M. Faraday, "Experimental Researches in Electricity.--Seventh Series," *Philosophical Transactions of the Royal Society of London,* vol. 124, pp. 77-122, 1834.

[5] W. Crookes, "On Repulsion Resulting from Radiation.--Part II," *Philosophical Transactions of the Royal Society of London,* vol. 165, pp. 519-547, 1875.

[6] E. Goldstein, "Vorläufige Mittheilungen über elektrische Entladungen in verdünnten Gasen," *Berlin Akd. Monatsber,* vol. 279, 1876.

[7] E. Goldstein, "Über eine noch nicht untersuchte Strahlungsform an der Kathode inducirter Entladungen," *Annalen der Physik,* vol. 300, pp. 38-48, 1898.

[8] J. Perrin, "Nouvelles propriétés des rayons cathodiques," *Comptes Rendus Hebdomadaires des Séances de l'Académie des Sciences de Paris,* vol. 121, p. 1130, 1895.

[9] J. J. Thomson, "XL. Cathode Rays," *Philosophical Magazine Series 5,* vol. 44, pp. 293-316, 1897.

[10] H. Hertz, "On the Passing of Cathode Rays through Thin Metallic Sheets," *Wiedemanns Ann,* vol. 45, pp. 28-32, 1892.

[11] H. A. Lorentz*, La théorie électromagnétique de Maxwell et son application aux corps mouvants* vol. 25: EJ Brill, 1892.

[12] W. Wien, "Untersuchungen über die electrische Entladung in verdünnten Gasen," *Annalen der Physik* 301.6: 440-452, 1898.

[13] J. J. Thomson, "Bakerian lecture: Rays of positive electricity," *Proceedings of the Royal Society of London. Series A,* vol. 89, pp. 1-20, 1913.

[14] J. J. Thomson, "LVIII. On the masses of the ions in gases at low pressures," *Philosophical Magazine Series 5,* vol. 48, pp. 547-567, 1899.

[15] J. J. Thomson, "LXXXIII. Rays of positive electricity," *Philosophical Magazine Series 6,* vol. 20, pp. 752-767, 1910.

[16] J. J. Thomson, "XXVI. Rays of positive electricity," *Philosophical Magazine Series 6,* vol. 21, pp. 225-249, 1911/02/01 1911.

[17] J. J. Thomson, "XIX. Further experiments on positive rays," *Philosophical Magazine Series 6,* vol. 24, pp. 209-253, 1912.

[18] J. J. Thomson, "XLVII. On rays of positive electricity," *Philosophical Magazine Series 6,* vol. 13, pp. 561-575, 1907.

[19] F. W. Aston, "LXXIV. A positive ray spectrograph," *The London, Edinburgh, and Dublin Philosophical Magazine and Journal of Science,* vol. 38, pp. 707-714, 1919.

[20] F. A. Lindemann and F. W. Aston, "XLVIII. The possibility of separating isotopes," *The London, Edinburgh, and Dublin Philosophical Magazine and Journal of Science,* vol. 37, pp. 523-534, 1919.

[21] F. W. Aston, "The constitution of the elements," *Nature,* vol. 104, p. 393, 1919.

[22] F. Aston and E. Lindemann, "The Separability of Isotopes," *Phil. Mag,* vol. 37, p. 523, 1919.

[23] F. Aston, "Neon," *Nature,* vol. 104, p. 334, 1919.

[24] A. J. Dempster, "A new Method of Positive Ray Analysis," *Physical Review,* vol. 11, pp. 316-325, 1918.

[25] A. J. Dempster, "Positive Ray Analysis of Magnesium," *Proceedings of the National Academy of Sciences of the United States of America,* vol. 7, p. 45, 1921.

[26] A. Dempster, "Positive-Ray Analysis of Potassium, Calcium and Zinc," *Physical Review,* vol. 20, p. 631, 1922.

[27] W. Bleakney, "A new method of positive ray analysis and its application to the measurement of ionization potentials in mercury vapor," *Physical Review,* vol. 34, p. 157, 1929.

[28] J. Mattauch and R. Herzog, "Über einen neuen Massenspektrographen," *Zeitschrift für Physik,* vol. 89, pp. 786-795, 1934.

[29] R. Herzog, "Ionen-und elektronenoptische Zylinderlinsen und Prismen. I," *Zeitschrift für Physik,* vol. 89, pp. 447-473, 1934.

[30] K. Bainbridge, "A mass spectrograph," *Phys. Rev,* vol. 40, pp. 130-132, 1933.

[31] A. Nier, "Electron impact mass spectrometry," *Rev Sci Instrum,* vol. 18, p. 415, 1947.

[32] A. Hustrulid, P. Kusch, and J. T. Tate, "The Dissociation of Benzene (C_6H_6), Pyridine (C_5H_5N) and Cyclohexane (C_6H_{12}) by Electron Impact," *Physical Review,* vol. 54, p. 1037, 1938.

[33] W. Bleakney, "A New Method of Positive Ray Analysis and its Application to the Measurement of the Probability and Critical Potentials for the Formation of Multiply Charged Ions in Mercury Vapor by Electron Impact," 1930.

[34] A. J. Dempster, "New methods in mass spectroscopy," *Proceedings of the American Philosophical Society,* vol. 75, pp. 755-767, 1935.

[35] K. T. Bainbridge and E. B. Jordan, "Mass spectrum analysis 1. The mass spectrograph. 2. The existence of isobars of adjacent elements," *Physical Review,* vol. 50, p. 282, 1936.

[36] A. O. Nier, "A mass spectrometer for routine isotope abundance measurements," *Review of Scientific Instruments,* vol. 11, pp. 212-216, 1940.

[37] A. O. Nier, "A mass spectrometer for isotope and gas analysis," *Review of Scientific Instruments,* vol. 18, pp. 398-411, 1947.

[38] E. G. Johnson and A. O. Nier, "Angular aberrations in sector shaped electromagnetic lenses for focusing beams of charged particles," *Physical Review,* vol. 91, p. 10, 1953.

[39] W. Stephens, "A pulsed mass spectrometer with time dispersion," *Phys. Rev,* vol. 69, p. 46, 1946.

[40] R. Herzog and F. Viehböck, "Ion source for mass spectrography," *Physical Review,* vol. 76, p. 855, 1949.

[41] H. Liebl, "Ion microprobe mass analyzer," *Journal of Applied Physics,* vol. 38, pp. 5277-5283, 1967.

[42] J. Hipple, H. Sommer, and H. A. Thomas, "A precise method of determining the Faraday by magnetic resonance," *Physical Review,* vol. 76, pp. 1877-1878, 1949.

[43] H. Sommer, H. A. Thomas, and J. Hipple, "The Measurement of e/m by Cyclotron Resonance," *Physical Review,* vol. 82, p. 697, 1951.

[44] E. O. Lawrence and M. S. Livingston, "The Production of High Speed Light Ions Without the Use of High Voltages," *Physical Review,* vol. 40, pp. 19-35, 1932.

[45] W. Paul, "Apparatus For Separating Charged Particles Of Different Specific Charges," US 2939952, 1960.

[46] U. Von Zahn, "Monopole spectrometer, a new electric field mass spectrometer," *Review of Scientific Instruments,* vol. 34, pp. 1-4, 1963.

[47] É. Sheretov, V. Gurov, M. Dubkov, and O. Korneeva, "A new monopole mass-analyzer based on a hyperboloid electrode system," *Technical Physics Letters,* vol. 26, pp. 21-22, 2000.

[48] Beynon, J. H, “The use of the mass spectrometer for the identification of organic compounds”, *Microchimica Acta,* 44, 437-453, 1956.

[49] J. Hardouin, "Protein sequence information by matrix-assisted laser desorption/ionization in-source decay mass spectrometry," *Mass spectrometry reviews,* vol. 26, pp. 672-682, 2007.

[50] M. S. B. Munson and F. H. Field, “Chemical Ionization Mass Spectrometry. I. General Introduction,” *Journal of the American Chemical Society,* 88 (12), 2621-2630, 1966.

[51] M. Dole, L. Mack, R. Hines, R. Mobley, L. Ferguson, and M. d. Alice, "Molecular beams of macroions," *The Journal of Chemical Physics,* vol. 49, p. 2240, 1968.

[52] J. B. Fenn, M. Mann, C. K. Meng, S. F. Wong, and C. M. Whitehouse, "Electrospray ionization for mass spectrometry of large biomolecules," *Science,* vol. 246, pp. 64-71, 1989.

[53] G. Hoch and B. Kok, "A mass spectrometer inlet system for sampling gases dissolved in liquid phases," *Archives of biochemistry and biophysics,* vol. 101, pp. 160-170, 1963.

[54] S. Woldring, G. Owens, and D. C. Woolford, "Blood gases: continuous in vivo recording of partial pressures by mass spectrography," *Science,* vol. 153, pp. 885-887, 1966.

[55] M. J. Hayward, T. Kotiaho, A. K. Lister, R. G. Cooks, G. D. Austin, R. Narayan, and G. T. Tsao, "On-line monitoring of bioreactions of Bacillus polymyxa and Klebsiella oxytoca by membrane introduction tandem mass spectrometry with flow injection analysis sampling," *Analytical Chemistry,* vol. 62, pp. 1798-1804, 1990.

[56] M. B. Comisarow and A. G. Marshall, "Fourier transform ion cyclotron resonance spectroscopy," *Chemical Physics Letters,* vol. 25, pp. 282-283, 1974.

[57] R. Ernst and W. Anderson, "Application of Fourier transform spectroscopy to magnetic resonance," *Review of Scientific Instruments,* vol. 37, pp. 93-102, 1966.

[58] D. Wineland, P. Ekstrom, and H. Dehmelt, "Monoelectron oscillator," *Physical Review Letters,* vol. 31, pp. 1279-1282, 1973.

[59] V. Tal'Rose, G. Karpov, I. Grdetskii, and V. Skurat, "Capillary system for the introduction of liquid mixtures into an analytical mass spectrometer," *Russian Journal of Physical Chemistry,* vol. 42, pp. 1658-1664, 1968.

[60] M. Baldwin and F. McLafferty, "Direct chemical ionization of relatively involatile samples. Application to underivatized oligopeptides," *Organic Mass Spectrometry,* vol. 7, pp. 1353-1356, 1973.

[61] R. Yost and C. Enke, "Selected ion fragmentation with a tandem quadrupole mass spectrometer," *Journal of the American Chemical Society,* vol. 100, pp. 2274-2275, 1978.

[62] R. Macfarlane and D. Torgerson, "Californium-252 plasma desorption mass spectroscopy," *Science,* vol. 191, pp. 920-925, 1976.

[63] M. Barber, R. S. Bordoli, R. D. Sedgwick, and A. N. Tyler, "Fast atom bombardment of solids (FAB): A new ion source for mass spectrometry," *Journal of the Chemical Society, Chemical Communications,* pp. 325-327, 1981.

[64] M. Yamashita and J. B. Fenn, "Electrospray ion source. Another variation on the free-jet theme," *The Journal of Physical Chemistry,* vol. 88, pp. 4451-4459, 1984.

[65] K. Tanaka, H. Waki, Y. Ido, S. Akita, Y. Yoshida, T. Yoshida, and T. Matsuo, "Protein and polymer analyses up to m/z 100 000 by laser ionization

time- of- flight mass spectrometry," *Rapid Communications in Mass Spectrometry,* vol. 2, pp. 151-153, 1988.

[66] M. Karas, D. Bachmann, and F. Hillenkamp, "Influence of the wavelength in high-irradiance ultraviolet laser desorption mass spectrometry of organic molecules," *Analytical Chemistry,* vol. 57, pp. 2935-2939, 1985.

[67] R. J Cotter, "Laser mass spectrometry: an overview of techniques, instruments and applications," *Analytica chimica acta,* vol. 195, pp. 45-59, 1987.

[68] H. R. Morris, T. Paxton, A. Dell, J. Langhorne, M. Berg, R. S. Bordoli, J. Hoyes, and R. H. Bateman, "High sensitivity collisionally-activated decomposition tandem mass spectrometry on a novel quadrupole/orthogonal-acceleration time-of-flight mass spectrometer," *Rapid Communications in Mass Spectrometry,* vol. 10, pp. 889-896, 1996.

[69] A. Makarov, "The Orbitrap: a novel high-performance electrostatic trap," in *Proceedings of the 48th ASMS conference on mass spectrometry and allied topics, Dallas, TX*, 1999.

[70] Q. Hu, R. J. Noll, H. Li, A. Makarov, M. Hardman, and R. Graham Cooks, "The Orbitrap: a new mass spectrometer," *Journal of Mass Spectrometry,* vol. 40, pp. 430-443, 2005.

[71] K. H. Kingdon, "A Method for the Neutralization of Electron Space Charge by Positive Ionization at Very Low Gas Pressures," *Physical Review,* vol. 21, pp. 408-418, 1923.

[72] R. M. Caprioli, T. B. Farmer, and J. Gile, "Molecular imaging of biological samples: localization of peptides and proteins using MALDI-TOF MS," *Analytical Chemistry,* vol. 69, pp. 4751-4760, 1997.

[73] E. R. Amstalden van Hove, D. F. Smith, and R. Heeren, "A concise review of mass spectrometry imaging," *Journal of chromatography A,* vol. 1217, pp. 3946-3954, 2010.

[74] Z. Takats, J. M. Wiseman, B. Gologan, and R. G. Cooks, "Mass spectrometry sampling under ambient conditions with desorption electrospray ionization," *Science,* vol. 306, pp. 471-473, 2004.

[75] D. R. Ifa, C. Wu, Z. Ouyang, and R. G. Cooks, "Desorption electrospray ionization and other ambient ionization methods: current progress and preview," *Analyst,* vol. 135, pp. 669-681, 2010.

[76] J. Balog, L. Sasi-Szabó, J. Kinross, M. R. Lewis, L. J. Muirhead, K. Veselkov, R. Mirnezami, B. Dezső, L. Damjanovich, A. Darzi, J. K. Nicholson, and Z. Takáts, "Intraoperative Tissue Identification Using Rapid Evaporative Ionization Mass Spectrometry," *Science Translational Medicine,* vol. 5, 2013.

[77] J. M. Wiseman, D. R. Ifa, A. Venter, and R. G. Cooks, "Ambient molecular imaging by desorption electrospray ionization mass spectrometry," *Nature Protocols,* vol. 3, pp. 517-524, 2008.

[78] A. G. Graham, S. Ray, C. Enke, C. Barinaga, D. Koppenaal, and G. Hieftje, "First Distance-of-Flight Instrument: Opening a New Paradigm in Mass Spectrometry," *Journal of the American Society for Mass Spectrometry,* vol. 22, pp. 110-117, 2011.

[79] S. Taylor and V. M. Bierbaum, "Focus on Harsh Environment Mass Spectrometry," *Journal of the American Society for Mass Spectrometry,* vol. 19, pp. 1375-1376, 2008.

[80] S. Petrie and D. K. Bohme, "Ions in space," *Mass spectrometry reviews,* vol. 26, pp. 258-280, 2007.

[81] J. H. Hoffman, R. C. Chaney, and H. Hammack, "Phoenix Mars mission—the thermal evolved gas analyzer," *Journal of the American Society for Mass Spectrometry,* vol. 19, pp. 1377-1383, 2008.

[82] P. H. Dawson, "Quadrupole mass spectrometry and its applications," 1976.

[83] D. Douglas, "Linear quadrupoles in mass spectrometry," *Mass spectrometry reviews,* vol. 28, pp. 937-960, 2009.

[84] É. Mathieu, "Mémoire sur le mouvement vibratoire d'une membrane de forme elliptique," *Journal de mathématiques pures et appliquées,* pp. 137-203, 1868.

[85] G. W. Hill, "On the part of the motion of the lunar perigee which is a function of the mean motions of the sun and moon," *Acta Mathematica,* vol. 8, pp. 1-36, 1886.

[86] N. Christofilos, "Focussing System for Ions and Electrons," US Patent, 2736799, 1950.

[87] E. D. Courant, M. S. Livingston, and H. S. Snyder, "The strong-focusing synchroton—A new high energy accelerator," *Physical Review,* vol. 88, p. 1190, 1952.

[88] R. Post and L. Heinrieh, "University of California Radiation Laboratory Report," *S. Shewehuek) UCRL,* vol. 2209, 1953.

[89] W. Paul, "Electromagnetic traps for charged and neutral particles (Nobel lecture)," *Angewandte Chemie International Edition in English,* vol. 29, pp. 739-748, 1990.

[90] W. Paul and M. Raether, "Das elektrische massenfilter," *Zeitschrift für Physik,* vol. 140, pp. 262-273, 1955.

[91] W. Paul, H. Reinhard, and U. Von Zahn, "Das elektrische massenfilter als massenspektrometer und isotopentrenner," *Zeitschrift für Physik,* vol. 152, pp. 143-182, 1958.

[92] C. Brunnée, "The ideal mass analyzer: fact or fiction?," *International journal of mass spectrometry and ion processes,* vol. 76, pp. 125-237, 1987.

[93] U. Von Zahn, "Präzisions-Massenbestimmungen mit dem elektrischen Massenfilter," *Zeitschrift für Physik,* vol. 168, pp. 129-142, 1962.

[94] D. Douglas and N. Konenkov, "Influence of the 6th and 10th spatial harmonics on the peak shape of a quadrupole mass filter with round rods," *Rapid Communications in Mass Spectrometry*, vol. 16, pp. 1425-1431, 2002.

[95] D. Denison, "Operating parameters of a quadrupole in a grounded cylindrical housing," *Journal of Vacuum Science and Technology,* vol. 8, pp. 266-269, 1971.

[96] A. Reuben, G. Smith, P. Moses, A. Vagov, M. Woods, D. Gordon, and R. Munn, "Ion trajectories in exactly determined quadrupole fields," *International journal of mass spectrometry and ion processes,* vol. 154, pp. 43-59, 1996.

[97] J. R. Gibson and S. Taylor, "Numerical investigation of the effect of electrode size on the behaviour of quadrupole mass filters," *Rapid Communications in Mass Spectrometry,* vol. 15, pp. 1960-1964, 2001.

[98] J. R. Gibson and S. Taylor, "Prediction of quadrupole mass filter performance for hyperbolic and circular cross section electrodes," *Rapid Communications in Mass Spectrometry,* vol. 14, pp. 1669-1673, 2000.

[99] W. Brubaker and W. Chamberlin, "Theoretical and experimental performance studies of quadrupole mass analyzers with round and hyperbolic field forming surfaces, noting resolving power superiority of hyperbolic rods," 1970.

[100] J. R. Gibson and S. Taylor, "Asymmetrical features of mass spectral peaks produced by quadrupole mass filters," *Rapid Communications in Mass Spectrometry*, vol. 17, pp. 1051-1055, 2003.

[101] W. Brubaker, "Advances in Mass Spectrometry," *Vol 4Elsevier, Amsterdam,* p. 293, 1968.

[102] W. M. Brubaker, "Auxillary Electrodes for Quadrupole Mass Filter," US3129327, 1964.

[103] W. M. Brubaker, "An improved quadrupole mass analyzer," *Adv. Mass Spectrom,* vol. 4, pp. 293-299, 1968.

[104] Fite, W. L, “Spatial separation of fringe fields in quadrupole mass filters,” *Review of Scientific Instruments*, 47, 326-330, 1976.

[105] E. T. Barnett, WS; Turner, WR, "An Improved Multipole Mass Filter," GB1242031, 1971.

[106] P. Dawson, "Ion optical properties of quadrupole mass filters," *Advances in Electronics and Electron Physics,* vol. 53, pp. 153-208, 1980.

[107] K. L. Hunter and B. J. McIntosh, "An improved model of the fringing fields of a quadrupole mass filter," *International journal of mass spectrometry and ion processes*, vol. 87, pp. 157-164, 1989.

[108] B. J. McIntosh and K. L. Hunter, "Influence of realistic fringing fields on the acceptance of a quadrupole mass filter," *International journal of mass spectrometry and ion processes,* vol. 87, pp. 165-179, 1989.

[109] F. Ma and S. Taylor, "Simulation of ion trajectories through the mass filter of a quadrupole mass spectrometer," *IEE Proceedings-Science, Measurement and Technology,* vol. 143, pp. 71-76, 1996.

[110] S. Hiroki, T. Abe, and Y. Murakami, "Separation of helium and deuterium peaks with a quadrupole mass spectrometer by using the second stability zone in the Mathieu diagram," *Review of Scientific Instruments,* vol. 63, pp. 3874-3876, 1992.

[111] S. Hiroki, T. Abe, and Y. Murakami, "Detection of a 10-4 helium peak in a deuterium atmosphere using a modified high-resolution quadrupole mass spectrometer," *Review of Scientific Instruments,* vol. 65, pp. 1912-1917, 1994.

[112] N. Konenkov, G. Mogilchenko, S. Silakov, and G. Shagimuratov, "Quadrupole mass spectrometer with high resolution ability," *Prib Tekh Eksp,* vol. 2, pp. 179-181, 1990.

[113] T. J. Hogan and S. Taylor, "Performance simulation of a quadrupole mass filter operating in the first and third stability zones," *Instrumentation and Measurement, IEEE Transactions on*, vol. 57, pp. 498-508, 2008.

[114] Z. Du, D. Douglas, and N. Konenkov, "Elemental analysis with quadrupole mass filters operated in higher stability regions," *J. Anal. At. Spectrom.,* vol. 14, pp. 1111-1119, 1999.

[115] M. Yang, T.-Y. Kim, H.-C. Hwang, S.-K. Yi, and D.-H. Kim, "Development of a palm portable mass spectrometer," *Journal of the American Society for Mass Spectrometry,* vol. 19, pp. 1442-1448, 2008.

[116] J. Wang, X. Zhang, F. Mao, M. Xiao, Y. Cui, D. den Engelsen, and W. Lei, "Study of a micro chamber quadrupole mass spectrometer," *Journal of Vacuum Science & Technology A: Vacuum, Surfaces, and Films,* vol. 26, pp. 239-243, 2008.

[117] D. Holkeboer, T. Karandy, F. Currier, L. Frees, and R. Ellefson, "Miniature quadrupole residual gas analyzer for process monitoring at milliTorr pressures," *Journal of Vacuum Science & Technology A: Vacuum, Surfaces, and Films,* vol. 16, pp. 1157-1162, 1998.

[118] E. R. Badman and R. Graham Cooks, "Miniature mass analyzers," *Journal of Mass Spectrometry,* vol. 35, pp. 659-671, 2000.

[119] S. Boumsellek and R. J. Ferran, "Trade-offs in miniature quadrupole designs," *Journal of the American Society for Mass Spectrometry,* vol. 12, pp. 633-640, 2001.

[120] O. Orient, A. Chutjian, and V. Garkanian, "Miniature, high-resolution, quadrupole mass-spectrometer array," *Review of Scientific Instruments,* vol. 68, pp. 1393-1397, 1997.

[121] R. Ferran and S. Boumsellek, "High-pressure effects in miniature arrays of quadrupole analyzers for residual gas analysis from 10-9 to 10-2 Torr," *Journal of Vacuum Science & Technology A: Vacuum, Surfaces, and Films,* vol. 14, pp. 1258-1265, 1996.

[122] H. Kleinpoppen and J. Schumann, "Static Quadrupole Field for three-dimensional stabilisation of electrons," Univ., Tuebingen, Ger., 1967.

[123] S. Beu, C. Hendrickson, and A. Marshall, "Excitation of Radial Ion Motion in an rf-Only Multipole Ion Guide Immersed in a Strong Magnetic Field Gradient," *Journal of the American Society for Mass Spectrometry,* vol. 22, pp. 591-601, 2011.

[124] R. T. McIver Jr, "Trajectory calculations for axial injection of ions into a magnetic field: overcoming the magnetic mirror effect with an rf quadrupole lens," *International journal of mass spectrometry and ion processes,* vol. 98, pp. 35-50, 1990.

[125] Y. Huang, S. Guan, H. S. Kim, and A. G. Marshall, "Ion transport through a strong magnetic field gradient by r.f.-only octupole ion guides," *International journal of mass spectrometry and ion processes,* vol. 152, pp. 121-133, 1996.

[126] G. Gervasini, M. De Angeli, and G. Gittini, "Design and test of magnetic shields for quadrupole mass spectrometers," *Journal of Vacuum Science & Technology A: Vacuum, Surfaces, and Films,* vol. 25, pp. 269-274, 2007.

[127] H. Poritsky and R. Jerrard, "An integrable case of electron motion in electric and magnetic field," *Journal of Applied Physics,* vol. 23, pp. 928-930, 1952.

[128] E. Fischer, *Z. Phys*., vol. 156, pp. 1-26, 1959.

[129] P. Kubícek, "Theoretical possibilities of a solenoid as mass filter," *Czechoslovak Journal of Physics B,* vol. 20, pp. 475-486, 1970.

[130] J. P. Carrico, “Applications of Inhomogeneous Oscillatory Electric Fields in Ion Physics," *Dynamic Mass Spectrometry,* vol. 3, (Ed. D. Price), Heyden & Son, London, 1, pp1-65, 1972.

[131] Y. G. Pavlenko and A. Toropova, "A new class spectrometer: A quadopole in a magnetic field," *Journal of communications technology & electronics,* vol. 41, pp. 471-475, 1996.

[132] J. Tunstall, S. Taylor, A. Vourdas, J. Leck, and J. Batey, "Application of a static magnetic field to the mass filter of a quadrupole mass spectrometer," *Vacuum*, vol. 53, pp. 211-213, 1999.

[133] B. Srigengan, J. Gibson, and S. Taylor, "Ion trajectories in quadrupole mass spectrometer with a static transverse magnetic field applied to mass filter," in *Science, Measurement and Technology, IEE Proceedings-*, pp. 274-278, 2000.

[134] S. U. Syed, J. Sreekumar, B. Brkic, J. R. Gibson, and S. Taylor, "Effect of an axial magnetic field on the performance of a quadrupole mass spectrometer," *Journal of the American Society for Mass Spectrometry,* vol. 21, pp. 2070-2076, 2010.

[135] S. U. Syed, J. Sreekumar, J. Gibson, and S. Taylor, "QMS in the third stability zone with a transverse magnetic field applied," *Journal of the American Society for Mass Spectrometry,* vol. 22, pp. 1381-1387, 2011.

[136] S. Maher, S. U. Syed, D. M. Hughes, J. R. Gibson, and S. Taylor, "Mapping the Stability Diagram of a Quadrupole Mass Spectrometer with a Static Transverse Magnetic Field Applied," *Journal of the American Society for Mass Spectrometry,* pp. 1-8, 2013.

Chapter 3 : Quadrupole Mass Filter

FUNDAMENTAL THEORY

3.1 Basic Theory: Conventional Quadrupole Mass Filter

A simple quadrupole mass filter (QMF) has four parallel electrodes of constant cross section with their axes parallel to the z-axis; they are equispaced around the z-axis and touch an imaginary inscribed circle with radius, r_0. If the electrodes have hyperbolic cross-section and are perfectly aligned then the field is linear and is a quadrupolar field[6]. In practice, to make the manufacturing process easier, circular cross section electrodes with radius, r, are often used (figure 3.1). This leads to reduced performance. In practice, the electrodes are finite in length, l, and result in a close approximation to the ideal quadrupole electric field (figure 3.2) provided ${}^{r}/_{r_0} \cong 1.127$ [1]. For normal filter operation the potential between opposite electrodes is given by,

$$\emptyset_0 = U - V\cos\omega t \tag{3.1}$$

where U is direct potential, V is the zero to peak amplitude of the alternating potential, ω is the angular frequency of the alternating potential given by, $\omega = 2\pi f$, and t is time.

---

[6] The term quadrupolar field refers to the potential at a point being proportional to the square of the distance from the origin of reference.

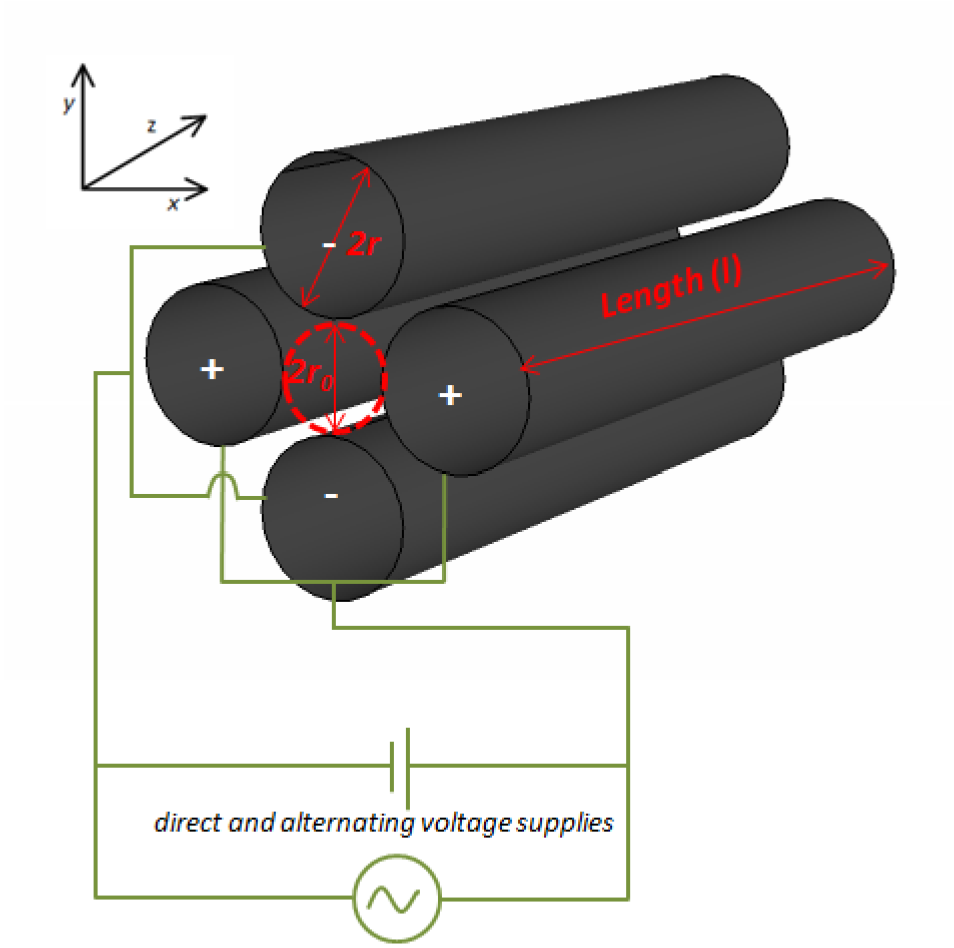

Figure 3.1: Schematic of quadrupole mass filter with circular electrodes

3.1.1 Qualitative Description

The electrode structure of a QMF is shown in figure 3.1. The effect of the applied voltages is to create an electro-dynamic quadrupole field in the central region between the electrodes. The QMF separates ions of different *m/z* according to the path stability within the device. The ideal quadrupole field increases linearly with increasing displacement from the central axis and is independent in *x* and *y*.

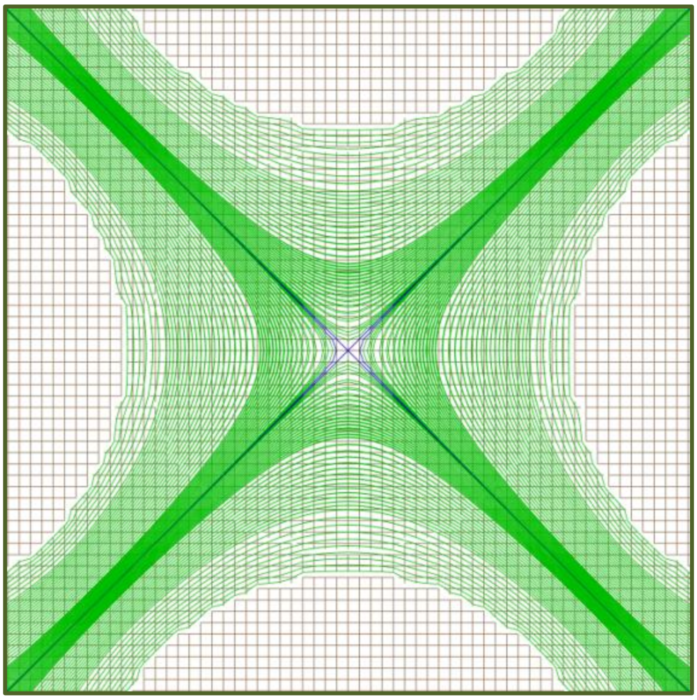

Figure 3.2: Plot of equipotentials in the *xy* plane generated with SIMION® 8.0

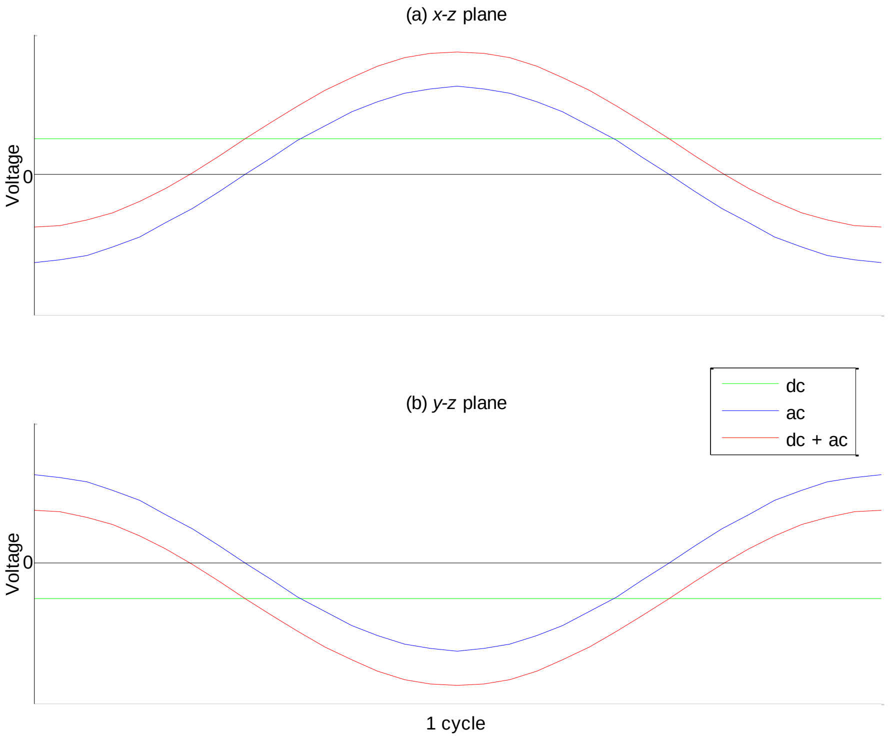

Figure 3.3: Constant alternating and direct potentials on *x* and *y* pair electrodes

The effect of the quadrupolar field on an ion can be understood qualitatively by considering the effects of the alternating and direct potentials (figure 3.3), in the *x*-*z* and *y*-*z* planes independently [2]. We consider the case for a *single positively* charged ion:

x-z plane

The *x* electrode pair is held at a positive direct potential and the *y* electrode pair is held at a negative direct potential. Hence the direct potential has a focusing effect in the *x*-*z* plane. Consider the effect of a sinusoidal potential in isolation (i.e., with zero potential offset). For one half of a cycle the ions will be repelled and for the other half of the cycle they will be attracted to the electrodes. Certain factors, which are discussed in the following sections of this chapter, will dictate whether an ion strikes the electrode during the negative half of the cycle.

The superposition of the alternating and direct potentials will modify the motion of the ions according to their respective masses. Heavy ions are largely invariant to the alternating potential and respond to the average potential of the electrodes thus being focused towards the centre of the axis. Lighter ions will respond more readily to the alternating potential and if sufficiently light will have an unstable trajectory. In this respect, the *x*-*z* plane filters out lighter ions due to the speed with which they can respond to the defocussing (negative) portion of the alternating potential. Hence the *x*-*z* plane acts as a high mass pass filter.

y-z plane

Conversely for the *y*-*z* plane, the *y* electrode pair is held at a negative direct potential and the alternating potential is the same magnitude but opposite in sign (i.e. 180° phase shift between alternating potential applied to the two pairs of electrodes). Heavier ions, because of their greater inertia, are still largely influenced by the direct potential which has a defocussing effect on positively charged ions. This causes the ions which are sufficiently heavy to become unstable. The lighter ions are more responsive to the alternating potential and are focused towards the centre of the field region. Hence the *y*-*z* plane can be thought of as a low mass pass filter.

Net Effect

For an ideal quadrupole field the motion of an ion is independent in all three dimensions (*x, y, z*). By combining the high mass pass filtering action of the *xz* plane with the low mass pass filtering action of the *yz* plane, the net result can be thought of as a band pass mass filter where ions of some intermediate mass may be stable in both planes. For an ion to traverse the length of the field region, it must be sufficiently light such that it is not destabilised in the *yz* plane but not too light so as to be destabilised in the *xz* plane. The width of the band pass region is dictated by a number of factors, including: the instantaneous amplitude of the potentials, the alternating potential frequency (i.e. the time period of the ac waveform), the position and velocity of the ion, the mass of the ion and the limit of the field region. These are discussed below.

3.1.2 The Quadrupole Mass Filter Field

A quadrupole field is expressed by a linear dependence on position [3]. Using Cartesian co-ordinates (x, y, z):

$$\boldsymbol{E} = \emptyset_0(ax + by + cz) \tag{3.2}$$

where a, b, c are weighting constants and $\emptyset_0$ is a position-independent factor which may be a function of time. Since the component of the electric field in any direction is given by:

$$\boldsymbol{E} = -\nabla\emptyset \tag{3.3}$$

Then,

$$\emptyset = -\frac{\emptyset_0}{2}(ax^2 + by^2 + cz^2) + C \tag{3.4}$$

where *C* is a constant of integration and would refer physically to a fixed, offset potential. Assuming a charge-free region in the space between the electrodes then the Laplace equation (special case of Poisson's equation) holds true:

$$\nabla \cdot \boldsymbol{E} = \nabla^2\emptyset = \frac{\partial^2\emptyset}{\partial x^2} + \frac{\partial^2\emptyset}{\partial y^2} + \frac{\partial^2\emptyset}{\partial z^2} = 0 \tag{3.5}$$

Substituting (3.4) into (3.5) and solving yields:

$$\nabla^2\emptyset = -\emptyset_0(a + b + c) = 0 \tag{3.6}$$

Since $\emptyset_0$ in (3.6) is non-zero:

$$a + b + c = 0 \tag{3.7}$$

There are an infinite number of solutions to satisfy (3.7), however the simplest that have been chosen in practice for the QMF case are [4]:

$$a = -b = 1 \quad c = 0 \tag{3.8}$$

Since $c = 0$ the z dimension becomes redundant and the field is two-dimensional (x, y). Substituting the result from (3.8) into (3.4) yields:

$$\emptyset = -\frac{\emptyset_0 a}{2}(x^2 - y^2) + C \tag{3.9}$$

If we assume the offset potential to be zero then we can ignore *C* and (3.9) becomes:

$$\emptyset = -\frac{\emptyset_0 a}{2}(x^2 - y^2) \tag{3.10}$$

Now, let r_0 be the nearest electrode surface to the origin. Substituting into (3.10) for the boundary condition ($\emptyset = \emptyset_0$), which occurs when, $x = r_0$ and $y = 0$, yields,

$$\emptyset_0 = -\frac{\emptyset_0 a r_0^2}{2} \tag{3.11}$$

Therefore,

$$a = -\frac{2}{r_0^2} \tag{3.12}$$

Thus, the electrode geometry must have hyperbolic cross section, and the electrostatic field in the space between the electrodes is given by substituting (3.12) into (3.10):

$$\emptyset = \emptyset_0 \frac{(x^2 - y^2)}{r_0^2} \tag{3.13}$$

where, $\emptyset_0$ is specified in equation (3.1) which gives:

$$\emptyset(x, y, t) = \frac{(x^2 - y^2)}{r_0^2}(U - V\cos\omega t) \tag{3.14}$$

It is important to note that the analytical potential assumes the equipotential lines extend to infinity. However, in practice the electrodes have finite dimensions and the field is slightly perturbed at the truncation points of the hyperbolic electrodes. Furthermore it should be noted, in using the Laplace equation it is assumed that the space charge effect (charge density) within the QMF is negligible.

3.1.3 Equations of Ion Motion in the Quadrupole Mass Filter

In this section we consider the equations of motion for a singly charged ion and for non-relativistic speeds. From Newton's second law of motion we have:

$$\boldsymbol{F} = m\boldsymbol{a} = m\frac{d^2\boldsymbol{u}}{dt^2} \tag{3.15}$$

where $\boldsymbol{F}$ is force, m is mass, $\boldsymbol{a}$ is acceleration, $\boldsymbol{u}$ is displacement (x, y, z), and t is time. According to the Lorentz force law, the force on an ion of charge e in an electric field is given by:

$$\boldsymbol{F} = e\boldsymbol{E} \tag{3.16}$$

Equating (3.15) and (3.16) yields:

$$e\boldsymbol{E} = m\frac{d^2\boldsymbol{u}}{dt^2} \tag{3.17}$$

And substituting (3.3) into (3.17):

$$-e\nabla\emptyset = m\frac{d^2\boldsymbol{u}}{dt^2} \tag{3.18}$$

Expanding (3.18) and using unit vectors ($\hat{\boldsymbol{\imath}}, \hat{\boldsymbol{\jmath}}, \widehat{\boldsymbol{k}}$):

$$-e\left(\frac{\partial\emptyset}{\partial x}\hat{\boldsymbol{\imath}} + \frac{\partial\emptyset}{\partial y}\hat{\boldsymbol{\jmath}} + \frac{\partial\emptyset}{\partial z}\widehat{\boldsymbol{k}}\right) = m\left(\frac{d^2x}{dt^2}\hat{\boldsymbol{\imath}} + \frac{d^2y}{dt^2}\hat{\boldsymbol{\jmath}} + \frac{d^2z}{dt^2}\widehat{\boldsymbol{k}}\right) \tag{3.19}$$

Re-arranging (3.19) to combine terms for each dimension yields:

$$\left(\frac{d^2x}{dt^2} + \frac{e}{m}\frac{\partial\emptyset}{\partial x}\right)\hat{\boldsymbol{\imath}} + \left(\frac{d^2y}{dt^2} + \frac{e}{m}\frac{\partial\emptyset}{\partial y}\right)\hat{\boldsymbol{\jmath}} + \left(\frac{d^2z}{dt^2} + \frac{e}{m}\frac{\partial\emptyset}{\partial z}\right)\widehat{\boldsymbol{k}} = 0 \tag{3.20}$$

where, expanding (3.14) gives:

$$\frac{\partial\emptyset}{\partial x} = \frac{2x}{r_0^2}(U - V\cos\omega t) \tag{3.21}$$

$$\frac{\partial\emptyset}{\partial y} = -\frac{2y}{r_0^2}(U - V\cos\omega t) \tag{3.22}$$

$$\frac{\partial\emptyset}{\partial z} = 0 \tag{3.23}$$

Considering each dimension in isolation we obtain three linear, second order, ordinary differential equations:

$$\frac{d^2x}{dt^2} + \frac{e}{m}(U - V\cos(\omega t))\frac{2x}{r_0^2} = 0 \tag{3.24}$$

$$\frac{d^2y}{dt^2} - \frac{e}{m}(U - V\cos(\omega t))\frac{2y}{r_0^2} = 0 \tag{3.25}$$

$$\frac{d^2z}{dt^2} = 0 \tag{3.26}$$

There is no field in z and hence no force. By integrating (3.26) it is seen that the ion will travel with constant axial velocity given by its initial value:

$$\frac{dz}{dt} = C \tag{3.27}$$

where, C is a constant determined by the initial conditions, specifically the axial velocity (v_z) with which the ion enters the QMF.

Integrating a second time (for position):

$$z(t) = v_z t + C \tag{3.28}$$

where, C is a constant of integration determined by the initial conditions, specifically the initial axial position (z_0), which is zero for an ion at the entrance to the QMF (at $z = 0$).

3.1.4 Mathieu Equation

The equations of motions (3.24 and 3.25) are a form of the Mathieu equation. The Mathieu equation is a special case of the Hill equation [5] having only one harmonic mode and is covered comprehensively in various texts [6-8]. The standard and commonly accepted (canonical) form of the Mathieu equation can be obtained by the following substitutions:

$$\xi = \frac{\omega t}{2} \tag{3.29}$$

$$a_u = a_x = -a_y = \frac{8eU}{mr_0^2\omega^2} \tag{3.30}$$

$$q_u = q_x = -q_y = \frac{4eV}{mr_0^2\omega^2} \tag{3.31}$$

where u is displacement (x or y), ξ is a dimensionless modified time parameter given by, $\xi = {}^{\omega t}/_{2}$, ω is the angular frequency of the alternating potential given by, $\omega = 2\pi f$, t is time, a_u and q_u are dimensionless stability parameters.

The equations of motion can then be written as:

$$\frac{d^2u}{d\xi^2} + (a_u - 2q_u\cos(2\xi))u = 0 \tag{3.32}$$

The expression (3.32) now has two constants (a, q) and two variables (u, ξ). The properties of the Mathieu equation are well established and solutions can be classified according to their boundedness (stability). Bounded (stable) solutions do not exceed a finite excursion, and unbounded (unstable) solutions increase in displacement without limit as ξ tends to infinity.

From Floquet's[7] theorem [9], the complete solution to the Mathieu equation can be expressed as a linear combination of $u(-\xi)$ and $u(\xi)$:

$$u = ce^{\mu\xi}P(\xi) + c'e^{-\mu\xi}P(-\xi) \tag{3.33}$$

where $P(\xi)$ is a periodic function with the same periodicity as the coefficient in (3.32), μ is the characteristic exponent, c and *c'* are constants of integration that depend upon the initial conditions ($u_0, \left(\frac{du}{d\xi}\right)_0, \xi_0$). The solution has two summative terms since $u(-\xi)$ is also a solution. This is because the cosine term of the Mathieu function is even and the equation remains unchanged if $-\xi$ is exchanged for ξ. This solution is independent from $u(\xi)$, since $u(-\xi)$ is not a constant multiple of $u(\xi)$.

The characteristic exponent can be expressed as $\mu = \alpha + i\beta$. The value of μ is dependent on a and q. The solutions that can be classified as stable or unstable according to the value of μ as summarised in figure 3.4. When μ has any real number term ($\mu \neq 0$) the solution is unstable. The solution can be stable or unstable when μ is an imaginary number (without any real part, i.e., $\mu = i\beta$). If β is an integer, the solutions are periodic but unstable given by an oscillatory function with a growing exponential windowing function. If β is not an integer, the solutions are periodic and stable.

β is a complex function dependent on a and q. The boundaries between stable and unstable regions of the stability diagram (see 3.1.5) correspond to the characteristic values of a and q for which β is an integer (see appendix A).

---

[7] Floquet's theorem states that a solution to a second-order linear differential equation, with coefficients that are periodic single-valued functions of an independent variable (such as the Mathieu equation for fixed values of a, q), is of the form $e^{\mu u}P(u)$ where u is the independent variable, μ is a constant and $P(u)$ is a periodic function with the same periodicity as the equation.

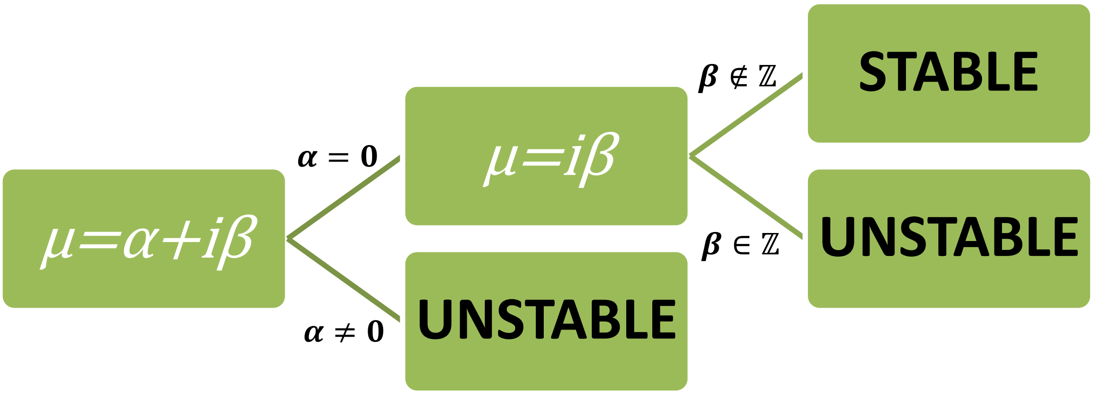

Figure 3.4: Summary of solution classification depending on μ, assuming $\mu \neq 0$

3.1.5 Stability Diagram

Mathematically the stability of an ion in x or y is dependent on the values of a and q. The initial conditions (those conditions at the entrance to the field) determine only the magnitude of oscillation. The stability (or boundedness) of solutions to the Mathieu equation, as a function of dimensionless parameters (a, q), are characterized by transition curves (see appendix A). Solutions to the Mathieu equation provide an insight into the stability of ion motion in the x and/or y co-ordinate directions. The stability diagram consists of overlapping regions of solutions which represent zones of operation where ion trajectories will be stable in both x and y co-ordinate directions. Within these overlapping stability zones the trajectory of an ion is bounded and hence stable. Outside of these zones the trajectory of an ion will become unbounded and thus is classified as unstable. The primary concern for QMF operation is to classify stable and unstable solutions. The composite 2 dimensional

Mathieu stability diagram is obtained by superimposing the separate stability regions for each dimension (figure 3.5).

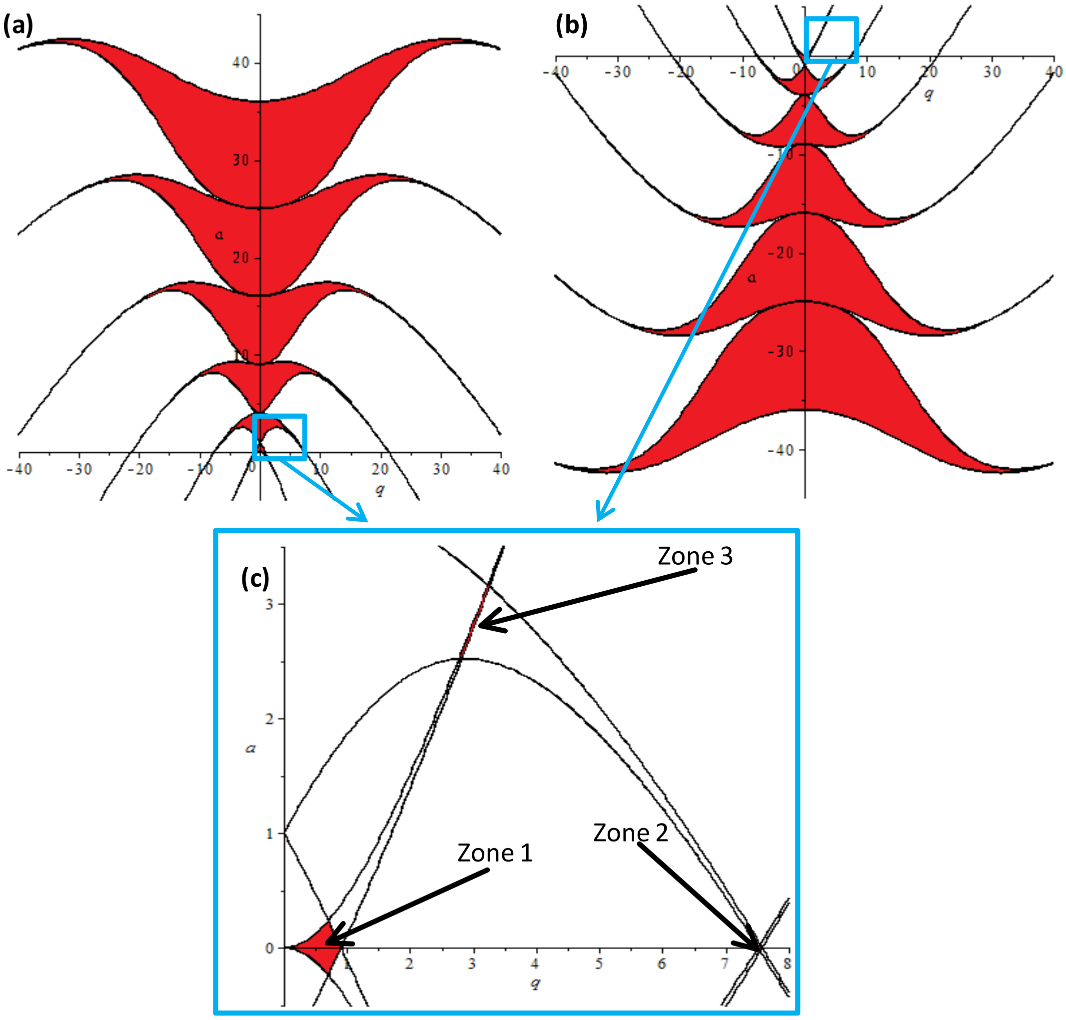

Figure 3.5: Mathieu stability regions, (a) *x* stable, (b) *y* stable (c) composite (*x* and *y* stable)

There are theoretically an infinite number of stability regions, however zone 1 is commonly used for QMS operation due to its proximity to the origin. This reduces the power requirement for QMF operation since $a \propto U$ and $q \propto V$ (see equations 3.30 and 3.31). However, certain advantages (such as improved resolution) can be obtained when operating in stability zone 3. The stability diagram is a mathematical construct and assumes ideal conditions, essentially an infinite quadrupole field. Henceforth, it does not take into account the physical constraints of the field nor the initial ion conditions since it is assumed that the ion is always in the field. Stability zones 1 and 3 are shown in more detail in figures 3.6 and 3.7 respectively.

The stability zone areas are symmetrical about the a axis (i.e., $q = 0$) for both the independent x and y dimensions (figure 3.5 (a) & (b)). This is because the condition of stability (or instability) is independent of the initial phase of the alternating field (ξ_0). However, not all of the transition boundaries are symmetrical about the a axis (only those of even order – see appendix A). Similarly, the stability zone areas are symmetrical about the q axis (i.e., $a = 0$) although the transition boundaries are not (figure 3.6).

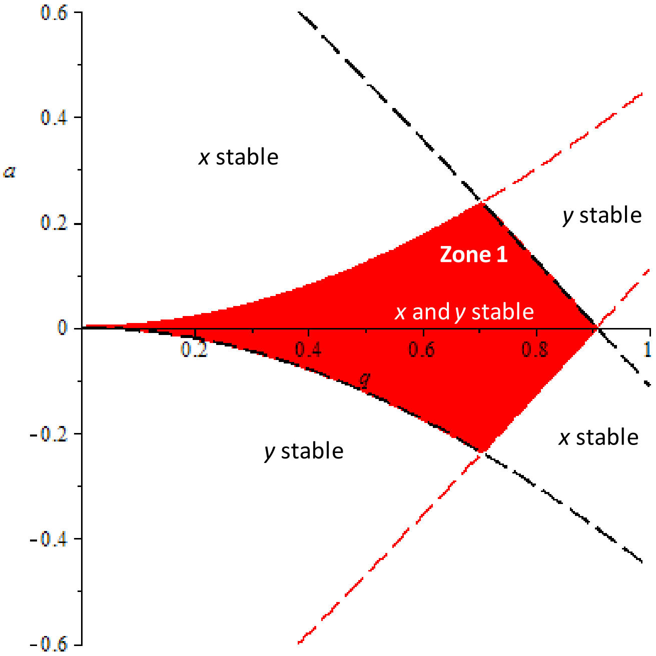

Figure 3.6: Stability Zone 1 (first and fourth quadrants of *a*-*q* space)

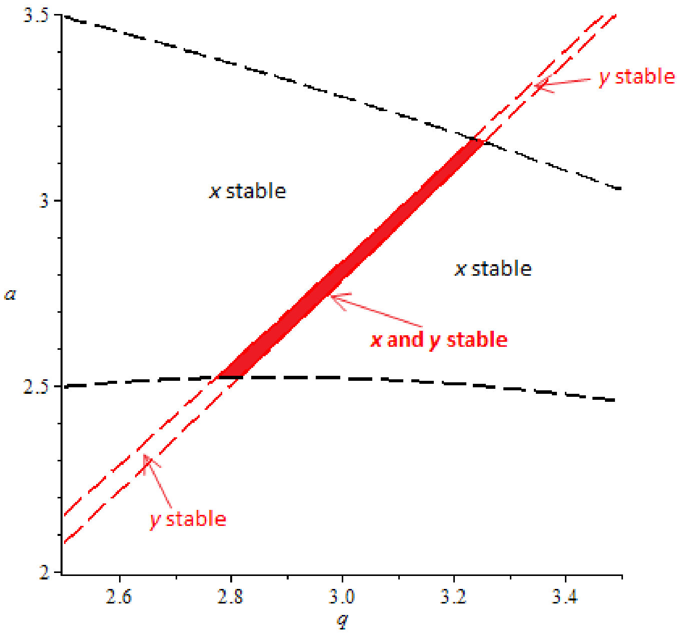

Figure 3.7: Stability Zone 3 (first quadrant of *a*-*q* space)

3.1.6 Quadrupole Mass Filter Operation

In order to provide mass selectivity over a given range, a QMF is operated in such a way that it scans through a narrow portion of the stability region. This may be achieved by choosing any arbitrary operating values for *a* and *q*. In practice, the QMF is usually operated such that the values of *a* and *q* are related. This is typically achieved by ramping the direct (*U*) and alternating (*V*) electrode voltages concurrently. The ratio *a*/*q*, from equations 3.30 and 3.31, gives $a/q = 2U/V$. By scanning the amplitudes of *U* and *V*, at a given fixed ratio, a mass scan line is able to cut through the stability diagram producing a mass spectrum whose resolution is dependent on the voltage ratio $\left(\frac{U}{V}\right)$. We can define the scan line in *a*-*q* space as:

$$a = \left(\frac{a_{apex}}{q_{apex}}\right) \times \eta \times q \tag{3.34}$$

This represents a straight line passing through the origin where η represents the gradient of the scan line defined such that the apex of the stability zone corresponds to $\eta = 1$ (figure 3.8).

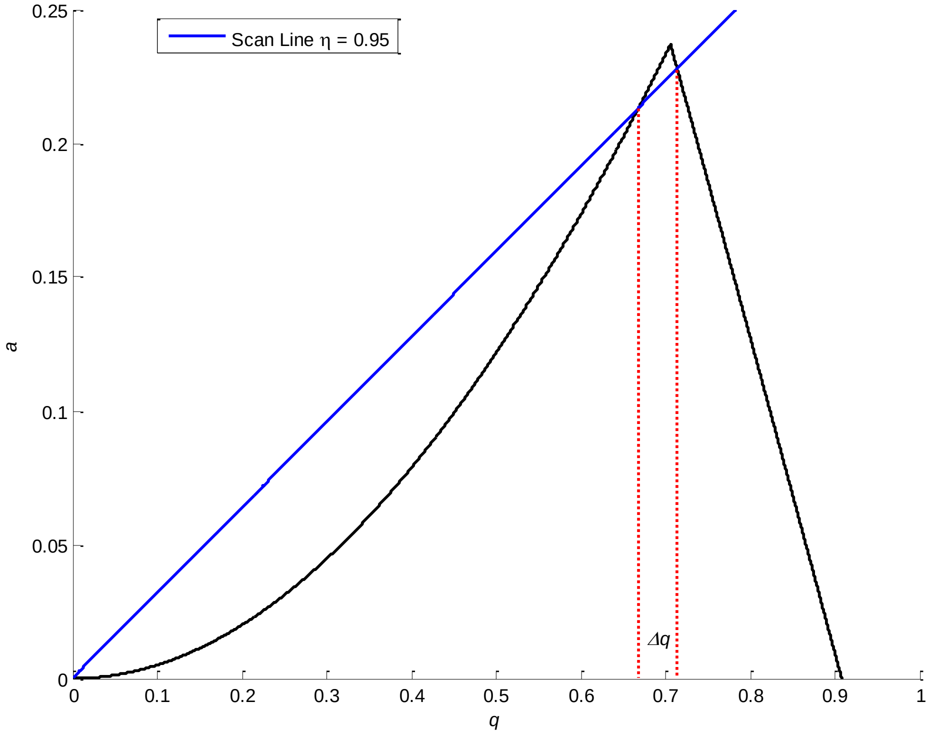

Figure 3.8: Scan line 'cutting' through stability zone 1

A particular scan line is chosen to be in close proximity to the apex of the stability zone. As the stability tip is approached, the intersection of the scan line with the stability region becomes narrower ($\Delta q \rightarrow 0$) causing only a narrow band of *m/z* to be stable, thus increasing the instrument resolution. In practise, the maximum ion displacement tends to increase as the stability tip is approached. The result is that increased resolution tends to be associated with decreased useable aperture and hence poor ion transmission [3].

The width of the intersection of the scan line with the stability zone is related to the resolution of the instrument. The equation for resolution, R, (as defined in (1.1)) is repeated here for convenience:

$$R = \frac{m}{\Delta m}$$

where Δm is related to the width of a mass spectral peak. Equation (3.31) can be generalised by making q a function of mass and assuming all other parameters as constant [10]:

$$q = km^{-1} \tag{3.35}$$

where k is a constant. Since,

$$dq = \frac{dq}{dm}dm \tag{3.36}$$

Then,

$$dq = -\frac{k}{m^2}dm \tag{3.37}$$

Substituting (3.35) into (3.37) and re-arranging gives:

$$\frac{dq}{q} = -\frac{dm}{m} \tag{3.38}$$

If $|-dm| \cong \Delta m$ and $dq \cong \Delta q$

Then,

$$R = \frac{m}{\Delta m} = \frac{q}{\Delta q} \tag{3.39}$$

By following a similar procedure with equation (3.30) a similar expression can be obtained for Δa, which can also be used for calculating QMF resolution [11]:

$$R = \frac{a}{\Delta a} \tag{3.40}$$

Scanning over a mass range can be illustrated by considering the stability diagram(s) in *U*-*V* space. In *U*-*V* space a stability diagram can be drawn for each *m/z* species [12]. *U* and *V* are proportional to *m/z* (equations (3.30) & (3.31)) and ramping *U* and *V* concurrently at a fixed ratio leads to a constant resolution mass spectrum for ions in order of increasing *m/z* (figure 3.9) [8]. Commercial QMS systems often employ a constant peak width scan. This can be achieved by using a non-linear scan line or can be approximated by using a linear scan line with a dc offset [13].

---

[8] In *a*-*q* space, larger values of *m/z* refer to points closer to the origin.

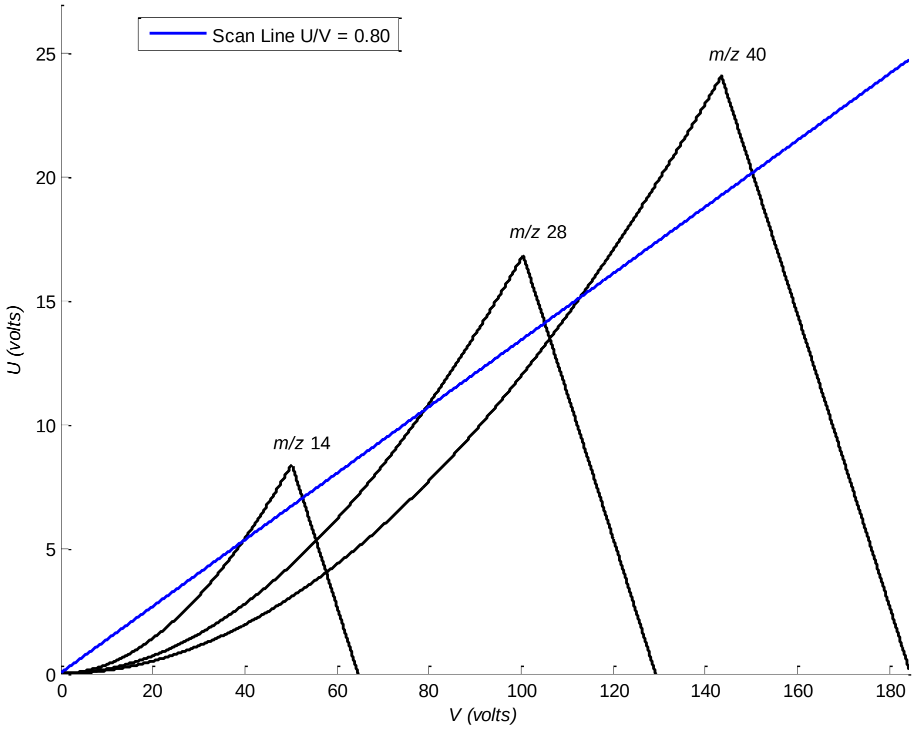

Figure 3.9: Stability diagrams for *m/z* species 14, 28 and 40 in zone 1, where f = 1.86MHz and r_0 = 2.67mm

An alternative method of QMF operation is to scan the frequency (f) whilst maintaining U and V constant. Since a and q are inversely proportional to the square of the angular frequency of the alternating potential (equations (3.30) & (3.31)) then rearranging equation 3.30 yields,

$$f = \sqrt{\frac{eV}{\pi^2 r_0^2 m q_u}} \tag{3.41}$$

A similar expression can be obtained in terms of a by re-arranging 3.31. The advantages of frequency scanning include: only having one parameter to vary (as opposed to two in sync), and potentially an increased mass range (see 1.1 & 3.1.7). However, reducing the frequency means that the ion experiences fewer field cycles in the QMF which leads to reduced resolution (see 3.1.7). Furthermore, the acceptance of the QMF is proportional to the square of the frequency which leads to reduced sensitivity at lower operating frequencies [14].

3.1.7 Quadrupole Mass Filter Resolution and Mass Range

Two of the fundamental considerations for QMF design are the instrument resolution and mass range. These are dependent upon five basic parameters: length of electrodes, maximum ac voltage output, alternating supply frequency, inscribed electrode radius, and the ion injection energy. The interdependence of these performance criteria is illustrated in figure 3.10.

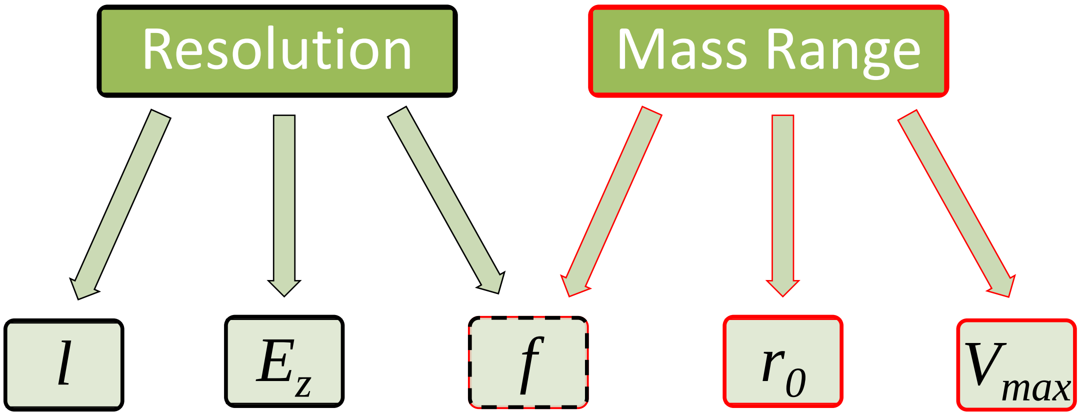

Figure 3.10: Resolution and Mass Range dependence on basic parameters

Resolution

The resolution of a QMF is dependent upon the number of field cycles an ion experiences within the device [3] and is given by:

$$\frac{m}{\Delta m} = \frac{1}{K} N^n \tag{3.42}$$

where N is the number of field cycles an ion experiences, and the values of constants K and n are dependent on the stability zone operated in as well as the definition used for Δm. For zone 1, a value of $n \approx 2$ and $K \approx 20$ are often assumed (for all practical purposes) [3].

The number of field cycles an ion spends in a QMF of length, l, is given by:

$$N = fl\sqrt{\frac{m}{2E_z}} \tag{3.43}$$

where E_z is the axial ion energy (in Joules).

Increasing the number of cycles an ion experiences within the field leads to increased resolution (equation 3.42). However, recent studies have shown that increasing the number of field cycles eventually causes the resolution to saturate. It follows that the theoretical maximum resolution is limited by the intersection of the mass scan line with the stability zone [11, 15].

Mass Range

For a QMF power supply with a maximum ac voltage limit (V_{max}), the maximum *m/z* that can be analysed is:

$$({}^{m}/_{z})_{max} = \frac{4eV_{max}}{q_{tip} r_0^2 \omega^2} \quad (3.44)$$

where $q_{tip} \approx 0.706$ and is the value of q at the stability zone apex (in zone 1).

A trade-off exists between increasing instrument mass range whilst maintaining sufficient resolution which is dependent on the alternating potential frequency (figure 3.9). The mass range is inversely proportional to the square of the frequency and so a reduced frequency yields an increased mass range allowing larger *m/z* to be investigated (equation 3.44). However, the analyser resolution is related to the number of cycles an ion spends in the field which is proportional to the frequency. Hence reducing the frequency increases the mass range but reduces resolution.

3.2 Computer Simulation of a Quadrupole Mass Filter

In practice investigating QMF performance for different design parameters (e.g., electrode length, inscribed radius) is often a difficult, costly and time consuming task. Simulation of instrument performance provides a cost-effective manner for predicting instrument behaviour and investigating various design options.

A custom software model developed at the University of Liverpool is described here which solves the Mathieu equation numerically. Earlier versions solved the electric fields in two dimensions (x and y) [16]. The latest version solves the fields in three dimensions (3D) [17]. The equation is solved utilising the 4th order[9] Runge-Kutta algorithm (RK4) [18]. The program operates by creating a random distribution of a large number of (typically 10^6 or more) ions within a user defined circular area centred on the quadrupole axis. All ion entrance positions are assumed equally probable. The number of ions simulated is defined by the user. Each ion has a uniformly distributed initial phase with respect to the alternating potential frequency. Furthermore, each ion has a user defined initial transverse velocity and axial velocity.

There are two distinct versions of the two-dimensional (2D) model used in this thesis:

1. Assumes QMF electrodes are ideal and have perfect hyperbolic cross sections that are accurately positioned (QMS-Hyperbolic).
2. The other version uses electric field values which are obtained by computing the potential distribution within a boundary set by user defined electrode geometry and applied potentials (QMS-2D).

---

[9] Typically a method is nth order if its error term is $O(h^{n+1})$.

There is little difference between the implementation of the numerical integration algorithm for each of these cases. For case 2, electric field values (E_x and E_y) are incorporated into the equations of motion. The only difference in terms of the program input and the graphical user interface (GUI) is that a field file must be specified (for QMS-2D).

3.2.1 Assumptions

The following assumptions apply to both 2D model versions (1 & 2):

(i) $E_z = 0 \left(\Rightarrow \frac{d^2z}{dt^2} = 0 \right)$ & $v_z = v_{z_0} = constant.$

(ii) Positive voltage is applied to *x* electrodes (and negative to *y* electrodes).

(iii) 'End' effects (fringing fields) are ignored. Ions enter/exit the field at its full value.

(iv) Trajectories are calculated over the user defined QMF length.

(v) Ion density is assumed to be low enough to ignore space charge effects.

(vi) Ion motion in each Cartesian co-ordinate direction is assumed to be independent (only strictly true for case 1, QMS-Hyperbolic).

(vii) Earth's fields (electric, magnetic, gravitational) are considered to be negligible.

3.2.2 Electric Field Solving

In order to simulate a QMF with non-hyperbolic electrodes, it is necessary to calculate the electric field at discrete points over the area enclosed by the electrodes. This requires that the electric field is known to a high enough degree of accuracy at all positions (x, y) within the field radius r_0. The model uses the field values to calculate the trajectories of ions as they traverse along the length of the QMF.

Calculating the potential distribution requires Laplace’s equation (equation 3.5) to be solved in an interior domain set by the boundary of the electrode geometry and potentials. Assuming an infinitely long QMF (i.e. ignoring ‘end’ effects) reduces the solution to two-dimensions (x, y). Various methods can be used to solve the Laplace equation [19]. The boundary element method (BEM) [20] is used and a field solving application has been developed at the University of Liverpool for this case [21].

Boundary Element Method

The electrodes are replaced by a number of line charges positioned on (what would be) the electrode surfaces. Infinite length line charges of infinitesimal diameter are assumed. The charges are selected such that the potentials at specified points on all the electrode surfaces are equal to the potential applied to the electrodes (figure 3.11). Thus, the set of charges produce the same potential as the electrodes at any defined point. The line charges are used to find the potential at any specified position. This is achieved in practice by finding the potential at each point in a user defined $n \times n$ square grid for the central field area between the electrodes (as illustrated in figure 3.11).

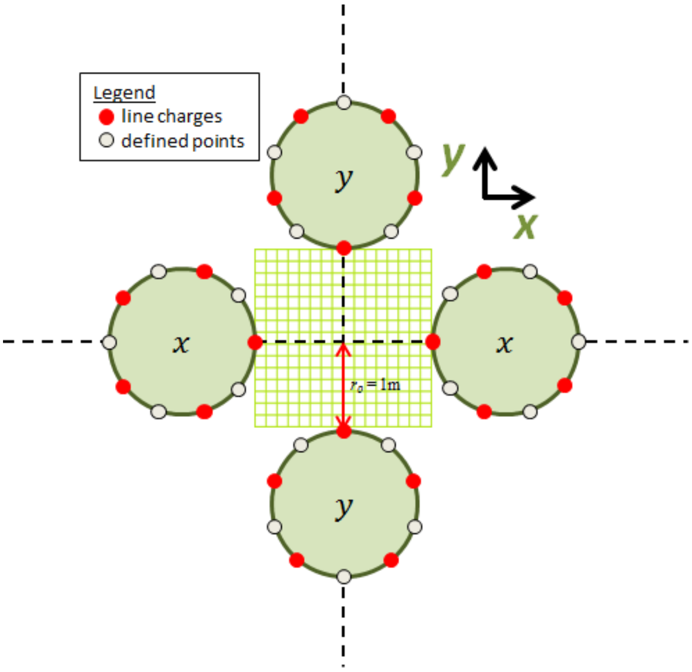

Figure 3.11: Selection of charge and defined points for circular electrode QMF

The solution assumes +1V on the surface of the *x* electrodes and -1V on the surface of the *y* electrodes using a scale such that r_0 is unity. Since the field is conservative (path independent) the field values can be scaled according to the user defined QMF model input parameters. Therefore a specific electrode geometry field solution only needs to be computed once.

3.2.3 Numerical Integration Implementation

The major advantage of the 4th order Runge-Kutta (RK4) algorithm is that no formulas for the higher derivatives need to be computed. Moreover, the method has good stability and accuracy (compared to other techniques such as Euler method) and is relatively straightforward to implement. It is used to solve the second-order Mathieu equation (3.32) which has been written here to include the initial phase of the alternating potential, ξ_0:

$$\frac{d^2u}{d\xi^2} + \left(a_u - 2q_u \cos\left(2(\xi - \xi_0)\right)\right)u = 0 \tag{3.45}$$

The electric field solution determines the field components for $r_0 = 1\text{m}$, and the nominal voltages are +1 and -1 Volt. The field is then scaled according to the user defined values of r_0 and the applied potentials giving the equations of motion:

$$\frac{d^2s}{d\xi^2} = \frac{2e}{mr_0^2} E_s(x,y)\big(U - V\cos\big(2(\xi - \xi_0)\big)\big)s \quad ^{10}(3.46)$$

where $E_s(x,y)$ is the computed field value and s is x or y. This is the case for QMS-2D. For QMS-Hyperbolic (the ideal case), the equations of motion would be as in 3.24 & 3.25.

This second order ordinary differential equation (3.46) is converted into a system of four first order ordinary differential equations by using the following variable substitutions:

$$W_x = \frac{dx}{d\xi} = \frac{2}{\omega}\frac{dx}{dt} \tag{3.47}$$

$$W_y = \frac{dy}{d\xi} = \frac{2}{\omega}\frac{dy}{dt} \tag{3.48}$$

where W_x and W_y can be thought of as modified velocity terms. Now equation 3.46 can be written as:

$$\frac{dW_x}{d\xi} = -\frac{2e}{mr_0^2} E_x(x,y)\big(U - V\cos\big(2(\xi - \xi_0)\big)\big)x \tag{3.49}$$

$$\frac{dW_y}{d\xi} = \frac{2e}{mr_0^2} E_y(x,y)\big(U - V\cos\big(2(\xi - \xi_0)\big)\big)y \tag{3.50}$$

---

[10] E_s is dimensionless and has to be scaled linearly with voltage hence the presence of the r_0^2 term. One r_0 is used to scale the inscribed radius dimension and the other includes the dimension per unit length in E (dimensional analysis confirms this. Note that all quantities are in S.I. units).

3.2.3.1 Runge-Kutta Algorithm

The fourth-order Runge-Kutta algorithm is well-known [22]. Consider the initial value problem:

$$\frac{dg}{dt} = f(t, g) \tag{3.51}$$

The value of g at time, t_0, is,

$$g(t_0) = g_0 \tag{3.52}$$

At the initial time, t_0, the function f and the values t_0 and g_0 are known. A suitable time step, h, is chosen such that $h > 0$. Then g_{n+1} gives an approximation of $g(t_{n+1})$, according to:

$$g_{n+1} = g_n + \frac{1}{6}(k_1 + 2k_2 + 2k_3 + k_4) \tag{3.53}$$

where, $n = 1, 2, \ldots$, correspond to successive time steps and,

$$k_1 = hf(t_n, g_n) \tag{3.54}$$

$$k_2 = hf\left(t_n + \frac{h}{2}, g_n + \frac{k_1}{2}\right) \tag{3.55}$$

$$k_3 = hf\left(t_n + \frac{h}{2}, g_n + \frac{k_2}{2}\right) \tag{3.56}$$

$$k_4 = hf(t_n + h, g_n + k_3) \tag{3.57}$$

The $n+1$ value is determined by the n^{th} value plus the weighted average of the four increments where each is the product of the size of the time step interval, h. The first weighting (3.54) refers to the gradient at the beginning of the time step, the second (3.55) and third (3.56) refer to the midpoint gradient, and the fourth (3.57) refers to the gradient at the end of the time step. In averaging the four increments, greater weight is given to the midpoints.

The time step for the model is in the modified time parameter ξ and is given as $\Delta\xi$. To prevent any harmonic effects the time step, ΔT, is given as a non-integer fraction, Y, of the alternating potential time period, T:

$$\Delta T = T \times \frac{1}{Y} \tag{3.58}$$

$$\therefore \Delta\xi = \frac{\omega \Delta T}{2} = \frac{\pi}{Y} \tag{3.59}$$

3.2.3 QMS-2D

The custom software application is written in C++ and developed using Microsoft Visual Studio 2012. The graphical user interface (GUI) allows the user to specify various parameters including: the operating parameters, integration step size, QMF geometry and certain ion conditions (figure 3.12). The program requires two input files, one for the initial ion conditions and the other for the field values.

The ion file is created using a separate application which generates 1×10^6 random initial ion conditions according to the user defined input (figure 3.13). The field file is also created with a separate application which allows the user to define a 2D electrode geometry according to a set of pre-defined electrodes shapes, including: hyperbolic, circular and square (figure 3.14).

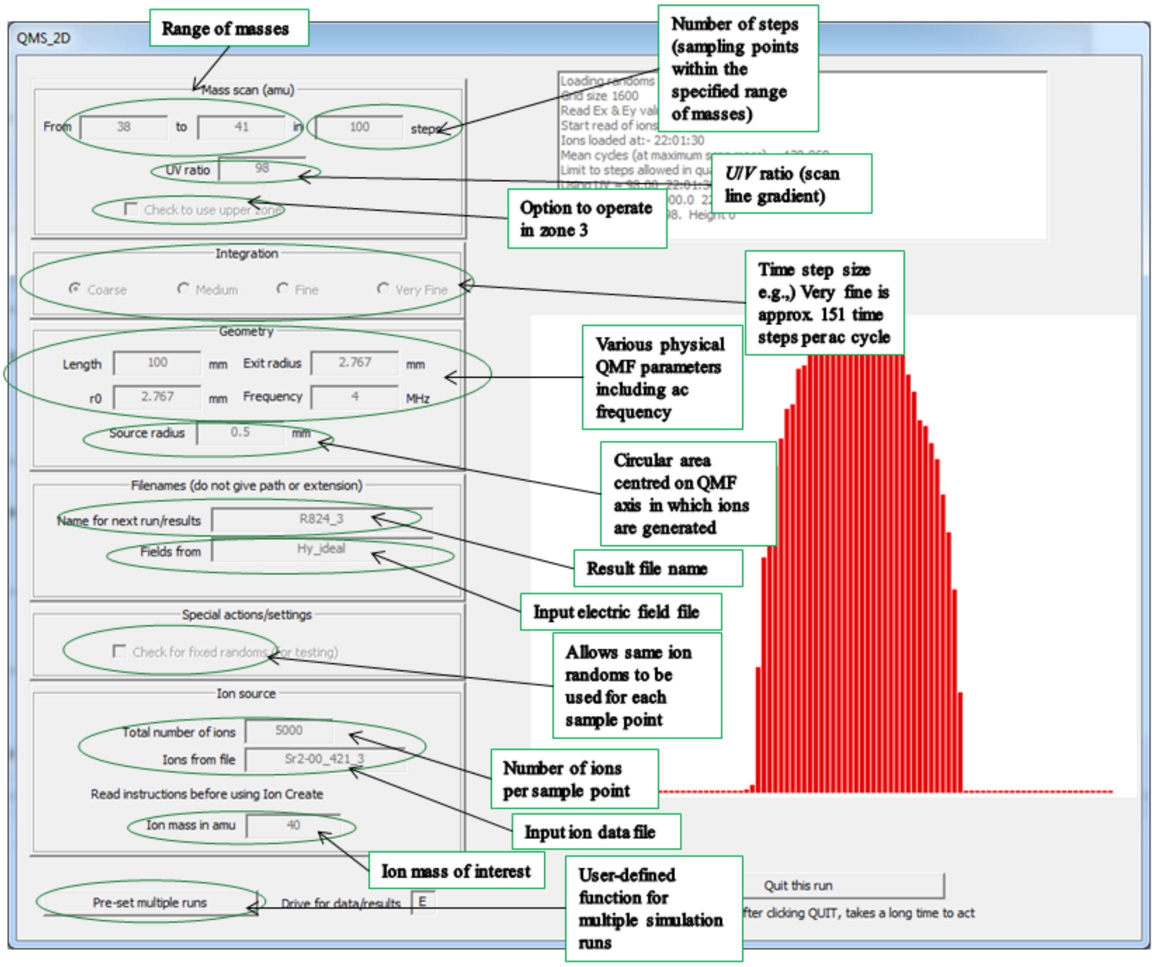

From 38 to 41 in 100 steps

UV ratio 98

☐ Check to use upper zone

● Coarse ○ Medium ○ Fine ○ Very Fine

Length 100 mm Exit radius 2.767 mm

r0 2.767 mm Frequency 4 MHz

Source radius 0.5 mm

Name for next run/results R824_3

Fields from Hy_ideal

☐ Check for fixed randoms (for testing)

Total number of ions 5000

Ions from file Sr2-00_421_3

Ion mass in amu 40

Drive for data/results E

Loading randoms
Grid size 1600
Read Ex & Ey val
Start read of ions
Ions loaded at:- 22:01:30
Mean cycles (at maximum s
Limit to steps allowed in qu
00.0 2
8. Height 0

Range of masses

Number of steps (sampling points within the specified range of masses)

***U/V* ratio (scan line gradient)**

Option to operate in zone 3

Time step size e.g.,) Very fine is approx. 151 time steps per ac cycle

Various physical QMF parameters including ac frequency

Circular area centred on QMF axis in which ions are generated

Result file name

Input electric field file

Allows same ion randoms to be used for each sample point

Number of ions per sample point

Input ion data file

Ion mass of interest

User-defined function for multiple simulation runs

Figure 3.12: Graphical User Interface (GUI) for QMS-2D

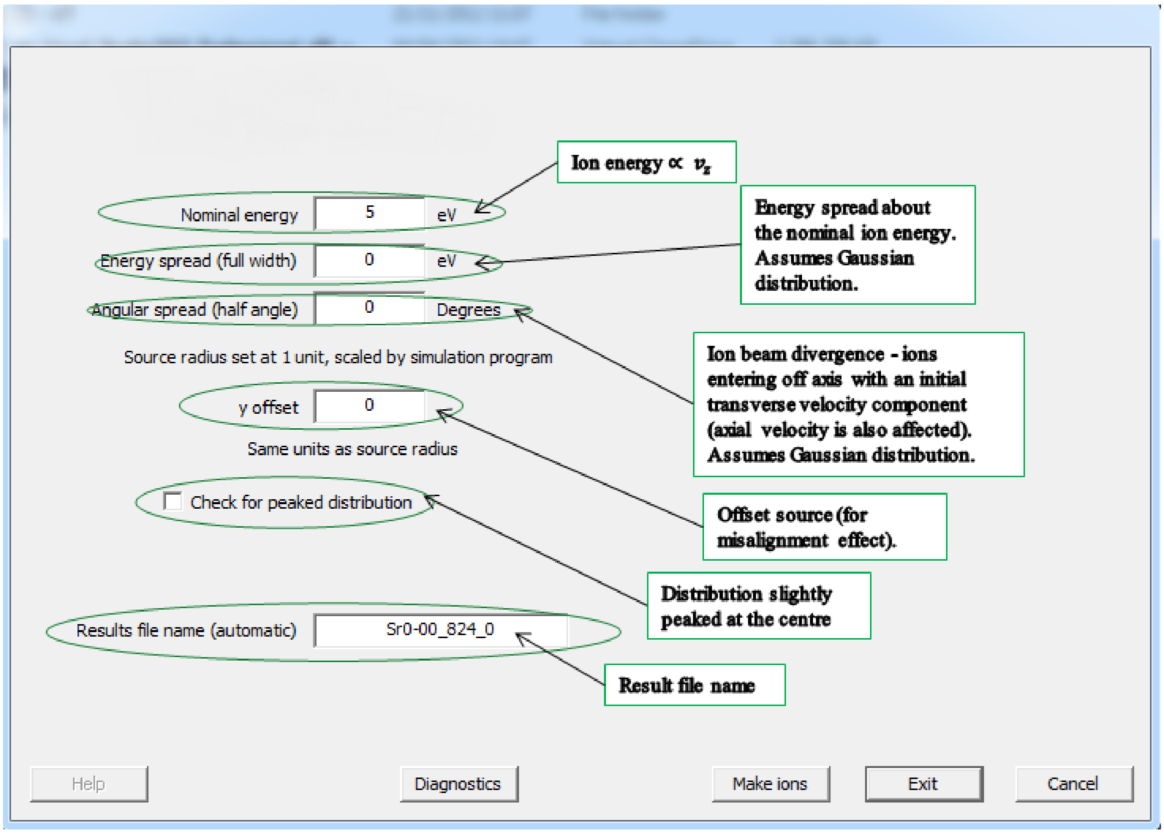

Nominal energy 5 eV

Energy spread (full width) 0 eV

Angular spread (half angle) 0 Degrees

Source radius set at 1 unit, scaled by simulation program

y offset 0

Same units as source radius

☐ Check for peaked distribution

Results file name (automatic) Sr0-00_824_0

Ion energy ∝ v_z

Energy spread about the nominal ion energy. Assumes Gaussian distribution.

Ion beam divergence - ions entering off axis with an initial transverse velocity component (axial velocity is also affected). Assumes Gaussian distribution.

Offset source (for misalignment effect).

Distribution slightly peaked at the centre

Result file name

Figure 3.13: Ion generation GUI

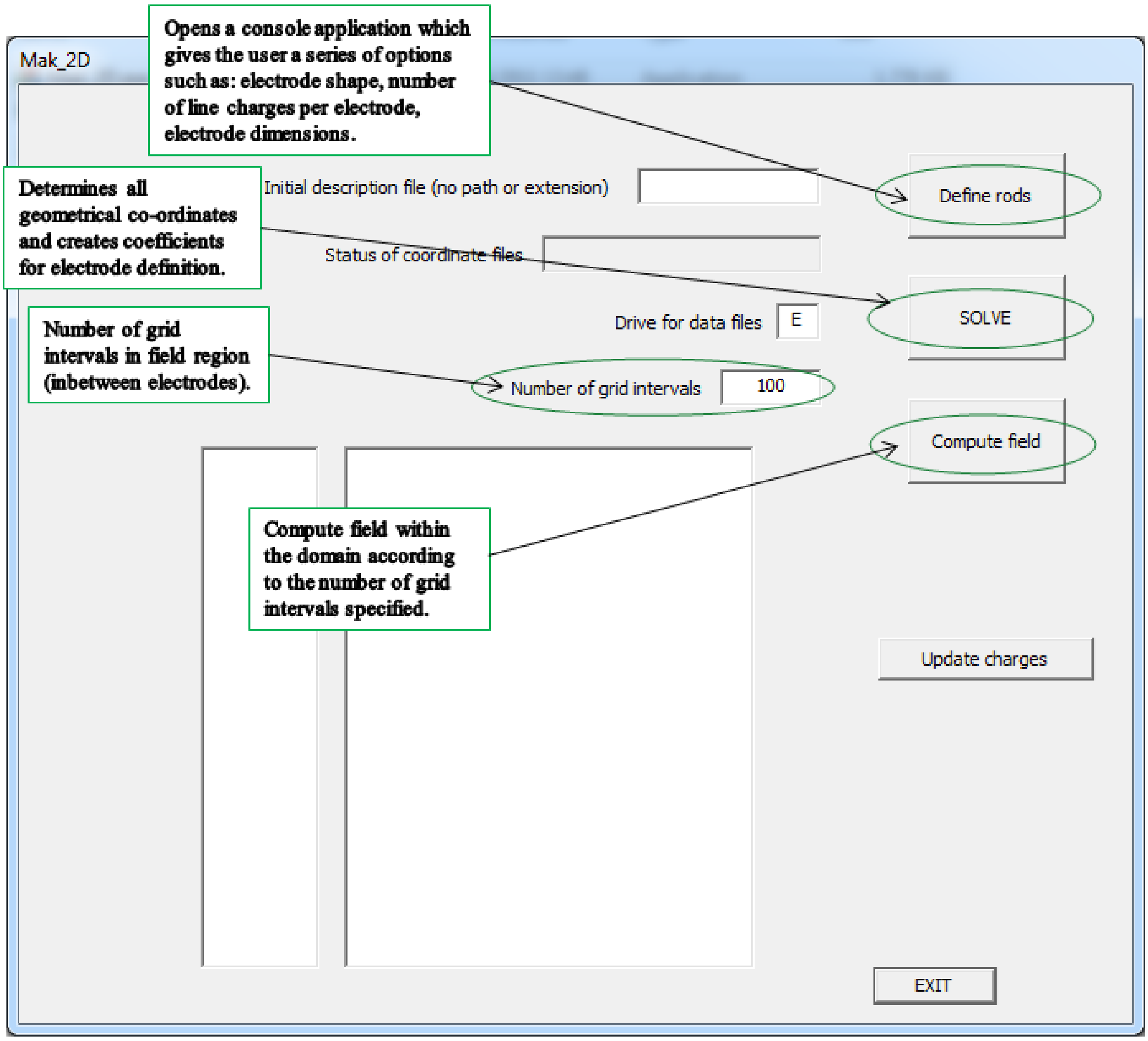

Opens a console application which gives the user a series of options such as: electrode shape, number of line charges per electrode, electrode dimensions.

Determines all geometrical co-ordinates and creates coefficients for electrode definition.

Number of grid intervals in field region (inbetween electrodes).

Compute field within the domain according to the number of grid intervals specified.

Initial description file (no path or extension)

Status of coordinate files

Drive for data files E

Number of grid intervals 100

Figure 3.14: GUI for determination of electric fields

3.3 Simulation Model Results – QMF Performance Zone 3

It was noted in the literature review (chapter 2.2.2.3) that QMF operation in zone 3 can provide improved instrument performance in terms of resolution. The predicted performance of a quadrupole mass filter (QMF) operating in zone 3 of the Mathieu stability diagram is described in detail using computer simulations (QMS-Hyperbolic). This investigation considers the factors that limit the ultimate maximum resolution (R_{max}) and percentage transmission (%Tx), which can be obtained for a given QMF for a particular scan line of operation. The performance curve (i.e., the resolution (R) versus number (N) of radio frequency (rf) cycles experienced by the ions in the mass filter) has been investigated for the upper and lower tip of stability zone 3. The saturation behaviour of the performance curve observed in practice for zone 3 is explained. Furthermore, new design equations are presented by examining the intersection of the scan line with stability zone 3. Resolution versus transmission characteristics of stability zones 1 and 3 are compared and the dependence of performance for zones 1 and 3 is related to particular instrument operating parameters.

When the resolution is limited by ion residence time in the QMF, the resolution (R) is known to be dependent on the number (N) of radio frequency (rf) cycles experienced by the ions in the mass filter [11], according to equation 3.42. For operation of QMF in stability zone 3, Hiroki et al. performed computer simulations and determined the relationship at the upper tip $R = 1.7N^2$ and at the lower tip $R = 0.69N^2$ [23]. The same simulations showed $R = \frac{N^2}{10.9}$ for stability zone 1, which is in reasonable agreement with the calculation of Paul et al [24]. Titov found $R = 1.7N^2$ and Du et al. measured $R = 1.4N^2$ (using 50 % peak height definition for Δm) [25, 26]. Konenkov and Kratenko experimentally found $R = 0.7N^2$ [27]. They also found that with increasing N^2, the resolution approached a constant saturation level. This was thought to be a consequence of inefficient coupling between the ion source and the analyser, as well as poor quadrupole field quality producing increased amplitude of ion oscillations with increasing R.

3.3.1 Simulation Method

All the simulations use 200 steps across the mass range with 5×10^5 ions injected at each mass point. Mass peaks for $^{40}Ar^+$ are generated for an ideal (i.e., zero mechanical misalignments) hyperbolic quadrupole mass filter with inscribed radius (r_0) of 1.5 mm using QMS-Hyperbolic. The frequency of the ac voltage used in the simulation was 4 MHz and the input ion energy (E_z) was chosen as 5eV. The ion source radius (r_{ie}) was selected as 0.5 mm. The length of the mass filter was varied in order to vary the number of rf field cycles the ion experiences. It is assumed in the model that the QMF control setting U/V = 100 % corresponds to the U/V ratio at q = 3.0 and a = 2.8, which is near the centre of stability zone 3, in the middle region (MR) of the stability zone (figure 3.15a). With increasing U/V ratio the scan line approaches the upper left tip of stability zone 3 (a = 3.16, q = 3.23) i.e. the upper tip region (UTR). With decreasing U/V ratio the scan line approaches the lower right tip of stability zone 3 (a = 2.52, q = 2.82) i.e. the lower tip region (LTR). A U/V of 104.8311% corresponds to the upper left tip of zone 3, whereas a U/V of 95.94243 % corresponds to the lower right tip of zone 3. For zone 1 operation, U/V = 100 % corresponds to q = 0.70600, a = 0.23699. In the simulations the initial velocities in the x and y directions are zero.

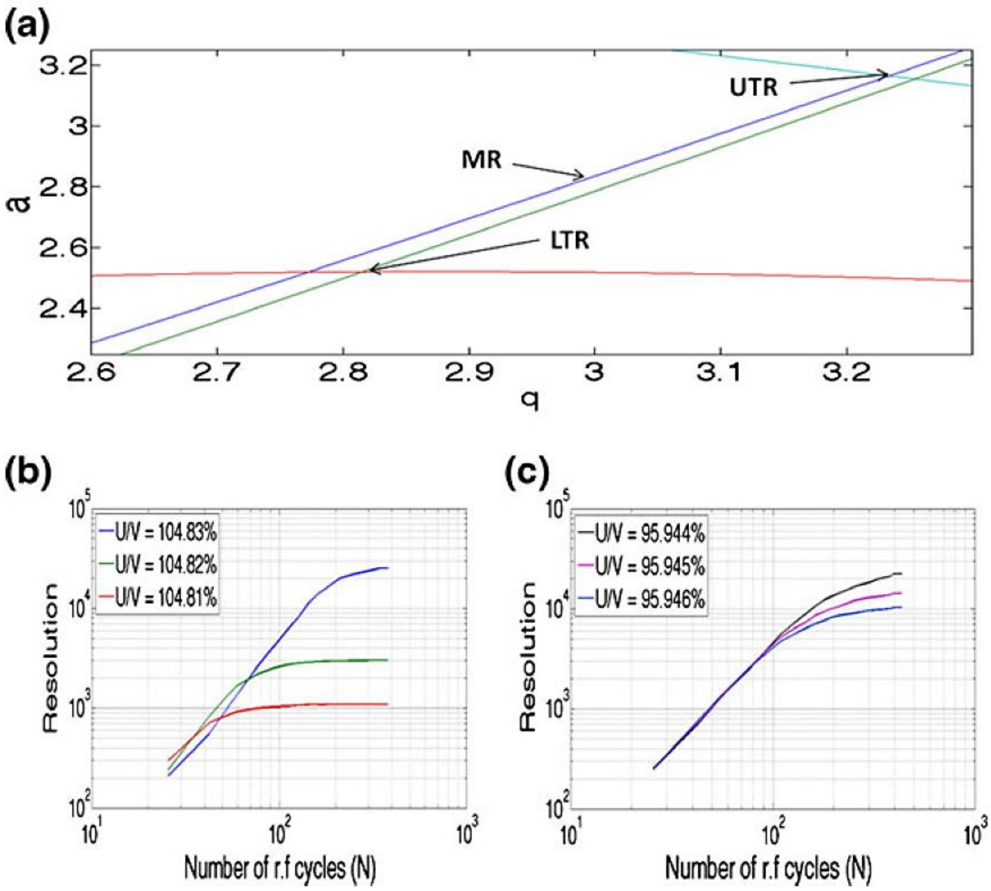

Figure 3.15: (a) Details of stability zone 3; (b) the dependence of resolution on the number of rf field cycles for QMF operation at the upper tip region (UTR) of stability zone 3 at different *U/V* predicted by QMS-Hyperbolic; (c) the dependence of resolution on the number of rf field cycles for QMF operation at the lower tip region (LTR) of stability zone 3 at different *U/V* ratios predicted by QMS-Hyperbolic

3.3.2 Performance of a QMF Operating in Stability Zone 3

Figure 3.15b shows the dependence of resolution measured using 10% peak height definition, on the number of rf field cycles at three different *U*/*V* ratios 104.81%, 104.82%, and 104.83% for the UTR of stability zone 3. It can be seen from Figure 3.15b that as the number of rf field cycles increases, resolution increases with a finite slope until the curve begins to saturate. From equation 3.42, the values of *n* and *K* for the linear region of the performance curve for *U*/*V* at 104.83% are 2.14 and 10.3, for *U*/*V* 104.82% are 2.17 and 4.22, and for *U*/*V* 104.81 % are 1.56 and 0.43, respectively. These values are in agreement with those obtained experimentally by Konenkov and Kratenko [26]. Figure 3.15c shows the dependence of resolution on number of rf field cycles at three different U/V ratios 95.946%, 95.945% and 95.944% for the LTR of stability zone 3. Similar to the case for UTR, resolution increases with number of rf cycles until it eventually saturates. The values of n and K for the linear region of the performance curve for U/V 95.946% are 2.04 and 2.81, for U/V 95.945% are 2.09 and 3.41, and for U/V 95.944% are 2.14 and 4.20 respectively.

Using QMS-Hyperbolic, experimentally observed performance curve saturation for the QMF operating in the UTR (obtained by Konenkov and Kratenlo [27] shown in figure 3.16a and by Du et al. [26] shown in figure 3.16c) has been simulated and reproduced (figures 3.16b and d). Comparing figure 3.16a with figure 3.16b, and figure 3.16c with figure 3.16d, the behaviour of the performance curve is similar. Resolution (measured using 50% peak height definition) increases with increasing N^2 and then the curve saturates. Syed et al. show in [15] that the intersection of the scan line below the tip increases the pass-band and in turn limits the resolution of a QMF to a finite maximum value. This is given by $R_{max} = \frac{q}{\Delta q}$ (see equation 3.39) for a given mass even if the number of rf field cycles is increased by increasing the length or frequency or by decreasing ion energy (see equation 3.43). The experimentally observed saturation behaviour in resolution [26, 27] with increasing N^2 is thus seen to be an inherent feature of the QMF and, therefore, not necessarily due to mechanical deficiencies, such as poor coupling between the ion source and the analyser or poor quadrupole field quality. However, mechanical deficiencies can affect the peak shapes e.g., increase in low and/or high mass tailing and loss of transmission, thus decreasing resolution. This is the likely reason that there is a discrepancy between measured values of resolution and simulated values at certain points of N^2, upon comparison of figure 3.16a with 3.16b, and figure 3.16c with 3.16d, respectively.

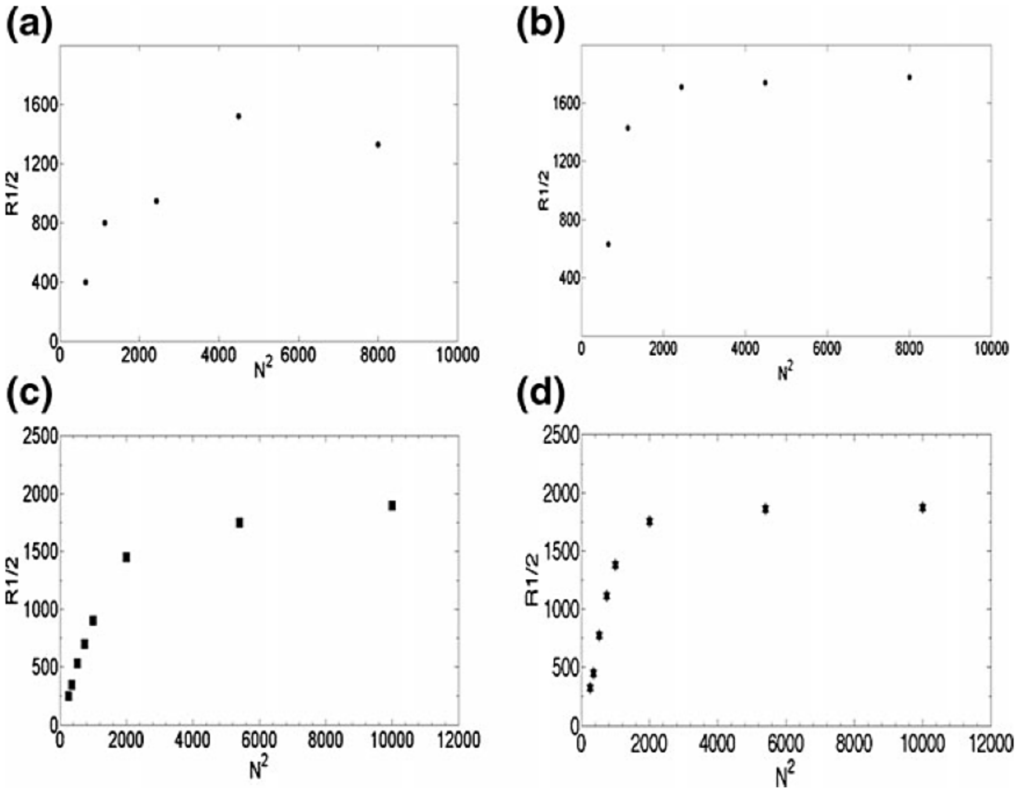

Figure 3.16: (a) The measured resolution at half height $R_{1/2}$ for $^{40}Ar^+$ versus the square of the number of cycles spent in the quadrupole field (N^2) for operation at the UTR of zone 3, reproduced from [26]; (b) the simulated resolution at half height $R_{1/2}$ for $^{40}Ar^+$ versus the square of the number of cycles (N^2) (same as figure 3.16a) using, U/V = 104.805%; (c) the measured resolution at half height $R_{1/2}$ for $^{36}Ar^+$ versus the square of the number of field cycles spent in the quadrupole field (N^2) for operation at the UTR of zone 3, reproduced from [27]; (d) The simulated resolution at half height $R_{1/2}$ for $^{36}Ar^+$ versus of field cycles squared (N^2) (same as Figure 3.16c) using, U/V = 104.811%

Equation 3.42 ($R = \frac{1}{K}N^n$) is not valid for the saturation regions of performance curves obtained for the UTR or for the LTR. In figure 3.17a and b, the saturation regions are modelled using OriginPro 8.5 (OriginLab, Northampton, MA). A good representation of the saturation behaviour of the performance curve for both UTR and LTR is given by $R = a - bc^N$, where a, b, and c are constants which depend upon the U/V ratio. Figure 3.17a (UTR, U/V ratio 104.83%) and figure 3.17b (LTR, U/V ratio 95.944%) show the relationship between N and R obtained using

QMS-Hyperbolic (square symbols) and a fitted curve to the data (red line). The value of the coefficient of determination (COD) termed as R_c^2 for both the cases was found to be around ~0.99, indicating a good regression fit between the curves (R_c^2 of 1 indicates that the regression line fits perfectly with the data).

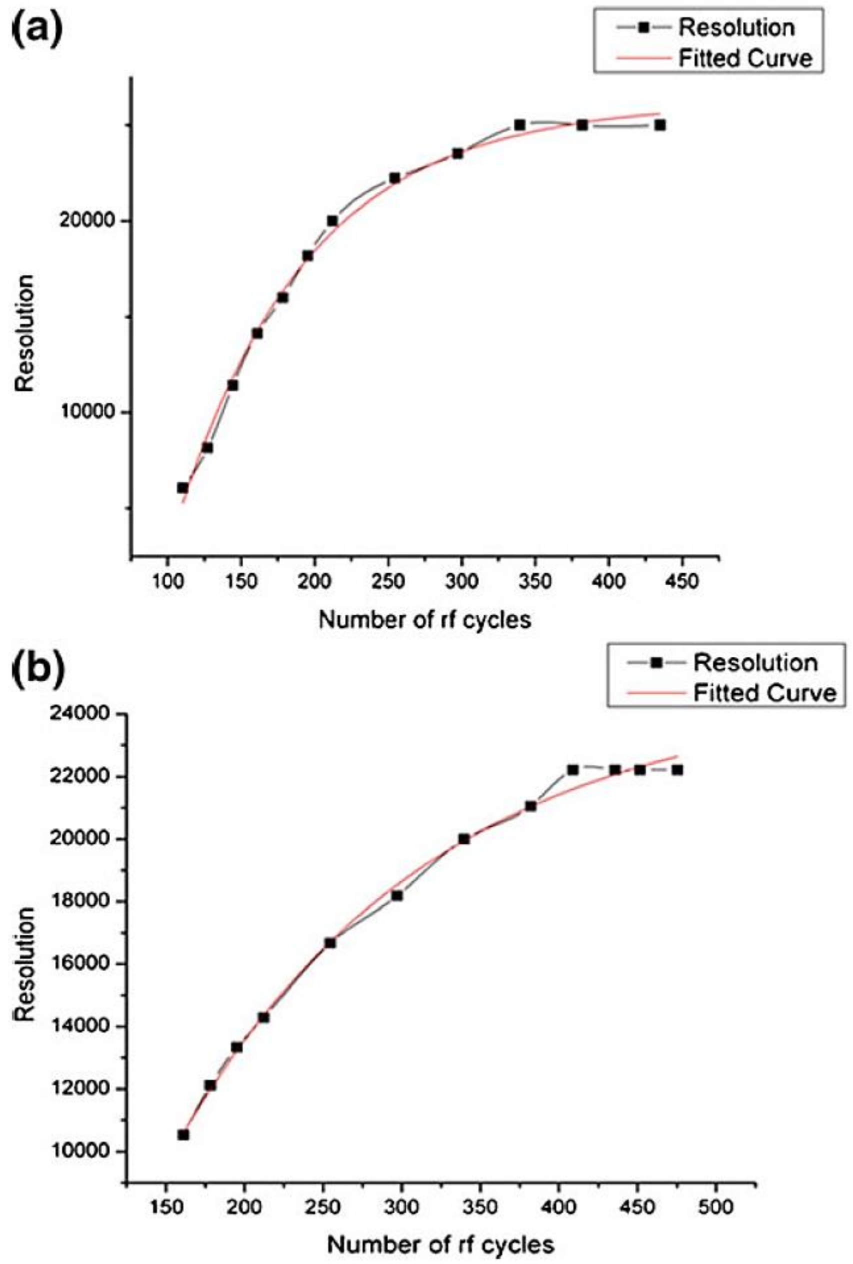

Figure 3.17: (a) The dependence of resolution for $^{40}Ar^+$ on number of rf field cycles for stability zone 3 (fit obtained using OriginPro 8.5) at *U*/*V* = 104.83% (UTR); (b) the dependence of resolution for $^{40}Ar^+$ on number of rf field cycles for stability zone 3 (fit obtained using OriginPro 8.5) at *U*/*V* 95.944% (LTR)

3.3.3 Dependence of Ultimate Maximum Resolution on U/V Ratio for QMF Operating in Stability Zone 3

A program that is a direct conversion of the corresponding Fortran program in Zhang and Jin [28] was used to calculate the details of the Mathieu stability zones. The program generates the boundaries of the stable and unstable regions of the Mathieu stability diagram in a discrete form. These values are then imported into a Matlab program, which plots the full Mathieu stability diagram. The scan line is then drawn over the Mathieu equation and the points of intersection with the Mathieu stability boundaries are determined. By altering the active area of the graph and the scan line, different scan line-stability zone combinations can be plotted. The reliance of R_{max} on the stability parameter a has been investigated in this work, and it is established that R_{max} can be related to a by $R_{max} = \frac{a}{\Delta a}$ (see equation 3.40), where Δa is the width of the intersection of the operating scan line with the stability zone (measured on the a-axis). Furthermore, the intersection of scan line with stability zone 3 at different values of U/V has been investigated; this enabled Δq and Δa to be calculated.

Figure 3.18a shows the variation of Δq along the whole range of U/V ratios that includes LTR, MR, and UTR for stability zone 3; correspondingly, figure 3.18b shows variation of Δa along the whole range of U/V that includes LTR, MR, and UTR. Curve fitting relationships were obtained using OriginPro 8.5. It can be seen from the variation of Δq and Δa with U/V ratio in figure 3.18a and b that the three regions (LTR, MR, and UTR) can be divided according to U/V ratios or (a, q). The lower tip region LTR covers U/V from 95.94243% (corresponding to the lower right tip of zone 3) to 97.4%. The middle region MR covers U/V from 97.4% to 103.8%, whereas, the upper tip region UTR covers U/V from 103.8% to a U/V of 104.8311% that corresponds to the upper left tip of stability zone 3.

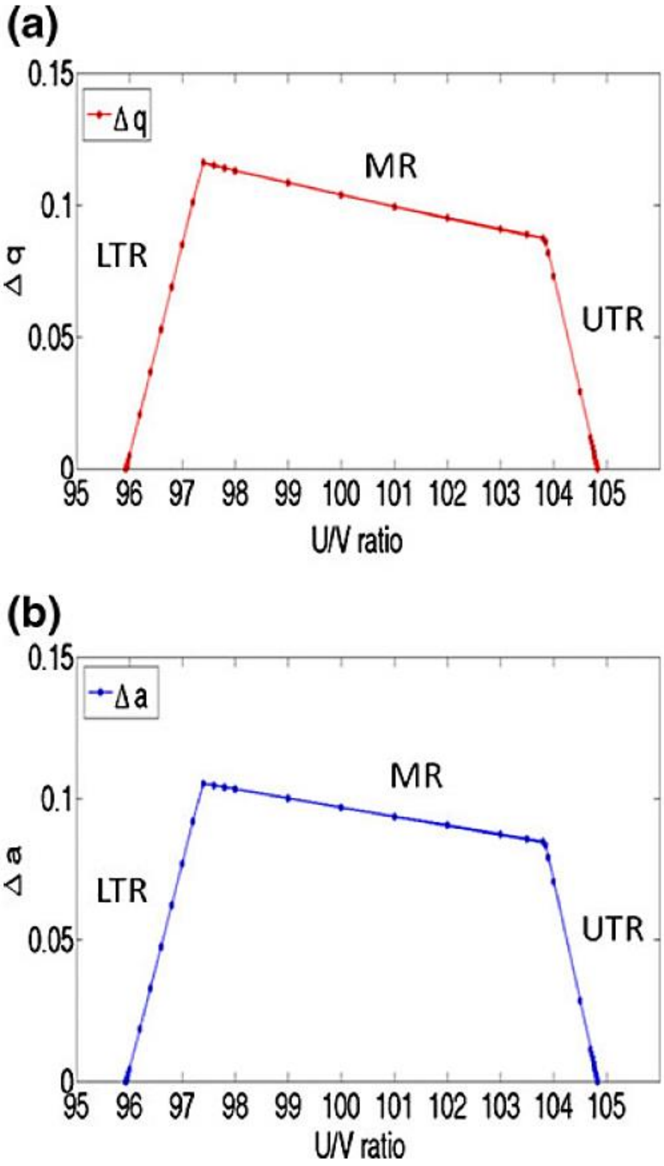

Figure 3.18: (a) Variation of Δq with U/V ratio for stability zone 3; (b) variation of Δa with U/V ratio for stability zone 3

It is evident from figure 3.18 that zone 3 has three regions of operation (i.e., LTR, MR, and UTR). A good mathematical relationship between (1) Δq and U/V; (2) Δa and U/V for three different regions is shown in table 3.1. In the derived relationships, a high number of significant figures were found to be necessary to achieve maximum accuracy in the resolution calculation, particularly when close to the boundaries of the stability diagram (i.e., at LTR, MR, and UTR). This is because the curve fitting is calculated with respect to the origin at zero. Due to this a higher accuracy than is actually required is implied by the relationships. By substituting the value of Δq in $R_{max} = \frac{\Delta q}{q}$ and Δa in $R_{max} = \frac{\Delta a}{a}$, the following relationships between the maximum resolution (R_{max}) for a particular scan line (*U*/*V* ratio in percentage) have been established.

Region	$\boldsymbol{\Delta q}$	$\boldsymbol{\Delta a}$
LTR	$(-7.68116 + 0.08006009\, U/V)$	$(-6.97891 + 0.072740521\, U/V)$
MR	$(0.54974 - 0.004460000\, U/V)$	$(0.42089 - 0.003240000\, U/V)$
UTR	$(9.21060 - 0.087861304\, U/V)$	$(8.92643 - 0.085150563\, U/V)$

Table 3.1: Mathematical Relationship between Δ*q*, Δ*a* and *U*/*V* ratio

For the Lower tip region LTR, R_{max} can be related to *U*/*V* ratio as:

$$R_{max} = q/\left(-7.8116 + 0.080060091\,\frac{U}{V}\right) \tag{3.60}$$

$$R_{max} = a/\left(-6.97891 + 0.072740521\,\frac{U}{V}\right) \tag{3.61}$$

For the Middle region MR, R_{max} can be related to *U*/*V* ratio as:

$$R_{max} = q/\left(0.54974 - 0.004460000\,\frac{U}{V}\right) \tag{3.62}$$

$$R_{max} = a/\left(0.42089 - 0.003240000\,\frac{U}{V}\right) \tag{3.63}$$

For the Upper tip region UTR, R_{max} can be related to *U*/*V* ratio as:

$$R_{max} = q/\left(9.21060 - 0.087861304\frac{U}{V}\right) \tag{3.64}$$

$$R_{max} = a/\left(8.92643 - 0.085150563\frac{U}{V}\right) \tag{3.65}$$

It should be noted that in the above relationships, the values of a and q are constant in all the equations. Since the program QMS-Hyperbolic considers a *U*/*V* of 100% at the centre of stability zone 3, the equations are developed according to q = 3.0 and a = 2.8, which are the values of a and q near the centre of stability zone 3. Figure 3.19a shows a comparison of maximum resolution obtained in the simulations and the R_{max} calculated for the ideal case (equations 3.60 – 3.65) using the Mathieu stability diagram at different U/V ratios for LTR (95.94243% to 97.4%), MR (97.4% to103.8 %), and UTR (103.8% to 104.8311%), respectively. It can be seen from the figure that there is a good correlation between simulated and theoretical calculated values of R_{max} for MR. Moreover, there is a good correlation between simulated and theoretical values of R_{max} for LTR and UTR, except at *U*/*V* ratios operating near the tip. A discrepancy between simulated and theoretical values of R_{max} can be seen at *U*/*V* of 95.944% for LTR and at a *U*/*V* of 104.83% for UTR. This discrepancy is due to the fact that the simulation is for finite field radius and finite length. There are differences from the ideal case using Mathieu Stability diagram calculations since: (1) some ions, which are theoretically unstable, are transmitted in the simulation because of the slow increase in the ion trajectory envelope with distance along the QMF; (2) similarly, some ions, which are theoretically stable, are lost because the ion trajectory envelope is so high that they collide with the electrode because the QMF has finite field radius.

However, in all cases, the trend observed is similar to the theoretical model (stability diagram), and only at high *U*/*V* ratios is there a discrepancy in the maximum resolution, since a slight change in Δq or Δa in the simulations will change the resolution by a large amount. Figure 3.19b shows the variation of percentage transmission along the whole range of U/V ratios. The U/V ratio values correspond to the three defined operating regions: LTR, MR, UTR (fig. 3.18). It can be seen from figure 3.19b that transmission is generally higher at the LTR compared with UTR of zone 3; thus LTR has better resolution versus transmission characteristics. For example, with an R_{max} of 4938 at 95.95% U/V, the percentage transmission is 0.58%, whereas for a much smaller resolution of 2985 at 104.82% in the UTR, the percentage transmission is 0.12%. Therefore, for a QMF operating in stability zone 3, the lower tip region has an advantage over the upper tip region in terms of transmission.

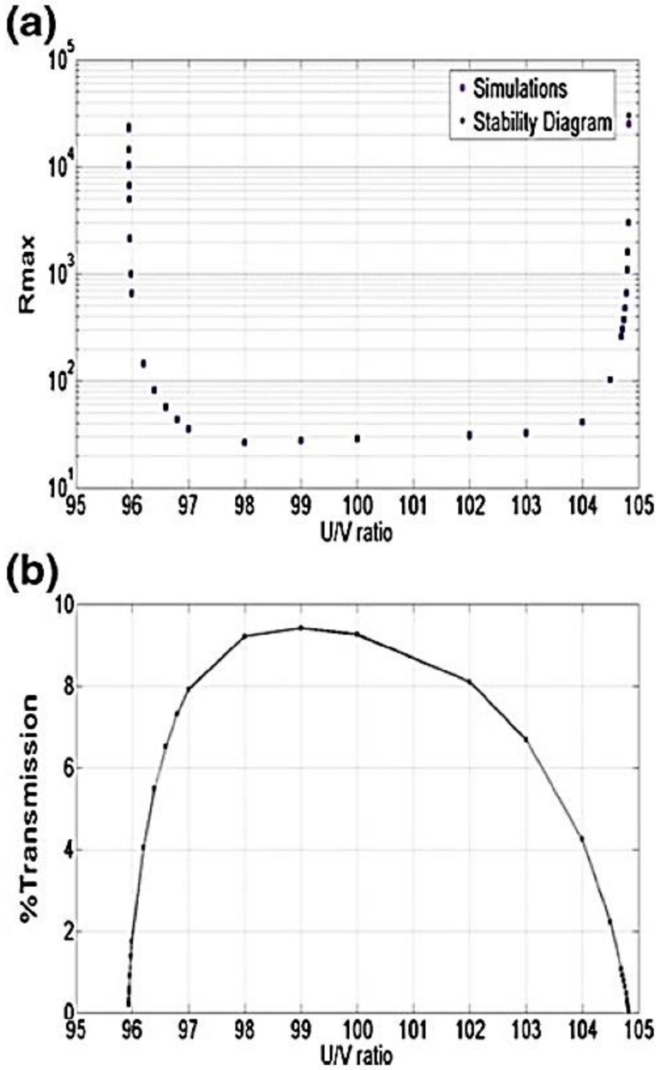

Figure 3.19: (a) Comparison of maximum resolution obtained in the simulations and the R_{max} calculated for the ideal case using the Mathieu Stability diagram at different *U*/*V* ratios for LTR, MR and UTR; (b) the variation of percentage transmission with *U*/*V* ratio

3.3.4 Resolution versus Transmission Characteristics

Resolution versus transmission characteristics for QMF operation in stability zones 1 and 3 have been studied for different operating conditions. Figure 3.20a shows resolution (green line) versus percentage transmission (blue line) characteristics at different r_0/r_{ie} ratio for three different cases, stability zone 1, LTR of zone 3, UTR of zone 3 (where r_{ie} is the ion source exit radius) . To get an appropriate comparison, the QMF is simulated at a saturation point of the performance curves and at a *U*/*V* ratio that gives an R_{max} of approximately 1000 for all the three different cases. As observed from figure 3.20a, transmission increases linearly with increase in r_0/r_{ie} ratio for all the cases, but the increase is higher for stability zone 1. At $r_0/r_{ie} = 40$, the relative transmission for stability zone 1 is approximately 67.50%, for zone 3 LTR it is 31.00% and for zone 3 UTR it is 29.00%. From these observations, and for this particular case, it can be seen that zone 1 has better resolution versus transmission characteristics compared with stability zone 3. Also, it should be noted that zone 3 LTR has slightly better transmission than zone 3 UTR for the same value of resolution.

Figure 3.20a tends to agree with the conventional understanding [26, 27] that zone 3 suffers from a large amount of loss in transmission compared with zone 1. However, this is not always the case. Figure 3.20b shows resolution versus percentage transmission characteristics with increasing r_0/r_{ie} for a QMF of length 200 mm (N = 168) for the same case as figure 3.20a, but operated with U/V ratio close to the tip: 99.998% for zone 1, 95.95% for LTR of zone 3, and 104.825% for UTR of zone 3, providing a resolution of 1339, 3875, and 4710, respectively. In all the three cases, zone 1, LTR of zone 3, and UTR of zone 3, transmission increases linearly with increase in r_0/r_{ie} ratio. Nevertheless, the increase at $r_0/r_{ie} = 40$ is quite low (7.90%) for UTR of zone 3 compared with LTR of zone 3 (11.87%) and stability zone 1 (12.54%). From the results, at $r_0/r_{ie} = 40$, it is evident that even though there is a slight loss in transmission from 12.54 % to 11.87 %, resolution is greatly enhanced by a factor of more than 2.5 (from 1339 to 3875) if the QMF is operated in LTR of zone 3 rather than zone 1. UTR of zone 3 has better resolution than both zone 1 and LTR of zone 3, but it suffers from considerable loss of transmission. It can be concluded from the case studied, as shown in Figure 3.20b, that LTR of stability zone 3 has the optimum resolution versus transmission characteristic.

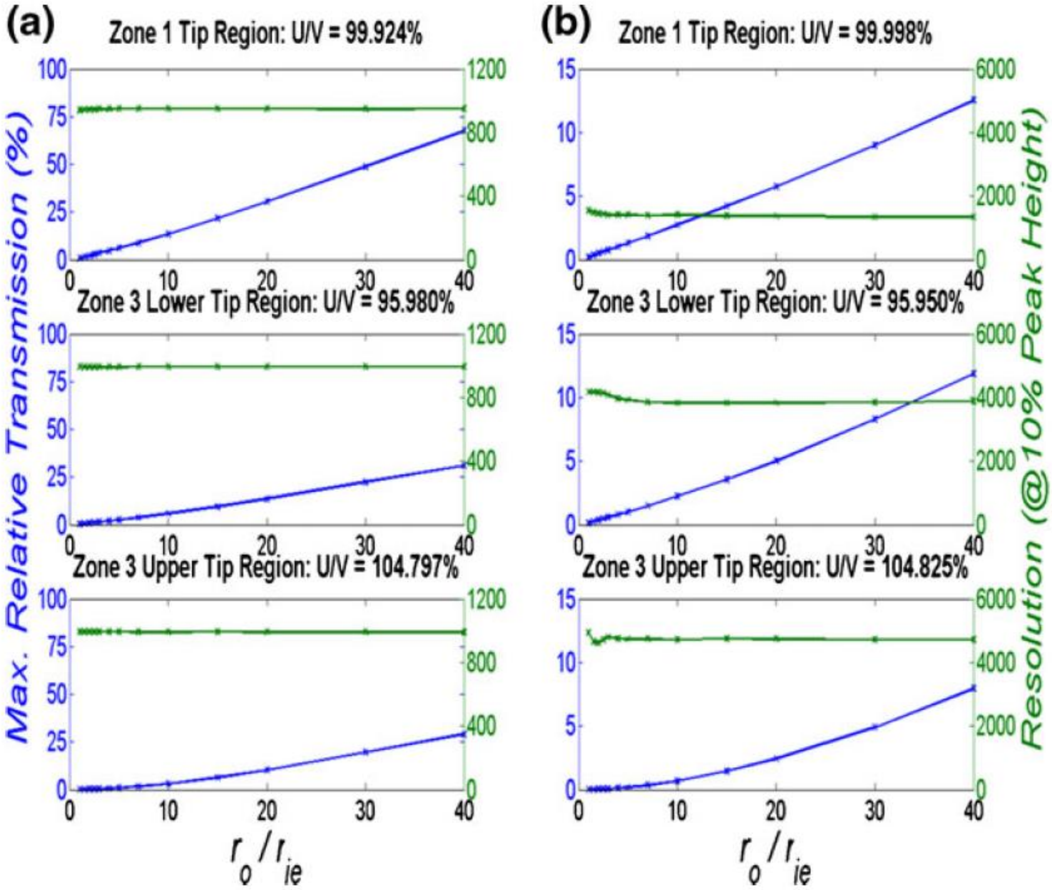

Figure 3.20: The variation of resolution and percentage transmission with r_0/r_{ie} ratio for zone 1, LTR of zone 3 and UTR of zone 3: (a) At *U*/*V* ratios providing an R_{max} of 1000, (b) *U*/*V* ratios chosen close to the tip region (*L* = 200 mm)

3.4 Conclusions

The fundamental theory of QMF operation has been examined. Custom software applications developed at the University of Liverpool provide a means of investigation for ideal electrode geometry (hyperbolic) QMF and non-ideal electrode geometries.

QMS-Hyperbolic has been used to investigate QMF performance and operation in stability zone 3. The performance curve (i.e., the resolution (*R*) versus number (N) of radio frequency (rf) field cycles experienced by the ions in the mass filter) has been modelled for upper left tip and lower right tip of stability zone 3. The model has been used to accurately simulate experimental performance curves, previously published for operation in this stability zone. The saturation behaviour of the performance curve observed in practice is seen to be the limiting feature of QMF operation and this is apart from any restriction due to mechanical deficiencies. The reason for the saturation behaviour is attributed to the fact that for a QMF, there is a finite theoretical limit to its resolution at a particular operating point (scan line), since at that particular point Δq or Δa cannot go beyond a certain minimum value with any meaningful ion transmission. Furthermore, new design equations are established by examining the intersection of the scan line with stability zone 3. The maximum resolution R_{max} can also be related to stability parameter a as $R_{max} = \frac{a}{\Delta a}$ (see equation 3.40); the R_{max} dependence on U/V ratio and stability parameters a and q has been presented. According to the relationship given (with parameters shown in table 3.1), the equations developed will be of importance to the QMS community in designing QMFs for operation in stability zone 3 together with electronics to drive them.

The Mathieu stability zone 3 can be divided into three regions of operation: lower tip region, middle region, and upper tip region. The lower tip region of zone 3 has better resolution versus transmission characteristics than the upper tip region. It has been previously published that transmission in zone 3 is consistently poorer than in zone 1. Whilst this is generally the case, our simulations indicate that for operation near the stability tip in zone 1, zone 3 operation can deliver similar transmission but with superior resolution. The performance varies for zones 1 and 3 depending on the instrument operating parameters.

References

[1] J. R. Gibson and S. Taylor, "Prediction of quadrupole mass filter performance for hyperbolic and circular cross section electrodes," *Rapid Communications in Mass Spectrometry,* vol. 14, pp. 1669-1673, 2000.

[2] P. E. Miller and M. B. Denton, "The quadrupole mass filter: basic operating concepts," *Journal of Chemical Education,* vol. 63, p. 617, 1986.

[3] P. H. Dawson, "Quadrupole mass spectrometry and its applications," 1976.

[4] R. E. March and J. F. J. Todd, "Theory of Quadrupole Instruments," in *Quadrupole Ion Trap Mass Spectrometry*, ed: John Wiley & Sons, Inc., 2005, pp. 34-72.

[5] G. W. Hill, "On the part of the motion of the lunar perigee which is a function of the mean motions of the sun and moon," *Acta Mathematica,* vol. 8, pp. 1-36, 1886.

[6] N. W. McLachlan, *Theory and application of Mathieu functions* vol. 127: Dover Publications New York, 1964.

[7] E. L. Ince, *Ordinary differential equations*: Courier Dover Publications, 1956.

[8] G. Blanch, "Mathieu functions," *M. Abromowitz, IA Stegun: Handbook of mathematical functions, Dover, New York,* 1965.

[9] G. Floquet, "Sur les equations differentielles lineaires," *Ann. ENS [2],* vol. 12, pp. 47-88, 1883.

[10] J. Campana, "Elementary theory of the quadrupole mass filter," *International Journal of Mass Spectrometry and Ion Physics,* vol. 33, pp. 101-117, 1980.

[11] S. U. Syed, T. J. Hogan, M. J. A. Joseph, S. Maher, and S. Taylor, "Quadrupole Mass Filter: Design and Performance for Operation in Stability Zone 3," *Journal of the American Society for Mass Spectrometry,* 24, 10, pp. 1493-1500, 2013.

[12] J. Batey, "Quadropole gas analysers," *Vacuum,* vol. 37, pp. 659-668, 1987.

[13] R. E. Pedder, "Practical quadrupole theory: graphical theory," *Excel Core Mass Spectrometers, Pittsburgh, PA, Extrel Application Note RA_2010 A,* 2001.

[14] D. Douglas, "Linear quadrupoles in mass spectrometry," *Mass spectrometry reviews,* vol. 28, pp. 937-960, 2009.

[15] S. U. Syed, T. Hogan, J. Gibson, and S. Taylor, "Factors influencing the QMF resolution for operation in stability zones 1 and 3," *Journal of the American Society for Mass Spectrometry,* vol. 23, pp. 988-995, 2012.

[16] J. Gibson, S. Taylor, and J. Leck, "Detailed simulation of mass spectra for quadrupole mass spectrometer systems," *Journal of Vacuum Science & Technology A: Vacuum, Surfaces, and Films,* vol. 18, pp. 237-243, 2000.

[17] J. R. Gibson, K. G. Evans, S. U. Syed, S. Maher, and S. Taylor, "A method of computing accurate 3D fields of a quadrupole mass filter and their use for prediction of filter behavior," *Journal of the American Society for Mass Spectrometry,* vol. 23, pp. 1593-1601, 2012.

[18] J. Butcher, "A history of Runge-Kutta methods," *Applied numerical mathematics,* vol. 20, pp. 247-260, 1996.

[19] M. N. Sadiku, *Numerical techniques in electromagnetics*: CRC press, 2010.

[20] C. Brebbia and J. Dominguez, "Boundary element methods for potential problems," *Applied Mathematical Modelling,* vol. 1, pp. 372-378, 1977.

[21] J. R. Gibson, K. G. Evans, and S. Taylor, "Modelling mass analyzer performance with fields determined using the boundary element method," *Journal of Mass Spectrometry,* vol. 45, pp. 364-371, 2010.

[22] J. C. Butcher, *Numerical methods for ordinary differential equations*: John Wiley & Sons, 2008.

[23] S. Hiroki, T. Abe, and Y. Murakami, "Separation of helium and deuterium peaks with a quadrupole mass spectrometer by using the second stability zone in the Mathieu diagram," *Review of Scientific Instruments,* vol. 63, pp. 3874-3876, 1992.

[24] W. Paul, H. Reinhard, and U. Von Zahn, "Das elektrische massenfilter als massenspektrometer und isotopentrenner," *Zeitschrift für Physik,* vol. 152, pp. 143-182, 1958.

[25] V. V. Titov, "Detailed study of the quadrupole mass analyzer operating within the first, second, and third (intermediate) stability regions. II. Transmission and resolution," *Journal of the American Society for Mass Spectrometry,* vol. 9, pp. 70-87, 1998.

[26] Z. Du, D. Douglas, and N. Konenkov, "Elemental analysis with quadrupole mass filters operated in higher stability regions," *J. Anal. At. Spectrom.,* vol. 14, pp. 1111-1119, 1999.

[27] N. Konenkov and V. Kratenko, "Characteristics of a quadrupole mass filter in the separation mode of a few stability regions," *International journal of mass spectrometry and ion processes,* vol. 108, pp. 115-136, 1991.

[28] J. Jin and S. Zhang, *Computation of special functions*: Wiley-Interscience, New York, 1996.

Chapter 4 : Investigating QMF Fringe Field Effects

In this chapter the boundary element method (BEM) of field calculation is used which enables the three-dimensional (3D) fields of a simple quadrupole mass filter (QMF) to be determined to a high accuracy. Due to the 3D nature of the field calculation technique accurate field values are produced in the fringe field region of the QMF as well as in the centre of the QMF. Based on fields obtained by this method, typical filter performance is determined and shown to differ from that predicted when fringe fields are ignored. The computed performance using the 3D model replicates features obtained experimentally. The model also predicts more complex variation with ion mass and other parameters than when fringe fields are ignored.

4.1 Introduction

Fringing fields, particularly at the entrance of the QMF, can be detrimental to ion transmission (as discussed in chapter 2.2.2.2). Several investigations have attempted to determine the effects on filter behaviour arising because electrodes have finite length and because there are end plates, usually at zero potential, to hold the ion source at one end and the detector system at the other [1-12]. The fields in regions extending from the end plates for some distance into the filter are fringe fields; they are complex (being time and geometry dependent) and do not match the ideal fields required. Most previous investigations have used some form of approximation to represent the fringe fields. Fringe fields are not always defocussing (causing ions to move away from the central axis of the QMF) and Dawson [5] showed that fringe fields may alter ion trajectories to such an extent that transmission (the proportion of ions that pass through the filter at the position of the mass peak) increases compared with the value predicted using fields for infinite length electrodes. The first investigation of fringe field effects was by Brubaker [4], who used the results to develop rf only pre-filters. Pre-filters usually improve performance and are incorporated in high specification instruments. However, many low-specification instruments, usually known as residual gas analysers (RGAs), do not have pre-filters, and accurate models that predict their behaviour for a wide range of conditions are not reported.

When the electric field used is that for infinitely long electrodes, the field is referred to as two-dimensional (2D) field because the field in the axial, *z*, direction is zero at all positions and the *x* and *y* field components do not vary in the *z*-direction. Fields are computed by solving Laplace's equation (equation 3.5) with boundary conditions set by the electrodes. Gibson et. al [13] showed that the boundary element method (BEM) formulated by Read and co-workers [14, 15] produced accurate field values, especially in regions distant from the electrodes where the ions move (see 3.2.2). This technique was also used by Beaty [16] and by Douglas et al. [17].

The technique which provides accurate field evaluation is used to predict the behaviour of QMF systems with finite length electrodes and zero potential end plates as shown in figure 4.1[11]. Since all three field components now vary in all directions (*x*, *y*, *z*), the fields determined are referred to as three dimensional (3D). The model evaluates the field in the region from the entrance plate, throughout the QMF and up to the exit plate.

---

[11] For clarity the gaps between the ends of the rods and the end plates are exaggerated in figure 4.1.

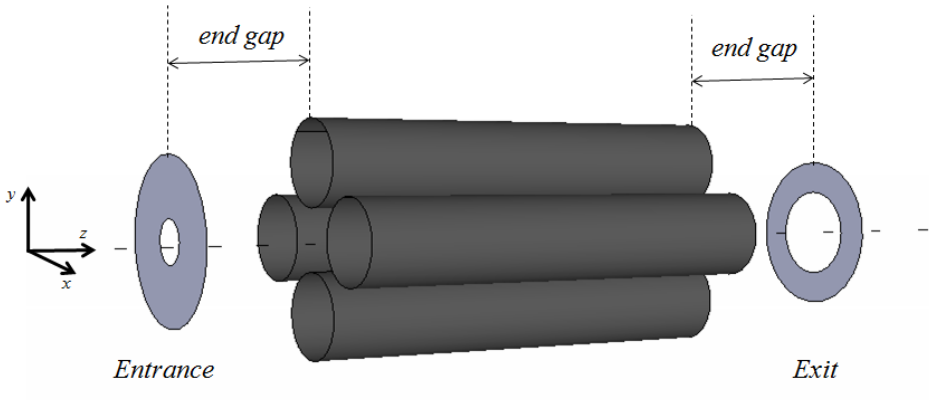

Figure 4.1: Schematic diagram of a simple QMF

4.2 Field Determination

The method (as outlined in chapter 3.2 for 2D fields [13]) replaces each electrode by a set of infinite line charges parallel to the filter axis. Points on the electrode surface, referred to as defined points, are required to be at the electrode potential. The potential at each defined point is that due to all the line charges; using this requirement a set of linear equations are developed and solved to determine the line charges. The field components at any required position are then determined from the computed line charges, using Coulomb's law.

For 3D field determination, the electrodes are divided into sections, typically about 100, in the *z*-direction. Sections near the electrode ends are very short, 0·05 to 0·1 times r_0, and section lengths increase towards the centre of the filter in a simple geometric progression. Each electrode section is replaced by a set of line charges of the same length and parallel to the *z* axis; about 40 line charges per electrode section are adequate. For finite length charges the problem of setting the potential to zero an infinite distance from the charges does not exist so the solution is simplified [13].

To compute an ion trajectory, the field is required at every position of the ion as it is traced using a Runge-Kutta algorithm. Exact field evaluation at each point, while computing the trajectory, is too slow. Instead, the three field components are determined at all points on a set of uniform square grids, and interpolation used to find the field at any point. Using tri-linear interpolation (linear interpolation extended to three dimensions) would require a large amount of memory (~48GBytes, for 1600 x 1600 grids at 800 z positions). Instead a complete three dimensional second order interpolation process was developed; this was constrained by adding a requirement that the results satisfied Maxwell's Equations. The process results in a set of 15 coefficients associated with a cuboid defined by eight lattice nodes; the coefficients are only evaluated once at every grid position and stored for use computing ion trajectories when determining filter performance. Interpolation methods were tested with known field distributions similar to those found in the fringe field regions at the end of the electrodes as this is where changes in all field components are greatest and interpolation accuracy will be lowest. Similar accuracy to tri-linear interpolation was achieved but with much reduced memory requirements.

The grids have sides $2\times r_0$ and are in planes at right angles to the filter axis; that is, z is constant over each grid plane. The planes are not equally spaced; spacing is very small in the regions near the end plates, typically $0{\cdot}002\ r_0$ to $0{\cdot}01\ r_0$, as the field changes rapidly in the z direction and is larger, about $1{\cdot}5\ r_0$ to $2{\cdot}0\ r_0$, near the centre of the filter. Around 800 sets of grid values (i.e., at 800 z positions) are used for a typical RGA with length in the range $25\ r_0$ to $50\ r_0$.

4.3 Determining QMF Behaviour

Once the 3D fields are known, QMF behaviour is determined as they were for 2D fields (chapter 3.2) except that the z component of the field is finite; it is significant near the end plates and all three field components vary in all three directions. For 2D fields the z component of the field is zero everywhere so the z component ion velocity is constant; also the x and y field components do not vary in the z direction. Ions originate with random rf phase at random positions on a circular disc with z coordinate that of the end plate surface facing the electrodes. A fourth order Runge–Kutta algorithm is used to trace the motions of large numbers of ions through the filter. This is the 2D field program (QMS-2D) modified to include the nonzero z component of the field and variation of all field components in the z direction.

The ion motion is more complicated for the 3D system so slightly smaller time steps were used when evaluating the Runge–Kutta algorithm although tests indicated that this was not essential. Unlike the 2D case, different field calculations are required for each length of filter; separate calculations are also necessary for each different gap between the end plates and the electrodes and for different entrance and exit apertures. However, all dimensions and voltages may be scaled linearly without affecting the field geometry; fields were evaluated with filters described using lengths in units such that $r_0 = 1$ and, for normal operation, unit voltages on the electrodes. The behaviour of a particular QMF only requires the grids of field interpolation coefficients, the actual dimension r_0, the position on the mass scale, the frequency of the applied rf, and the resolution setting in order to determine the path any ion takes through the filter.

4.4 Model Testing

While the model was tested in many ways a useful requirement to be met by any model of ion motion in a time varying electric field is a consequence of the following analysis. At any point in a 3D field a charged particle moves according to Newton's Second Law. Equation 3.15 is repeated here for convenience where the force is due to the electric field,

$$m\frac{d^2\boldsymbol{u}}{dt^2} = q\boldsymbol{E} \tag{4.1}$$

where m is the ion mass, q its charge, $\boldsymbol{u}$ is the vector from the origin to the current position and $\boldsymbol{E}$ is the electric field; both $\boldsymbol{u}$ and $\boldsymbol{E}$ have components in all three directions and vary with time.

The spatial dimensions are normalised using $\gamma = \frac{\boldsymbol{u}}{r_0}$ and for time using $\tau = \omega t$ where ω is the angular frequency of the applied rf. Replacing $\boldsymbol{E}$ using $\boldsymbol{E} = \frac{V\boldsymbol{\varepsilon}}{r_0}$ where $\boldsymbol{\varepsilon}$ is a function of the normalised field, time and resolution setting. The equation of motion then may be written,

$$m\frac{d^2\gamma}{d\tau^2} = \lambda\varepsilon \tag{4.2}$$

where,

$$\lambda = \frac{qV}{m\omega^2 r_0^2} \tag{4.3}$$

This result (equation 4.2) is achieved by using the chain rule,

$$\frac{d}{dt} = \frac{d\tau}{dt}\frac{d}{d\tau} = \omega\frac{d}{d\tau} \tag{4.4}$$

so that,

$$\frac{d^2}{dt^2} = \frac{d\tau}{dt}\frac{d}{d\tau}\left(\frac{d}{dt}\right) = \omega^2 \frac{d^2}{d\tau^2} \tag{4.5}$$

Since,

$$s = \gamma r_0 \tag{4.6}$$

Then,

$$m\frac{d^2\gamma}{d\tau^2} r_0 \omega^2 = \frac{qV\varepsilon}{r_0} \tag{4.7}$$

which yields equation (4.2) after re-arranging and substituting for λ (equation 4.3).

When equation 4.2 is used to find the trajectory of an ion within a filter for various combinations of the parameters m, V and ω, then each solution will be the same provided that the value of λ is the same; in addition, the initial conditions, initial normalised spatial position, normalised velocity of the ion and the phase of the rf field are the same. The filter behaviour is deduced by finding the trajectories of ensembles of ions; each ensemble typically has 10^5 to 10^6 ions with a large randomised spread of starting conditions. A different ensemble is used at each of a number of settings of electrode voltages U and V (with constant value of the resolution setting $\frac{U}{V}$) corresponding to different positions on the mass scale. The percentage of ions transmitted at each position is recorded and used to produce a simulated mass peak. If identical ensembles of ions (identical normalised starting conditions) are used then identical results should be obtained if λ and the resolution setting are the same. That is, many different combinations of ion mass, initial ion energy and rf frequency should produce identical results. This test was applied to a large number of results and showed that filter behaviour using fields and trajectories, computed as described, satisfied this requirement.

4.5 Simulations

Due to the large computing effort necessary to determine filter behaviour for variation of all parameters most initial investigations were restricted to circular section electrodes with r/r_0 = 1·127, the optimum ratio [18] for approximating the quadrupolar field (see chapter 2.2.2.1). A number of models of the apertures in the entrance end plate were tested using various aperture diameters up to $0{\cdot}5r_0$. Hunter and McIntosh [9] state that the effect of an aperture on the fringing fields is negligible for aperture radius less than $0{\cdot}5r_0$. Small changes were found in fringe fields with aperture size, which produced small, but insignificant, variations in QMF behaviour. The choice of model used to represent the exit end plate has little effect on QMF performance and is discussed later. Results shown are for a typical RGA with r_0 = 2·76mm, rod length 100mm, both end gaps 1mm and a source radius of 1mm. Most computations used an rf frequency of 4MHz although tests were performed to confirm that frequency changes, with changes in mass and energy made to maintain λ constant, produced identical results. Typical results at moderate ion energies are shown in figure 4.2 for several settings of filter resolution with initial ion energy set to 4eV for ions with m/z equal to 4. The filter resolution setting, η, is set according to the apex of stability zone 1 (see chapter 3.16) and is given in terms of U and V as,

$$U = \eta k V \tag{4.8}$$

where $k \approx 0.1678$ corresponds to the peak of stability zone 1 when $\eta = 1$ for an ideal QMF with hyperbolic electrodes. Results in figure 4.2 are for low mass, hence high velocity, ions where the effect of the fringe fields on the 3D results is not so large that the mass peaks are grossly distorted. Under these conditions, the peaks using 2D and 3D fields are similar in shape although the maximum transmissions (height of the mass peak) differ significantly; transmission is computed as the percentage of the injected ions that pass through the filter and reach the detector.

Conditions selected for figure 4.2 are such that fringe field effects are not large; for a wider range of conditions, results using 2D and 3D fields often produce different peak shapes. Using 3D fields there is usually a much smaller low mass tail and the range of peak shapes is larger with some peaks extremely distorted compared with those for an ideal QMF. Maximum transmission differs using 2D and 3D fields with both significantly larger and smaller transmissions being found using 3D fields. The 3D field computed peak shapes for m/z 4 are similar to those found experimentally by Gibson et al [19] (figure 4.3).

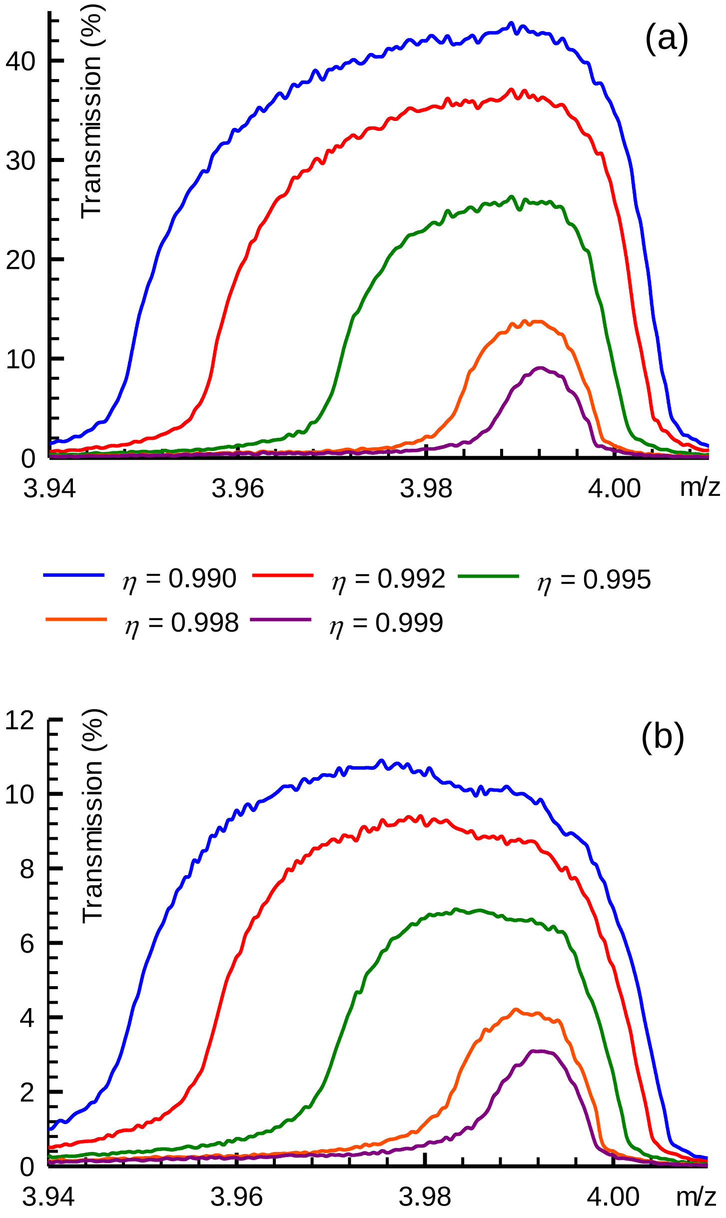

Figure 4.2: Predicted QMF mass scan peaks using (a) 3D fields, (b) 2D fields (QMS-2D)

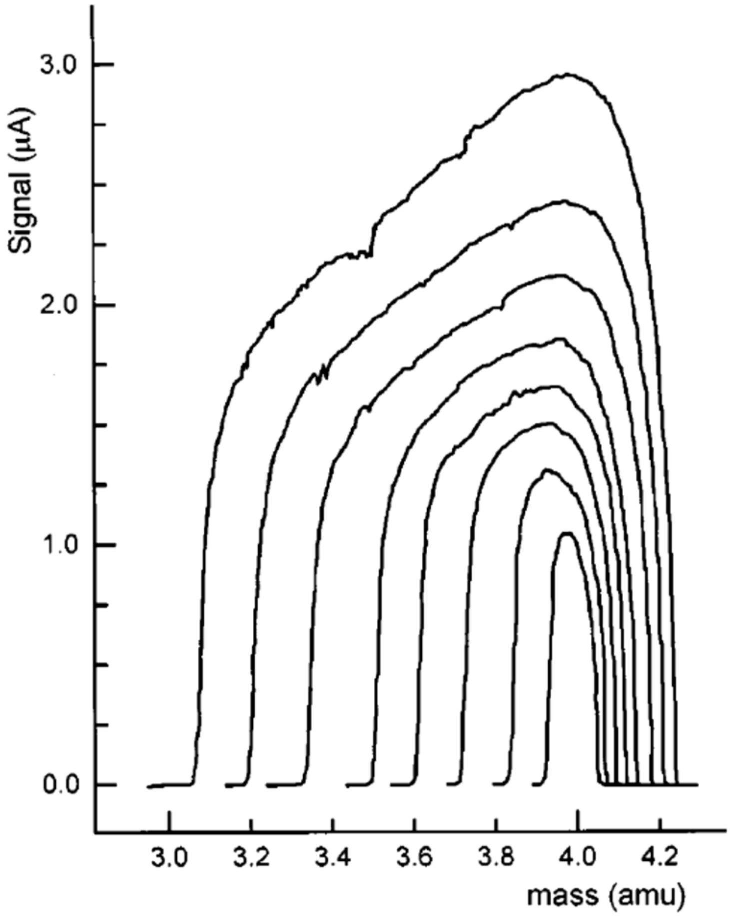

Figure 4.3: Experimental spectra of He$^+$ mass peak for equal steps in resolution control setting obtained with high resolution QMF with length = 228.6mm, frequency = 8MHz and ion energy = 2eV [19]

In general, there is much greater variation in performance determined for a particular filter design using 3D fields than using 2D ones. Changing the separations between the rods and end plates, or changing the manner in which the entrance aperture is modelled, both predict large changes in behaviour. A few peak shapes are illustrated later and compared with experimental results.

Using 2D fields and circular section electrodes (provided ions experience at least seventy cycles of the alternating (rf) field) the peak height is almost constant for fixed QMF dimensions, resolution setting and frequency [20]. If ions experience more than 70 rf cycles, transmission decreases very slightly. For results using the 3D fields the transmission behaves in a more complex manner; this is illustrated by examining the heights of mass peaks for simulated mass scans using one filter geometry and a range of ion masses and energies. Since behaviour is the same for a fixed value of λ (equation 4.2) the results are shown as mass peak height as a function of initial ion velocity which is proportional to $(V_{ion}/m)^{\frac{1}{2}}$ where V_{ion} is the nominal ion source accelerating voltage. Figure 4.4 shows the results with the filter dimensions used for figure 4.2; several different ion masses are required to cover the ion velocity range shown when ion energy is restricted to typical values used in practice. If any filter dimension is changed, the curves change by a large amount. There is always a peak but both its height and position vary. There is usually a complex structure on the low velocity side of the peak and a smoothly changing form on the high velocity side.

The second, normalised velocity, abscissa in figure 4.4, is to illustrate that many combinations of filter parameters lead to the same value of transmission. Using the normalized velocity scale the peak transmission is at approximately $0.1 \times r_0 rad^{-1}$, which is equivalent to approximately 1·6 cycles per r_0. A similar value of ion velocity for peak transmission was found by Dawson [6].

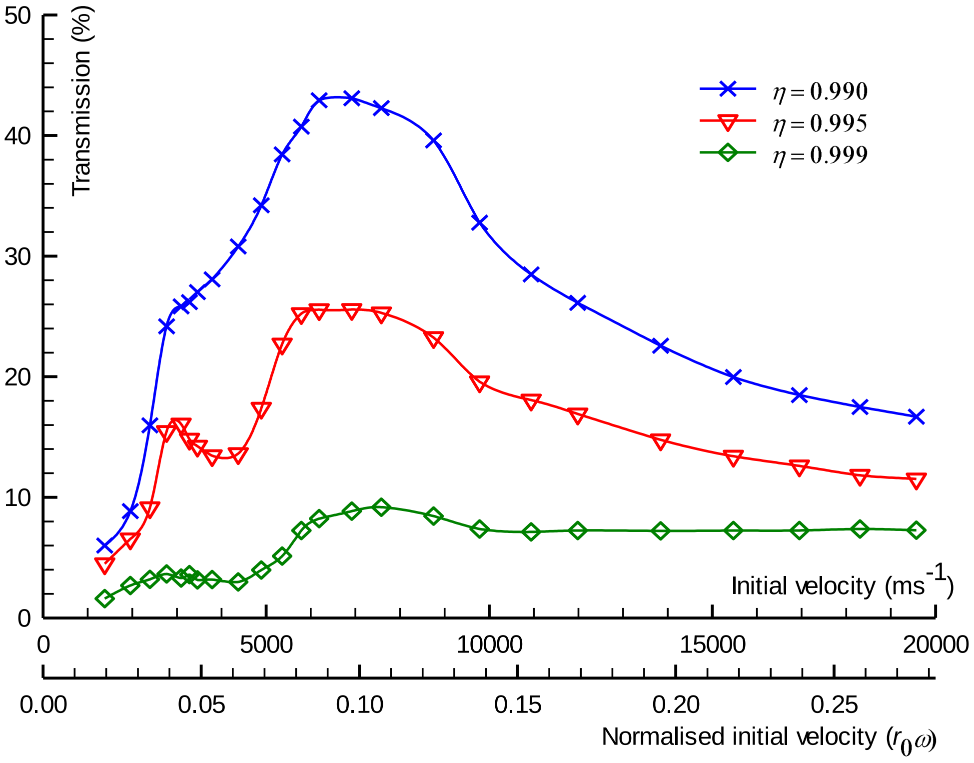

Figure 4.4: Mass peak height variation with ion velocity

Ehlert [21] shows experimental results with features found in figure 4.4, and computations by Dawson [2, 6] show similar trends. In [2, 6, 21], the horizontal axis is in the opposite sense to that of figure 4.4; it is drawn as a function of ion mass with all ions having the same energy. Consequently, for [2, 6, 21] the axis scale is proportional to the inverse of the ion velocity squared. Ehlert's curve does show a small amount of structure corresponding to the left of the peak in figure 4.4, but it is not as great; however it was found that small changes in end gaps, source radius, frequency, and resolution setting produce very large changes in the curves.

An investigation was made to determine the distance into the filter after which the fringe fields may be ignored and behaviour can be modelled using 2D fields (QMS-2D). The field was modified so that it changed from the 3D to the 2D field at different distances into the filter; very small effects were observed when the change was at distances from about 7·5×r_0 down to 2·5×r_0, but significant effects on filter behaviour were observed with the changes at distances of 2·5×r_0 or less.

The effect of the fringe field at the exit end plate was found to be negligible; even an extreme case using the 2D fields from the centre of the filter to the exit position produced only small changes in the results. Provided the filter is longer than about 25×r_0, very few ions that reach the exit fringe field region ever move a distance greater than r_0 from the axis, regardless of the model used to create the fringe field. For all forms of exit aperture model examined, all the ions that reached the exit position with their distance from the axis less than r_0 were regarded as transmitted. The behaviour when only ions inside a smaller radius at the exit position are considered to be transmitted produced complex effects; these include peak splitting and have been observed experimentally [11, 12].

4.6 Experimental Results

Measurements were made with an MKS Microvision Plus RGA (MKS Spectra Products, Crewe, UK), which has dimensions close to those of the typical system used for the previous figures. The QMF is 100mm long, electrode diameter (r) is 6.35mm, inscribed field radius (r_0) is 2.76mm and alternating potential frequency remains constant at 1.843MHz. The QMS was housed in a stainless steel chamber evacuated by a turbo pump, backed by a diaphragm pump providing a residual gas pressure of ~1×10^{-7}torr. After admitting the sample gas into the vacuum chamber the working pressure was raised to 2×10^{-5}torr.

It was only possible to obtain measurements providing short sections of curves similar to those of figure 4.4 because the range of ion velocities shown requires measurements for ions with several different masses and energies. The output of any ion source varies with mass and nominal energy of ejection of the ions from the source and the variation is usually unknown. Hence, the actual filter transmission value cannot be determined experimentally although variation in transmission can be measured over a small range of ion velocity. There are few quantitative studies of ion source behaviour; those there are, for example [22], show that behaviour is complex and output may vary with ion mass, ion energy and ion type.

Although curves showing variation of filter transmission with initial ion velocity could not be determined experimentally over a wide range of conditions it was possible to obtain results showing the variation in mass peak shape with ion mass. Figure 4.5 compares mass peaks for four ion species using the MKS instrument and are computed using the dimensions and operating frequency of the RGA. The mass scale for the measurements has been adjusted to align measurements and the computations as the two mass scales are calibrated using different methods. The experimental signal is scaled to match the transmission predicted by the model because the input ion current is unknown. A further feature of commercial instruments, such as the MKS Microvision Plus, is that resolution is automatically adjusted with position on the mass scan so that peak width, Δm, is constant. The model follows the usual theoretical description of QMF devices (a fixed scan line passing through the origin of the stability diagram) and maintains constant resolution, $\Delta m/m$ (see equation 3.39). The resolution was adjusted for each computation of a mass peak so that the peak width approximately matched the measured one; for ions with an *m*/*z* equal to four, the resolution is extremely low. For best fit to the experimental data the ion energy used for the computed peaks was slightly lower than that indicated by the instrument.

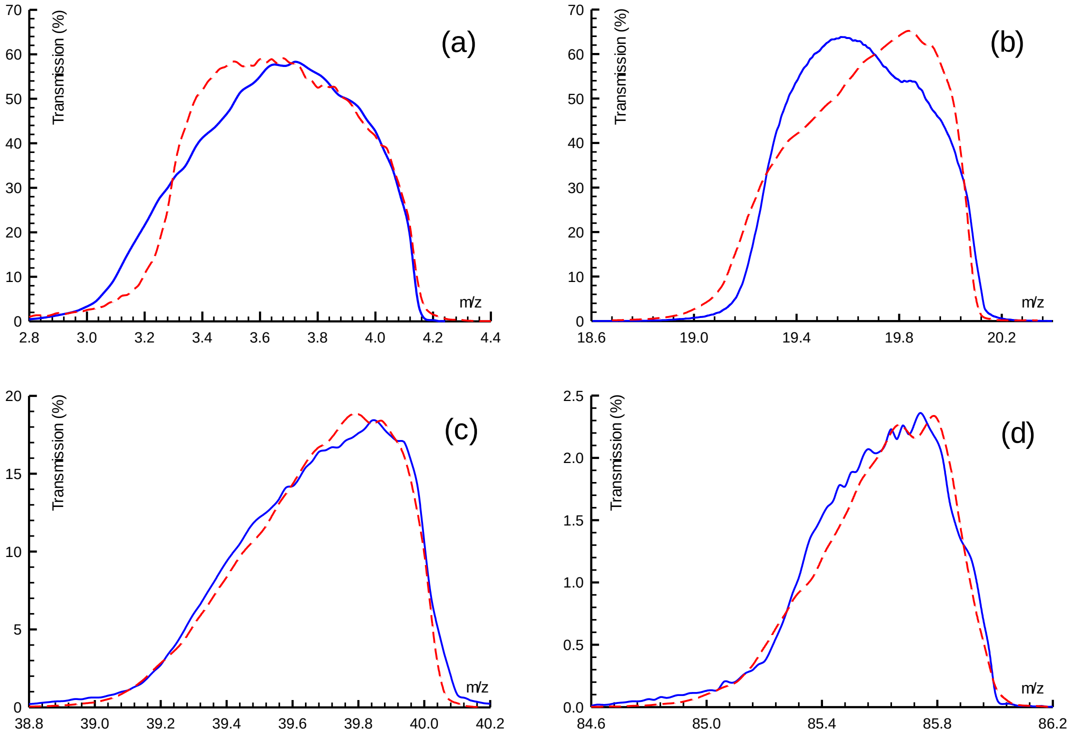

Figure 4.5: Comparison of computed (solid blue line) and measured (red broken line) mass peaks for various ion masses for the same nominal ion energy: (a) *m/z* 4, (b) *m/z* 20, (c) *m/z* 40, (d) *m/z* 86

To produce figure 4.5, a fixed end gap and ion source model were used with the ion energy set at 3eV; the MKS Microvision Plus ion energy was set to a nominal value of 4eV. It is possible to obtain better agreement for each ion mass if the end gap value, ion source model, and experimental setting of ion energy are varied by small amounts with mass. The ion source model is simpler than an actual ion source having uniform illumination, no energy spread and no beam spread. The ion source and ion extraction of the MKS instrument will produce a more complicated ion beam which will probably vary with ion mass.

The mass peaks in figure 4.5, although not identical, show similar trends in peak shape variation for the computations and experiment. Mass peaks simulated for an ideal QMF (hyperbolic electrodes and no fringe fields) show a rather rounded shape, similar to those in Figure 4.2, and this is also true of many observations using QMFs. However, the model and the experiment both produce distorted peaks with the most severe distortion at the higher masses (lower ion velocity) in figure 4.5. At the higher masses, the peaks have a ‘triangular’ shape and the shapes change towards the more usual form as the ion mass is decreased although the model shows a more rapid change in shape than the experiment. This is evident in figure 4.5(d) were the computed response shows some fine structure in the mass peak which may be an artefact of the model and requires further investigation. The model is able to produce results at even lower ion velocities than is possible experimentally and the peaks become even more distorted.

Titov [3] suggests that fringe fields may lead to the formation of precursors (i.e., satellite peaks). No evidence of this has been observed in the results obtained using the model. With very large end gaps, the computed mass peaks do exhibit structure; this might appear to be precursor formation.

4.7 Conclusions

The results of figure 4.4 confirm and expand those of Dawson [2, 6] and Ehlert [21]; the filter behaviour shown by figure 4.4 and [2, 6, 21] can be divided into two regions. If conditions are such that the operation of the filter corresponds to the region from the peak position of the curves to higher ion velocities, the behaviour is similar to that predicted by the 2D model except that peak heights are usually larger; in some cases, by nearly an order of magnitude. Peak height falls towards the value for 2D fields as ion velocity increases although convergence is very slow. In this high ion velocity region peak shapes are generally similar to those for 2D fields and resolution (peak width) is almost the same for the 2D and 3D fields. The reduction in the low mass tail found with 3D fields means that where mass peaks with large height differences are close together results using 3D fields suggest that the peaks will be more easily resolved than is predicted using 2D fields.

For the region of figure 4.4 with ion velocities below the peak position, the variation of transmission is more complicated and varies with changes in filter geometry. Mass peak shape and height vary by a large amount for small changes in initial ion velocity, and peaks often have distorted shapes. In some cases, the distorted shapes result in improved resolution but as peak shape varies rapidly with ion velocity (with mass if ion energy is constant) the resolution varies with mass. The results obtained so far give no obvious general rules governing behaviour in this low ion velocity region. The mass peak distortion depends critically on how the source region is modelled; distortion does appear to increase slightly when the diameter of the ion source is decreased.

Different filter behaviour in the two regions arises because of the different number of cycles of the rf field which ions experience while in the fringe field region. At velocities higher than the value at the peak position of figure 4.4, ions experience less than one rf cycle while in the fringe field. Conversely, ions entering the filter with low initial velocity experience many rf cycles while in the fringe field; some ions are lost while in the fringe field and the remainder enter the region beyond the fringe field with positions and velocities that do not lead to trajectories such that the ions pass through the filter.

The very variable results for transmission and large variation in mass peak shape obtained for low ion velocity values suggest that a QMF should be operated on the basis that the highest mass ion to be observed has a velocity slightly higher than the position of the peak of figure 4.4. Filters are normally operated with fixed ion energy so the filter sensitivity (transmission) will be higher the greater the mass of the ion. For a given choice of QMF length and end gap, the peak position in figure 4.4 is set by the combination of ion energy (ion velocity) and operating frequency. The highest mass ions should experience less than one rf cycle while in the fringe field. Once ion energy and operating frequency are set, the number of cycles experienced by an ion passing through a filter can be determined for any ion mass (see equation 3.43); as mass falls, the number of cycles fall, and filter performance decreases. Hence, the model suggests that the mass range of a particular design of RGA is restricted by the fringe fields at the entrance. Choice of a high upper mass will raise the useful low mass limit.

The techniques described allow accurate computation of the fields within a full 3D model of a QMF device; so far they have only been applied to systems without a pre-filter or a post-filter. Results obtained show complex behaviour, especially if ion velocities are low, and suggest that ion velocity should be above a certain limiting value determined by the computational techniques described. The value must be determined for each design of QMF; even small modifications in dimensions may produce large changes in predicted performance.

References

[1] P. Dawson, "A detailed study of the quadrupole mass filter," *International Journal of Mass Spectrometry and Ion Physics,* vol. 14, pp. 317-337, 1974.

[2] P. Dawson, "Ion optical properties of quadrupole mass filters," *Advances in Electronics and Electron Physics,* vol. 53, pp. 153-208, 1980.

[3] V. V. Titov, "Ion separation in imperfect fields on the quadrupole mass analyser Part V. Experimental verification," *International journal of mass spectrometry and ion processes,* vol. 141, pp. 57-65, 1995.

[4] W. M. Brubaker, "An improved quadrupole mass analyzer," *Adv. Mass Spectrom,* vol. 4, pp. 293-299, 1968.

[5] P. Dawson, "Fringing fields in the quadrupole mass filter," *International Journal of Mass Spectrometry and Ion Physics,* vol. 6, pp. 33-44, 1971.

[6] P. Dawson, "The acceptance of the quadrupole mass filter," *International Journal of Mass Spectrometry and Ion Physics,* vol. 17, pp. 423-445, 1975.

[7] P. Dawson, "Fringing fields in quadrupole-type mass analyzers," *Journal of Vacuum Science and Technology,* vol. 9, pp. 487-491, 1972.

[8] V. V. Titov, "Ion separation in imperfect fields of the quadrupole mass analyzer Part II. Ion beam dynamics in the phase-space of the fringing field," *International journal of mass spectrometry and ion processes,* vol. 141, pp. 27-35, 1995.

[9] K. L. Hunter and B. J. McIntosh, "An improved model of the fringing fields of a quadrupole mass filter," *International journal of mass spectrometry and ion processes*, vol. 87, pp. 157-164, 1989.

[10] B. J. McIntosh and K. L. Hunter, "Influence of realistic fringing fields on the acceptance of a quadrupole mass filter," *International journal of mass spectrometry and ion processes,* vol. 87, pp. 165-179, 1989.

[11] K. Blaum, C. Geppert, P. Müller, W. Nörtershäuser, E. Otten, A. Schmitt, N. Trautmann, K. Wendt, and B. Bushaw, "Properties and performance of a quadrupole mass filter used for resonance ionization mass spectrometry," *International journal of mass spectrometry,* vol. 181, pp. 67-87, 1998.

[12] K. Blaum, C. Geppert, P. Müller, W. Nörtershäuser, K. Wendt, and B. Bushaw, "Peak shape for a quadrupole mass spectrometer: comparison of computer simulation and experiment," *International journal of mass spectrometry,* vol. 202, pp. 81-89, 2000.

[13] J. R. Gibson, K. G. Evans, and S. Taylor, "Modelling mass analyzer performance with fields determined using the boundary element method," *Journal of Mass Spectrometry,* vol. 45, pp. 364-371, 2010.

[14] F. Read, "Zero gap electrostatic aperture lenses," *Journal of Physics E: Scientific Instruments,* vol. 4, p. 562, 1971.

[15] F. Read, A. Adams, and J. Soto-Montiel, "Electrostatic cylinder lenses. I. Two element lenses," *Journal of Physics E: Scientific Instruments,* vol. 4, p. 625, 1971.

[16] E. C. Beaty, "Calculated electrostatic properties of ion traps," *Physical Review A,* vol. 33, p. 3645, 1986.

[17] D. Douglas, T. Glebova, N. Konenkov, and M. Y. Sudakov, "Spatial harmonics of the field in a quadrupole mass filter with circular electrodes," *Technical Physics,* vol. 44, pp. 1215-1219, 1999.

[18] J. R. Gibson and S. Taylor, "Asymmetrical features of mass spectral peaks produced by quadrupole mass filters," *Rapid Communications in Mass Spectrometry,* vol. 17, pp. 1051-1055, 2003.

[19] J. Gibson, S. Taylor, and J. Leck, "Detailed simulation of mass spectra for quadrupole mass spectrometer systems," *Journal of Vacuum Science & Technology A: Vacuum, Surfaces, and Films,* vol. 18, pp. 237-243, 2000.

[20] J. R. Gibson and S. Taylor, "Prediction of quadrupole mass filter performance for hyperbolic and circular cross section electrodes," *Rapid Communications in Mass Spectrometry*, vol. 14, pp. 1669-1673, 2000.

[21] T. C. Ehlert, "Determination of transmission characteristics in mass filters," *Journal of Physics E: Scientific Instruments*, vol. 3, p. 237, 1970.

[22] W. Austin, J. Leck, and J. Batey, "Study of the performance of a group of quadrupole mass spectrometers," *Journal of Vacuum Science & Technology A: Vacuum, Surfaces, and Films*, vol. 10, pp. 3563-3567, 1992.

Chapter 5 : QMS with a Static Magnetic Field Applied

Resolution enhancement is demonstrated for a Quadrupole Mass Spectrometer (QMS) under the influence of a static magnetic field. Generally, QMF resolution can be improved by increasing the number of field cycles experienced by an ion passing through the mass filter. In order to improve the resolution, the dimensions of the QMF or the operating parameters need to be changed. However, geometric modifications to improve performance increase the manufacturing cost and usually the size of the instrument. By applying a magnetic field, a low cost, small footprint instrument with reduced power requirements can be realised with enhanced performance.

5.1 Introduction

Magnetic fields have long been used in mass spectrometry (MS) and can be traced back to the first mass spectrometer of J. J. Thomson [1] (chapter 2). The conventional QMS operates without the use of any magnetic fields and separates ions based on their stability in an electric field. At the end of the 20th century, Tunstall et al. [2] first applied a static magnetic field to the body of a QMS (transverse to the central QMF axis) and demonstrated experimentally an increase in instrument resolution.

The orientation of the ***B*** field vector is described in terms of a Cartesian coordinate system whereby the ***B*** field is projected transversely (along either the *x*- or *y*- axes), or axially (along the *z*-axis) - figures 5.1 and 5.2 respectively. With respect to the QMF, the *x*-axis refers to the plane consisting of the positive potential electrodes and the *y*-axis refers to the plane of the negative potential electrode pair.

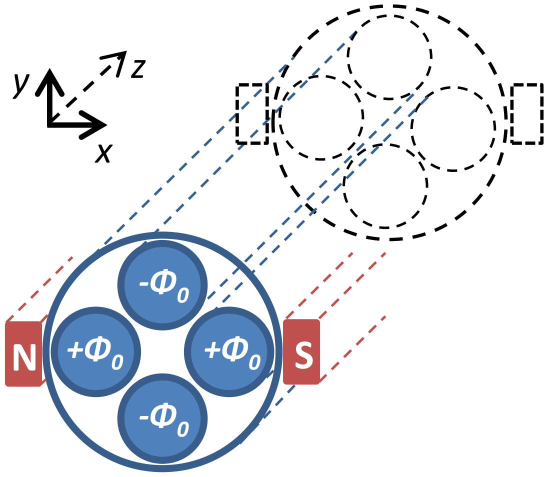

Figure 5.1: Application of a static transverse magnetic field (B_x) in the x-z plane of a QMF, where $\varnothing_0$ is the composite direct and alternating potential applied to the electrodes

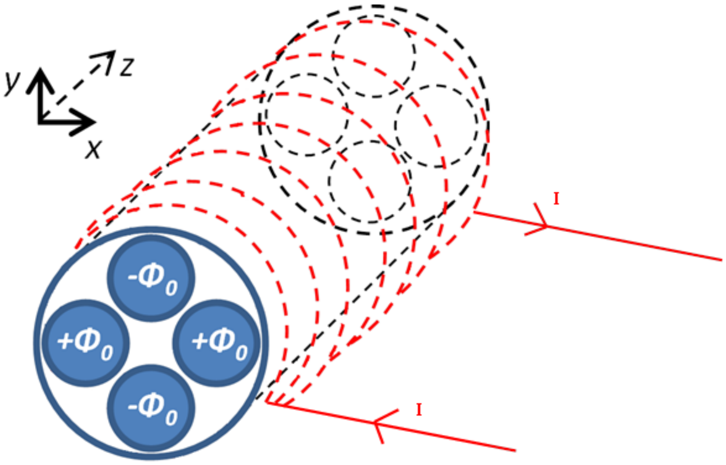

Figure 5.2: Application of a static axial magnetic field (B_z). *I* is the current supplied to the solenoid and $\varnothing_0$ is the composite direct and alternating potential applied to the electrodes

Since the initial investigation of Tunstall et al. few subsequent research efforts have been undertaken. Authors in [3] have demonstrated the effect on the ion trajectories of a QMF in a static transverse magnetic field. They concluded that the component of the magnetic field in the *x* direction is responsible for the resolution enhancement. By contrast, Syed et al. [4] investigated the effect of an axial magnetic field (B_z) on the performance of a QMF as well as the effect of a transverse magnetic field (B_x) on a QMF operated in stability zone 3 [5].

In this chapter, new analytical theory is developed for the case of a static magnetic field applied to a QMF. A new method is developed allowing the effective stability diagram to be mapped numerically thus providing an important insight into the fundamental operation of a QMF under the influence of a static transverse magnetic field. Ion transmission factors for a transverse magnetic field applied to a QMF are investigated in detail. In addition, the magnetic field effect is examined for the case of a QMF employing circular cross-section electrodes; both new experimental and simulation results are presented examining the behaviour of the QMF under the influence of a transverse magnetic field.

5.1.1 Transverse Magnetic Field Applied to QMF

Applying a magnetic field in the transverse plane (x or y) of a QMF was examined experimentally by Tunstall et al [2]. It was concluded that applying a magnetic field along the x axis causes a significant increase in resolution, whereas the same size magnetic field applied in the y axis plane has no effect. Further investigations by Srigengan et al. [3] regarding a static transverse magnetic field applied to a QMS showed that the magnetic field applied along the x axis (B_x) caused a reduction on the low mass side of a mass peak. This effect was attributed to an increase in the Lorentz force influencing ion motion in the y-z plane. Furthermore, the effect of the angle of the transverse magnetic field was investigated and it was concluded that the component of the magnetic field in the x-direction was responsible for the observed resolution enhancement.

Another study investigated the effect of a transverse magnetic field applied to a QMS operated in stability zone 3 [5]. The same trend reported by Srigengan et al. [3] was observed, whereby the transmission on the low mass side of a mass peak reduces (compared with $\boldsymbol{B} = 0$) upon application of a B_x field. The separation of HT^+ (mass = 4.0238Da) and D_2^+ (mass = 4.0282Da) was simulated using a magnetic field and resolution was shown not to increase indefinitely.

5.1.2 Axial Magnetic Field Applied to QMF

The effect of applying an axial magnetic field to a QMF is somewhat different compared with that of applying a transverse magnetic field. Upon application of a B_z field there is reduction in the low mass side as well as high mass side of a mass peak. This was first investigated theoretically by Tunstall et al. [2] who predicted that application of a B_z field would provide a marginal increase in resolution. Investigation by Syed et al. confirmed the theoretical predictions and described in detail the case of an axial magnetic field applied to a QMS [4].

With an axial magnetic field applied, the mass filter can be operated close to the tip of the stability zone 1. In [4] it was shown for a QMF of length 100mm the resolution increased as B_z was varied from 0 - 0.035T and then decreased as B_z was further increased up to 0.06T. QMF resolution will not increase indefinitely because as B_z increases transmission reduces and the peak shape eventually degrades. A similar effect was observed for shorter and longer QMFs: resolution rises with applied B_z reaching a maximum value, then decreases. Moreover, it was shown that the effect of an axial magnetic field is more pronounced at a higher number of rf cycles [4].

5.2 Magnetic Field

The physical phenomena of magnetism has long been known and put to practical use in the mariner's compass. The origin of the word "magnet" can be traced to the mineral Magnesia (a form of magnesium oxide) which according to Roman philosopher Lucretius (99-55 B.C.) was a peculiar substance which exerted mysterious attractive forces upon pieces of iron [6]. Modern ideas on magnetism originated with Oersted who in 1820 discovered that an electric current produces a magnetic field [7] and subsequently Ampere showed that parallel wires having current flow in the same direction attract one another [8]. The complementary phenomenon, the production of electric currents from magnetism (electromagnetic induction), was demonstrated in 1831 by Faraday [9].

The experimental work of Faraday, in particular his visualisation of force transmission via field action, provided the basis for Maxwell to develop his theory of electro-magnetism [10]. The theory asserted that an electric field exists in the space where a magnetic field is changing and that the complement is also true; a magnetic field exists in space where an electric field is changing. From Maxwell's equations Lorentz was able to derive the force due to a magnetic field on a moving point charge [11].

5.2.1 Effect of a Magnetic Force on a Moving Charge

The effect of a magnetic force acting on a moving point charge at a given point and time is perpendicular to both the velocity of the charge and the direction of the magnetic field (figure 5.3). This is described by the magnetic force component of the Lorentz force law equation,

$$\boldsymbol{F} = q(\boldsymbol{v} \times \boldsymbol{B}) \qquad (5.1)$$

where q is the charge on the particle, $\boldsymbol{v}$ is the velocity of the particle and $\boldsymbol{B}$ is the magnetic flux density. In general the magnitude of this force is given as,

$$F = qvB\sin\theta \tag{5.2}$$

where θ is the angle subtended between the direction of motion of the charged particle and the direction of the magnetic field. The complete form of the Lorentz force law incorporates the total electromagnetic force on a charged particle, in the presence of both an electric field ($\boldsymbol{E}$) and magnetic field ($\boldsymbol{B}$) and is given as,

$$\boldsymbol{F} = q(\boldsymbol{E} + \boldsymbol{v} \times \boldsymbol{B}) \tag{5.3}$$

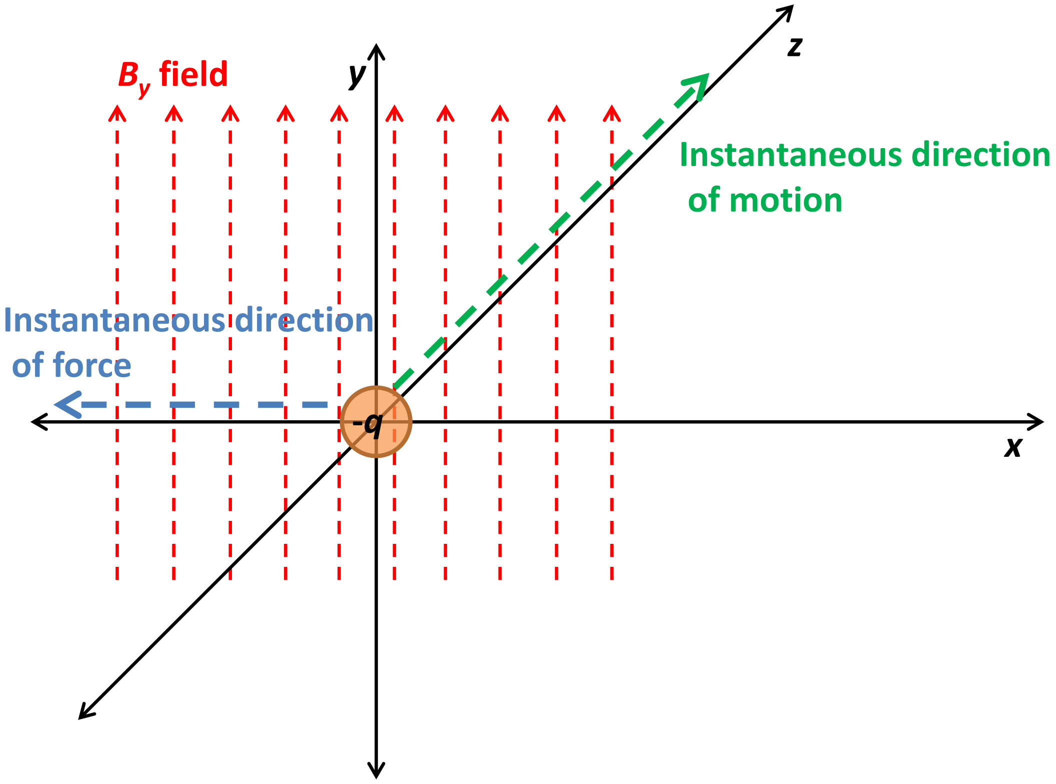

Figure 5.3: Force on a charged particle moving in a magnetic field

5.2.2 Generating a Magnetic Field

Generating a homogeneous magnetic field in the axial and/or transverse planes with respect to the QMF can be achieved by using permanent magnets or electromagnets. The choice between permanent or electromagnet is influenced by the geometric dimensions of the QMF. For a typical QMF the length of the electrodes is usually larger than the outer diameter of the electrode assembly. Consequently the QMF is usually enclosed within a cylindrical stainless steel vacuum housing.

Axial

An effective and efficient manner for generating a uniform magnetic field in the axial direction is by using a solenoid (coil of wire) wrapped around the vacuum housing (and insulated from it). For a long solenoid, the magnetic field is uniform across the diameter and close to the centre. The axial magnetic field (B_z) generated by a constant current, I, can be approximated as:

$$B_z = \mu_0 n I \tag{5.4}$$

where μ_0 is the permeability of free space and n is the number of turns per metre.

Transverse

For the typical geometric configuration of a QMF it is possible to generate an approximate uniform field in the transverse plane using permanent bar magnets. This is achieved by facing the opposing pole planes of two permanent bar magnets along a common axis with the QMF in between. The uniformity can be increased by using larger magnets (or reducing the gap between). A simple way of increasing the uniformity of the field between bar magnets is to connect them with an iron yoke.

5.3 Fundamental Theory of a QMF with a Static Magnetic Field Applied

The total force experienced by an ion injected into the QMF is given by the Lorentz force (equation 5.3). For a conventional QMF there is no magnetic field term and the equations of motion (as derived in chapter 3) are found to be of the form (repeated here for convenience):

$$\frac{d^2u}{d\xi^2} + (a_u - 2q_u \cos(2\xi))u = 0 \tag{5.5}$$

Where, u is displacement (x or y), ξ is a dimensionless modified time parameter given by, $\xi = {}^{\omega t}/_{2}$, ω is the angular frequency of the alternating potential given by, $\omega = 2\pi f$, t is time, a_u and q_u are dimensionless stability parameters given by, $a_u = a_x = -a_y = \frac{8eU}{mr_0^2\omega^2}$, and $q_u = q_x = -q_y = \frac{4eV}{mr_0^2\omega^2}$.

Upon application of a general magnetic field, $\boldsymbol{B} = (B_x, B_y, B_z)$, the equations of motion will include an additional force term arising from the term $\boldsymbol{v} \times \boldsymbol{B}$ of equation 5.3. Using unit vectors $(\hat{\boldsymbol{\imath}}, \hat{\boldsymbol{\jmath}}, \widehat{\boldsymbol{k}})$ this term can be expressed as,

$$\left(\frac{\partial y}{\partial t}B_z - \frac{\partial z}{\partial t}B_y\right)\hat{\boldsymbol{\imath}} + \left(\frac{\partial z}{\partial t}B_x - \frac{\partial x}{\partial t}B_z\right)\hat{\boldsymbol{\jmath}} + \left(\frac{\partial x}{\partial t}B_y - \frac{\partial y}{\partial t}B_x\right)\widehat{\boldsymbol{k}} \tag{5.6}$$

Using Newton's second law (as in chapter 3.1.3) the equations of motion in each co-ordinate direction are obtained:

$$\frac{\partial^2 x}{\partial t^2} = -\frac{e}{mr_0^2}(U - V\cos(\omega - \omega t_0))x + \frac{e}{m}\left(\frac{\partial y}{\partial t}B_z - \frac{\partial z}{\partial t}B_y\right) \tag{5.7}$$

$$\frac{\partial^2 y}{\partial t^2} = \frac{e}{mr_0^2}(U - V\cos(\omega - \omega t_0))y + \frac{e}{m}\left(\frac{\partial z}{\partial t}B_x - \frac{\partial x}{\partial t}B_z\right) \tag{5.8}$$

$$\frac{\partial^2 z}{\partial t^2} = \frac{e}{m}\left(\frac{\partial x}{\partial t}B_y - \frac{\partial y}{\partial t}B_x\right) \tag{5.9}$$

If the following substitutions are made (as in chapter 3.1.4),

$$\xi = \frac{\omega t}{2} \tag{5.10}$$

$$a_u = a_x = -a_y = \frac{8eU}{mr_0^2\omega^2} \qquad (5.11)$$

$$q_u = q_x = -q_y = \frac{4eV}{mr_0^2\omega^2} \qquad (5.12)$$

then equations (5.7 – 5.9) can be re-written as,

$$\frac{\partial^2 x}{\partial \xi^2} = \left(-a + 2q\cos\left(2(\xi - \xi_0)\right)\right)x + \left(\frac{\partial y}{\partial \xi}B_3 - \frac{\partial z}{\partial \xi}B_2\right) \qquad (5.13)$$

$$\frac{\partial^2 y}{\partial \xi^2} = \left(a - 2q\cos\left(2(\xi - \xi_0)\right)\right)y + \left(\frac{\partial z}{\partial \xi}B_1 - \frac{\partial x}{\partial \xi}B_3\right) \qquad (5.14)$$

$$\frac{\partial^2 z}{\partial \xi^2} = \left(\frac{\partial x}{\partial \xi}B_2 - \frac{\partial y}{\partial \xi}B_1\right) \qquad (5.15)$$

where,

$$(B_1, B_2, B_3) = \left(\frac{2eB_x}{m\omega}, \frac{2eB_y}{m\omega}, \frac{2eB_z}{m\omega}\right)$$

From equations 5.13 – 5.15, it is evident that upon application of a transverse magnetic field ($B_1\ or\ B_2$) a variable resultant axial force along the QMF *z*-axis exists (equation 5.15). This means that the axial velocity (v_z) is no longer constant (as it is for the conventional QMS case). Furthermore there is an additional Lorentz magnetic force in the other orthogonal direction (so that a B_x field causes an additional force in the *y* plane and *vice versa*). If an axial magnetic field is applied (B_3) then there is no resultant force in the *z* direction and the axial velocity remains constant (as in the conventional case) and there is an additional Lorentz magnetic force orthogonal to the *z*-axis (in *x* and *y*).

The implications arising from the application of magnetic field can be simplified by considering the magnetic field vector oriented in each Cartesian dimension (*x*, *y*, *z*) in isolation. By doing so the following equations of motion for each case are obtained:

Transverse Field, $\boldsymbol{B} = (B_x, 0, 0)$

$$\frac{\partial^2 x}{\partial \xi^2} = \left(-a + 2q\cos\left(2(\xi - \xi_0)\right)\right)x \tag{5.16}$$

$$\frac{\partial^2 y}{\partial \xi^2} = \left(a - 2q\cos\left(2(\xi - \xi_0)\right)\right)y + \frac{\partial z}{\partial \xi}B_1 \tag{5.17}$$

$$\frac{\partial^2 z}{\partial \xi^2} = -\frac{\partial y}{\partial \xi}B_1 \tag{5.18}$$

Integrating equation 5.18 gives,

$$\frac{\partial z}{\partial \xi} = -B_1 \int \frac{\partial y}{\partial \xi}\partial \xi + C \tag{5.19}$$

$$\frac{dz}{d\xi} = -B_1 y(\xi) + C \tag{5.20}$$

where the value *C* is determined by initial conditions. When $\xi = 0$, it is equivalent to t = 0 since $\xi = {}^{\omega t}/_{2}$. Denoting the initial velocity, $v_0 = \left(v_{x_0}, v_{y_0}, v_{z_0}\right)$ and the initial position as, $u_0 = (x_0, y_0, z_0)$ then,

$$\left(\frac{dz}{d\xi}\right)_0 = -B_1 y_0 + C \tag{5.21}$$

$$C = \left(\frac{dz}{d\xi}\right)_0 + B_1 y_0 \tag{5.22}$$

$$\frac{dz}{d\xi} = -B_1 y(\xi) + \left(\frac{dz}{d\xi}\right)_0 + B_1 y_0 \tag{5.23}$$

Substituting this result into equation 5.17 yields,

$$\frac{\partial^2 y}{\partial \xi^2} - \left(a - 2q\cos\left(2(\xi - \xi_0)\right)\right)y = B_1\left(-B_1 y(\xi) + \left(\frac{dz}{d\xi}\right)_0 + B_1 y_0\right) \tag{5.24}$$

$$\frac{\partial^2 y}{\partial \xi^2} - \left(a - 2q\cos\left(2(\xi - \xi_0)\right)\right)y = -B_1^2 y(\xi) + B_1\left(\frac{dz}{d\xi}\right)_0 + B_1^2 y_0 \tag{5.25}$$

Equation 5.25 can be re-arranged into a non-homogenous Mathieu form,

$$\frac{\partial^2 y}{\partial \xi^2} - \left((a - B_1^2) - 2q\cos\left(2(\xi - \xi_0)\right)\right)y = B_1\left(B_1 y_0 + \left(\frac{dz}{d\xi}\right)_0\right) \tag{5.26}$$

Equation (5.16) is the homogeneous form of the Mathieu equation (as in the conventional case) and has the same solution as outlined in chapter 3. Equation 5.26 is not quite homogenous but is similar.

An expression for $z(\xi)$ can be obtained by further integration of equation 5.23,

$$z(\xi) \ = \int\big(-B_1 y(\xi)\big)\, d\xi + \int\left(\left(\frac{dz}{d\xi}\right)_0 + B_1 y_0\right) d\xi \tag{5.27}$$

$$z(\xi) \ = -B_1 \int y(\xi)\, d\xi + \left(\left(\frac{dz}{d\xi}\right)_0 + B_1 y_0\right)\xi + D \tag{5.28}$$

where D is a constant of integration determined by the initial conditions. Initially, $\xi = 0$ and $z = 0$,

$$0 = -B_1 \int y(\xi)\, d\xi + 0 + D \tag{5.29}$$

$$D = B_1\left(\int y(\xi)\, d\xi\right)_{\xi=0} \tag{5.30}$$

Thus,

$$z(\xi) \ = \left(\left(\frac{dz}{d\xi}\right)_0 + B_1 y_0\right)\xi + B_1\left(\left(\int y(\xi)\, d\xi\right)_{\xi=0} - \int y(\xi)\, d\xi\right) \tag{5.31}$$

Transverse Field, $\boldsymbol{B} = \left(0, B_y, 0\right)$

$$\frac{\partial^2 x}{\partial \xi^2} = -\big(a - 2q\cos\big(2(\xi - \xi_0)\big)\big)x - \frac{\partial z}{\partial \xi} B_2 \tag{5.32}$$

$$\frac{\partial^2 y}{\partial \xi^2} = \big(a - 2q\cos\big(2(\xi - \xi_0)\big)\big)y \tag{5.33}$$

$$\frac{\partial^2 z}{\partial \xi^2} = \frac{\partial x}{\partial \xi} B_2 \tag{5.34}$$

Applying a similar analysis as for the B_x case, equation 5.34 is integrated to obtain,

$$\frac{dz}{d\xi} = B_2\big(x(\xi) - x_0\big) + \left(\frac{dz}{d\xi}\right)_0 \tag{5.35}$$

Substituting this result into equation 5.32 yields,

$$\frac{\partial^2 x}{\partial \xi^2} + \big(a - 2q\cos\big(2(\xi - \xi_0)\big)\big)x = -B_2\left(B_2\big(x(\xi) - x_0\big) + \left(\frac{dz}{d\xi}\right)_0\right) \tag{5.36}$$

$$\frac{\partial^2 x}{\partial \xi^2} + \left((a + B_2^2) - 2q\cos\big(2(\xi - \xi_0)\big)\right)x = B_2\left(B_2 x_0 - \left(\frac{dz}{d\xi}\right)_0\right) \tag{5.37}$$

Equation 5.33 is the homogeneous form of the Mathieu equation (as in the conventional case) and has the same solution as outlined in chapter 3. Equation 5.37 is in a non-homogeneous form.

Axial Field, $\boldsymbol{B} = (0, 0, B_z)$

$$\frac{\partial^2 x}{\partial \xi^2} = \left(-a + 2q\cos\left(2(\xi - \xi_0)\right)\right)x + \frac{\partial y}{\partial \xi}B_3 \tag{5.38}$$

$$\frac{\partial^2 y}{\partial \xi^2} = \left(a - 2q\cos\left(2(\xi - \xi_0)\right)\right)y - \frac{\partial x}{\partial \xi}B_3 \tag{5.39}$$

$$\frac{\partial^2 z}{\partial \xi^2} = 0 \tag{5.40}$$

5.4 Simulation Software Description

The QMF simulation models developed at the University of Liverpool, QMS-Hyperbolic and QMS-2D (see chapter 3.2), were adapted to include the effect of an applied magnetic field in x, y, z. This was achieved by modifying the software code to solve the equations of motion with the additional components due to the magnetic field (equations 5.13 – 5.15).

Ion-TX

Furthermore an additional piece of software (Ion-TX) was developed based on QMS-Hyperbolic. Ion-TX solves equations 5.14 - 5.16 directly via Runge-Kutta numerical integration. The program has a graphical user interface (figure 5.4) and specifically allows ion transmission factors to be investigated. There is no limit imposed on the ion excursion (amplitude of oscillation). It uses as input the combined parameters (a, q, B_1, B_2, B_3) as well as the initial conditions $\left(\xi_0, \left(\frac{dz}{d\xi}\right)_0, y_0, x_0\right)$ appearing in equations 5.26 and 5.37. By setting the integration limit large enough the unlimited (i.e., infinite) response may be approximated ($\xi_{limit} = 300000$). The main output of the software is the peak amplitudes in x and y dimensions. The results were verified and showed excellent agreement with those obtained by solving the system of equations 5.14-5.16 using commercial software Maple 16 coupled with the Direct Search (version 2) optimisation package [12].

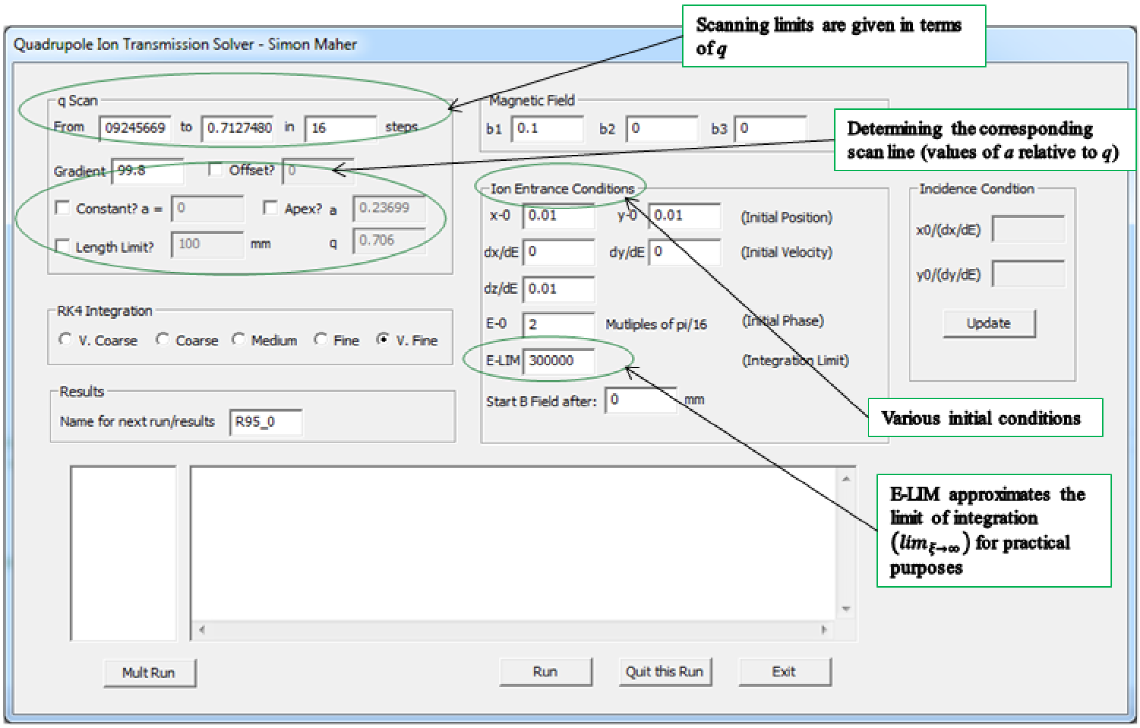

Quadrupole Ion Transmission Solver - Simon Maher

q Scan

From 09245669 to 0.7127480 in 16 steps

Gradient 99.8 ☐ Offset? 0

☐ Constant? a = 0 ☐ Apex? a 0.23699

☐ Length Limit? 100 mm q 0.706

RK4 Integration

○ V. Coarse ○ Coarse ○ Medium ○ Fine ● V. Fine

Results

Name for next run/results R95_0

Magnetic Field

b1 0.1 b2 0 b3 0

Ion Entrance Conditions

x-0 0.01 y-0 0.01 (Initial Position)

dx/dE 0 dy/dE 0 (Initial Velocity)

dz/dE 0.01

E-0 2 Mutiples of pi/16 (Initial Phase)

E-LIM 300000 (Integration Limit)

Start B Field after: 0 mm

Incidence Condtion

x0/(dx/dE)

y0/(dy/dE)

Scanning limits are given in terms of q

Determining the corresponding scan line (values of a relative to q)

Various initial conditions

E-LIM approximates the limit of integration ($lim_{\xi\to\infty}$) for practical purposes

Figure 5.4: Ion-TX GUI

5.5 Experimental Description

A conventional single filter QMS instrument (Microvision Plus RGA) supplied by MKS Spectra Products (Crewe, UK) was used. The QMF is 100mm long with an electrode diameter of 6.35mm and field radius of 2.76mm, with an rf frequency of 1.8342MHz. This was complemented by a hot filament ion source and Faraday detector. The QMS was housed in a stainless steel chamber evacuated by a turbo pump, backed by a diaphragm pump providing a residual gas pressure of ~1×10^{-7}torr. After admitting the sample gas into the vacuum chamber the working pressure was raised to about ~2×10^{-5}torr. The ion energy (of the electron ionisation source) is variable and was set to a value of 5eV, unless otherwise stated. The emission current was set as 0.3 mA and the electron energy was set to 70eV.

The QMS was operated using MKS software ‘Process Eye Professional’ with a fully automated high stability data acquisition electronic drive unit for fast dynamic scanning of the mass filter electrode voltages. The scan start mass, end mass, number of steps and sweep rate can be adjusted by the user. A visual display of each mass scan was displayed in real time on a laptop computer.

Permanent bar magnets were applied directly to the body of the QMF to produce the transverse magnetic field and measured using a Hall Effect sensor (GM08, Hirst Magnetic Instruments Ltd.). For the experiments in this chapter, the magnetic field was adjusted by altering the distance between the bar magnets. The magnetic field extended ~80% of the length of QMF. To demonstrate the effect of a static magnetic field, mass spectra were obtained for various ion species including: $^{4}He^{+}$, $^{40}Ar^{+}$ and Xe^{+} with and without an applied magnetic field (for experimental results see section 5.8).

5.6 Numerically Mapping the Effective Stability Diagram of a QMF

Under known operating conditions for a single simulated mass peak, it is possible to trace back the (a, q) values from the low and high mass sides of the peak, which correspond to the boundaries of the stability zone. By carefully adjusting the mass scan line (ac and dc voltages), several (a, q) points can be obtained from the simulated mass spectra and the stability diagram can be effectively mapped for a given configuration.

For a given mass scan line of operation (set of operating points), the ac (V) and dc (U) voltages are known at each point. Ions will be transmitted when the operating point lies within the stable region for that particular m/z. For a single simulated mass peak, the low mass side of the peak refers to the commencement of ion transmission and the high mass side refers to the end of transmission. Operating at a specific frequency (ω) for a given QMF design, using equations 3.30 and 3.31, the (a, q) points corresponding to the low mass side and high mass side of the peak can be plotted. Repeating this process for various operating lines allows several (a, q) points to be plotted and, hence, the stability diagram can be effectively mapped.

A similar method has been used previously for mapping the stability diagram experimentally for ion traps [13-15]. It is important to note that the mapping method gives an effective stability diagram that is obtained for the finite QMF design simulated. To verify the method using QMS-Hyperbolic, stability zone 1 was mapped for a conventional QMF (with no magnetic field applied). The ion investigated was m/z 40. The results, shown in figure 5.5, are compared with the analytical solution and show excellent agreement. A high density of mapped (a, q) points are plotted near to the apex to provide more detail as this is the operating region of interest for maximum performance.

This method allows the effective stability diagram to be mapped for a QMS under a range of conditions including, but not limited to, the case with a ***B*** field applied to the body of the filter.

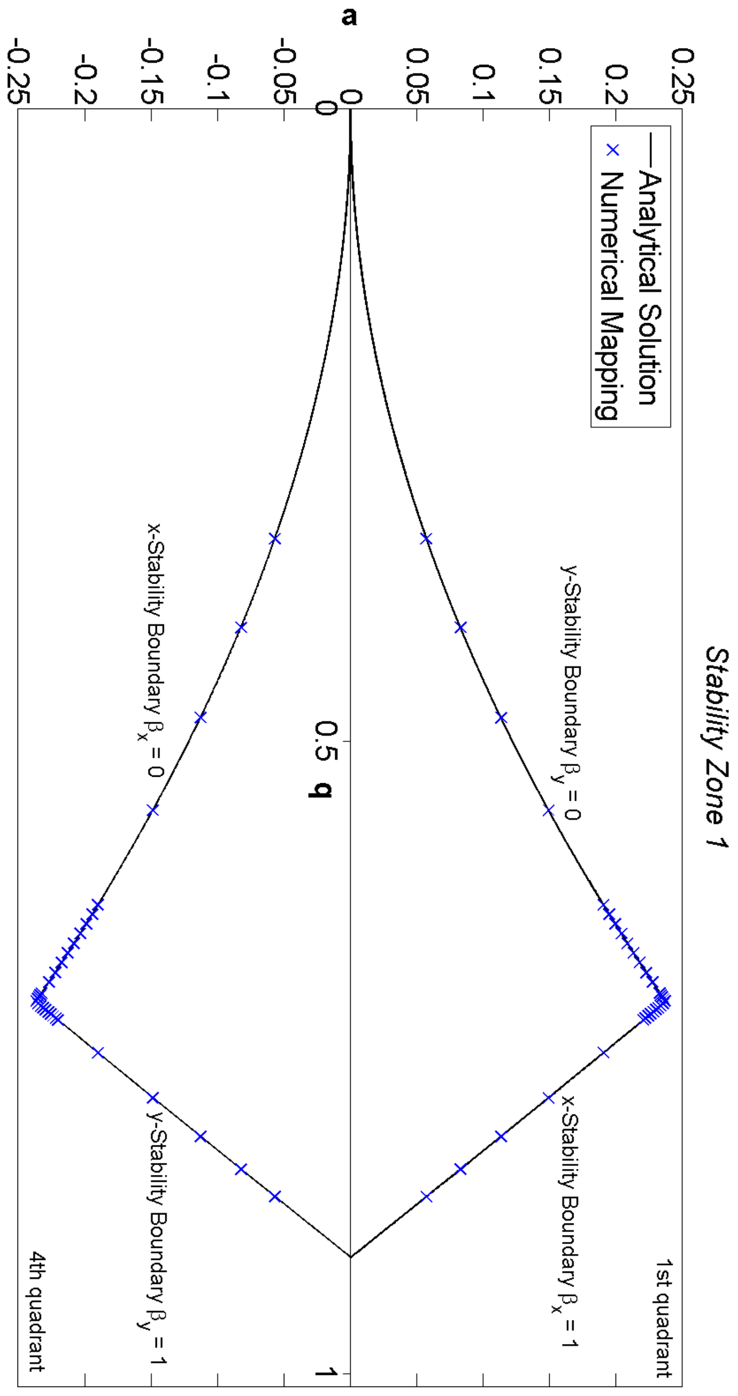

Figure 5.5: Mapping stability zone 1 (*blue crosses*) in two dimensions (*x* and *y*) against analytically determined boundaries (*solid black lines*) for a conventional QMF (no magnetic field applied) operated in the first and fourth quadrants. The Mathieu stability diagram is symmetrical about the *a*-axis

5.7 Mapping the Stability Diagram of a QMF with a Transverse Magnetic Field Applied

A transverse ***B*** field is applied at right angles to the central QMF axis (*z* axis), in the *x*-*y* plane. Any resultant transverse ***B*** field vector can be represented as a combination of the individual *x* and *y* components. The magnetic field is considered in each co-ordinate direction separately (B_x and B_y).

5.7.1 Simulation Software Parameters

Except for comparison with experimental spectra, all stability diagram mapping simulation results presented are for a QMF with inscribed radius (r_0) = 5mm, source radius = 0.5mm, exit radius = 5mm, rf frequency = 4MHz, and electrode length = 150mm. Across the scan range, 5 x10^5 ions were simulated at discrete intervals of *m/z* 0.005. The total number of ion trajectories simulated was of the order of 5 x10^8 for each simulation. The ions were injected into the QMF parallel to the *z*-axis (zero initial transverse velocity) with random phase compared to the rf at the time of entry. The model assumes a uniformly illuminated ion distribution across the user defined ion source exit radius with no energy spread and no beam spread. For stability diagram mapping investigations, mass spectral studies were performed for $^{40}Ar^+$ (*m*/*z* 40) with ion energy set at 5eV.

QMS-Hyperbolic was rebuilt as a console application and modified accordingly in order to utilise the HTCondor^{TM} [16] high throughput computing service available at the University of Liverpool. The service allows many independent jobs to be run concurrently on networked University PCs (which would otherwise be idle). This allows several (typically hundreds) of simulations to run concurrently, dramatically reducing the overall elapsed time as compared with operation on a single machine.

5.7.2 Transverse *B* Field Mapping Results

Effective Stability Diagram: Magnetic Field Applied along the x-axis, B_x

Figure 5.6 shows the numerically mapped tip region of stability zone 1 (1st quadrant) in a-q space for a static magnetic field applied transversely along the x co-ordinate axis of the mass filter. The figure was obtained using the mapping method described (section 5.6). The magnetic field vector applied transversely along the x-axis causes the stability region to become narrower for the y stability boundary $(\beta_y = 0)$ whilst the x stability boundary $(\beta_x = 1)$ remains unaffected. Increasing the x-magnetic field magnitude, for given operating conditions, leads to increased narrowing of the stable region as the y stability boundary decreases and this is shown up by a reduction in the low mass side of the simulated mass peak.

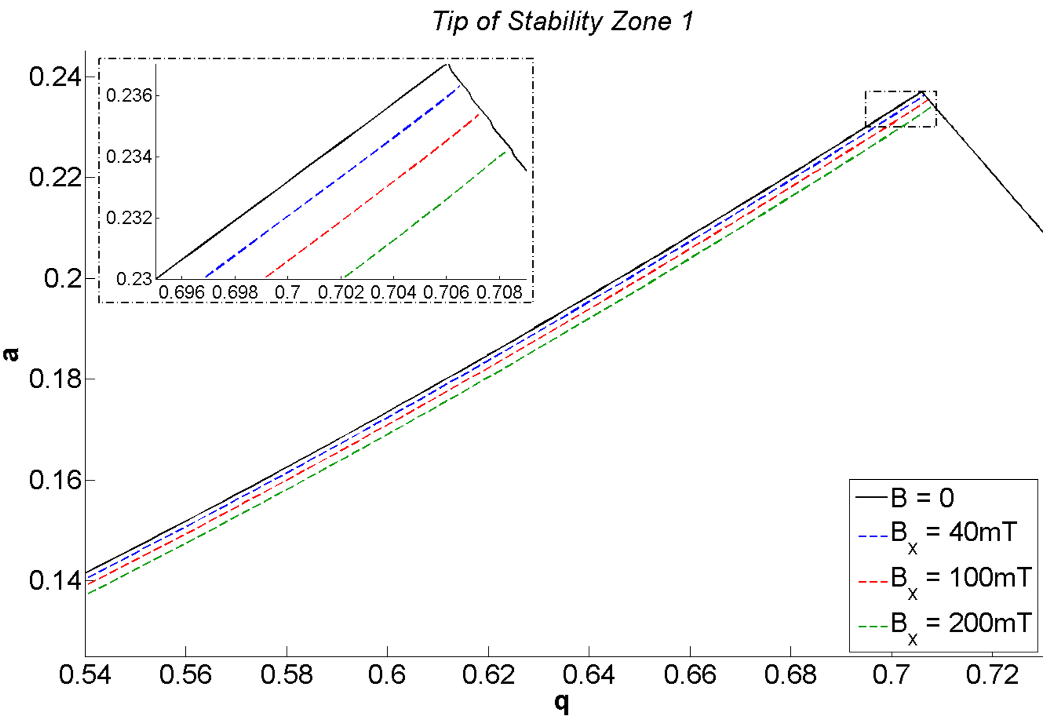

Figure 5.6: Mapping tip region of Stability Zone 1 (1st quadrant) for various values of transverse magnetic field (B_x)

Effective Stability Diagram: Magnetic Field Applied along the y-axis, B_y

Figure 5.7 shows the numerically mapped tip region of stability zone 1 (1st quadrant) in *a*-*q* space for a static magnetic field applied transversely along the *y* co-ordinate axis of the mass filter. The magnetic field vector applied transversely along the *y*-axis causes the stability region to become narrower as the *x* stability boundary decreases whilst the *y* stability boundary remains unaffected. Increasing the size of the *y*-magnetic field component, for constant operational conditions, leads to increased narrowing of the stable region as the *x* stability boundary decreases. This results in a reduction of the mass spectral peak width on the high mass side.

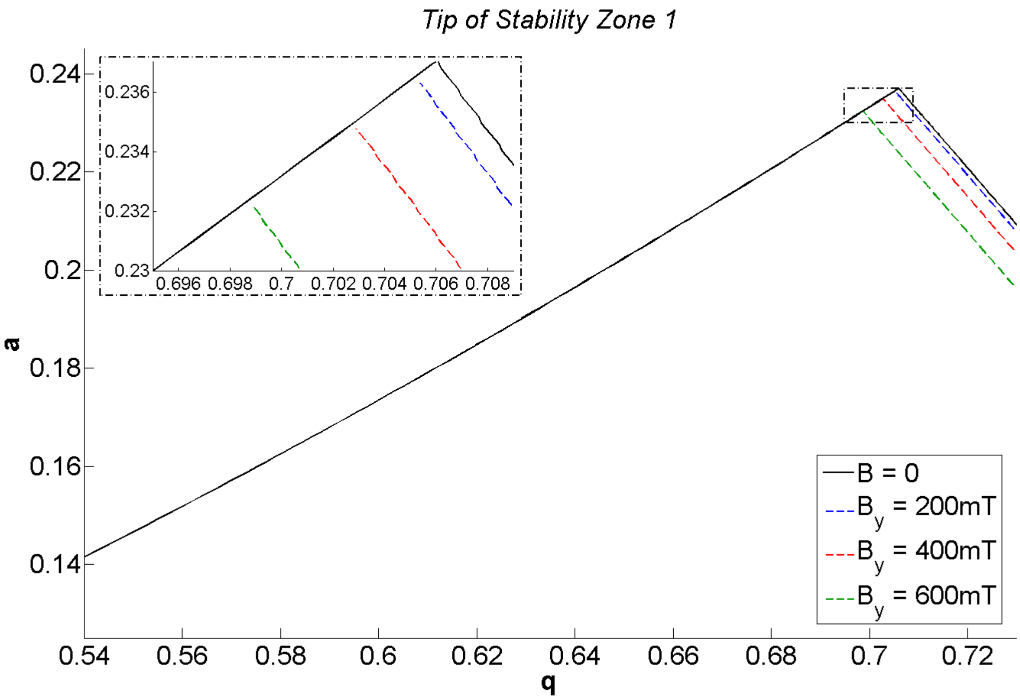

Figure 5.7: Mapping tip region of Stability Zone 1 (1st quadrant) for various values of transverse magnetic field (B_y)

The rate and the trend at which the effective stability region reduces in area as the magnetic field increases is different for the x and y oriented $\boldsymbol{B}$ field cases. As the magnetic field intensity along the y-axis is increased the x stability boundary tends to reduce at a rate proportional to $(B_y)^2$. For the x-axis oriented magnetic field vector, increasing the magnetic field results in increased instability but the trend is different and the rate of narrowing of the region, whilst initially large, tends to reduce with larger magnetic field values.

For a similar reduction in mass spectral peak width (i.e., improvement in resolution) a much larger magnetic field is required in y than in x. This asymmetry is similar to that observed when, for a conventional QMF (no magnetic field applied), the effect on spectra caused by electrode misalignment is more apparent for electrode displacement in y rather than x direction. From [17] it was shown that a small radial displacement of one of the y electrodes in a QMF results in severely reduced performance but for a similar small displacement of an *x* electrode there is little effect. Essentially these cases are not too dissimilar since moving an electrode along the *x*- or *y*- axes distorts the field mainly in that direction and when the magnetic field is applied the motion is distorted orthogonally so that B_x distorts in the same plane as E_y and B_y as E_x. Although the optimum electrode geometry is symmetrical about the *x*- and *y*-axes, the asymmetry in a conventional QMS is due to the mean potential applied to the electrodes affecting the ions. The mean potential, averaged over a number of cycles, is negative for the *y* electrodes and positive for the *x* electrodes due to the applied DC component (U). Thus for positively charged ions they will be, on average, repelled by the *x* electrodes and attracted to the *y* electrodes, resulting in an increased instability of the ions along the *y*-axis (chapter 3.1.1). Hence, for a similar reduction in mass spectral peak width to be observed, a relatively smaller ***B*** field magnitude is required in *x* than in *y*.

In [17] and [18] mention is made of the well-known, (but poorly documented property) that exchanging the connections of an underperforming QMS, due to y-electrode misalignment, can improve performance. The reason for this can be understood by considering the stability diagram quadrant of operation. Typically for a QMS the pair of electrodes in the *x*-*z* plane are supplied with a positive potential and the pair of electrodes in the *y*-*z* plane are supplied with a negative potential [19-21], thus operating in the first quadrant of the stability diagram (fig. 5.6). When these electrical connections are interchanged operation is in the fourth quadrant of the stability diagram. The Mathieu stability diagram is symmetrical about the *a*-axis for both the independent *x* and *y* dimensions (chapter 3.1.5), thus only the first and fourth quadrants in *a*-*q* space are considered.

Although for a conventional QMF (with no magnetic field applied) the stability zone area is symmetrical about the *q*-axis, the transition curves are not and, in the fourth quadrant, the *x*-stability boundary determines the low mass side and the *y*-stability boundary determines the high mass side of a mass spectral peak. Hence, the misalignment of a *y* electrode in the *y*-axis, when operated in the fourth quadrant, has little effect on the QMS performance as the ions will have an increased stability in the *y*-axis due to the reversal of the mean potential on the electrode pairs.

When a transverse magnetic field is applied to the body of a QMF the stability diagram area is no longer symmetrical about the *q*-axis. This is due to the transition curves not being symmetrical about the *q*-axis (as mentioned above). Furthermore, with the electrode potentials reversed, (thus operating in the fourth quadrant of the stability diagram) identical trends are observed but these occur for the transverse magnetic field applied in the alternative transverse direction. Thus, applying the magnetic field along the *y*-axis (B_y) in the fourth quadrant, causes peak width reduction on the low mass side of a mass peak and is noticeable for relatively small field magnitudes. Applying the magnetic field along the *x*-axis (B_x) in the fourth quadrant, causes peak width reduction on the high mass side of a mass peak and is noticeable for relatively larger field magnitudes.

5.7.3 Analytical Stability Diagram with Transverse *B* Field Applied to QMF

The analytical derivations for this case (transverse ***B*** field applied to a QMF) are given in section 5.3. The result is a non-homogeneous type Mathieu equation for the dimension orthogonal to the direction of the applied transverse ***B*** field. In each case the contribution of the stability parameter *a* is modified by the addition or subtraction of the combined magnetic field parameter (B_1 or B_2). These are given by equations 5.26 and 5.37 respectively (repeated here for convenience):

$$\frac{\partial^2 y}{\partial \xi^2} - \left((a - B_1^2) - 2q\cos\left(2(\xi - \xi_0)\right)\right) y = B_1 \left(B_1 y_0 + \left(\frac{dz}{d\xi}\right)_0 \right)$$

$$\frac{\partial^2 x}{\partial \xi^2} + \left((a + B_2^2) - 2q\cos\left(2(\xi - \xi_0)\right)\right) x = B_2 \left(B_2 x_0 - \left(\frac{dz}{d\xi}\right)_0 \right)$$

These equations indicate that there is an increased instability upon application of transverse magnetic field in *x* (figure 5.8) or *y* (figure 5.9) for a given operating scan line, regardless of the sign (direction) of the field ($\pm B_x$ or $\pm B_y$). In each case the stability boundary shifts according to the square of the combined magnetic field parameters (B_1^2 or B_2^2). The same trend is observed using the numerical stability mapping method (section 5.7.2).

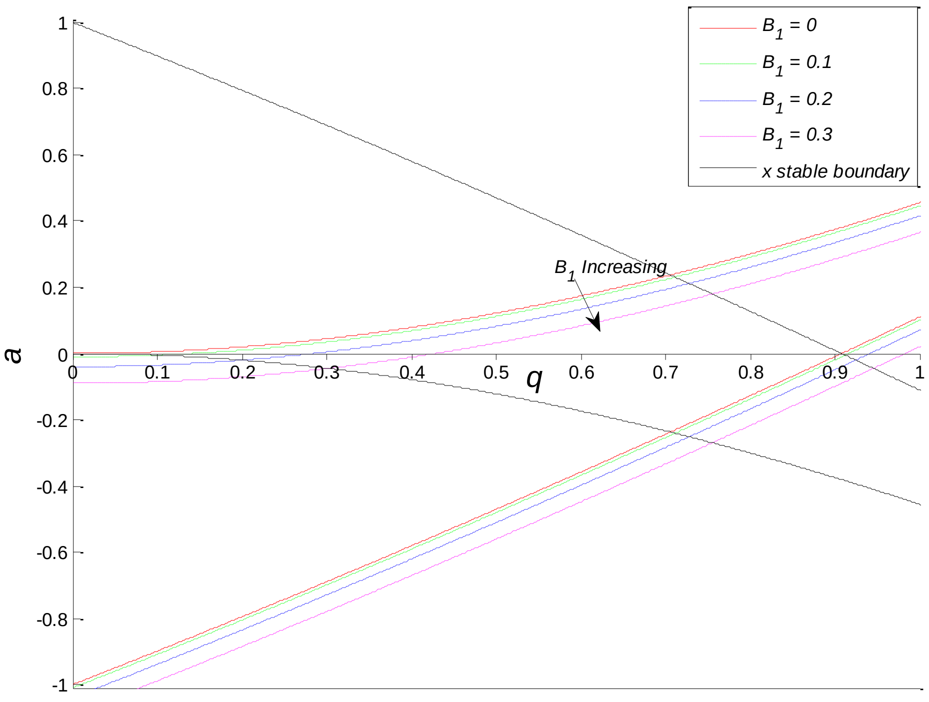

Figure 5.8: The *y*-stability boundary shifts as B_1 increases reducing the effective stability zone region in the 1st quadrant

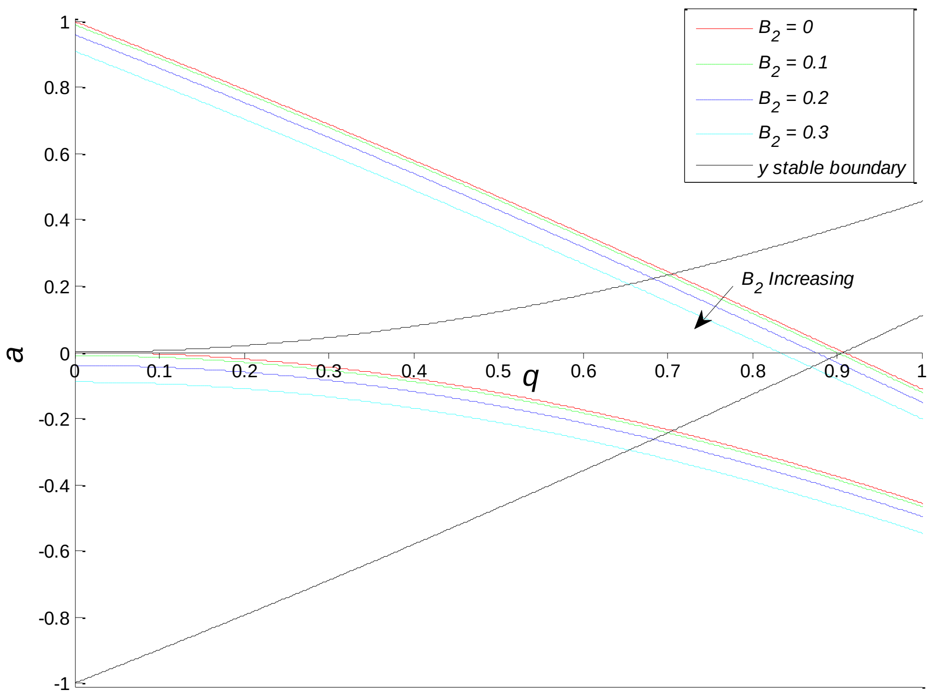

Figure 5.9: The *x*-stability boundary shifts as B_2 increases reducing the effective stability zone region in the 1st quadrant

5.7.4 Verifying Trends: Experimental and Simulated Mass Spectra

These findings are confirmed by experiment. Figure 5.10 shows experimental and simulated mass spectra for $^{28}N_2^+$ with and without a transverse magnetic field applied along the *x*- or *y*-axes. Figures 5.10(a) and 5.10(c) were obtained experimentally (as detailed in section 5.5) and figures 5.10(b) and 5.10(d) were obtained from QMS-Hyperbolic simulation software using input parameters to imitate the experimental set up as closely as possible.

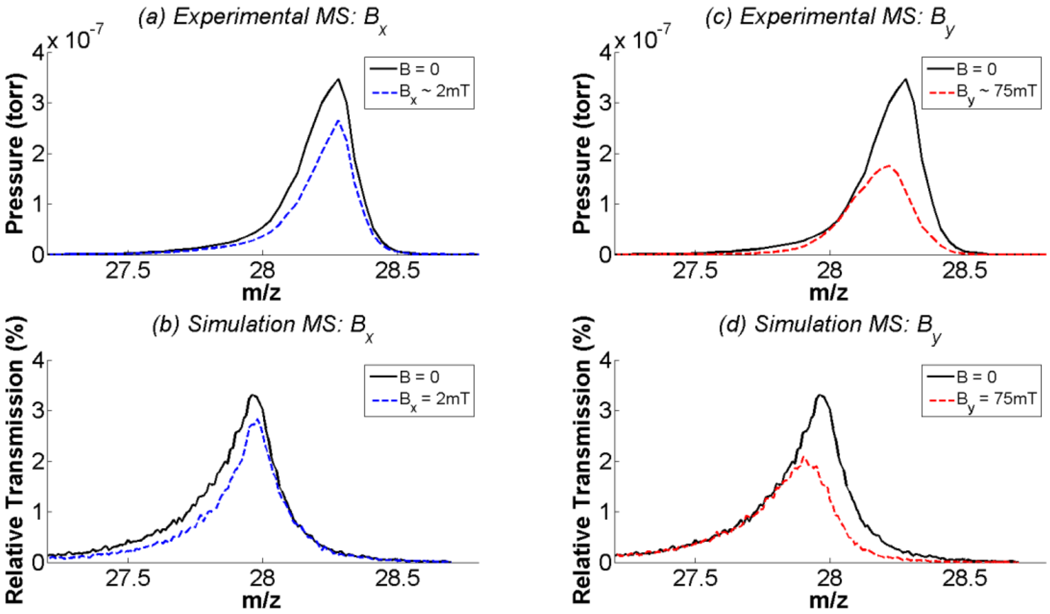

Figure 5.10: Experimental and Simulated Mass Spectra for $^{28}N_2^+$ with and without B_x field applied, (a) & (b) respectively; Experimental and Simulated Mass Spectra for $^{28}N_2^+$ with and without B_y field applied, (c) & (d) respectively

These experimental measurements demonstrate, for operation in the 1st quadrant, reduction on the low mass side of the mass spectral peak when a B_x field is applied (fig. 5.10(a)) and reduction on the high mass side of the spectrum when a B_y field is applied (fig. 5.10(c)). Both show good agreement with the numerical model (figures 5.10(b) and (d) respectively). In both instances it can be seen that reduction in peak width is accompanied by a reduction in transmission. The reduction in transmission for this experimental arrangement is more pronounced for B_y than B_x.

Discrepancies between simulation and experiment such as the peak shape are likely due to complex fringe fields (3-dimensional (3D) effects), particularly at the QMF entrance, which are not accounted for by the simulation software. The relative shift on the mass scale between experimental and simulated results is due to the different experimental scanning method used (which is dc offset), whereas the model uses the theoretical description of QMF devices and maintains constant resolution with the scan line passing through the origin of the stability diagram.

Figure 5.11 shows ion trajectories relating to specific ions of the simulated $^{28}N_2^+$ mass peaks from figure 5.10. The effect of the transverse magnetic field applied along each co-ordinate axis (B_x and B_y) is shown for a low *m*/*z* ion and a higher *m*/*z* ion on the mass scale that is transmitted when no magnetic field is applied.

For the lower *m*/*z* ion (fig. 5.11(a)-(d)) with a magnetic field applied along the *x*-axis, the *x*-*z* plane trajectory remains virtually unaltered. However, the *y*-*z* plane trajectory increases in amplitude causing the ion to be rejected due to the increased Lorentz Force, which is experienced by the ion in the *y*-*z* plane perpendicular to the magnetic field vector (fig. 5.11(d)). This does not strictly indicate that the ion has become unbounded but rather that its amplitude has exceeded the given threshold (r_0). Conversely for the higher mass ion (fig. 5.11(e)-(h)) with a magnetic field applied along the *y*-axis: the increase in ion amplitude in the *x*-*z* plane increases due to the Lorentz force in the *x* direction (fig. 5.11(g)) which at some stage will cause the ion to exceed the field radius limit. The trajectory in the *y*-*z* plane, which is parallel to the magnetic field vector, remains largely unaltered.

The slight shift between $\boldsymbol{B} = 0$ and B_x, B_y traces in figure 5.11 is due to the minor variation in the axial velocity (v_z). Although $E_z = 0$ for the ideal hyperbolic fields assumed by the model, the transverse magnetic field introduces an axial force (equation 5.15) and the subsequent axial velocity varies in accordance with the transverse velocity orthogonal to the magnetic field vector.

Considering the additional Lorentz force due to the static magnetic field from equation 5.1 (repeated here for convenience):

$$F = q(\boldsymbol{v} \times \boldsymbol{B})$$

The axial force (F_z) is given by:

$$F_z = q\left(v_x B_y - v_y B_x\right) \tag{5.42}$$

By introducing Newton's second law the axial velocity is obtained:

$$v_z = v_{z_0} + \frac{q}{m}\left(B_y \int v_x \, dt - B_x \int v_y \, dt\right) \tag{5.43}$$

Hence, the variation in v_z is insignificant, and the effect on the number of ion cycles is negligible; the initial velocity dominates since typically, $v_{z_0} \gg v_x, v_y$ (where v_{z_0} is the initial velocity).

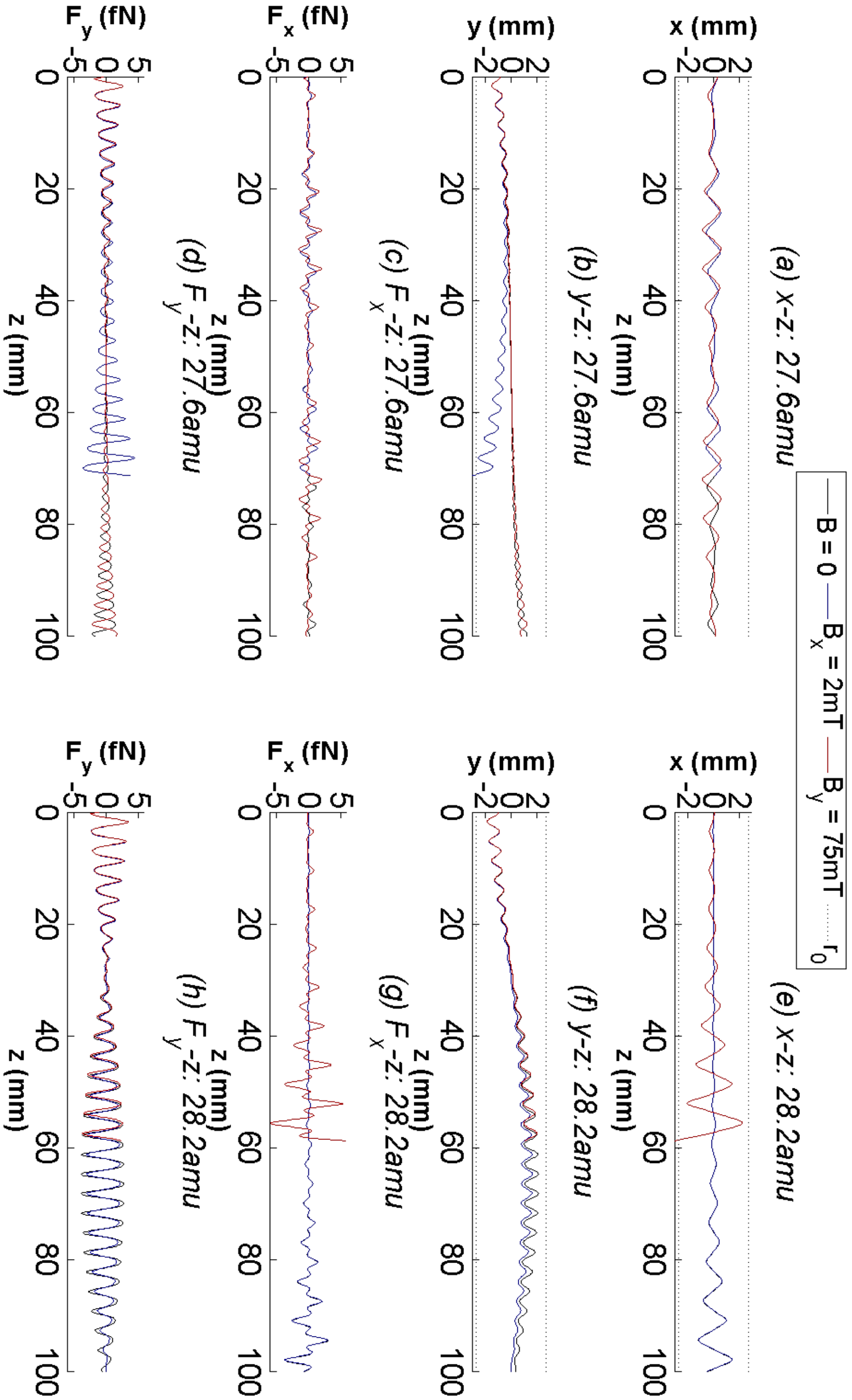

Figure 5.11: Simulated ion trajectories of a low mass ion (a-d) and high mass ion (e-h) on the mass scale from simulated $^{28}N_2^+$ spectra for B = 0, B_x = 2mT and B_y = 75mT. Note: top four figures (a), (b), (e) & (f) relate to ion displacement in space (x, y). Bottom four figures (c), (d), (g) & (h) relate to the force on the ion (x, y)

5.8 QMF Behaviour under the Influence of Transverse B_x Field, $B = (B_x, 0, 0)$

In this section further investigations are carried out to determine the behaviour of the QMF under the influence of a B_x field.

5.8.1 Experimental Results

Experimental results were carried out according to the general description given in section 5.5.

5.8.1.1 Ion Species: $^4He^+$

Figure 5.12(a) shows typical mass spectral peaks obtained experimentally for $^4He^+$ with and without a magnetic field. A relative increase in resolution is clearly observed upon application of a B_x field. The resolution improvement arises from a reduction in peak width with applied magnetic field and this occurs on the low-mass side of the peak. Figure 5.12(b) shows the resolution as a function of B_x field magnitude. The resolution increases by up to a factor of ~5 as B_x increases from 0 - 0.021T, and then resolution decreases as it is further increased from 0.021 - 0.025T. That is QMF resolution does not increase indefinitely with applied B_x. As B_x increases, the peak shape eventually degrades because of decrease in sensitivity (peak height). For a given operating scan line, as B_x is further increased the stability boundary shifts which leads to reduced peak width.

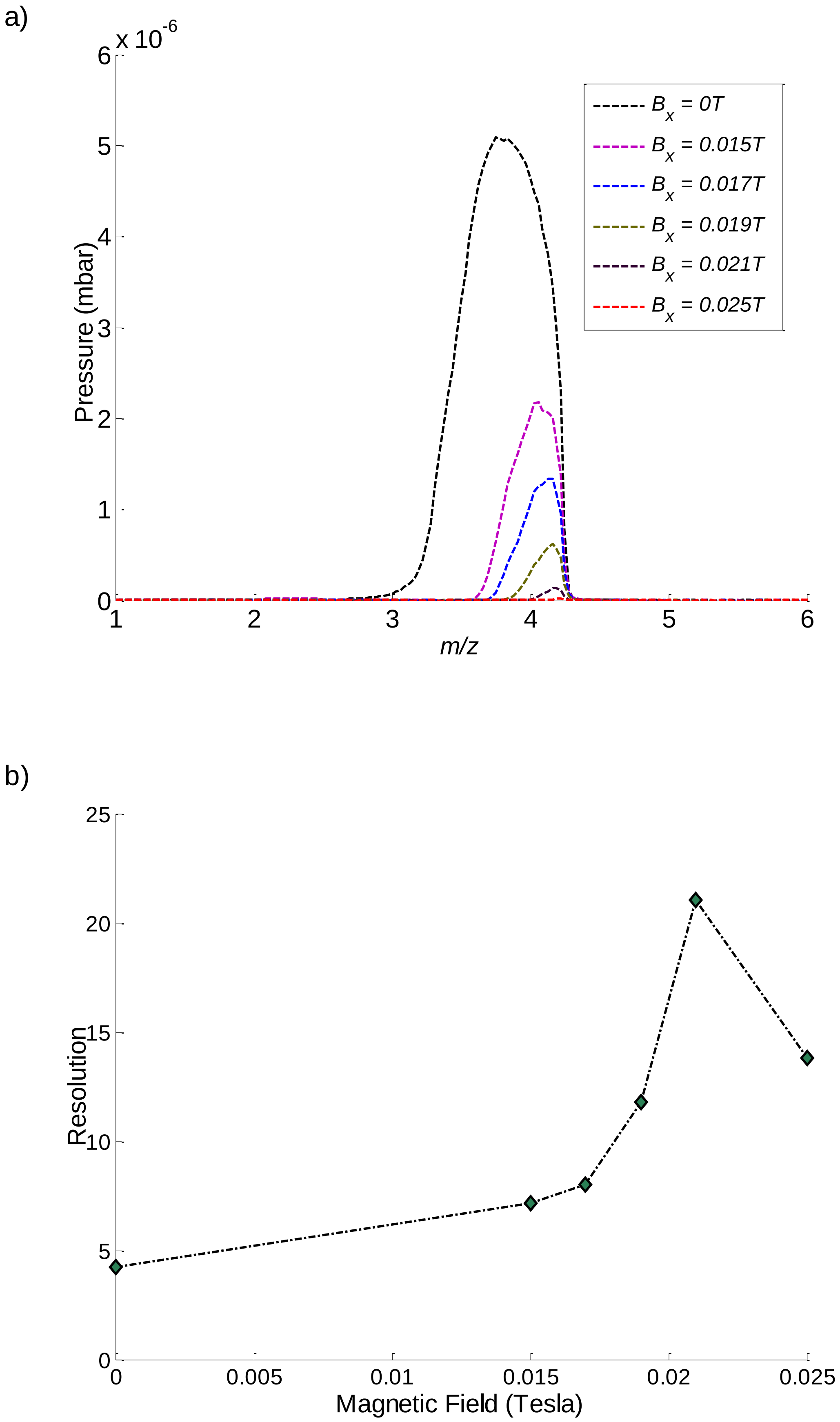

Figure 5.12: (a) Experimental mass peaks obtained for $^4He^+$ with and without B_x field applied; (b) Resolution as a function of B_x field magnitude for $^4He^+$

5.8.1.2 Ion Species: ^{40}Ar^{+}

Figure 5.13(a) shows typical mass peaks obtained experimentally for ^{40}Ar^{+} with and without magnetic field. From figure 5.13(a) the following observations are made:

(i) There is an improvement in resolution in all cases in which the magnetic field is applied compared with the conventional case $\boldsymbol{B} = 0$.

(ii) For the case $B_x = 0.015$T there is an increase in transmission as well as resolution. For larger values of magnetic field $B_x > 0.015$T transmission through the QMF decreases as magnetic field increases.

(iii) Resolution does not increase indefinitely as B_x increases because the peak height (sensitivity) decreases.

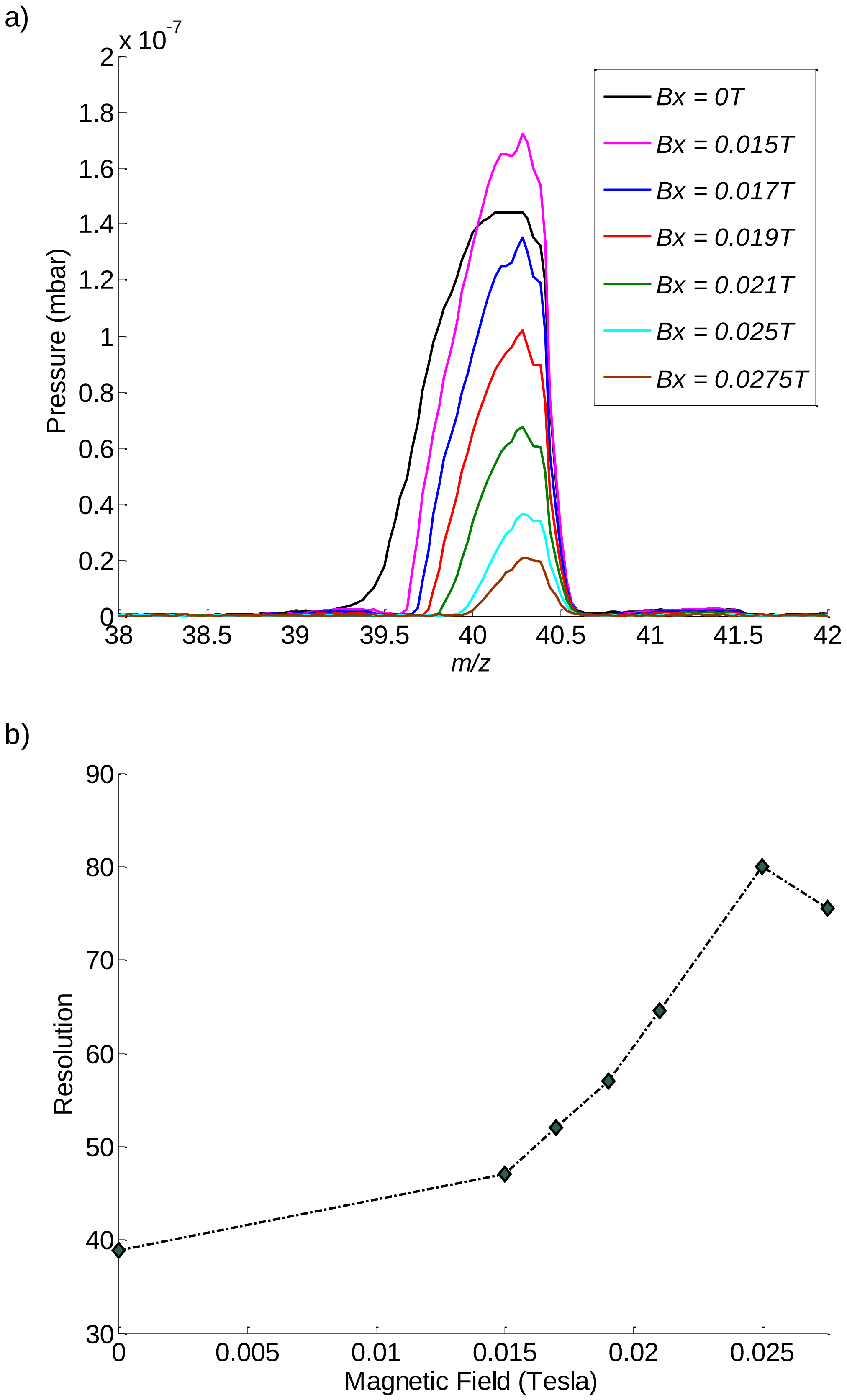

Figure 5.13: (a) Experimental mass peaks obtained for $^{40}Ar^{+}$ with and without B_x field applied; (b) Resolution as a function of B_x field magnitude for $^{40}Ar^{+}$

The increase in transmission for the case B_x = 0.015T (observation (ii)) could be due to leakage flux from the permanent magnet affecting the ion source. A small amount of leakage flux into the ion source could cause increased electron path lengths. This would lead to increased ionisation efficiency and hence a larger number of ions injected into the QMF for a given electron emission current. However, at larger magnetic field intensities (observation (ii)), transmission decreases (also related to observation (iii)). The following possible reasons are proposed:

1) Increased B_x magnitude leads to increased instability as the stability boundary shifts and more ions are rejected (section 5.7.2). This is because of the additional magnetic component of the Lorentz force which modifies ion motion inside the QMF.
2) At high magnetic field intensities magnetic flux penetration into the ion source causes more electrons to remain confined (or trapped) close to the ionisation region. The resulting negative space charge has the effect of impeding electrons from reaching the ionization chamber. The ion source geometry and the magnetic field direction can contribute significantly to the onset of this effect to the extent that it causes a reduction of ion injection into the QMF.

   Reduction in instrument sensitivity by as much as 70% has been reported for experiments investigating the effect of the Earth’s magnetic field (~25-65μT) on the performance of an electron ionisation source coupled to a mobile MS system [22].

3) Larger magnetic fields may affect the detection of ions because fringe fields at the exit of the QMF (due to the magnetic field) may cause some ions to be lost resulting in reduced sensitivity.

Figure 5.13(b) shows the behaviour of the resolution as a function of B_x field for the mass spectral peaks in fig. 5.13(a). The resolution (R) increases by more than a factor of ~2 compared to $\boldsymbol{B} = 0$, from $R \cong 39$ at to $R \cong 100$ at $B_x = 0.025$T. Further increase in B_x magnitude from 0.025 - 0.0275T leads to reduced resolution as peak shape degrades.

5.8.1.3 Ion Species: $^{(124\text{-}136)}Xe^+$ (various *m/z* isotopes)

Figure 5.14(a) shows a typical mass spectrum obtained experimentally for Xe^+ with $\boldsymbol{B} = 0$T (conventional QMS operation), whereas figure 5.14(b) shows a typical mass spectrum obtained experimentally for Xe^+ with $B_x = 0.045$T. Xenon has nine naturally occurring stable isotopes (table 5.1). As seen from figure 5.14(a) in the absence of magnetic field the isotopes of xenon between 128 and 132Da are not completely separable from each other for the given set up. The application of magnetic field (fig. 5.14(b)) ensures that the minimum resolution required to distinguish the isotopes has been achieved at the expense of reduced sensitivity. This experimental result clearly illustrates the relative resolution enhancement provided by application of a B_x field.

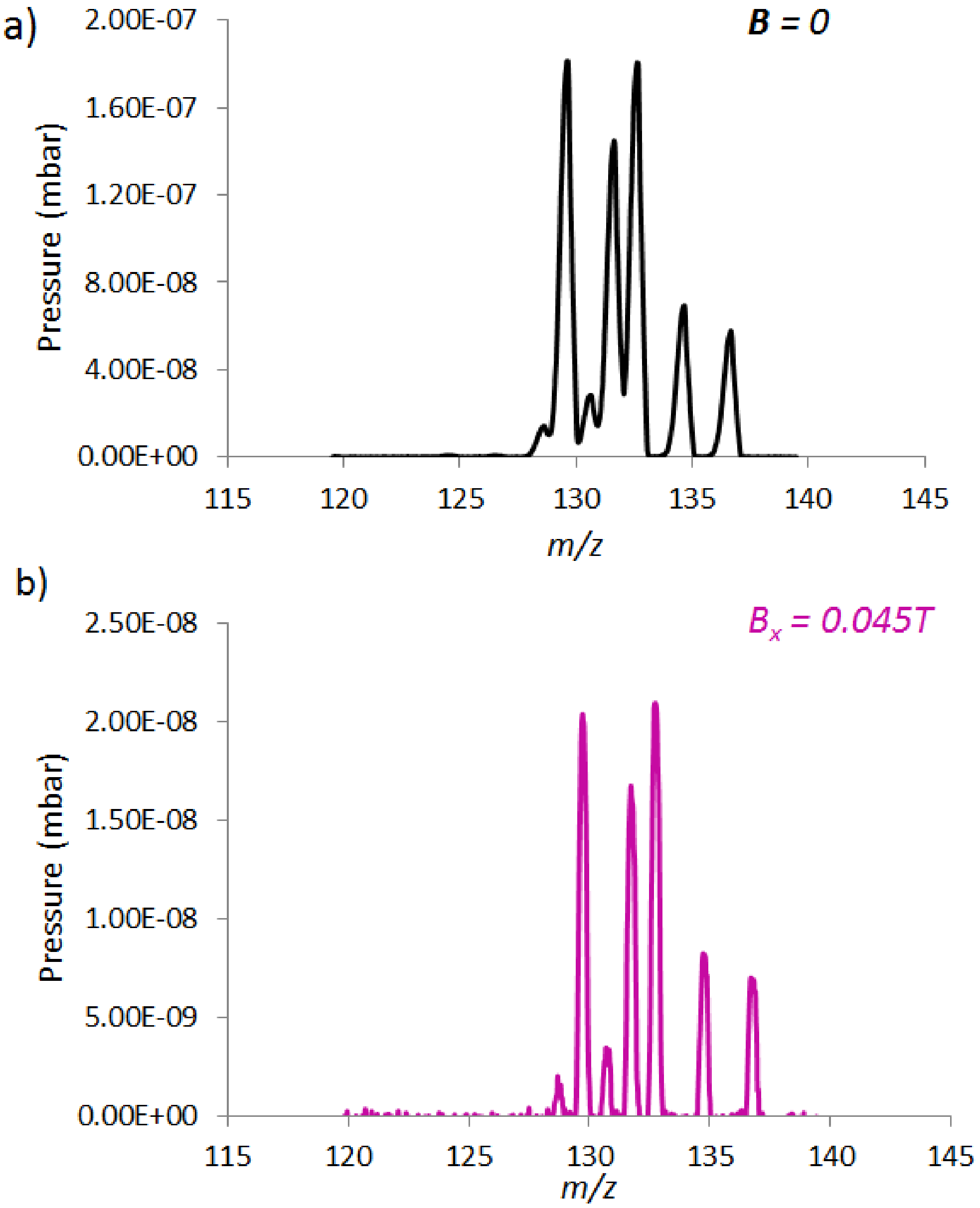

Figure 5.14: Mass peak for $^{132}Xe^+$ (a) B = 0T; (b) B_x = 0.045T

Isotope	Natural Abundance (%)
^{124}Xe	0.09
^{126}Xe	0.09
^{128}Xe	1.92
^{129}Xe	26.44
^{130}Xe	4.08
^{131}Xe	21.18
^{132}Xe	26.89
^{134}Xe	10.44
^{136}Xe	8.87

Table 5.1: Naturally occurring stable isotopes of xenon

5.8.1.4 Effect of Ion Energy on QMF Behaviour with B_x Field Applied

Figure 5.15 shows the effect of ion energy on resolution in the presence of a magnetic field. With a transverse magnetic field applied, the effect of ion energy on resolution is different to that normally observed for a conventional QMS (with no ***B*** field applied). For the conventional case, resolution increases with decreasing ion energy because the number of rf cycles experienced by an ion increases (equation 3.43). In fig. 5.15, the resolution increases with increase in ion energy from 4-7eV and then decreases. This effect is attributed to the increased Lorentz force (experienced by higher energy ions) in the transverse direction due to the magnetic field. The minimum ion energy was set at 4eV to get a measurable signal and increased in steps of 1eV. Figure 5.15(a) shows measured spectra for ^{40}Ar^{+} at different ion energies with a magnetic field of B_x = 0.02T; whereas, figure 5.15(b) shows the dependence of resolution on ion energy with an applied magnetic field.

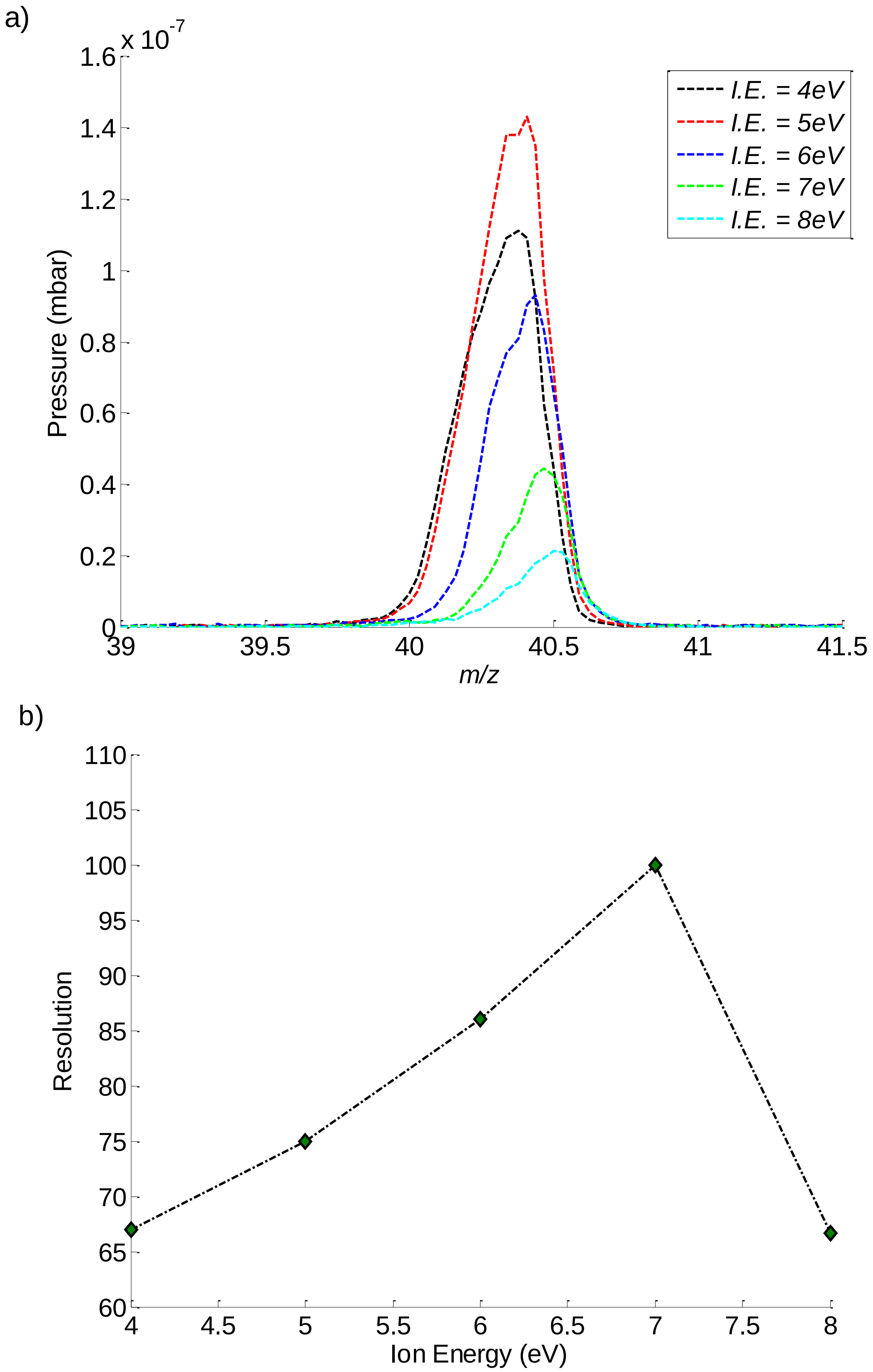

Figure 5.15: (a) Experimental mass peaks for $^{40}Ar^{+}$ at different ion energies with applied magnetic field of B_x = 0.02 T; (b) Dependence of resolution on ion energy for the experimental results given in (a)

5.8.2 Simulation Results

There are various practical factors which limit the investigations which can be carried out experimentally. Therefore, a series of simulation studies have been carried out to investigate the behaviour of a QMF under the influence of a transverse B_x field.

Certain standard parameters are chosen based on typical values used for a conventional QMF. Other parameters of interest are then varied accordingly. The simulation software used was QMS-Hyperbolic. Table 5.2 shows the standard parameters chosen. All simulations investigate m/z 40 ions and simulate 1×10^5 ions every 0.01Da across the defined range. The total number of ion trajectories simulated was of the order of ~9 $\times 10^7$ for each simulation. The same set of random initials values were used for certain simulation tests to allow direct comparison.

Parameter	**Value**
Length	100mm
Inscribed Radius	2.6mm
Source Radius	0.5mm
Frequency	4MHz
Nominal Ion Energy	5eV

Table 5.2: Standard simulation parameters

5.8.2.1 Performance Enhancement

Whilst it is clear that, for a given experimental arrangement, increasing the magnetic field will yield an increased resolution due to the narrowing of the effective stability boundary the question arises as to whether the same benefit would be achieved by adjusting the U/V ratio for a conventional QMS (no magnetic field applied)? However, this is not the case for a magnetic field oriented along the *x*-axis (1st quadrant operation), since applying a transverse magnetic field can yield a ~75% increase in resolution for the same relative transmission of ~5%. This is illustrated in figure 5.16 where the maximum relative transmission is plotted against the resolution for various B_x magnitudes.

Fig. 5.16 clearly illustrates the performance benefit for the QMF with a B_x field applied. For the case of no magnetic field applied ($\boldsymbol{B} = 0$), at the performance limit, the curve begins to move back on itself as resolution and transmission both decrease; this effect is associated with peak degradation. At the limit of the instrument performance, with a B_x field applied, the resolution continues past the maximum for $\boldsymbol{B} = 0$ until transmission drops off as the new stability limit is approached. At the ultimate performance limit a resolution enhancement of ~2x (greater) is achieved compared to the conventional case ($\boldsymbol{B} = 0$) for the conditions simulated. The magnitude of the field required to obtain this performance enhancement is relatively small (<20mT) and not problematic to achieve.

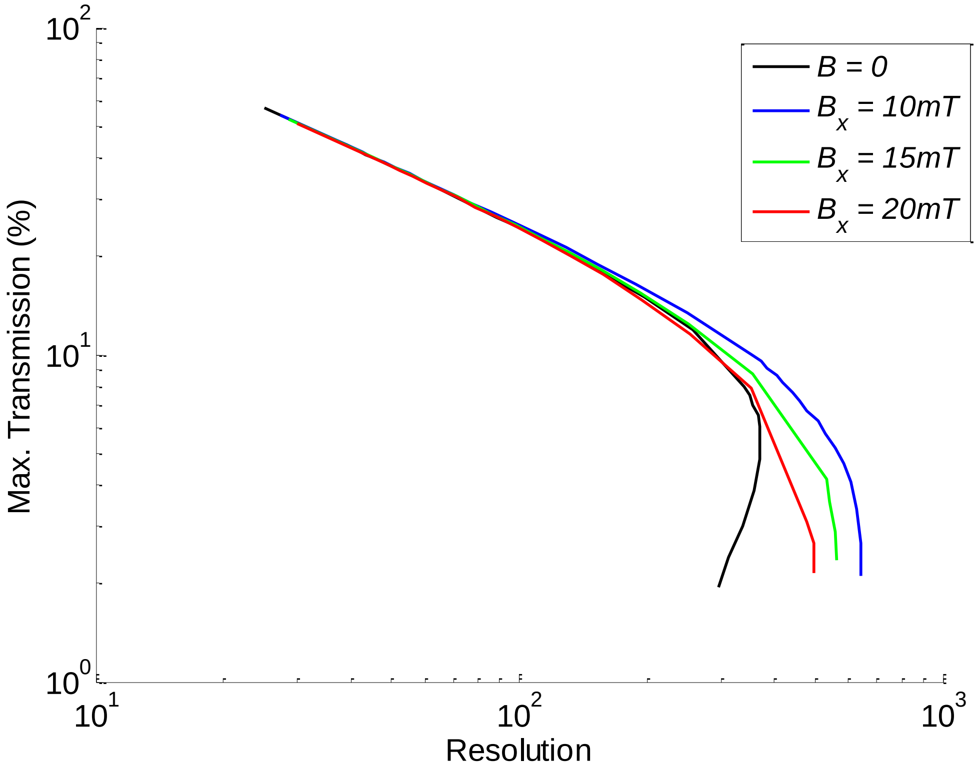

Figure 5.16: Simulated Resolution-Maximum Transmission curve for a typical QMF with $B = 0$ and various B_x magnitudes

5.8.2.2 Frequency Effect

For a conventional QMF (with $\boldsymbol{B} = 0$) the number of cycles an ion will spend in the QMF is proportional to the frequency of the alternating potential (equation 3.43). As the number of cycles increases the resolution increases (equation 3.42). Equation 3.43 is repeated here for convenience:

$$N = fl\sqrt{\frac{m}{2E_z}}$$

In order to understand the effect frequency has when a B_x field is applied it is necessary to ensure the number of field cycles remains constant. This is achieved by compensating the length of the QMF as the frequency is varied (table 5.3). The number of rf cycles for the standard simulation parameters (table 5.2) is ~81.4. This remains approximately constant even with a transverse ***B*** field applied (section 5.7.4).

Frequency (MHz)	**Length (mm)**
1	400
2	200
3	133.333
4	100
5	80
6	66.667
7	57.143
8	50

Table 5.3: Compensated length for each frequency

For the conventional case ($\boldsymbol{B} = 0$), using length compensation, the mass spectra obtained were identical for each frequency. The mass spectra for a particular value of B_x = 5mT at each frequency are shown in figure 5.17. As frequency reduces the resolution increases as the peak width reduces due to increased instability on the low mass side of the peak. The resolution and maximum percentage transmission for this case are shown in figure 5.18. In each figure, the conventional case ($\boldsymbol{B} = 0$) is shown for comparison.

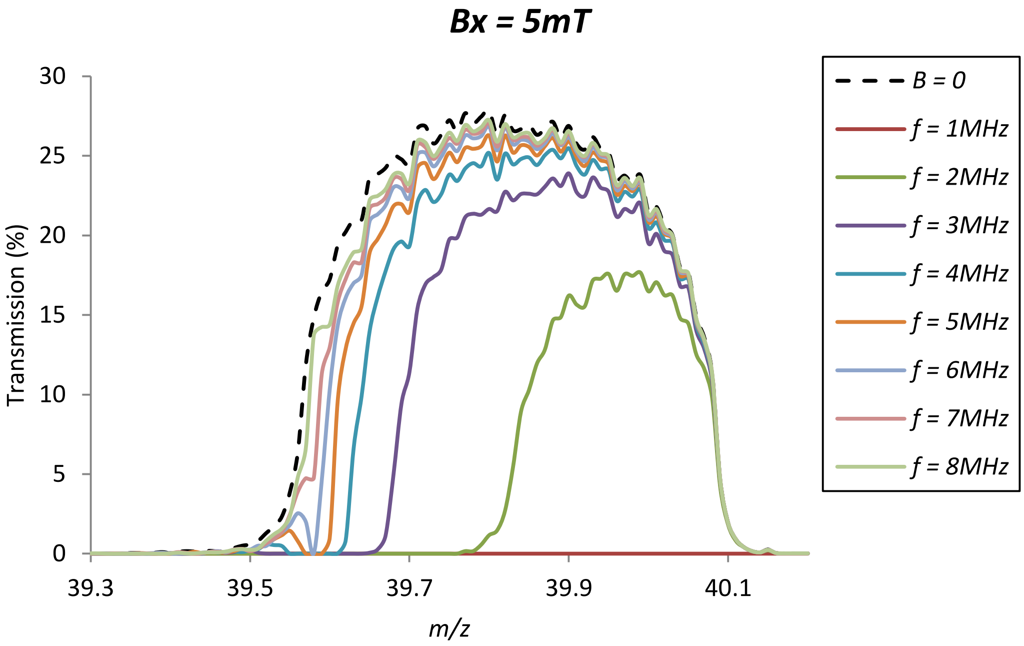

Figure 5.17: Frequency effect on mass spectral peaks for $^{40}Ar^+$ with B_x = 5mT. The case with $B = 0$ is also shown

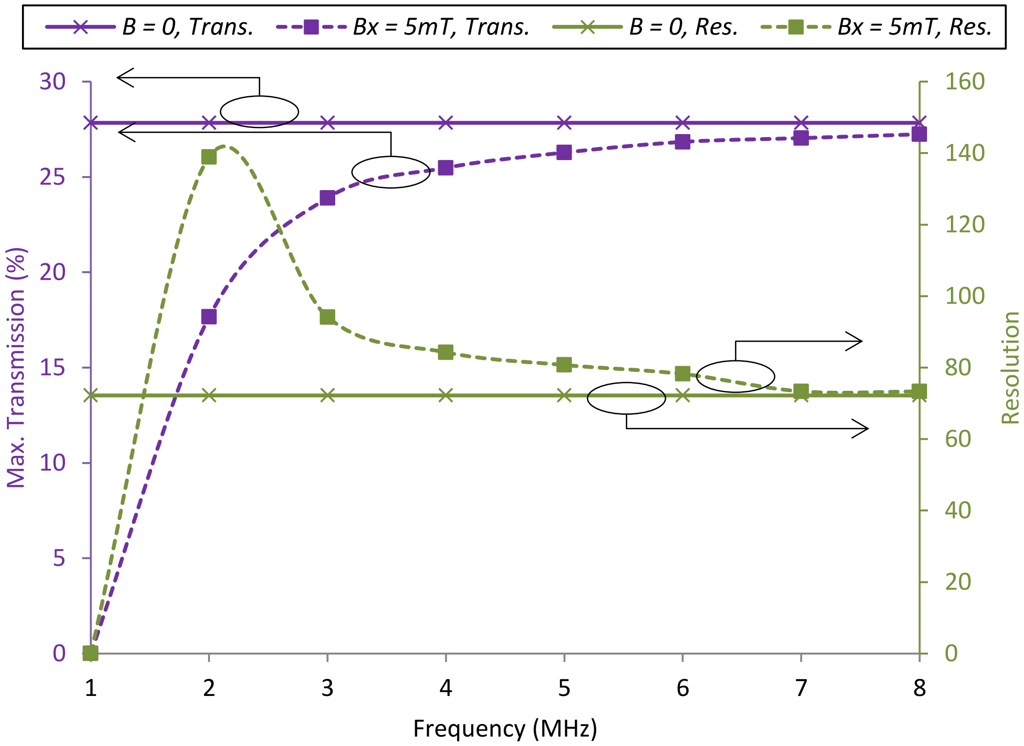

Figure 5.18: Plot of Maximum Peak Transmission and Resolution against Frequency for two cases: $B = 0$ and B_x = 5mT

Figures 5.19 and 5.20 show resolution and maximum transmission plotted against frequency for a variety of B_x magnitudes. For any particular value of B_x, as frequency increases the resolution and transmission tend towards the same value obtained for the conventional case. This is to be expected because as the frequency increases the magnitude of the combined magnetic field parameter in equation 5.26 tends to zero ($B_1 \rightarrow 0, since\ B_1 = \frac{2eB_x}{m\omega}$). As the combined magnetic field parameter tends to zero, the Mathieu equation approximates the conventional homogeneous case. Furthermore, for the conditions simulated, there is a trade-off between resolution and transmission dependent on frequency. The choice of operating frequency is important for a particular value of B_x. For example, in figures 5.19 and 5.20 for B_x = 10mT and frequency = 2MHz, the resolution increased by ~345% (from ~72 to ~322) whilst maximum percentage transmission dropped by ~90% (from ~27% to ~3%).

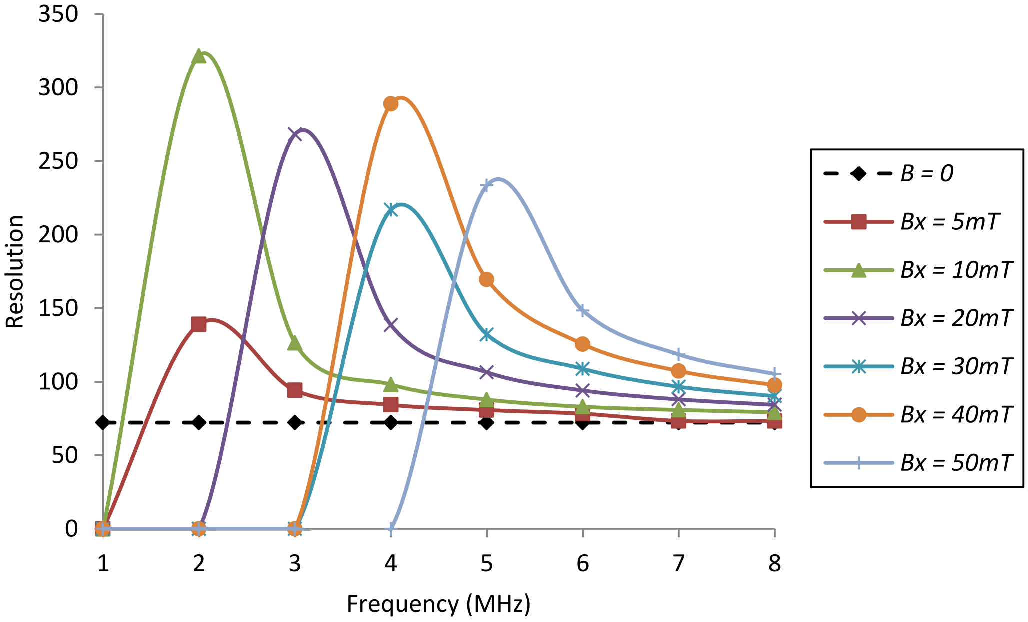

Figure 5.19: Resolution versus Frequency for a variety of B_x field magnitudes and B = 0

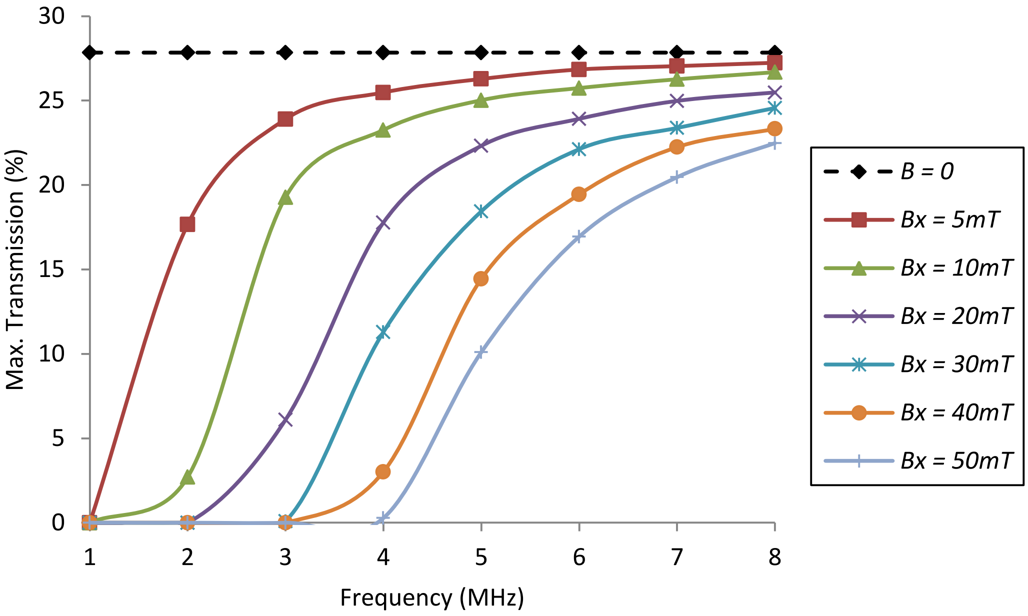

Figure 5.20: Maximum peak transmission versus Frequency for a variety of B_x field magnitudes and B = 0

5.8.2.3 Ion Energy Effect

The same method of length compensation to maintain an approximately constant number of rf cycles is used again for investigating the effect of varying the nominal ion energy (I.E.) in the presence of a B_x field (table 5.4). The energy and angular spread of the initial ion beam are assumed to be zero for each case.

Ion Energy (eV)	Length (mm)
1	44.721
2	63.246
3	77.460
4	89.443
5	100
6	109.545
7	118.322
8	126.491

Table 5.4: Compensated length for each ion energy

For the conventional case ($\boldsymbol{B}$ = 0), using length compensation, the mass spectra obtained were approximately identical for each ion energy. The negligible differences were due to the different random initial values generated when creating each ion file according to the specified nominal ion energy. The mass spectra for a particular value of B_x = 40mT at each ion energy are shown in figure 5.21. The resolution and maximum percentage transmission for this case are shown in figure 5.22. In each figure, the conventional case (***B*** = 0) is shown for comparison.

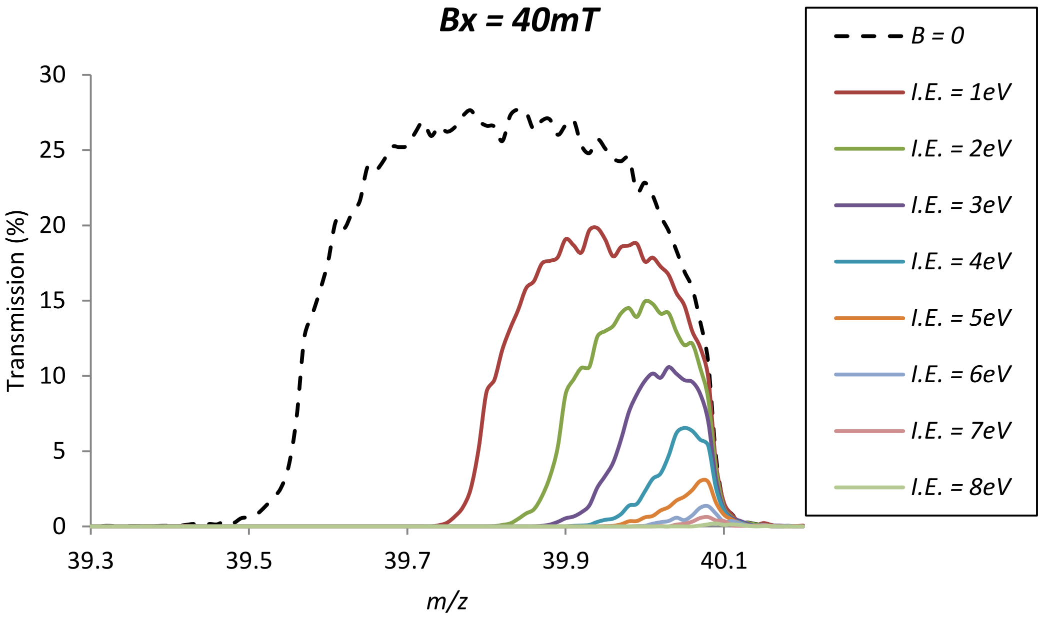

Figure 5.21: Mass spectra of $^{40}Ar^+$ for various values of ion energy with B_x = 40mT and B = 0 shown for comparison

The trend is similar to that observed experimentally (fig. 5.15). For a given static B_x field, the resolution increases with ion energy and then decreases as transmission falls and peak degradation occurs (fig. 5.22).

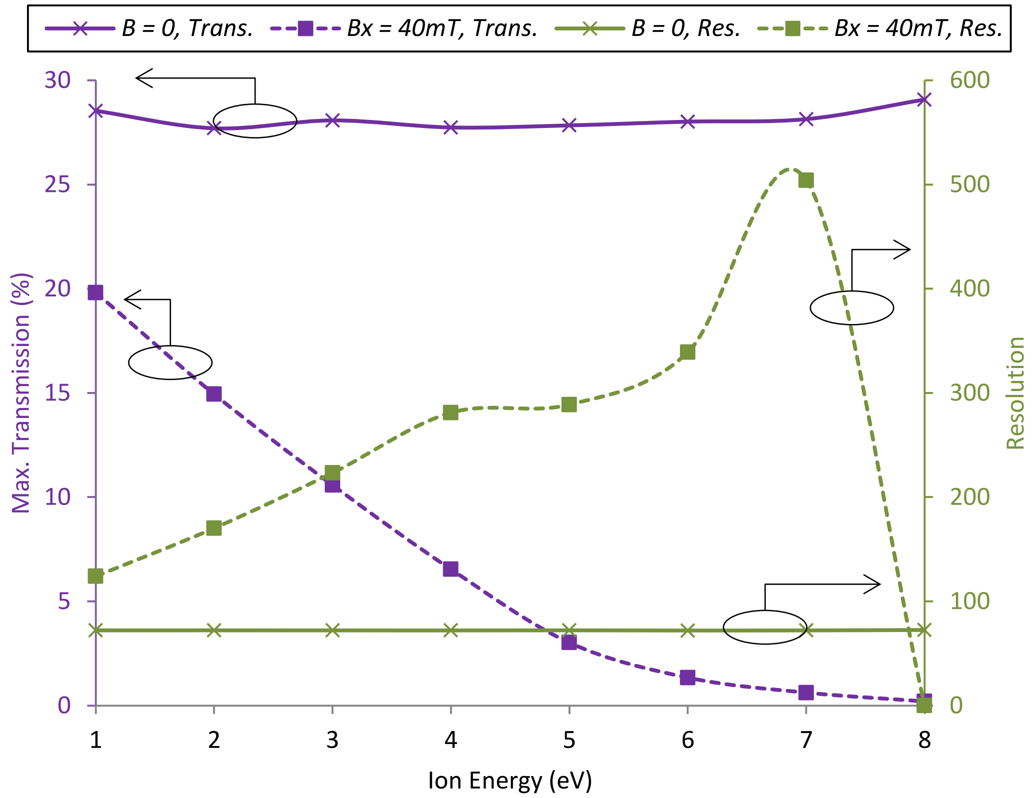

Figure 5.22: Maximum Peak Transmission and Resolution versus Ion Energy for two cases, *B* = 0 and B_x = 40mT

Figures 5.22 and 5.23 show resolution and maximum transmission plotted against ion energy for a variety of B_x magnitudes. For the conditions simulated, there is a trade-off between resolution and transmission dependent on ion energy. From figure 5.23, it is observed that as ion energy increases, for a particular value of B_x, ion transmission reduces. For larger magnitudes of B_x, ion transmission eventually ceases as the ion energy is increased.

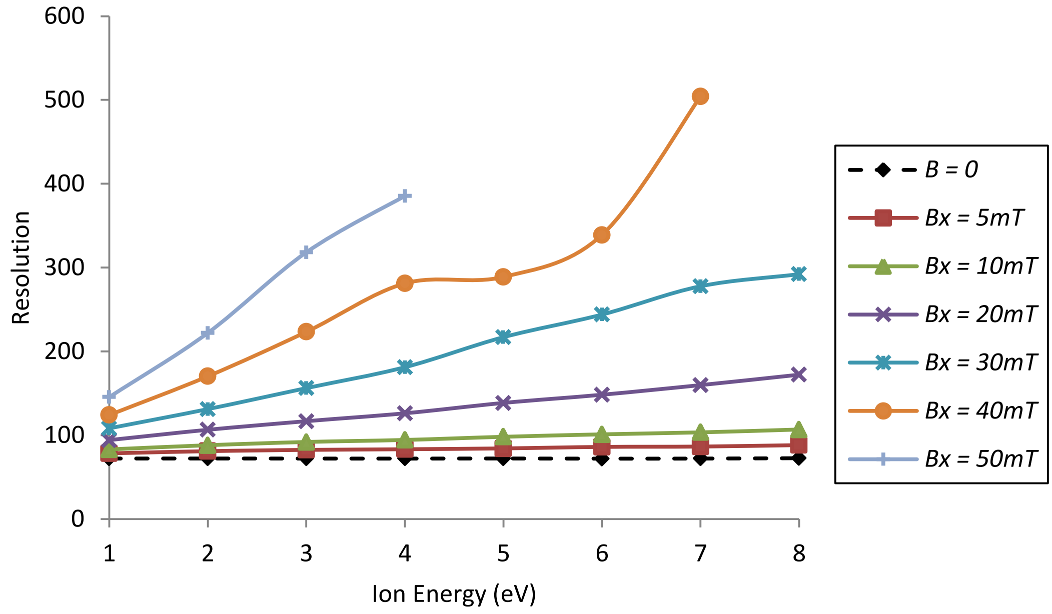

Figure 5.23: Resolution versus Ion Energy for a variety of B_x field magnitudes and B = 0

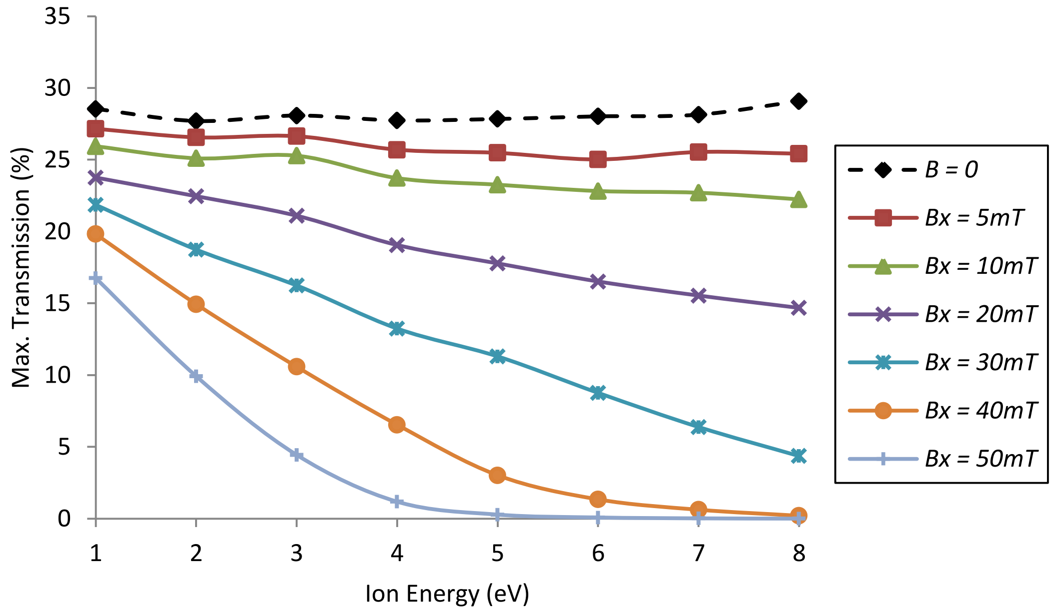

Figure 5.24: Maximum Peak Transmission versus Ion Energy for a variety of B_x magnitudes and B = 0

This effect can be examined further with the aid of plotting ion trajectories in the presence of a B_x field at different ion energies. Figures 5.25 and 5.26 show trajectories of ions transmitted with and without magnetic field applied, at ion energies of 2 and 5eV respectively. The corresponding traces shown in the figures are for the same ion injected into the QMF at the same point in time (rf phase) and space and at the same point on the mass scale (m = 39.80Da). In both figures the upper trace (a) is for the *x*-*z* plane and the lower trace (b) is for the *y*-*z* plane.

(a) x-z; Ion Energy = 2eV

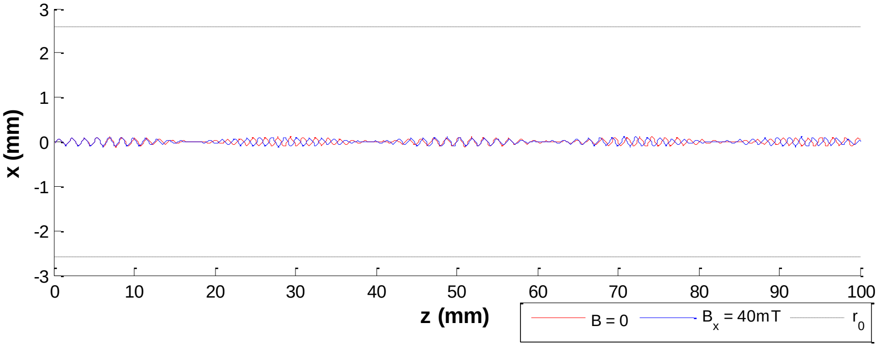

(b) y-z; Ion Energy = 2eV

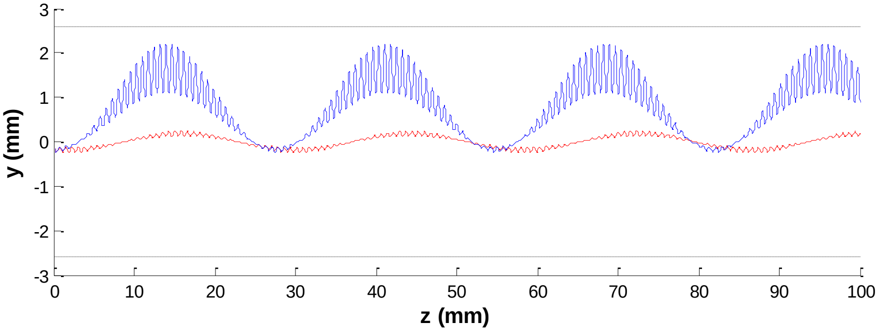

Figure 5.25: Ion trajectories for *m*/*z* 39.8 with Ion Energy = 2eV for two cases: *B* = 0 and B_x = 40mT; (a) *x*-*z* plane trajectory; (b) *y*-*z* plane trajectory

For the ion motion shown in figures 5.25 and 5.26 the ion originates with entrance co-ordinates $x = -6.26 \times 10^{-5} m$ and $y = -1.17 \times 10^{-4} m$ with an initial axial velocity of $3.10 \times 10^{3} m/s \left(= \sqrt{\frac{2 \times I.E.}{m}}\right)$. It can be seen from figure 5.25 that in the presence of a B_x field at lower ion energy (2eV) ion motion in the *y* direction is affected; however, the increase in amplitude of ion trajectory in the *y* direction is not sufficient for the ion to be rejected by colliding with the electrodes. In figure 5.26 the ion motion originates at the same position (as in fig. 5.25) and conditions except that the initial velocity is $4.91 \times 10^{3} m/s$ due to the ion energy being set at 5eV. It is observed that increase in ion energy (5eV) has a significant impact on behaviour of ion trajectories in the *y*-*z* plane in the presence of a B_x field. The amplitude of the ion trajectory in the *y* direction increases so far that the ion is lost by collision with electrodes (i.e., field radius is exceeded). It can be concluded that for a QMF with magnetic field applied in the *x* direction, the effect of the magnetic field on resolution enhancement is greater at higher ion energies because of the increased Lorentz force.

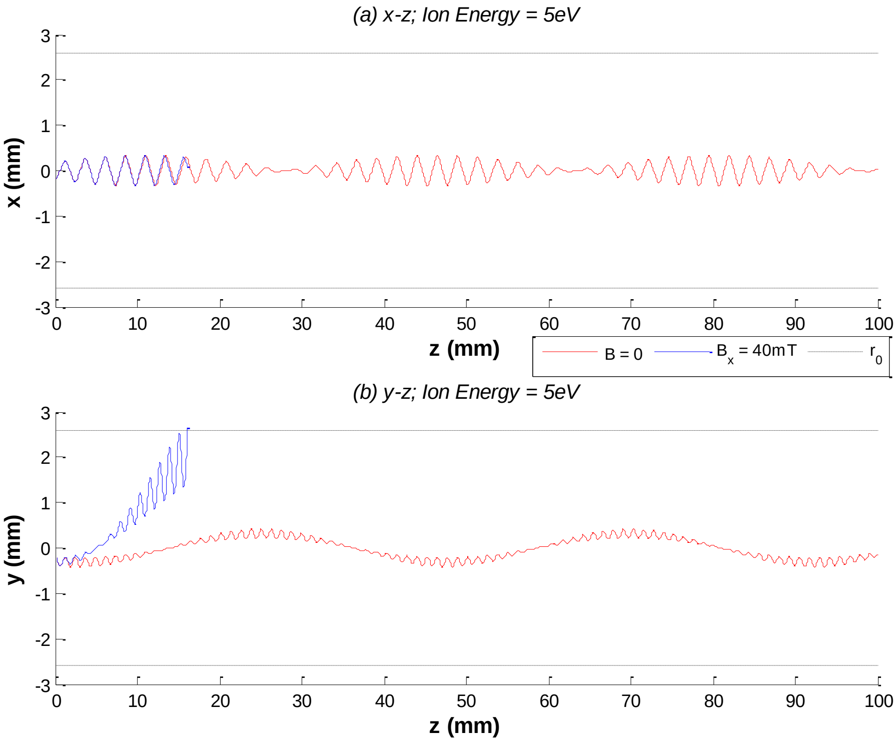

Figure 5.26: Ion trajectories for *m*/*z* 39.8 with Ion Energy = 5eV for two cases: *B* = 0 and B_x = 40mT; (a) *x*-*z* plane trajectory; (b) *y*-*z* plane trajectory

5.8.3 Performance with Circular Cross-Section Electrodes

Hyperbolic electrodes produce an optimal quadrupole field. This can be approximated by using circular electrodes with a specific electrode radius-to-inscribed QMF radius ratio ($^{r}/_{r_0}$). The circular cross-section geometry is easier to manufacture and provides a good approximation to the ideal hyperbolic case provided $^{r}/_{r_0}$ is chosen correctly (chapter 2.2.2.1).

5.8.3.1 Simulation Model

Hitherto modelling of the magnetically enhanced QMF has been for the ideal case with hyperbolic electrodes (using QMS-Hyperbolic). However it is well known that many important effects are observed for a QMF with circular cross-section electrodes which are widely used. Therefore QMS-2D, which allows simulation of any electrode geometry (chapter 3.2.3), was adapted to include the effect of a magnetic field applied. The software amendment with ***B*** field applied was verified by comparing the output with QMS-Hyperbolic. A hyperbolic field file was generated for QMS-2D and the same input parameters were chosen for each. The outputs were compared for a range of input parameters with and without ***B*** field applied and showed excellent agreement (figure 5.27).

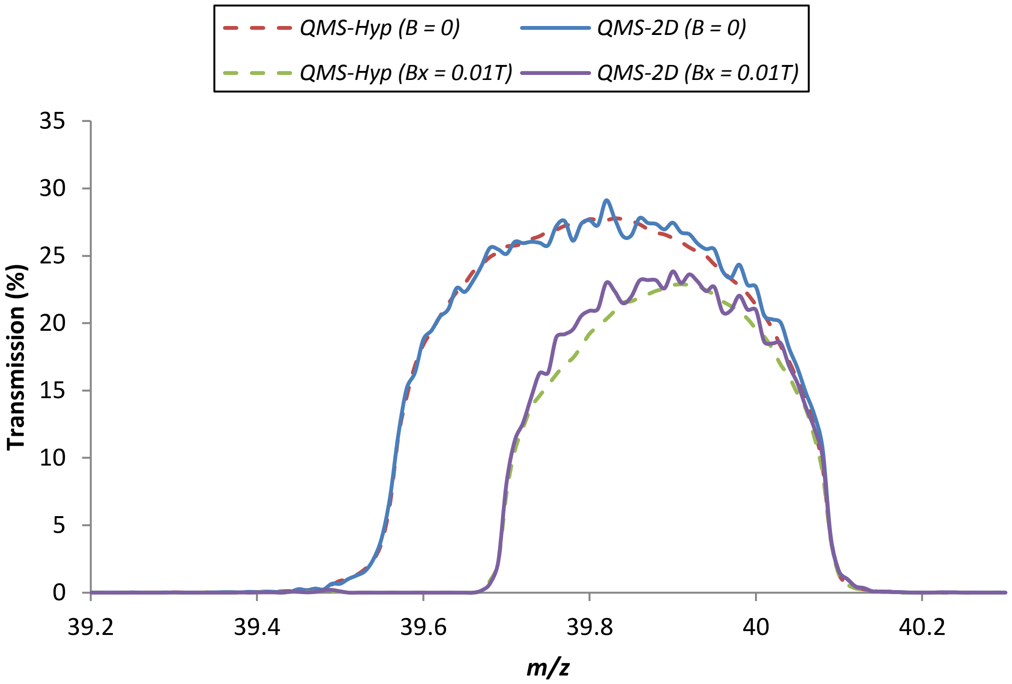

Figure 5.27: Comparison of QMS-2D and QMS-Hyperbolic with and without a B_x field applied

5.8.3.2 Circular vs. Hyperbolic Electrodes (*B* = 0)

Circular electrodes are more cost effective than hyperbolic, however they suffer from reduced performance due to, increased peak width (reduced resolution), lower transmission (reduced sensitivity), and a long low-mass tail [23]. The ideal $^{r}/_{r_0}$ for circular electrodes is ~1.127 [17]. Performance degradation factors typically observed with circular electrodes are illustrated in figure 5.28.

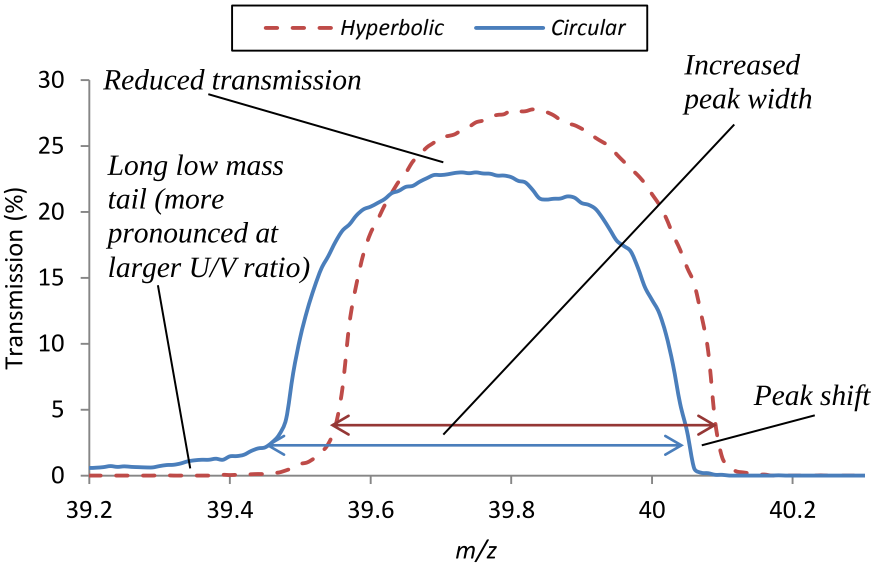

Figure 5.28: Performance degradation factors when using circular electrodes versus hyperbolic

5.8.3.3 QMF Performance with Circular Electrodes and B_x Field Applied

Applying a B_x field reduces the peak width by rejecting ions on the low mass side of the peak. Figure 5.29 shows the long low mass tail with circular electrodes ($^{r}/_{r_0} = 1.127$) is removed when applying a B_x field to the QMF.

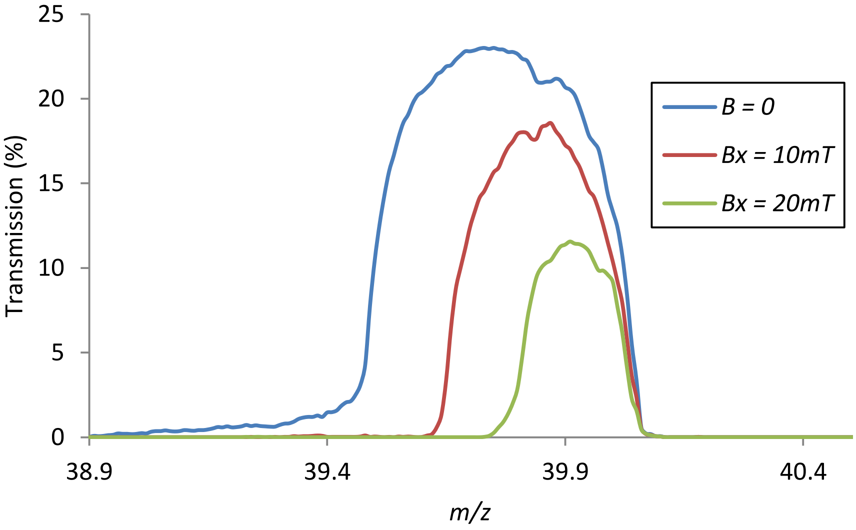

Figure 5.29: $^{40}Ar^{+}$ mass peaks for a circular cross section electrode QMF with and without B_x field applied

For a given configuration (table 5.2) the performance varies with $^{r}/_{r_0}$ ratio and B_x field magnitude. Minor changes to $^{r}/_{r_0}$ can have a significant impact upon transmission, resolution and peak shape. In figures 5.30 and 5.31 the peak transmission and resolution are plotted against ${}^{r}\!/_{r_0}$, from 1.0 to 1.16, for various magnitudes of B_x and $\boldsymbol{B} = 0$. In fig. 5.30, as ${}^{r}\!/_{r_0}$ increases there is an approximately linear drop off in peak transmission and this is more significant for larger B_x fields.

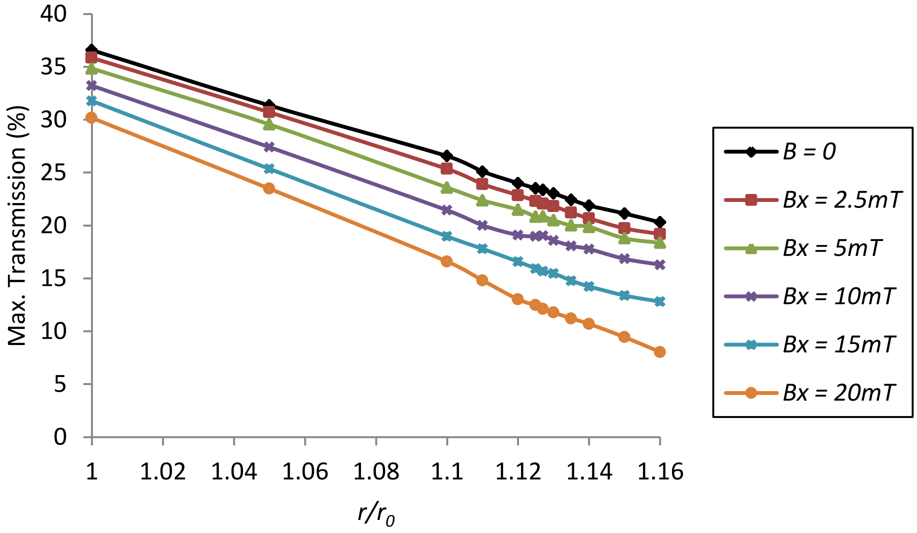

Figure 5.30: Maximum Peak Transmission versus r/r_0 for various B_x magnitudes

In fig. 5.31, resolution tends to increase as ${}^{r}\!/_{r_0}$ increases from 1.0 to a maximum point and then reduces. As B_x increases, the maximum occurs at slightly larger values of ${}^{r}\!/_{r_0}$.

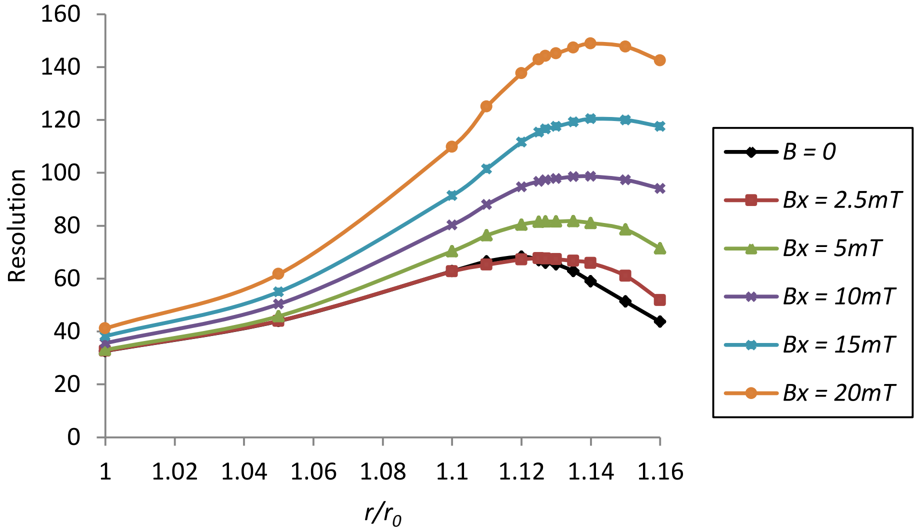

Figure 5.31: Resolution versus r/r_0 ratio for various B_x magnitudes

As B_x increases the resolution increases due to the stability boundary shifting (section 5.7). In fig. 5.31, the maximum resolution point for $\boldsymbol{B} = 0$ and B_x = 5mT is approximately the same ($1.12 \leq {}^{r}\!/_{r_0} \leq 1.13$). In figures 5.32 and 5.33, the transmission and resolution are plotted against U/V ratio for these two cases with ${}^{r}\!/_{r_0} = 1.127$.

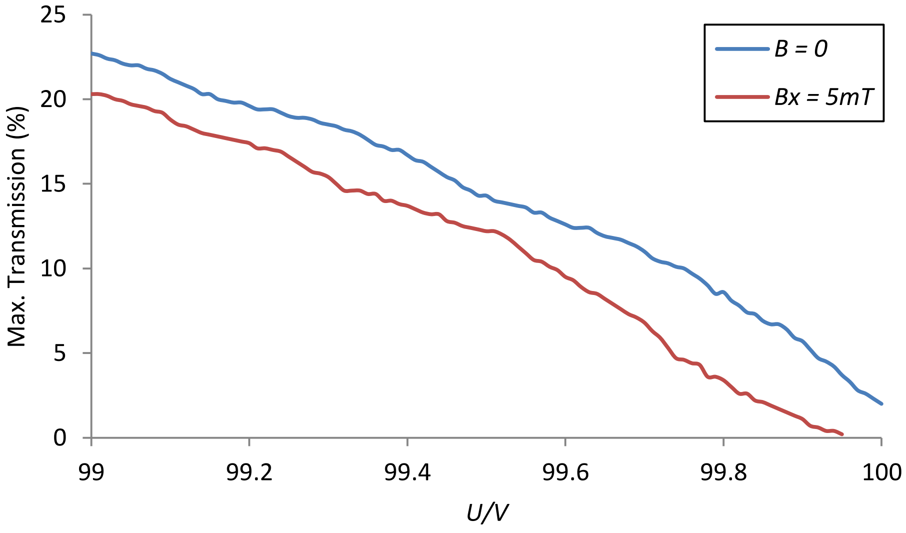

Figure 5.32: Maximum Peak Transmission versus U/V ratio with and without B_x field applied

The trend in figure 5.32 for ***B*** = 0 is similar to that obtained in [23]. As expected, the maximum transmission with a B_x field applied is lower for a given *U*/*V* ratio due to the stability boundary shifting. In figure 5.33, the resolution is plotted against *U*/*V* ratio for ***B*** = 0 and B_x = 5mT. For ***B*** = 0, the resolution increases gradually, fluctuates around 99.8% and then drops off as 100% is approached. This is because as transmission reduces the low mass tail becomes more significant and influences the peak width (at 10% peak height). For B_x = 5mT, the resolution continues to rise at an increasing rate until it falls off as transmission reduces and peak degradation occurs.

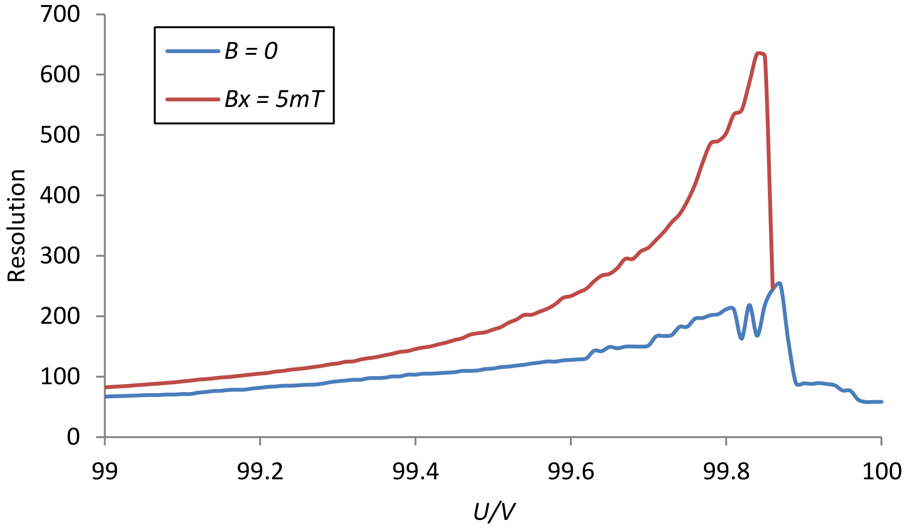

Figure 5.33: Resolution versus *U*/*V* ratio with and without B_x field applied

The difference in the mass spectral peaks for these two cases is shown in figure 5.34 where the peak transmission is approximately the same for both (~5%). The contribution of the low mass tail with a B_x field applied is reduced and the peak shape is more clearly defined.

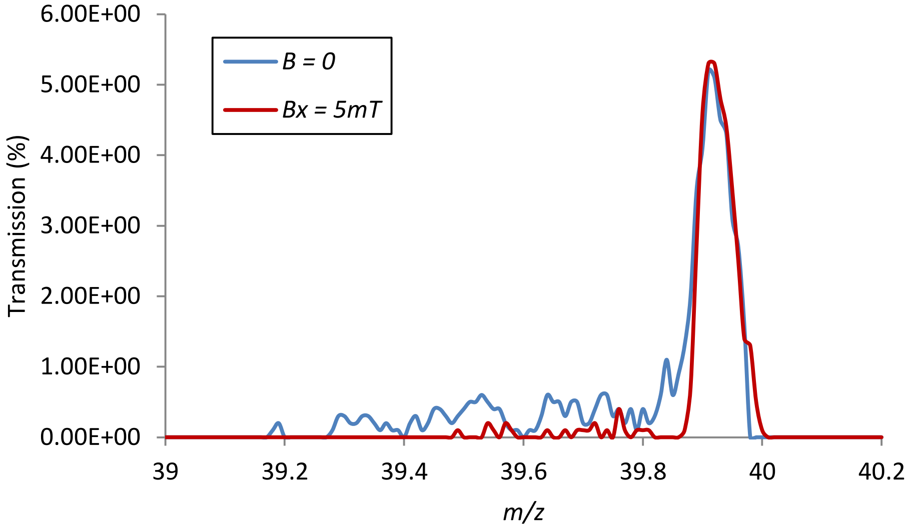

Figure 5.34: Mass spectral peaks for $^{40}Ar^{+}$ for $B = 0$ and $B_x = 40$mT with circular cross section electrodes

5.8.4 Ion Transmission Factors

The dependence of maximum ion amplitude is investigated numerically using custom software Ion-TX (section 5.4). For this investigation a particular scan line is chosen to be in close proximity to the apex of the stability diagram (the region of operation where the highest resolution can be attained) and an ideal QMF is assumed (i.e., hyperbolic cross-section electrodes). For the investigations carried out a value of $\eta = 0.998$ was used for the scan line gradient (equation 3.34). The scan line definition used provides a fair means of comparison between the two cases, that is with and without applied transverse magnetic field. The scan line is adjusted according to the shifted apex brought about by the magnetic field effect (B_1) and thus provides the same relative scan for each case. As a result the q-axis can be arbitrarily scaled to allow direct comparison of ion transmission results. The scan line consisted of seventeen equally spaced discrete points with the first four (#1-4) passing through the exclusive y-stable region and the last four (#14-17) passing through the exclusive x-stable region. The middle seven points (#6-12) lie within the overlap of the *x* and *y* stable regions with the remaining two points lying on *y*- (#5) and *x*- (#13) stability boundaries respectively (figure 5.35).

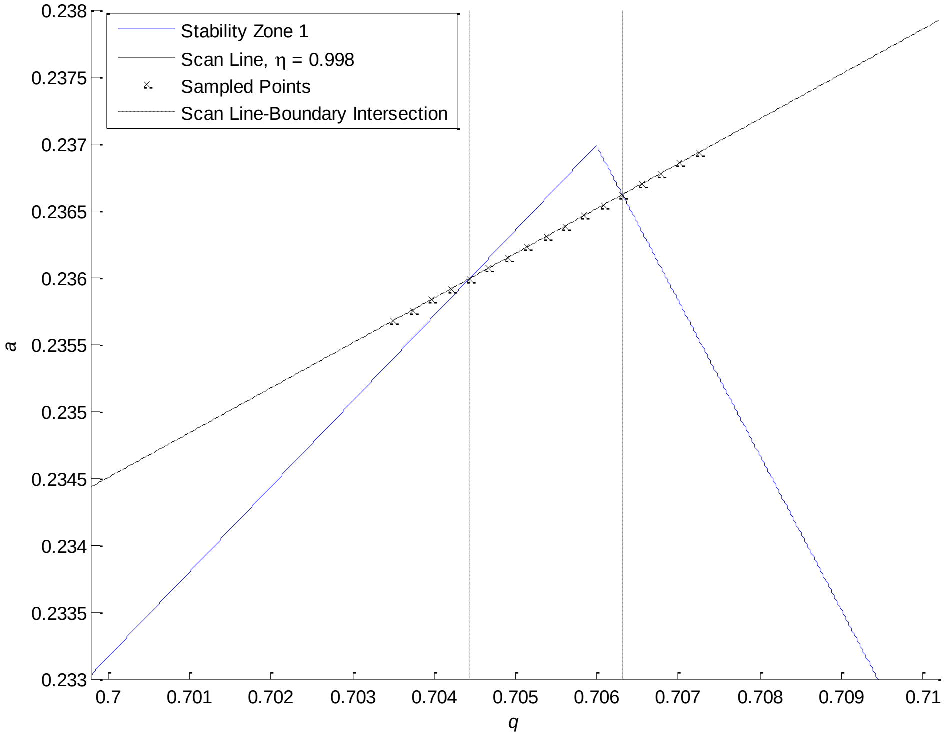

Figure 5.35: Stability zone 1 apex (for *B* = 0) showing the 17 discrete sampling points across the scan line

In examining the ion transmission factors only those parameters which appear in equations 5.13-5.15 are considered. One practical exclusion criterion for this investigation is that if the *z*-position of an ion becomes negative (i.e., $z < 0$) it is akin to an ion moving back out of the front of the mass filter; it is therefore classified as unstable (i.e. with unbounded oscillations). The standard parameter values used for the investigations are given in table 5.5 (unless otherwise stated).

Parameter	Value
$\boldsymbol{a}, \boldsymbol{q}$	Equation (3.34)
$\boldsymbol{\xi_0}$	$\frac{\pi}{8}$
$\left(\frac{\boldsymbol{dz}}{\boldsymbol{d\xi}}\right)_{\boldsymbol{0}}$	0.0004
$\left(\frac{\boldsymbol{dx}}{\boldsymbol{d\xi}}\right)_{\boldsymbol{0}} = \left(\frac{\boldsymbol{dy}}{\boldsymbol{d\xi}}\right)_{\boldsymbol{0}}$	0
$\boldsymbol{x_0} = \boldsymbol{y_0}$	0.01

Table 5.5: Standard parameter values for investigations

5.8.4.1 Initial Phase, ξ_0

Although the stability of an ion is not affected by the phase angle at which it enters the quadrupole field the peak amplitude of the ion is. Due to the nature of the sinusoidal function as exemplified in the Mathieu equation, the modulus of the peak amplitude variance is symmetrical and π periodic. Hence the initial phase is only investigated between 0 and $\pi/2$ [24].

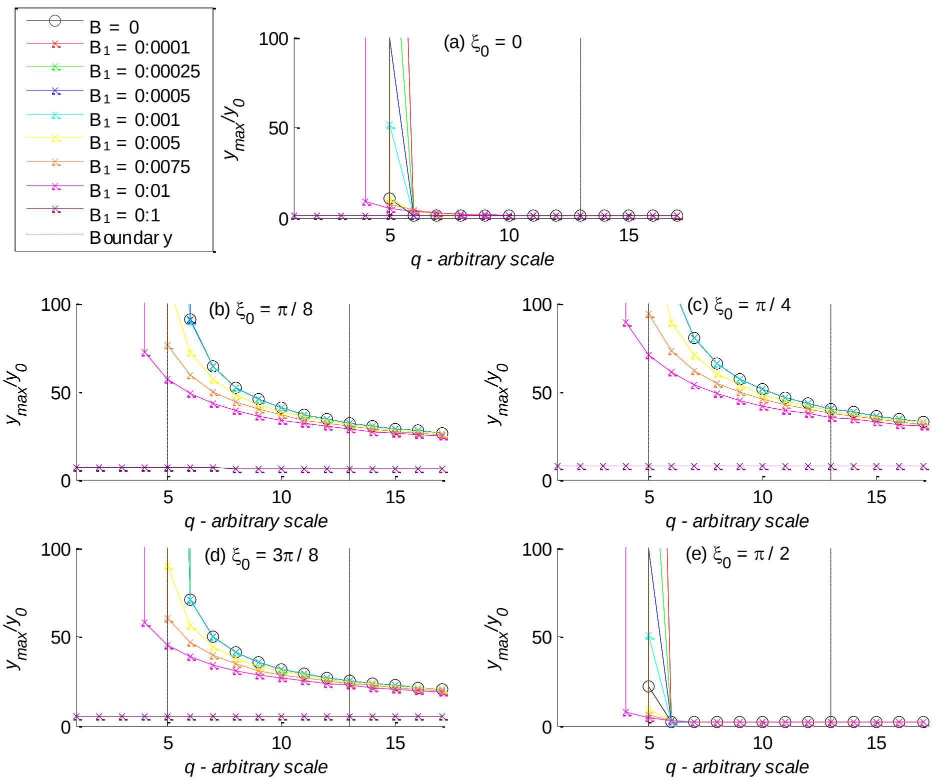

Figure 5.36: Dependence of y_{max}/y_0 on B_1 for a given initial phase angle (ξ_0) ranging from 0 - π/2. B = 0 is included for comparison

Figure 5.36 (a-e) show how y_{max}/y_0 changes with varying B_1 for each of the discrete initial phase angles over the range $0 - \frac{\pi}{2}$ and the case $\boldsymbol{B} = 0$ is included for comparison. The values investigated for B_1 range from 0.0001 to 0.1, covering 3 orders of magnitude. The general trend is that as B_1 increases, y_{max}/y_0 tends to reduce. In some instances, for a small value of B_1 there is no reduction in y_{max}/y_0 below the case of $\boldsymbol{B} = 0$, but a steep gradient for increasing ion amplitude as the *y*-stability boundary is approached.

With increasing values of B_1 there appears to be a breakdown in the stability boundary as the force due to the magnetic field ($\boldsymbol{F_B}$) dominates ($\boldsymbol{F_B} \gg \boldsymbol{F_E}$) and the force due to the electric field ($\boldsymbol{F_E}$) has little influence on the ion motion and consequent stability (or instability). With increasing magnetic field the influence on ion motion becomes very complex. This effect is illustrated in figures 5.37 – 5.40

where $q = 0.7056675$ and $a = 0.2363271$ (#10 on arbitrary q scale) for the same conditions as fig. 5.36(d). In each figure a sample of the ion trajectory is plotted in the *x*-*z* and *y*-*z* planes for $B_1 = 0, 0.001, 0.01, 0.1$. The same sample size was used for each trace, $0 \leq \xi \leq 500$.

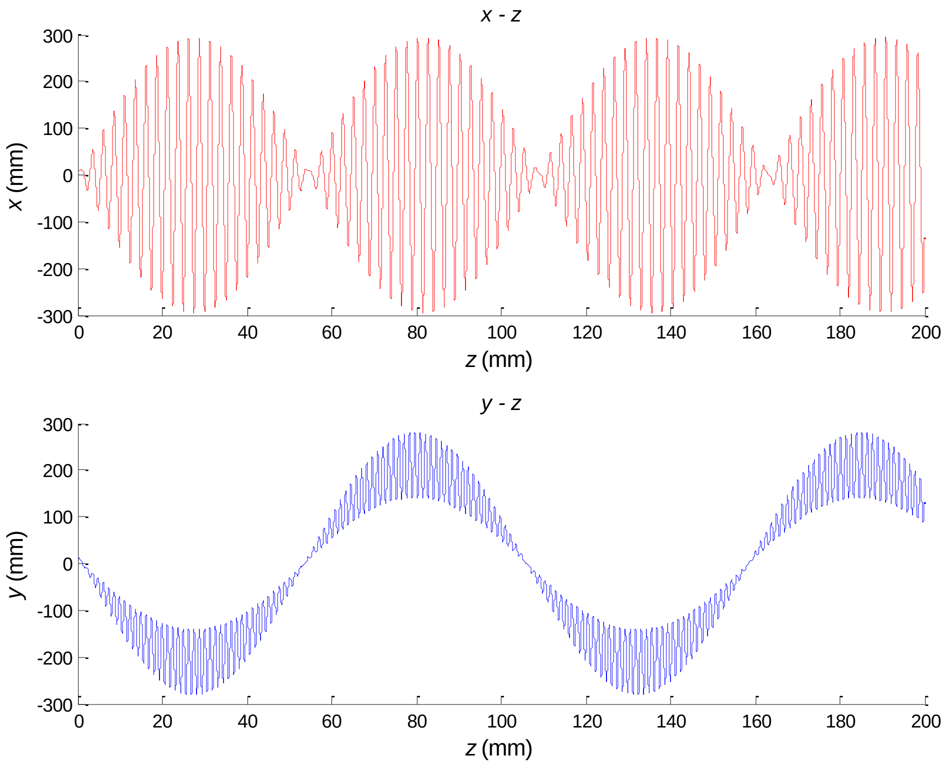

Figure 5.37: Ion trajectory in *x-z* (*red*) and *y-z* planes (*blue*) for B_1 = 0

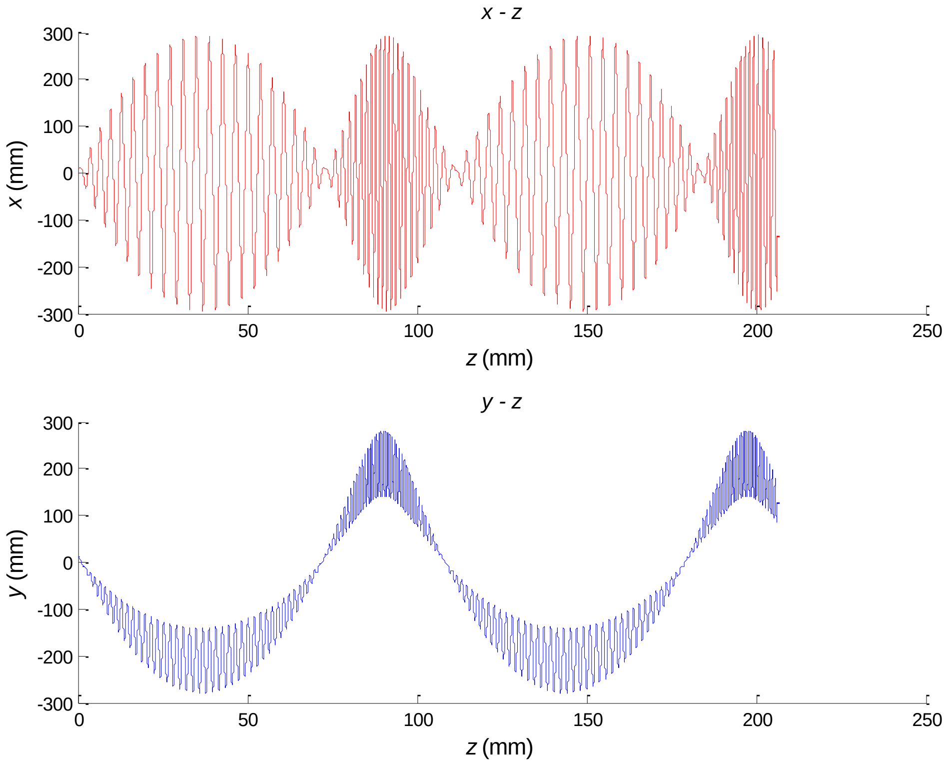

Figure 5.38: Ion trajectory in *x-z* (*red*) and *y-z* planes (*blue*) for B_1 = 0.001

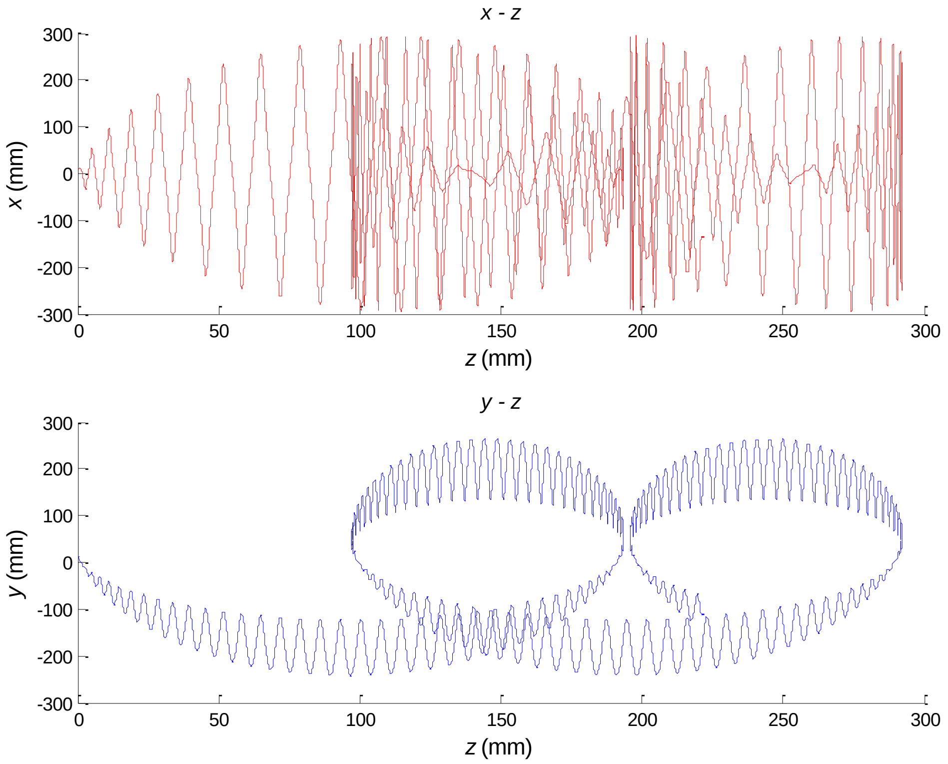

Figure 5.39: Ion trajectory in *x-z* (*red*) and *y-z* planes (*blue*) for B_1 = 0.01

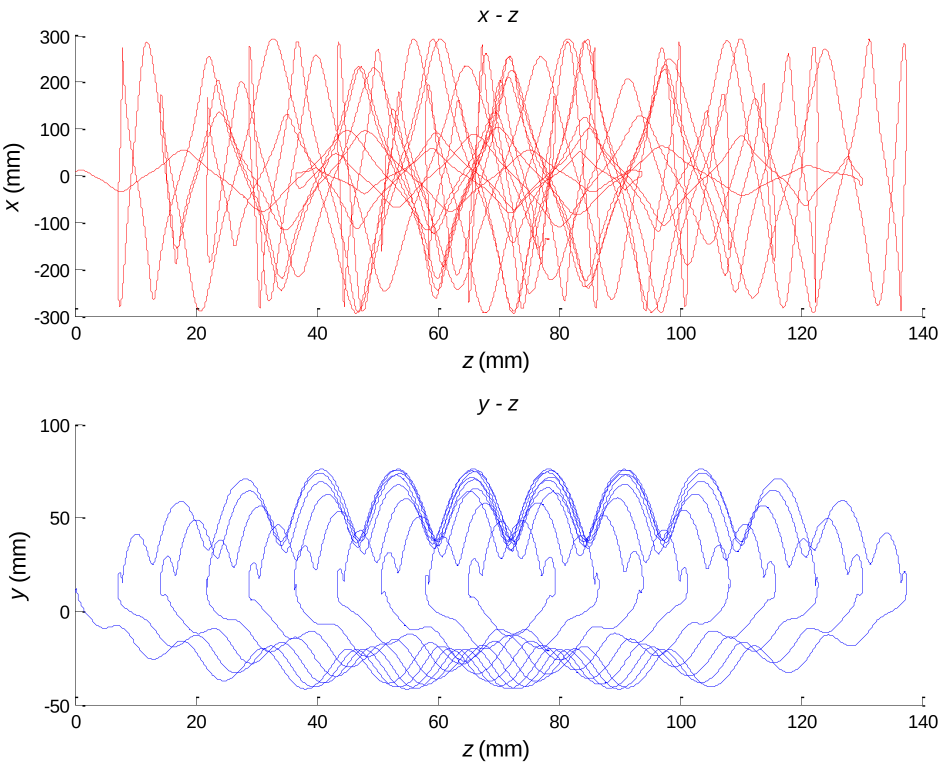

Figure 5.40: Ion trajectory in *x-z* (*red*) and *y-z* planes (*blue*) for B_1 = 0.1

As B_1 increases the Lorentz force increases and the magnetic component dominates. The effect of the transverse magnetic field on the *z* co-ordinate position is evident as in each case the distance travelled (along the *z*-axis) differs and for figures 5.39 and 5.40 the axial velocity fluctuates positive and negative as the ion motion spirals. The fluctuation in axial velocity is the reason why the motion in the *x-z* plane is affected. In figure 5.39, the increase in B_1 causes the motion in the *y-z* plane to spiral. In figure 5.40, the combined magnetic parameter is further increased ($B_1 = 0.1$) and the motion becomes very complex and moves in a spiral of irregular shape, effectively shifting along the *z*-axis at a slower rate (compared with the other *y-z* plane traces).

5.8.4.2 Initial Phase Displacement, y_0

With no magnetic field applied the peak amplitude in the y-dimension (y_{max}) is scaled linearly according to the initial y displacement (y_0). The same linear dependence exists for the transverse magnetic field case although the gradient is significantly smaller (figure 5.41 (a) & (b)). Figure 5.42 (a-f) shows how the maximum amplitude (y_{max}) varies for the same relative scan line when B_1 is varied at different initial displacements (y_0) ranging from 0.1mm to 500mm.

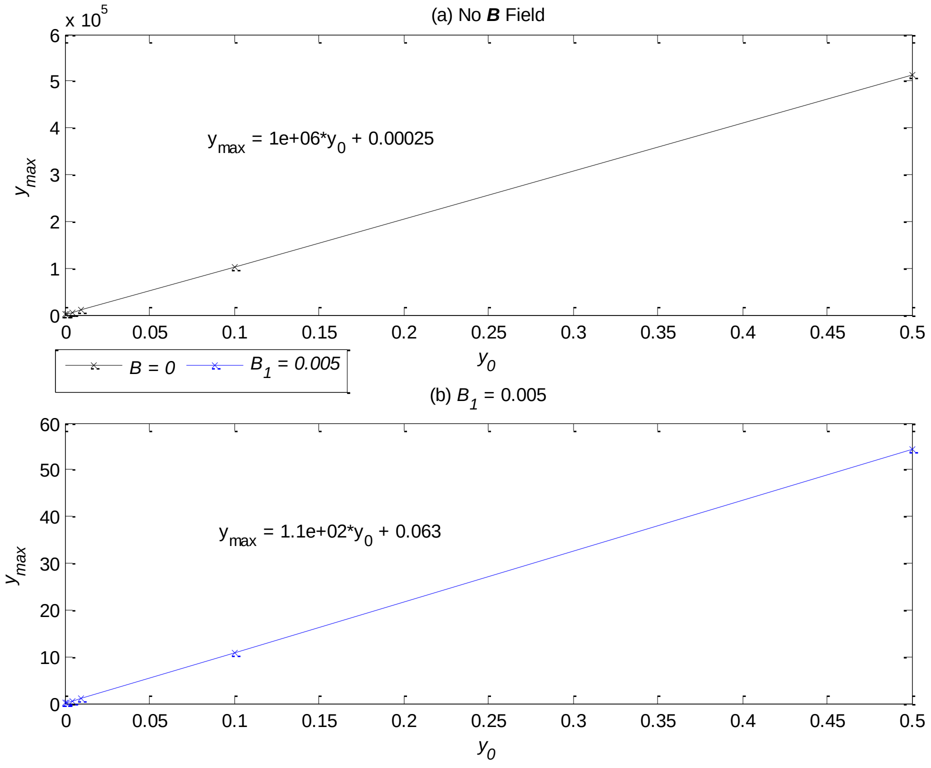

Figure 5.41: y_{max} versus y_0 for same relative conditions: (a) No magnetic field, (b) B_1 = 0.005

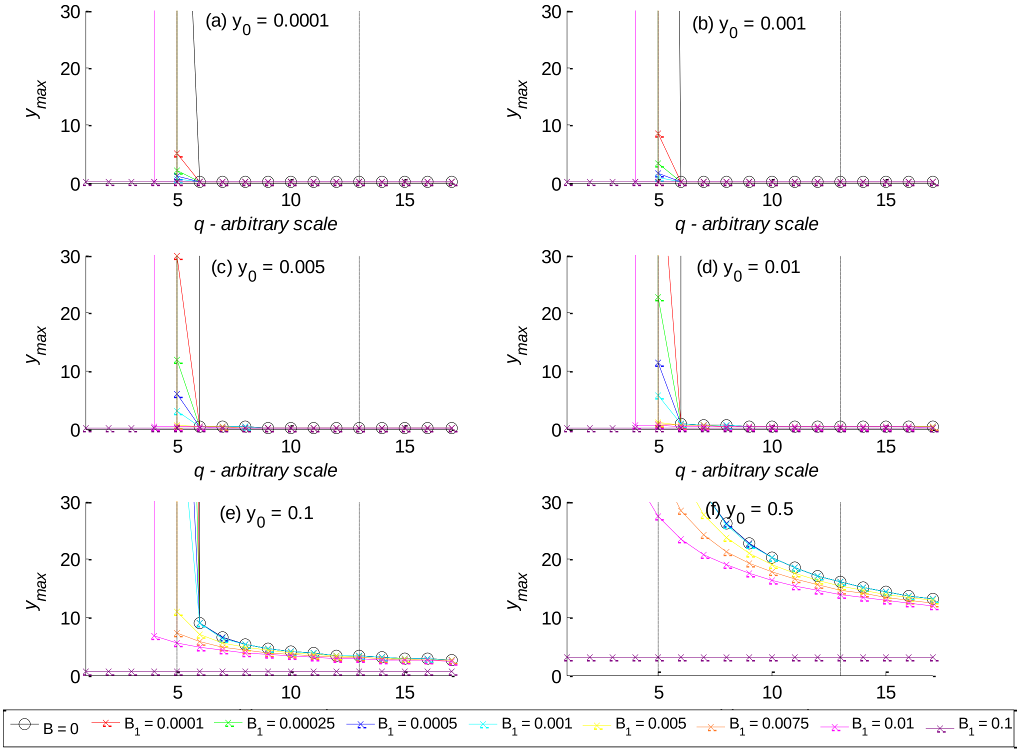

Figure 5.42: Dependence of peak *y* amplitude (y_{max}) on B_1 for a given initial *y* displacement (y_0). *B* = 0 is included for comparison

In figure 5.42, increasing B_1 tends to reduce the peak amplitude, particularly as the stability boundary is approached.

5.8.4.3 Initial Axial Velocity, $(dz/d\xi)_0$

For the conventional case (***B*** = 0) there is no resultant axial force (since $E_z = 0$) and the axial velocity remains constant. The axial velocity has no effect on the peak ion transmission. However, in practice for a finite length field, axial velocity does affect the resolution since the time an ion spends in the field depends on it. For these investigations the limit of integration is set to an extremely large value such that 'time spent in the field' has no effect (as previously mentioned) and, as expected, this was confirmed by examining the peak amplitudes for no magnetic field applied (***B*** = 0).

With a transverse magnetic field applied, the axial velocity is no longer constant and directly influences peak ion transmission (y_{max}). From figure 5.43 (a-d), it is observed that as the initial axial velocity increases the peak amplitude also increases. In the same figure, the conventional case for ***B*** = 0, which is invariant to initial axial velocity, is also included for comparison. In contrast with the case for ***B*** = 0 in figure 5.43(d) it is noted that for a larger initial axial velocity, applying B_1 leads to increased peak amplitude.

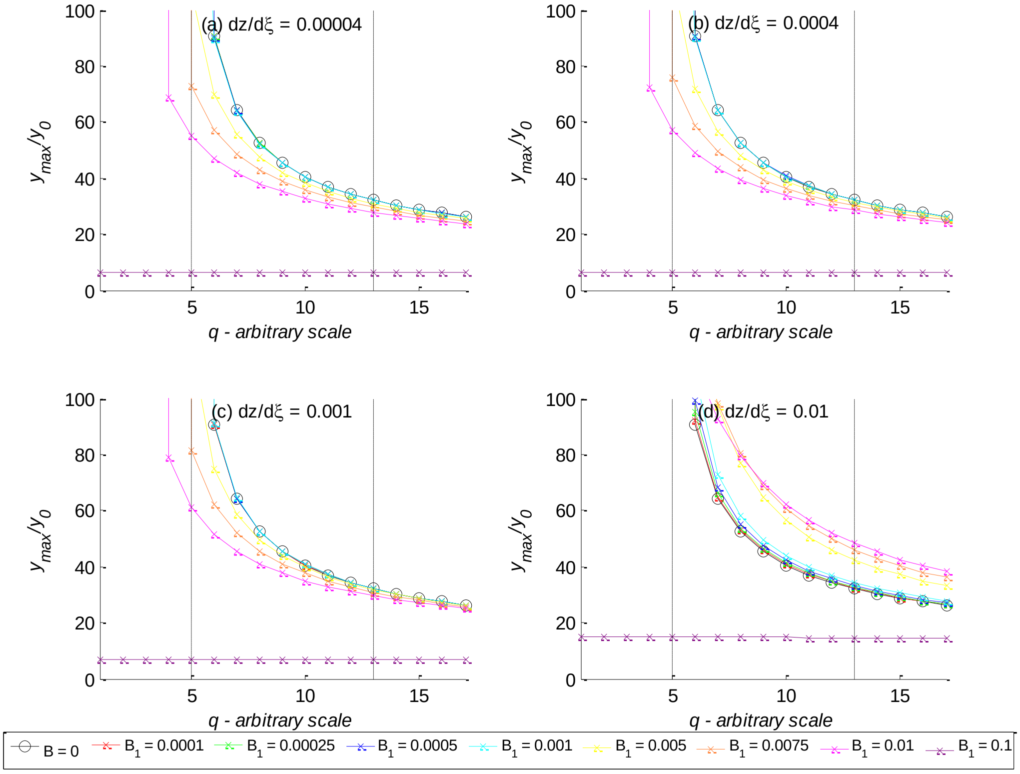

Figure 5.43: Dependence of y_{max}/y_0 on B_1 for a given initial axial velocity $(dz/d\xi)_0$ ranging from 0.0004 – 0.01. B = 0 is included for comparison

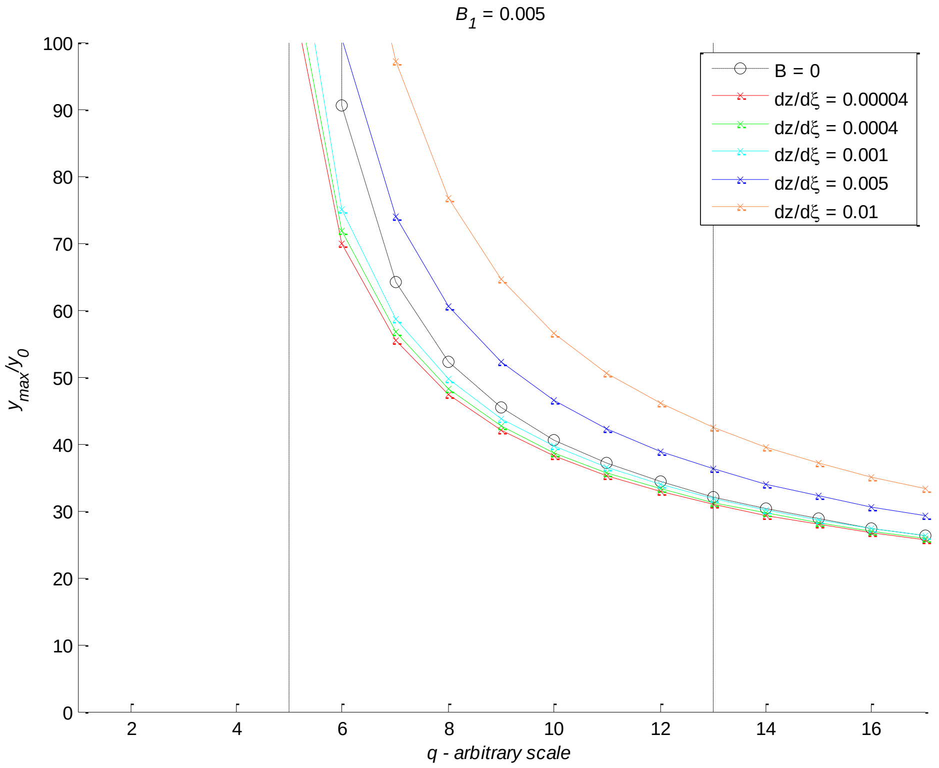

Figure 5.44: Dependence of y_{max}/y_0 on initial axial velocity $(dz/d\xi)_0$ for B_1 = 0.005. B = 0 is included for comparison

In figure 5.44 the same information (as in figure 5.42) is plotted but in a different format for $B_1 = 0.005$ and the initial axial velocity is varied. The case **B** = 0 is included for comparison. Here it is clear that y_{max}/y_0 tends to increase as the initial axial velocity is increased. For lower initial axial velocity values the maximum amplitude is lower than the case ***B*** = 0.

5.9 QMF Behaviour under the Influence of Transverse B_y Field, $\boldsymbol{B} = (0, B_y, 0)$

In previous work [2, 3], the effect of the magnetic field applied along the *y*-axis (B_y) has been overlooked as its effect on mass spectra only becomes observable at larger field values compared to that required for B_x; previous research compared like for like field values up to a maximum of 50mT (which was insufficient for an effect to be observed with B_y). In addition, the use of larger magnetic fields may have associated disadvantages in terms of size, cost, mounting and interference with other equipment (e.g., ion source).

In [3] the mass spectral peak for $^{40}\text{Ar}^+$ (*m*/*z* 40) was simulated for (i) $\boldsymbol{B} = 0\text{T}$, (ii) $B_x = 0.017\text{T}$ and (iii) $B_y = 0.017\text{T}$ showing a reduction in the low mass tail for case (ii) (compared to (i)) and negligible difference for case (iii) (compared to (i)). The same conditions have been simulated using QMS-Hyperbolic and the spectra are in excellent agreement with that of [3] (figure 5.45). The same set of initial random conditions were used for each test and the results, as suggested in [3], indicate that applying B_y has a negligible effect.

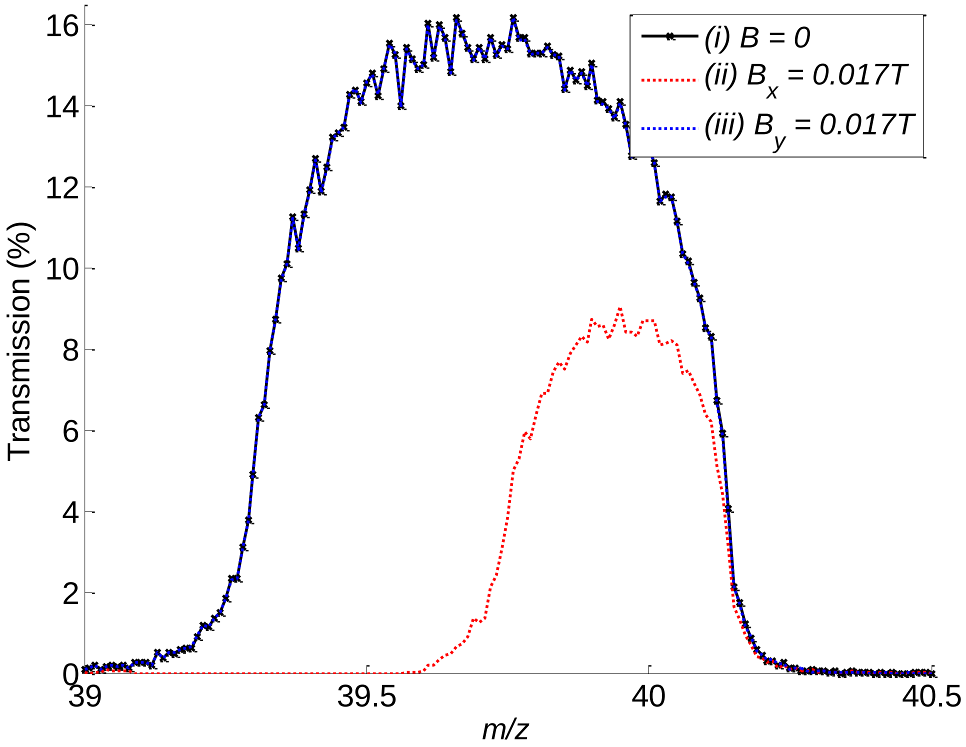

Figure 5.45: $^{40}Ar^+$ **mass spectral peaks for (i)** $B = 0$; **(ii)** $B_x = 0.017T$; **(iii)** $B_y = 0.017T$

However, in order for an effect to be observed for the case simulated a much larger B_y magnitude is required. The same conditions were simulated for values of B_y increased by an order of magnitude and more as shown in figure 5.46. The application of a B_y field results in a reduction in peak width brought about by increased instability on the high mass side of the peak. This result has been observed experimentally (fig. 5.10) but requires a comparatively larger magnetic field magnitude to be applied (as compared to B_x) for the same effect to be observed (section 5.7).

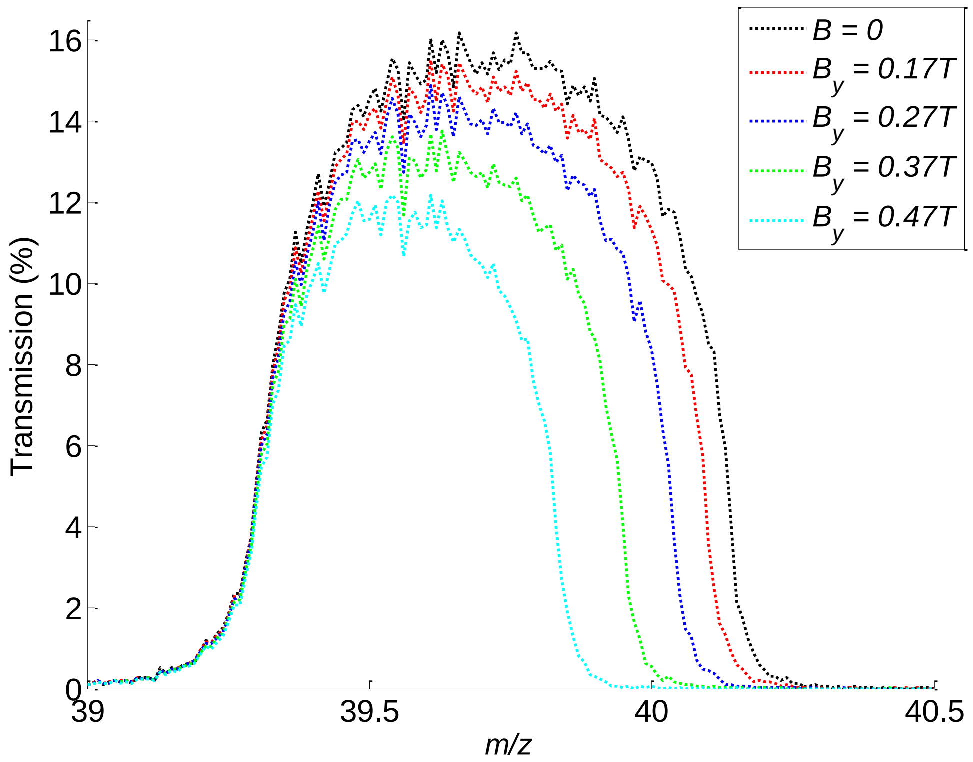

Figure 5.46: $^{40}\text{Ar}^{+}$ mass spectral peaks for $B = 0$ and various B_y field magnitudes

In the case of the *y*-magnetic field (fig. 5.47), for the same simulation parameters as fig 5.16, the resolution-transmission characteristic shows little difference to the conventional case when no magnetic field is applied ($\boldsymbol{B} = 0$) and ultimately no performance enhancement (for the given conditions simulated).

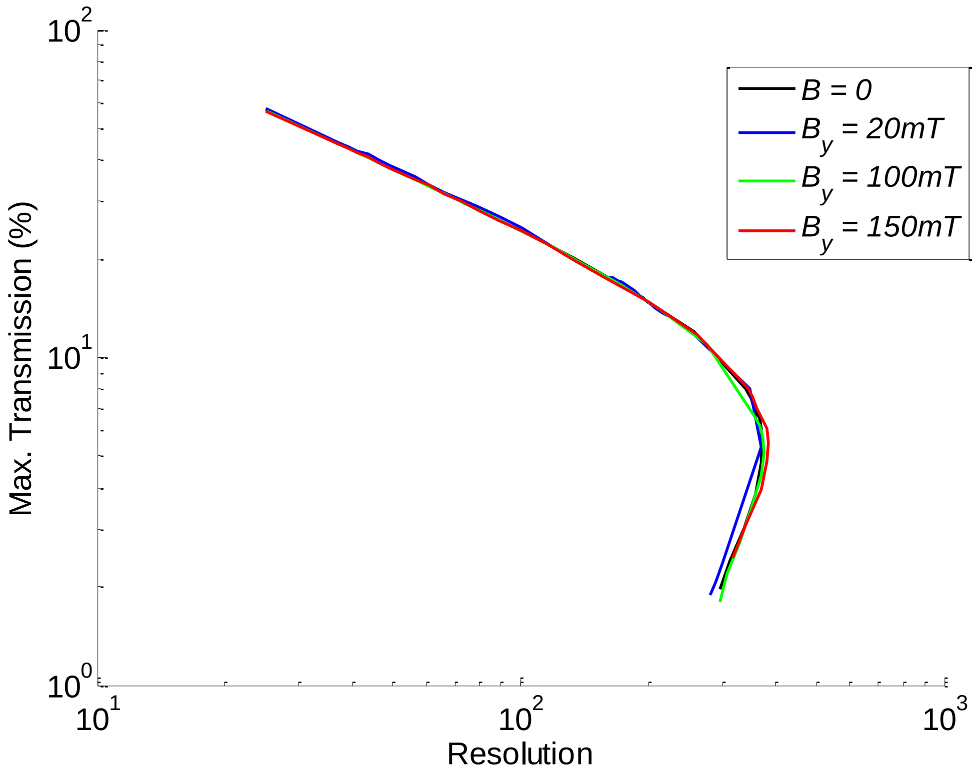

Figure 5.47: Simulated Resolution-Transmission curve for a typical QMF with $B = 0$ and various B_y magnitudes

5.10 Conclusions

Experimental results have shown a relative increase in resolution with a static transverse magnetic field applied to the mass filter for operation in stability zone 1. Moreover, it has been demonstrated experimentally that application of a static transverse magnetic field in the *y*-*z* plane of a QMF (operated in the first quadrant of *a*-*q* space) leads to a relative increase in resolution as the high mass side of a peak is reduced. The relative resolution enhancement observed experimentally has also been simulated theoretically. These effects may be explained by considering the additional magnetic component of the Lorentz force which an ion experiences when the magnetic field is applied. This results in rejection of ions in the low mass tail and/or high mass tail depending on the orientation of magnetic field giving a relative increase in resolution for a given set of operating parameters. Furthermore, a comprehensive simulation study has been carried out to show the effects of different QMF design parameters when a static transverse magnetic field is applied. The choice of frequency and ion energy were found to be of particular significance.

A method has been developed for accurately mapping the effective stability diagram of a QMF under a range of conditions including, but not limited to, the case with a static transverse ***B*** field applied to the body of the filter. The same method can be used to map the effective stability diagram for various design conditions, such as, a conventional QMF with different electrode geometries (e.g. circular, square).

Mapping the effective stability diagram (zone 1) of a QMS with an applied transverse ***B*** field provides an important insight into the fundamental operation of this novel instrument. By applying a static transverse magnetic field to the body of a QMS, the stability region narrows according to the direction and magnitude of the applied field. It has been explained how the electrode connection determines the stability diagram quadrant of operation and how the orientation of a transverse magnetic field is affected by this. The general trend was confirmed by deriving analytically the effect of a transverse magnetic field on the stability diagram.

In the first quadrant of stability zone 1, the effect of the magnetic field applied along the *y*-axis (negative electrode pair) has been shown to reduce the high mass side of a mass spectrum but with no ultimate increase in instrument performance (for the conditions simulated). Applying the magnetic field along the *x*-axis (positive electrode pair) has been simulated to show an ultimate increase in instrument performance by ~75%, for the same relative transmission, with a particular QMF design. This performance improvement cannot be obtained by further optimisation of the U/V ratio alone.

The reasons for this performance enhancement have been investigated using Ion-TX. By studying the ion transmission factors it was found that under certain conditions the maximum ion amplitude reduces within the theoretically stable region. Moreover in the theoretically unstable region, for a given set of conditions, the maximum ion amplitude increases. The net result can lead to increased resolution and transmission compared to the conventional case (with $\boldsymbol{B} = 0$).

Typically, QMFs are manufactured with circular cross section electrodes to approximate the ideal quadrupole field and reduce costs. The effect of applying a static transverse magnetic field (B_x) to a QMF with circular electrodes has been investigated. The application of a B_x field has been shown to lead to a significant reduction in the long, low mass tail of typically observed spectral peaks, hence the improved resolution and performance of a QMF operated in a transverse magnetic field.

References

[1] J. J. Thomson, "XIX. Further experiments on positive rays," *Philosophical Magazine Series 6,* vol. 24, pp. 209-253, 1912/08/01 1912.

[2] J. Tunstall, S. Taylor, A. Vourdas, J. Leck, and J. Batey, "Application of a static magnetic field to the mass filter of a quadrupole mass spectrometer," *Vacuum,* vol. 53, pp. 211-213, 1999.

[3] B. Srigengan, J. Gibson, and S. Taylor, "Ion trajectories in quadrupole mass spectrometer with a static transverse magnetic field applied to mass filter," in *Science, Measurement and Technology, IEE Proceedings-*, 2000, pp. 274-278.

[4] S. U. Syed, J. Sreekumar, B. Brkic, J. R. Gibson, and S. Taylor, "Effect of an axial magnetic field on the performance of a quadrupole mass spectrometer," *Journal of the American Society for Mass Spectrometry,* vol. 21, pp. 2070-2076, 2010.

[5] S. U. Syed, J. Sreekumar, J. Gibson, and S. Taylor, "QMS in the third stability zone with a transverse magnetic field applied," *Journal of the American Society for Mass Spectrometry,* vol. 22, pp. 1381-1387, 2011.

[6] C. Bailey, "Lucretius: De rerum natura," *English,* vol. 1, pp. 563-565, 1937.

[7] H. Oersted, "Experiment on the effects of a current on the magnetic needle," *Ann. Philos,* vol. 16, 1820.

[8] E. T. Whittaker, "History of the Theories of Ether and Electricity from the Age of Descartes to the Close of the Nineteenth Century," *London and Dublin,* 1910.

[9] P. Day, The Philosopher's Tree: A Selection of Michael Faraday's Writings, Taylor & Francis, 1999.

[10] J. C. Maxwell, *A treatise on electricity and magnetism* vol. 1: Clarendon press, 1881.

[11] H. A. Lorentz, *La théorie électromagnétique de Maxwell et son application aux corps mouvants* vol. 25: EJ Brill, 1892.

[12] S. N. Moiseev. (2010). *“DirectSearch optimization package, version 2”*. Available: http://www.maplesoft.com/applications/view.aspx?SID=101333

[13] J. V. Johnson, R. E. Pedder, R. A. Yost, and R. March, "The stretched quadrupole ion trap: Implications for the Mathieu au and qu parameters and experimental mapping of the stability diagram," *Rapid Communications in Mass Spectrometry,* vol. 6, pp. 760-764, 1992.

[14] J. F. J. Todd, R. M. Waldren, R. E. Mather, and G. Lawson, "On the relative efficiencies of confinement of Ar^+ and Ar^{2+} ions in a quadrupole ion storage trap (quistor)," *International Journal of Mass Spectrometry and Ion Physics,* vol. 28, pp. 141-151, 1978.

[15] E. R. Badman, R. C. Johnson, W. R. Plass, and R. G. Cooks, "A miniature cylindrical quadrupole ion trap: simulation and experiment," *Analytical Chemistry,* vol. 70, pp. 4896-4901, 1998.

[16] U. O. Wisconsin-Madison. *HTCondor High Throughput Computing*. Available: http://research.cs.wisc.edu/htcondor/

[17] S. Taylor and J. R. Gibson, "Prediction of the effects of imperfect construction of a QMS filter," *Journal of Mass Spectrometry,* vol. 43, pp. 609-616, 2008.

[18] T. J. Hogan and S. Taylor, "Effects of mechanical tolerances on QMF performance for operation in the third stability zone," *Instrumentation and Measurement, IEEE Transactions on,* vol. 59, pp. 1933-1940, 2010.

[19] P. H. Dawson, "Quadrupole mass spectrometry and its applications," 1976.

[20] R. E. March and J. F. J. Todd, "Theory of Quadrupole Instruments," in *Quadrupole Ion Trap Mass Spectrometry*, ed: John Wiley & Sons, Inc., 2005, pp. 34-72.

[21] D. Douglas, "Linear quadrupoles in mass spectrometry," *Mass spectrometry reviews,* vol. 28, pp. 937-960, 2009.

[22] R. J. Bell, N. Davey, M. Martinsen, R. T. Short, E. T. Krogh, and C. G. Gill, "Understanding the Effects of the Earth's Magnetic Field on Mobile Mass Spectrometry: Simulation, Experimentation and Solutions," in *51st ASMS conference on mass spectrometry and allied topics*, Minneapolis, MN, 2013.

[23] J. R. Gibson and S. Taylor, "Prediction of quadrupole mass filter performance for hyperbolic and circular cross section electrodes," *Rapid Communications in Mass Spectrometry,* vol. 14, pp. 1669-1673, 2000.

[24] P. Dawson, "A detailed study of the quadrupole mass filter," *International Journal of Mass Spectrometry and Ion Physics,* vol. 14, pp. 317-337, 1974.

Chapter 6 : QMS with a Dynamic Magnetic Field Applied

An ultimate increase in quadrupole mass spectrometer (QMS) resolution with a static transverse magnetic field applied along the *x* axis (B_x) has been verified for the case of a single mass spectral peak. The reduction in peak width due to increased instability on the low mass side of a peak has been verified both theoretically and experimentally. For a viable mass spectrometer instrument it is necessary to scan a given range of *m*/*z* and provide uniformity of the magnetic field effect. In this chapter, proof-of-concept for a magnetically enhanced QMS instrument is demonstrated.

6.1 Introduction

The ability to scan a range of masses may be achieved by applying a dynamic ***B*** field which is varied concurrently with the direct (*U*) and alternating potential amplitudes (*V*). Generally, for a conventional QMF with no magnetic field applied, the frequency is held constant whilst the magnitudes of the direct and alternating voltages are ramped concurrently at a fixed ratio (chapter 3.1.6). This method is typically adopted in commercial instruments providing a linear relationship between mass and voltage.

6.2 Theory

The dependence of the magnetic field effect on mass can be understood intuitively by considering the magnetic component of the Lorentz force. The magnitude of the force depends on the velocity normal to the magnetic field direction (equation 5.1). The axial velocity of an ion is also mass dependent for constant initial kinetic energy. Consider two singly charged ions of mass, m_0 and m_1, where $m_1 > m_0$. The velocity of each mass ion can be derived from the initial ion energy which depends on the nominal ion source accelerating voltage, V_{ion}, according to,

$$eV_{ion} = \frac{1}{2} m_0 v_0^2 \tag{6.1}$$

$$eV_{ion} = \frac{1}{2} m_1 v_1^2 \tag{6.2}$$

Thus,

$$\frac{v_0}{v_1} = \left(\frac{m_1}{m_0}\right)^{1/2} \tag{6.3}$$

Hence the lighter ion has greater velocity ($v_0 > v_1$) since $m_1 > m_0$. The increased velocity leads to an increased Lorentz force experienced by a lighter ion (of the same charge, e).

From equations 5.13 – 5.15 the combined magnetic field parameter is inversely proportional to mass. Therefore the magnetic field strength must be ramped linearly at a rate proportional to the increase in mass for the same effect to be observed throughout a given mass range. The shift in the stability diagram due to a transverse magnetic field applied in the *x*-*z* plane is dependent on the parameter, B_1.

For a singly charged ion and constant alternating voltage angular frequency (ω), initially B_1 is given by,

$$B_{1_0} = \frac{2eB_{x_0}}{m_0 \omega} \tag{6.4}$$

Scanning from mass, m_0, to a mass, m_1, the initial magnetic field magnitude (B_{x_0}) must be increased by some factor, C, such that:

$$B_{x_1} = B_{x_0} \cdot C \tag{6.5}$$

Then,

$$B_{1_1} = \frac{2eB_{x_0}C}{m_1\omega} \tag{6.6}$$

And therefore,

$$C = \frac{m_1}{m_0} \tag{6.7}$$

This concept is illustrated in figure 6.1 where the stability diagram (first quadrant, zone 1) for various *m/z* (14, 28, 40) present in atmospheric air are plotted in (*U*, *V*) space. The effect of the magnetic field is shown for a *static* and *dynamic* (linear ramp) case. With a static magnetic field applied (figure 6.1(a)), smaller *m/z* ions are influenced more than larger *m/z* and this is illustrated by the increased shift in the *y*-stability boundary. With a linear dynamic field applied (fig. 6.1(b)) the same relative shift is observed for each *m/z*. The linear dynamic B_x field required to achieve this is shown in figure 6.1(c).

(a) Stability Zone 1: Static Magnetic Field

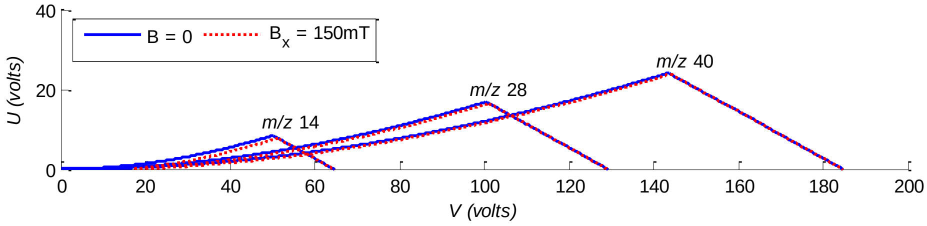

(b) Stability Zone 1: Dynamic Magnetic Field

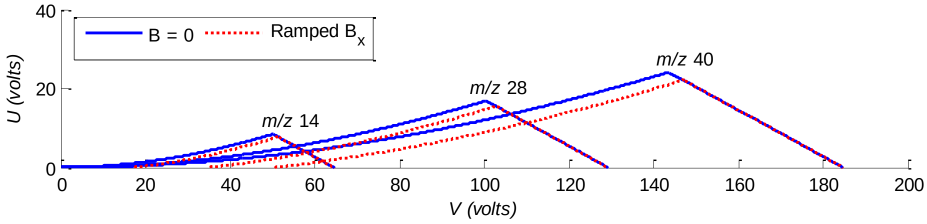

(c) Dynamic Magnetic Field

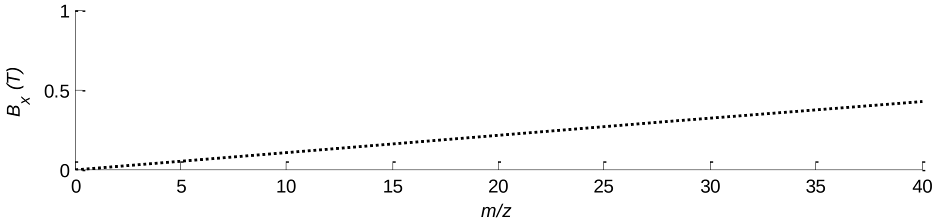

Figure 6.1: (a) Stability zone 1 in (*V*, *U*) space for *m/z* 14, 28 and 40 with a static B_x field applied. In (b) the same case is shown for a linear dynamic B_x field. The B_x field ramping rate versus *m/z* is shown in (c). The plot of (V, U) space is generated for conditions: *f* = 1.86MHz and r_0 = 2.67mm

6.3 Experimental Description

In order to implement the dynamic $\boldsymbol{B}$ field scanning method a Helmholtz type electromagnet is required to provide an adjustable magnetic field intensity that is approximately constant in the central region between the coils. The magnetic field intensity is adjusted by varying the current. A typical Helmholtz coil pair consists of two identical circular coils. The coils are typically spaced one radius apart and each is supplied with equal current in the same direction. The intensity of the field is directly proportional to the number of turns and the magnitude of the current. The coils produce an approximately uniform magnetic field in the central region between them. The magnetic field (B) generated by a current, *I*, at the point halfway between the two loops, is given by [1],

$$B = \left(\frac{4}{5}\right)^{3/2} \frac{\mu n I}{R} \tag{6.8}$$

where *R* is the radius of the coils and *n* is the number of turns in one of the identical coils.

The electromagnet (Newport Instruments, UK) used consisted of a pair of Helmholtz type coils made of lacquered copper wire on a plastic bobbin. The electromagnet has an iron yoke and two pole pieces to increase the maximum magnetic field intensity for a given current. Each pole piece is clamped into the iron yoke centred on the common axis. The Helmholtz coils are placed symmetrically either side of the QMF along a common axis generating an approximately uniform field.

A custom current ramp was designed and built to operate the Helmholtz type electromagnet (Appendix B), with adjustable sweep rate, gradient, amplitude and offset, the current controlled Helmholtz coil was manually synchronised with a commercial quadrupole mass spectrometer (MKS Spectra, Crewe, UK) to provide an approximately constant peak width mass scan. The mass scan range was *m/z* 10-46. The Helmholtz pair was positioned with the vacuum chamber of the QMF passing through the central region (between the coils) and aligned with the *x*-*z* electrode plane. The current ramp was manually synchronised to match the mass scan rate of the commercial instrument which swept at approximately 1Da/second. The maximum current output was ~0.15A which related to a magnetic field intensity of ~30mT as measured with a Hall effect probe (Hirst Magnetic Instruments Ltd., UK). The commercial mass spectrometer has been designed and calibrated to operate very close to the stability tip region for the conventional case (no ***B*** field). For this reason only a relatively small magnetic field range was required to observe the effect over the given mass range because increasing B_x further led to loss of signal (due to operating outside of the stability region).

The commercial single filter QMS instrument has circular cross-section electrodes with a diameter of 6.35mm, inscribed electrode radius 2.767mm, electrode length 100mm, and a source radius of 1mm. This was complemented by an electron impact ion source and Faraday detector. The system was housed in a stainless steel vacuum chamber with a residual gas pressure of ~5 x 10^{-7}torr. During the experiments, atmospheric air was leaked into the vacuum chamber raising the working pressure to ~5 x 10^{-5}torr. The ion energy was set at 6eV.

6.4 Dynamic *B* Field Mass Spectrum

Figure 6.2 shows a mass spectrum obtained from the QMS with and without a dynamic B_x field applied over the mass range *m/z* 10-46.Fig. 6.2(a) shows the full scale spectrum and fig. 6.2(b) is magnified on the *y* axis.

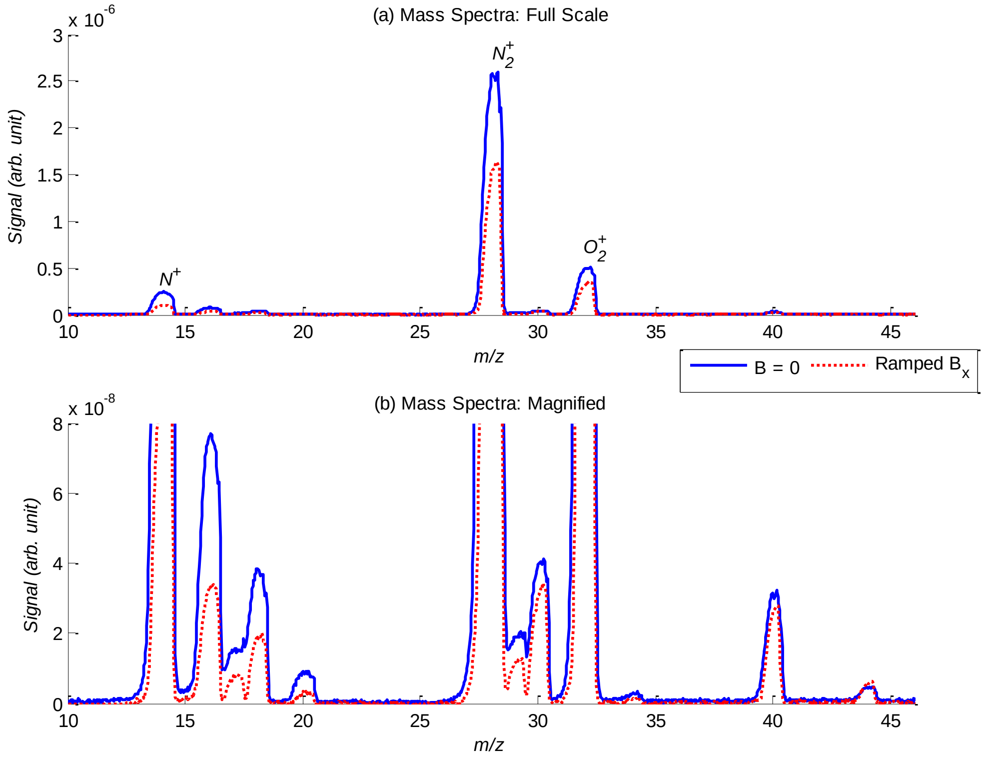

Figure 6.2: Mass spectra obtained from QMS with and without dynamic transverse B_x field applied. (a) is full scale and (b) is the same data magnified (or 'zoomed in') showing the y-axis over a smaller range

The dominant mass spectral peaks are at *m/z* 14 (N^+), 28 (N_2^+) and 32 (O_2^+). It is evident that with the application of a dynamic magnetic field the peaks at *m/z* 18 and 19 have become distinguishable and *m/z* 29 and 30 are more clearly defined.

The drawback with using electromagnets is mainly due to their size and weight especially if a small footprint, portable system is required. For a bench top instrument this would not be an issue. An alternative method for operation may be to incorporate static magnets either within or outside the vacuum chamber and to operate the device by varying the alternating waveform frequency. In this way the direct and alternating potential amplitudes would remain constant whilst the frequency is swept, since a, q and B_1 are inversely proportional to the square of the alternating potential frequency. The drawbacks of frequency sweeping for a conventional QMS are related to the reduced frequency required to investigate larger *m/z* ions. This leads to reduced resolution (due to fewer field cycles) and also reduced sensitivity (as quadrupole acceptance is proportional to square of frequency). However, the benefits include: only varying one parameter, reduced size (by incorporating static bar magnets within the instrument), and potentially an increased mass range (as mass range is inversely proportional to the square of the frequency – chapter 3.1.7).

Extending the mass range of a QMS is typically achieved by reducing the alternating waveform frequency as this can be achieved electronically. The interest in larger mass range QMSs has increased with the development of electrospray ionisation (ESI) [2] and also desorption electrospray ionisation (DESI) [3]. These are ionisation techniques which creates a high yield of multiply charged ions. However, to increase mass range and maintain acceptable resolution and sensitivity remains a problem for the QMS [4].

6.5 Conclusions

Operation of the magnetically enhanced QMS has been demonstrated using a linear dynamic transverse magnetic field applied in the *x*-*z* plane for operation in the first quadrant of stability zone 1. The dynamic field was generated by using a Helmholtz coil pair and manually synchronised with a commercial voltage scanning QMS. As predicted by simulation, the results showed increased resolution spectra across the mass range due to a reduced peak width on the low mass side of the peaks. The alternative QMF scanning method of frequency sweeping could potentially be used to operate a magnetically enhanced QMF with static bar magnets.

References

[1] Krongelb, S. Magnetic Materials, Processes, and Devices 9, *The Electrochemical Society*, pp 272, 2007.

[2] J. B. Fenn, "Electrospray wings for molecular elephants (Nobel lecture)," *Angewandte Chemie International Edition*, vol. 42, pp. 3871-3894, 2003.

[2] R. Graham Cooks, "Direct, trace level detection of explosives on ambient surfaces by desorption electrospray ionization mass spectrometry," *Chemical communications,* pp. 1950-1952, 2005.

[3] G. R. Hilton and J. L. Benesch, "Two decades of studying non-covalent biomolecular assemblies by means of electrospray ionization mass spectrometry," *Journal of The Royal Society Interface,* vol. 9, pp. 801-816, 2012.

Chapter 7 : Conclusions and Future Work

The research carried out in this thesis has been concerned with the performance of the Quadrupole Mass Spectrometer (QMS) operated under a range of conditions. In particular, special emphasis has been placed on a magnetically enhanced quadrupole mass spectrometer.

For a conventional quadrupole mass filter (QMF) (without magnetic field) performance in zone 3 has been investigated in detail and new design equations have been presented. It was confirmed that higher resolution is obtained by operating at the lower stability tip of zone 3. A three dimensional simulation model of the QMF has been developed to investigate fringe field effects particularly in the entrance region. It was found that for a QMF without a pre-filter, behaviour and performance are largely dependent on ion velocity and this is critical at low velocities. An optimal velocity region was found for ion transmission and it is suggested that a QMF should be operated such that the highest mass ion to be observed has a velocity in this region.

For the magnetically enhanced QMS, it has been demonstrated that upon application of a transverse magnetic field applied in the *x*-*z* plane (positive electrode pair) of the QMF an increase in performance is observed compared with $\boldsymbol{B} = 0$ (conventional case). Theoretically, an ultimate increase in instrument performance is predicted; maximum resolution was found to increase by a factor of ~2 and for the same ion transmission (of ~5%), resolution increased by ~75%. Further optimisation of QMF parameters should lead to further improved performance. This simple method of performance enhancement cannot be achieved with a conventional QMF (without magnetic field applied) by adjusting the U/V ratio alone.

The theory underpinning the behaviour of the magnetically enhanced QMS has been investigated in detail. It has been demonstrated through the use of a novel stability diagram mapping method also by analytical analysis that application of a transverse magnetic field causes the stability zone boundary to shift depending on the field orientation. For operation in the first quadrant of stability zone 1, it has been shown that applying the magnetic field in the *x*-*z* plane (positive electrode pair plane) leads to increased instability on the low mass side of a mass peak; by contrast applying the magnetic field in the *y*-*z* plane (negative electrode pair) leads to increased instability on the high mass side of a mass peak. These results have been verified experimentally. It was found that a larger magnitude magnetic field is required in the *y*-*z* plane (compared to the *x*-*z* plane) for the effect to be observed.

The improvement in performance with a transverse magnetic field applied along the *x* axis was investigated by considering ion transmission factors. It was found that for certain magnetic field conditions, inherently stable ions are more confined and the transition between bounded (stable) and unbounded (unstable) ions is sharper when compared to the case without a magnetic field applied.

A detailed simulation study was carried out to investigate the effect of altering various operating and geometrical parameters. It was found that for the magnetically enhanced QMF, rf frequency and ion energy are of particular importance. These parameters affect the velocity of an ion and therefore the Lorentz force the ion experiences. The magnetically enhanced QMS was simulated with circular cross section electrodes. QMFs with circular cross section electrodes are commonly used as they are easier to manufacture and align (than the ideal hyperbolic form) making them more economically viable. However, using circular electrodes leads to reduced performance in terms of ion transmission, resolution and irregular peak shape. It was predicted through simulation studies that applying a magnetic field along the *x* axis leads to improved performance with circular cross section electrodes compared to the conventional case with no magnetic field applied. The magnetic field applied along the QMF *x* axis leads to a reduction in the long low mass tail which is typically with no magnetic field applied. For QMF designs with circular cross section electrodes and transverse magnetic field applied along *x*, an increase in maximum resolution of ~150% was predicted using the theoretical model.

Low cost QMS instruments without a pre-filter have been simulated using simulation software QMS-3D. For a magnetically enhanced QMF, fringe effects associated with magnetic fields will also influence ion motion particularly in the entrance region. Extending the model to include this case would provide a powerful means of predicting behaviour and optimising design parameters for the magnetically enhanced case.

Future work should investigate, experimentally and theoretically, the effect of the magnetic field on the QMS instrument operating in higher stability zones. Furthermore, experimental results obtained hitherto have been for a relatively low resolution QMS and verification of performance enhancement for a high resolution instrument is necessary.

A magnetically enhanced QMS has been demonstrated using a dynamic transverse magnetic field manually ramped in sync with the electrode potentials of a commercial QMS. The natural progression of this work would be to automatically ramp the magnetic field in accordance with the electrode potentials using an electronic trigger. However, the possibility of frequency sweeping the QMF and incorporating static bar magnets within the electrodes or outside the vacuum chamber should also be investigated. This method of operation could provide magnetic enhancement without the need for electromagnets which increase the system size, weight and power required. Another advantage associated with frequency sweeping is that the mass range can be adjusted electronically. The long term goal of this work is to build and test a portable, rugged system (with analytical performance measures comparable to an equivalent benchtop instrument) that can be used in harsh environments for real-time on site monitoring.

Appendix A : Characteristic Curves

The canonical form of the Mathieu equation is given by equation 3.32 and repeated here for convenience:

$$\frac{d^2u}{d\xi^2} + (a_u - 2q_u\cos(2\xi))u = 0 \qquad \text{(A.1)}$$

This is a linear, second order equation with periodic coefficients. The solution takes different forms according to the values of a and q. The theory of Mathieu functions is covered in detail by McLachlan (N. W. McLachlan, Theory and application of Mathieu functions vol. 127: Dover Publications New York, 1964.).

Particular Series Solutions

Solution when q = 0 (i.e., dc only QMF)

$$\frac{d^2u}{d\xi^2} + au = 0 \quad \text{(A.2)}$$

Since:

$$\frac{d^2u}{d\xi^2} = -au$$

Then, $u = \pm\cos(m\xi)$ or $u = \pm\sin(m\xi)$

where: $a = m^2$, and m =1, 2, 3, …

Hence, there are pairs of distinct solutions: $\pm\cos(\xi)$, $\pm\sin(\xi)$, $\pm\cos(2\xi)$, $\pm\sin(2\xi)$, etc…

Since:

$$\frac{d}{d\xi}(\cos(m\xi)) = -m\sin(m\xi)$$

$$\frac{d}{d\xi}(\sin(m\xi)) = m\cos(m\xi)$$

When m = 0, the respective solutions are +1, 0. Since, $\cos(0) = 1$ and $\sin(0) = 0$ (assuming that the coefficient of $\cos(mz)$ and $\sin(mz)$ is unity for all q).

Periodic Solutions when $q \neq 0$

When $q \neq 0$, a and q must be interrelated for the solution to have period π or 2π and a is some function of q:

$$a = f(q)$$

Let,

$a = m^2 + \alpha_1 q + \alpha_2 q^2 + \alpha_3 q^3 + \cdots$ (A.3)

Then $a = m^2$ is obtained when q = 0 and the solution is as the previous section (for q = 0.

Particular Even Solution: First Order (m = 1)

For $a = m^2 = 1$, then from (A.3) for $q \neq 0$ we have:

$a = 1 + \alpha_1 q + \alpha_2 q^2 + \alpha_3 q^3 + \cdots$ (A.4)

When q = 0, the solutions should reduce to $u = \pm\cos(\xi)$ or $u = \pm\sin(\xi)$. For the solution to reduce to $u = \pm\cos(\xi)$, let,

$u = \cos(\xi) + qc_1(\xi) + q^2c_2(\xi) + q^3c_3(\xi) + \cdots$ (A.5)

where: c_1, c_2, … are functions of ξ to be determined.

Each term in equation (A.1) in considered separately. Taking the 2nd derivative of (A.5) and using the value for *a* from (A.4), we obtain:

- *For u'' term*: $\frac{d^2u}{d\xi^2} = -\cos(\xi) + qc_1'' + q^2c_2'' + q^3c_3'' + \cdots,$

- *For au term*: $au = (1 + \alpha_1 q + \alpha_2 q^2 + \alpha_3 q^3 + \cdots) \times (\cos(\xi) + qc_1(\xi) + q^2c_2(\xi) + q^3c_3(\xi) + \cdots)$

$\boldsymbol{q^6}$	$\boldsymbol{q^5}$	$\boldsymbol{q^4}$	$\boldsymbol{q^3}$	$\boldsymbol{q^2}$	$\boldsymbol{q^1 = q}$	
			$q^3\mathrm{c}_3(\xi)$	$q^2\mathrm{c}_2(\xi)$	$q\mathrm{c}_1(\xi)$	$\cos(\xi)$
			$q^3\alpha_3$	$q^2\alpha_2$	$q\alpha_1$	1
			$q^3\mathrm{c}_3(\xi)$	$q^2\mathrm{c}_2(\xi)$	$q\mathrm{c}_1(\xi)$	$\cos(\xi)$
		$q^4\alpha_1\mathrm{c}_3(\xi)$	$q^3\alpha_1\mathrm{c}_2(\xi)$	$q^2\alpha_1\mathrm{c}_1(\xi)$	$q\alpha_1\cos(\xi)$	
	$\cdots$	$\cdots$	$q^3\alpha_2\mathrm{c}_1(\xi)$	$q^2\alpha_2\cos(\xi)$		
$\cdots$	$\cdots$	$\cdots$	$q^3\alpha_3\cos(\xi)$			

$$\therefore au = \cos(\xi) + q(\mathrm{c}_1(\xi) + \alpha_1\cos(\xi)) + q^2(\mathrm{c}_2(\xi) + \alpha_1\mathrm{c}_1(\xi) + \alpha_2\cos(\xi))$$

$$+ q^3(\mathrm{c}_3(\xi) + \alpha_1\mathrm{c}_2(\xi) + \alpha_2\mathrm{c}_1(\xi) + \alpha_3\cos(\xi))$$

Consider the *q* containing term of equation (A.1),

- *For* $-(2q\cos(2\xi))u$ *term*: $-(2q\cos(2\xi))u = -2q\cos(2\xi) \times (cos(\xi) + qc_1(\xi) + q^2c_2(\xi) + q^3c_3(\xi) + \cdots)$

$\boldsymbol{q^4}$	$\boldsymbol{q^3}$	$\boldsymbol{q^2}$	$\boldsymbol{q^1 = q}$	
	$q^3\mathrm{c}_3(\xi)$	$q^2\mathrm{c}_2(\xi)$	$q\mathrm{c}_1(\xi)$	$\cos(\xi)$
			$-(2q\cos(2\xi))$	
$\cdots$	$-(2q^3\,\mathrm{c}_2(\xi)\cos(2\xi))$	$-(2q^2\,\mathrm{c}_1(\xi)\cos(2\xi))$	$-q(\cos(\xi) + \cos(3\xi))$	

Trigonometric Product-to-sum identity used: $\cos\theta\cos\emptyset = \frac{\cos(\theta-\emptyset)+\cos(\theta+\emptyset)}{2}$

$$-(2q\cos(2\xi))u$$
$$= -q(\cos(\xi) + \cos(3\xi)) - (2q^2\,\mathrm{c}_1(\xi)\cos(2\xi))$$
$$- (2q^3\,\mathrm{c}_2(\xi)\cos(2\xi))$$

Equating like powers of q:

Powers of q	**Equating Terms**
q^0	$\cos\xi - \cos\xi \equiv 0$ (A.6)
q^1	$c_1'' + c_1 - \cos 3\xi + (\alpha_1 - 1)\cos\xi = 0$ (A.7)
q^2	$c_2'' + c_2 + \alpha_1 c_1 - 2c_1\cos 2\xi + \alpha_2\cos\xi = 0$ (A.8)
q^3	$c_3'' + c_3 + \alpha_1 c_2 + \alpha_2 c_1 - 2c_2\cos 2\xi + \alpha_3\cos\xi = 0$ (A.9)

For equations (A.7-A.9), the complementary function is omitted. For example, the complementary function of (A.7) would violate the convention that the coefficient of $\cos(m\xi)$ is unity for all q (McLachlan). Furthermore, $\sin(\xi)$ is odd.

If there are multiple non-homogeneous terms then their particular integrals can be found separately and then added together.

For q^1 (A. 7):

The particular integral for the term $(\alpha_1 - 1)\cos\xi$ (i.e., $c_1'' + c_1 = -(\alpha_1 - 1)\cos\xi$)

is a non-periodic function (due to the ξ factor): $0.5(\alpha_1 - 1)\xi\sin\xi$

$\therefore$ since u is to be periodic $\alpha_1 = 1$, thus eliminating this term from (A.7), which leaves the other non-homogeneous term:

$c_1'' + c_1 = \cos 3\xi$ (A.7a)

If we assume a solution of the kind: $c_1(\xi) = A\cos(3\xi) + B\sin(3\xi)$

$$c_1''(z) = -9A\cos(3\xi) - 9B\sin(3\xi)$$

Then:

$$c_1(\xi) + c_1''(\xi) = (A\cos(3\xi) + B\sin(3\xi)) + (-9A\cos(3\xi) - 9B\sin(3\xi))$$

$$c_1(\xi) + c_1''(\xi) = (A - 9A)\cos(3\xi) + (B - 9B)\sin(3\xi)$$

Equating the right hand side with that of (A.7a):

$-8A = 1$ and $B = 0$

Therefore:

$$c_1(\xi) = -\frac{1}{8}\cos 3\xi$$

Note: the general formula for particular integrals of the kind, $v'' + v = A\cos m\xi$ (similar to (A.7a)) is:

$-\frac{A}{(m^2-1)}\cos m\xi$ (A.7b)

where, $m \neq 1$.

<u>For q^2 (A.8):</u>

$c_2'' + c_2 + \alpha_1 c_1 - 2c_1\cos 2\xi + \alpha_2\cos\xi = 0$ (A.8)

Substituting for α_1 and c_1:

$$c_2'' + c_2 - \frac{1}{8}\cos 3\xi + \frac{2}{8}\cos 3\xi\cos 2\xi + \alpha_2\cos\xi = 0$$

Using trigonometric product-to-sum identity for $\cos(3\xi)\cos(2\xi)$:

Trig. ID

$$\cos\theta\cos\emptyset = \frac{\cos(\theta-\emptyset)+\cos(\theta+\emptyset)}{2}$$

$$\frac{2}{8}\cos 3\xi\cos 2\xi = \frac{\cos(3\xi-2\xi)+\cos(3\xi+2\xi)}{2}$$

$$\rightarrow \frac{1}{8}(\cos(\xi)+\cos(5\xi))$$

Substituting into (A.8):

$$c_2'' + c_2 - \frac{1}{8}\cos 3\xi + \frac{1}{8}\cos 5\xi + \left(\frac{1}{8}+\alpha_2\right)\cos\xi = 0$$

As previously (eqn (A.7)) the particular integral pertaining to $\left(\frac{1}{8}+\alpha_2\right)\cos\xi$ is non-periodic, therefore: $\alpha_2 = -\frac{1}{8}$

Leaving:

$$c_2'' + c_2 = \frac{1}{8}\cos 3\xi - \frac{1}{8}\cos 5\xi$$

Using the general formula for particular integrals of this type (A.7b), the particular integral is:

$$c_2 = -\frac{1}{64}\cos 3\xi + \frac{1}{192}\cos 5\xi$$

$$c_2 = \frac{1}{64}\left(-\cos 3\xi + \frac{1}{3}\cos 5\xi\right)$$

For q^3 (A.9):

Proceeding in like manner:

$$c_3'' + c_3 + \alpha_1 c_2 + \alpha_2 c_1 - 2c_2 \cos 2\xi + \alpha_3 \cos \xi = 0 \qquad \text{(A.9)}$$

Substituting for α_1, α_2, c_1, and c_2:

$$c_3'' + c_3 - \frac{1}{64}\cos 3\xi - \frac{1}{192}\cos 5\xi + \frac{1}{64}\cos 3\xi$$
$$+ 2\left(\frac{1}{64}\cos 3\xi - \frac{1}{192}\cos 5\xi\right)\cos 2\xi + \alpha_3 \cos \xi = 0$$

Using the product-to-sum trig ID as before:

$$\frac{2}{64}\cos 3\xi \cos 2\xi = \frac{1}{64}(\cos \xi + \cos 5\xi)$$

$$-\frac{2}{192}\cos 5\xi \cos 2\xi = -\frac{1}{192}(\cos 3\xi + \cos 7\xi)$$

Substituting into (A.8):

$$c_3'' + c_3 - \frac{1}{192}\cos 3\xi + \left(\frac{1}{64} + \frac{1}{192}\right)\cos 5\xi - \frac{1}{192}\cos 7\xi + \left(\frac{1}{64} + \alpha_3\right)\cos \xi = 0$$

As previously the particular integral pertaining to $\left(\frac{1}{64} + \alpha_3\right)\cos \xi$ is non-periodic, therefore:

$$\alpha_3 = -\frac{1}{64}$$

Leaving:

$$c_3'' + c_3 = \frac{1}{192}\cos 3\xi - \left(\frac{1}{48}\right)\cos 5\xi + \frac{1}{192}\cos 7\xi = 0$$

Using the general formula (A.7b) to find the particular integral:

$$c_3 = -\frac{1/_{192}}{8}\cos 3\xi + \frac{1/_{48}}{24}\cos 5\xi + \frac{1/_{192}}{48}\cos 7\xi$$

$$c_3 = -\frac{1}{1536}\cos 3\xi + \frac{1}{1152}\cos 5\xi + \frac{1}{9216}\cos 7\xi$$

$$c_3 = -\frac{1}{512}\left(\frac{1}{3}\cos 3\xi - \frac{4}{9}\cos 5\xi + \frac{1}{18}\cos 7\xi\right)$$

<u>Equating powers q^4:</u>

$$\alpha_4 = -\frac{1}{1536}$$

$$c_4 = \frac{1}{4096}\left(\frac{11}{9}\cos 3\xi + \frac{1}{6}\cos 5\xi - \frac{1}{12}\cos 7\xi + \frac{1}{180}\cos 9\xi\right)$$

And so on, proceeding in a similar manner for higher powers of q…

Substituting these constants back into the original assumed solution (A.5), gives a solution of Mathieu's equation, periodic in ξ, with period 2π (first order solution). Equation (A.5) is repeated here for convenience:

$u = \cos(\xi) + qc_1(\xi) + q^2c_2(\xi) + q^3c_3(\xi) + \cdots$ (A.5)

α terms	**α factors**	***c terms***	***c factors***
α₁	1	**c₁**	$-\frac{1}{8}\cos 3\xi$
α₂	$-\frac{1}{8}$	**c₂**	$\frac{1}{64}\left(-\cos 3\xi+\frac{1}{3}\cos 5\xi\right)$
α₃	$-\frac{1}{64}$	**c₃**	$-\frac{1}{512}\left(\frac{1}{3}\cos 3\xi-\frac{4}{9}\cos 5\xi+\frac{1}{18}\cos 7\xi\right)$
α₄	$-\frac{1}{1536}$	**c₄**	$\frac{1}{4096}\left(\frac{11}{9}\cos 3\xi+\frac{1}{6}\cos 5\xi-\frac{1}{12}\cos 7\xi+\frac{1}{180}\cos 9\xi\right)$

This solution is denoted by $ce_1(\xi,q)$ (where, '*ce*' stands for 'cosine-elliptic') and is represented by the following series (only considered here up to the 4th power):

$$ce_1(\xi,q)=\cos\xi-\frac{1}{8}q\cos 3\xi+\frac{1}{64}q^2\left(-\cos 3\xi+\frac{1}{3}\cos 5\xi\right)-\frac{1}{512}q^3\left(\frac{1}{3}\cos 3\xi-\frac{4}{9}\cos 5\xi+\frac{1}{18}\cos 7\xi\right)+\frac{1}{4096}q^4\left(\frac{11}{9}\cos 3\xi+\frac{1}{6}\cos 5\xi-\frac{1}{12}\cos 7\xi+\frac{1}{180}\cos 9\xi\right)$$

(A.10)

Note: These functions in (A.10) are even in ξ, being unchanged if $-\xi$ is written for ξ.

The value of a necessary to find this solution is obtained by substituting for α into equation (A.3), which is repeated here for convenience:

$$a=m^2+\alpha_1 q+\alpha_2 q^2+\alpha_3 q^3+\cdots \qquad \text{(A.3)}$$

The first order (m = 1), even solution is given by:

$$a=1+q-\frac{1}{8}q^2-\frac{1}{64}q^3-\frac{1}{1536}q^4+\frac{11}{36864}q^5+O(q^6) \qquad \text{(A.11)}$$

The value of a found for a given q is known as the characteristic number of the Mathieu function $ce_1(\xi,q)$. Note: when q = 0 (dc only for QMF), a = 1, and the right hand side of equation (A.10) reduces to $\cos\xi$. The notation used here is the same as McLachlan. The notation $ce_m(\xi,q)$ signifies a cosine type of Mathieu function of order m, which reduces to $\cos m\xi$ when $q = 0$.

Particular Odd Solution: First Order (m = 1)

As shown for the solutions to equation (A.2), the other solution (when $m = 1$) reduces to $\sin\xi$ when $q = 0$. Similar to the even case we can assume a solution,

$$u = \sin(\xi) + qs_1(\xi) + q^2 s_2(\xi) + q^3 s_3(\xi) + \cdots \qquad \text{(A.12)}$$

Proceeding in a similar manner as with the even case we obtain sine type of Mathieu function which is denoted $se_1(\xi,q)$ (where, '*se*' stands for 'sine-elliptic'):

$$se_1(\xi,q) = \sin\xi - \frac{1}{8}q\sin 3\xi + \frac{1}{64}q^2\left(\sin 3\xi + \frac{1}{3}\sin 5\xi\right) - \frac{1}{512}q^3\left(\frac{1}{3}\sin 3\xi + \frac{4}{9}\sin 5\xi + \frac{1}{18}\sin 7\xi\right) + \frac{1}{4096}q^4\left(-\frac{11}{9}\sin 3\xi + \frac{1}{6}\sin 5\xi + \frac{1}{12}\sin 7\xi + \frac{1}{180}\sin 9\xi\right)$$

(A.13)

The Mathieu function is only shown up to and including the 4th power term. The value of a necessary for this solution is:

$$a = 1 - q - \frac{1}{8}q^2 + \frac{1}{64}q^3 - \frac{1}{1536}q^4 - \frac{11}{36864}q^5 + O(q^6) \qquad \text{(A.14)}$$

This value of a for a given q is the characteristic number of the Mathieu function $se_1(\xi,q)$, which is odd and periodic in ξ with period 2π.

Comment: First Order Even and Odd Solutions

Since $\cos\xi = \sin\frac{\pi}{2} - \xi$, then if ξ is replaced with $\frac{\pi}{2} - \xi$ in (A.10) and q is replaced by $-q$ in we obtain (A.13) and the reverse can be achieved. These two first order periodic Mathieu functions (ce_1 and se_1) are not solutions of the same equation (except for the case $q = 0$) because the values of a differ for each.

The characteristic numbers for ce_m and se_m (for order m) are designated by a_m and b_m respectively (McLachlan). The lowest order characteristic Mathieu functions (which correlate to boundaries of stability zone 1) are:

$$a_0 = -\frac{1}{2}q^2 + \frac{7}{128}q^4 - \frac{29}{2304}q^6 + \frac{68687}{18874368}q^8 + O(q^{10}) \qquad \text{(A.15)}$$

$$b_1 = 1 - q - \frac{1}{8}q^2 + \frac{1}{64}q^3 - \frac{1}{1536}q^4 - \frac{11}{36864}q^5 + O(q^6) \qquad \text{(A.16)}$$

For the QMF, these boundaries refer to the one-dimensional x stable boundaries closest to the origin. They correspond to the values, $\beta_x = \beta(a,q) = 0$ and $\beta_x = \beta(a,q) = 1$ respectively. The 1-dimensional y stable boundaries can be found by substituting for $-a$ into (A.15) & (A.16) for $\beta_y = \beta(-a,-q) = \beta(-a,q) = 1$ and $\beta_y = \beta(-a,-q) = \beta(-a,q) = 0$ respectively. These boundaries are illustrated in figure A.1 for $0 \leq q \leq 2$.

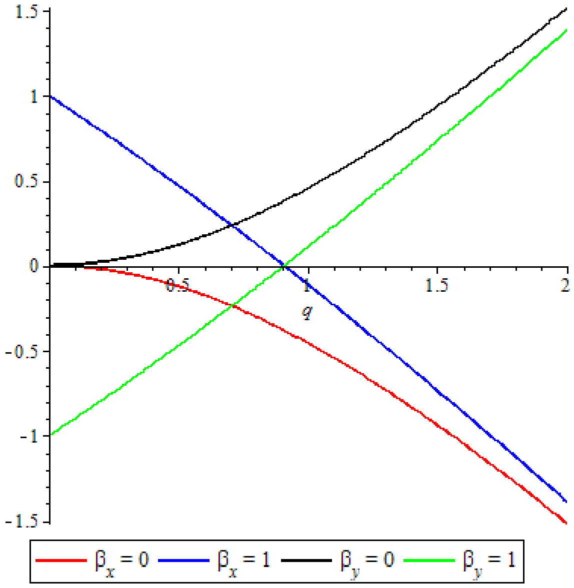

Figure A.1: Stability zone 1 boundaries

Appendix B : Ramped Magnetic Field

The uniformity of the field on the central axis in the region between the coils was measured with a Hall effect probe (Hirst Magnetic Instruments Ltd., UK) showing acceptable homogeneity[12].

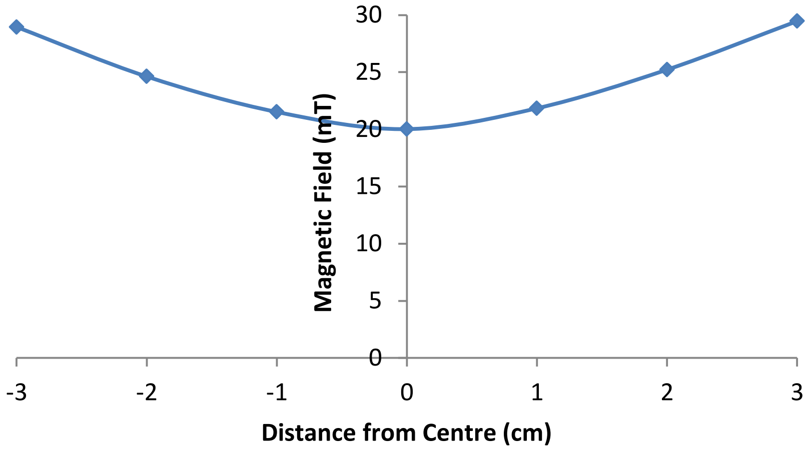

Figure B.1: Magnetic Field (mT) versus Distance (cm) from centre of Helmholtz coils on the central axis (constant current, *I* = 100mA)

Linear ***B*** field versus current response at the centre of Helmholtz coil pair:

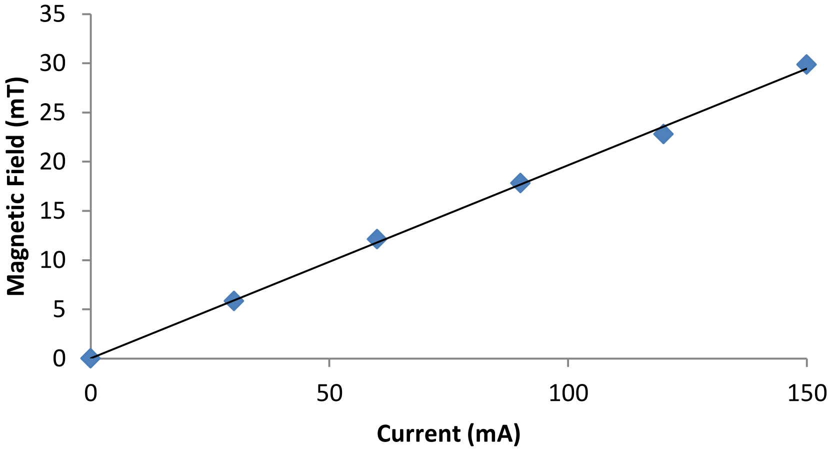

Figure B.2: Magnetic Field Intensity (mT) versus Current (mA) at centre of Helmholtz Coils

---

[12] For conventional Helmholtz type (air filled) coils the magnetic field intensity reduces with distance from the centre. With the iron yoke and pole pieces, the opposite occurs and the field intensity increases as the pole face is approached.

The Helmholtz coil resistive load was measured as ~180.3Ω when connected in series. A custom built voltage ramp was readily available. The voltage ramp has an adjustable ramping rate ranging from 0.1V/s to 2V/s. The voltage ramp gives a repeating triangular waveform from 0V to 10V to 0V, etc. This was used as the input for a voltage controlled current sink such that the current waveform through the Helmholtz coils matched the input voltage waveform.

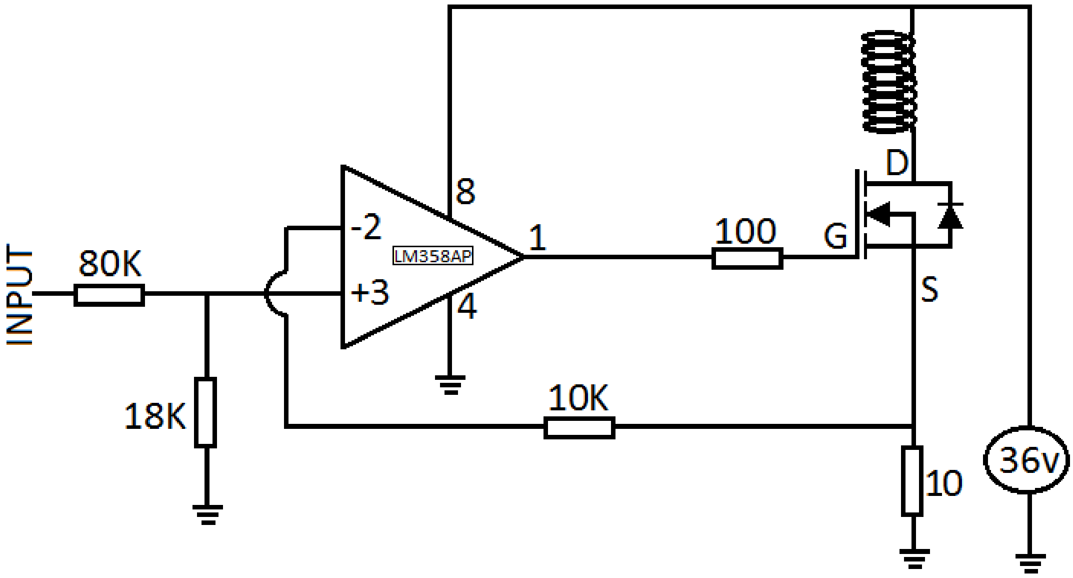

Figure B.3: Simplified Current Amplifier circuit diagram

In negative feedback configuration the output of the op-amp closely follows the input voltage. Therefore the voltage across the 10Ω resistor is approx. equal to the input voltage and controls the current through the Helmholtz coils.

Appendix C : List of Publications

Journals

1. J. R. Gibson, K. G. Evans, S. U. Syed, **S. Maher**, and S. Taylor, "A method of computing accurate 3D fields of a quadrupole mass filter and their use for prediction of filter behaviour," Journal of the American Society for Mass Spectrometry, vol. 23, pp. 1593-1601, 2012.
2. **S. Maher**, S. U. Syed, D. M. Hughes, J. R. Gibson, and S. Taylor, "Mapping the Stability Diagram of a Quadrupole Mass Spectrometer with a Static Transverse Magnetic Field Applied," Journal of the American Society for Mass Spectrometry, pp. 1-8, 2013.
3. S . U. Syed, T. J. Hogan, M. J. A. Joseph, **S. Maher**, and S. Taylor, "Quadrupole Mass Filter: Design and Performance for Operation in Stability Zone 3," Journal of the American Society for Mass Spectrometry, 24.10: 1493-1500, 2013.
4. V. A. Leus, R. T. Smith, and **S. Maher**, "The Physical Entity of Vector Potential in Electromagnetism," Applied Physics Research, vol. 5, p. p56, 2013.
5. S. U. Syed, **S. Maher**, and S. Taylor, "Quadrupole Mass Filter operation under the influence of magnetic field," Journal of Mass Spectrometry, 48.12: 1325-1339, 2013.
6. ***S. Maher**, et al., "Magnetically Enhanced Quadrupole Mass Spectrometer," (in preparation for submission).*

Conferences

1. **S. Maher**, S. U. Syed, J. Sreekumar, J. R. Gibson, and S. Taylor, “Performance enhancement for miniature QMS through application of a magnetic field,” The 8th Harsh Environment Mass Spectrometry (HEMS) Workshop, St. Pete Beach, Florida, USA, 2011.
2. S. U. Syed, **S. Maher**, J. R. Gibson, and S. Taylor, “Quadrupole Mass Spectrometry under the Influence of a Magnetic Field,” IET/IOP Meeting: Mass Spectrometry, Surface Tomography and Sensing, Liverpool, UK, 2012.
3. S. U. Syed, **S. Maher**, J. R. Gibson and S. Taylor, “Performance of a QMS operating in stability zones 1 and 3 under the influence of Magnetic Field,” British Mass Spectrometry Society Annual Meeting, AstraZeneca Conference Facility, Alderley Edge, UK, 2012.
4. **S. Maher**, S. U. Syed, J. R. Gibson, and S. Taylor, “Mapping the Stability Diagram of a QMS with an applied Magnetic Field,” 60th American Society for Mass Spectrometry Annual Conference, Vancouver, British Columbia, Canada, 2012.
5. **S. Maher**, S. U. Syed, and S. Taylor, “Resolution Enhancement of an RGA with Transverse Magnetic Field Applied,” VS3: 3rd Vacuum Symposium UK, Ricoh Arena, Coventry, UK, 2012.
6. S. U. Syed, **S. Maher**, T. J. Hogan, M. J. Joseph, and S. Taylor, “Design and Performance of Quadrupole Mass Filter operating in Stability Zones 1 and 3,” 61st American Society for Mass Spectrometry Annual Conference, Minneapolis, USA, 2013.

7. **S. Maher**, B. Brkic, and S. Taylor, “Calibration of a Membrane Inlet Mass Spectrometer for Environmental Monitoring,” 61st American Society for Mass Spectrometry Annual Conference, Minneapolis, USA, 2013.
8. V. A. Leus, R. T. Smith, and **S. Maher**, “Two Types of Electromagnetic Induction Existing in Nature,” 34th Progress In Electromagnetics Research Symposium (PIERS), Stockholm, Sweden, 2013.
9. **S. Maher**, F. P. Jjunju, S. U. Syed, and S. Taylor, “Performance of a Quadrupole Gas Analyser Operating in Stability Zones 1 and 3,” VS4: 4th Vacuum Symposium UK, Ricoh Arena, Coventry, UK, 2013.
10. F. P. Jjunju, A. Li, H. Hsu, P. Wei, **S. Maher**, S. Taylor, and R. G. Cooks, “Ambient Analysis of Non-basic Nitrogen compounds in Petroleum Oil using Desorption Atmospheric Pressure Chemical Ionization,” Royal Society of Chemistry, Chemistry in the Oil Industry XIII, Manchester Conference Centre, Manchester, UK, 2013.
11. [Article] **S. Maher**, “Calibration of a Membrane Inlet Mass Spectrometer for Environmental Monitoring”, BMSS newsletter, Mass Matters, 72nd ed., p22, 2013.

Awards

- ✓ Harsh Environment Mass Spectrometry - Student of Note
- ✓ Richard A. Schaeffer Memorial Award
- ✓ British Mass Spectrometry Society Travel Grant
- ✓ University of Liverpool Travel Grant
- ✓ American Society for Mass Spectrometry Travel Award
- ✓ Royal Society of Chemistry Student Award